STUDIES OF ELEMENTARY REACTIONS OF INTEREST IN HYDROCARBON PYROLYSIS

A thesis submitted for the degree of Doctor of Philosophy

by Phillip David Lightfoot

Worcester College, Oxford

Hilary Term 1986



STUDIES OF ELEMENTARY REACTIONS OF INTEREST IN HYDROCARBON PYROLYSIS

A thesis submitted for the degree of Doctor of Philosophy

by Phillip David Lightfoot

Worcester College, Oxford Hilary Term 1986

Abstract

A novel hydrogen atom source, involving the 193.3 nm photolysis of nitrous oxide in the presence of hydrogen, is described. The system is shown to provide a very clean source of hydrogen atoms, particularly at temperatures above 400K. The H + C_2H_4 addition reaction is studied as a function of pressure (50-750 Torr He) and temperature (285-604K). Resonance fluorescence was used to monitor hydrogen atom concentrations in real time, following excimer (ArF) photolysis of the N_2O/H_2 precursor. The data are analysed using the Troe factorisation method. A model is developed, which allows the accurate calculation of the rate constant for the H + C_2H_4 reaction over a wide range of temperature and pressure.

The direct observation of equilibration in the H + C_2H_4 = C_2H_5 system is reported for the first time, at temperatures between 775 and 850K. Hydrogen atom concentrations were monitored by resonance fluorescence, following 193.3 nm photolysis of the ethylene substrate. The equilibrium constant for the system, K_c, is determined much more precisely than has previously been possible. The standard heat of formation of the ethyl radical, $\Delta H^o_{f,298}(C_2H_5)$, is evaluated from the measured values of $K_c(T)$, using Third Law methods and the known molecular and atomic parameters of H, C_2H_4 and C_2H_5, giving $\Delta H^o_{f,298}(C_2H_5)$ = 28.36 ± 0.40 kcalmol^{-1}. The quoted errors refer to 95.45% confidence limits and include contributions from the scatter of the data and from estimates of possible systematic errors.

An excimer laser flash photolysis/ gas chromatographic end product analysis apparatus is described. The design of the photolysis cell allows its entire contents to be transferred to the analysis column, and enables total C_3 hydrocarbon yields as low as 2.6×10^{12} molecules to be detected. A study of the photolysis of acetone at 193.3 nm is presented. The dependence of product yields on pressure (10-500 Torr He), temperature (300,600K), laser pulse energy and the presence of radical scavengers (NO,C_2H_4) is described. Under all experimental conditions, methyl radicals account for >95% of the radical products of the photolysis. The ArF photolysis of acetone is demonstrated to provide a very clean source of methyl radicals, suitable for use in conventional laser flash photolysis /kinetic spectroscopy experiments, at temperatures of up to 825K.

Experiments are described, in which ethane and ethane/propylene mixtures, diluted to ∿5% in nitrogen, were pyrolysed in a quartz jet-stirred reactor. Temperatures and conversions comparable to those achieved in industrial pyrolysis were employed. A kinetic model of ethane pyrolysis is developed, which qualitatively reproduces the experimental results. It is shown that the model predictions are extremely sensitive to a number of poorly defined rate constants.

Acknowledgements

I would like to take this opportunity to thank some of the many people who have aided and abetted over the last few years.

Especial thanks to my supervisor, Mike Pilling. It has been a privilege and a great pleasure to work in his group; his unfailing enthusiasm has been a great encouragement. Thanks also to the members of the group for advice and assistance. In particular: Mark, who explained the intricacies of the resonance fluorescence apparatus; Andy, who did the same for the chromatograph and Steve, who performed some of the acetone experiments.

Thanks to Arthur Gough and his staff at I.C.I. Wilton, for making me very welcome and for providing funding after my grant had expired. Thanks also in this respect to Worcester College and the University Hardships Commitee.

Lastly, I would like to thank my fiancee, Patricia, for encouragement and assistance much above and beyond the call of duty during the writing and preparation of this thesis, and without whom things would have been a lot more difficult.

List of Contents

Chapter 1

Introduction 1

1.1 Hydrocarbon Cracking 1

1.1.1 Introduction 1

1.1.2 Mechanism 2

1.2 Direct Measurement of Radical Reaction Rates 7

1.2.1 Radical Sources 7

1.2.2 Radical Monitoring 10

1.3 Extrapolation and Estimation of Rate Constants 12

1.4 Aims of This Work 18

Chapter 2

The Reaction of Hydrogen Atoms With Ethylene 21

2.1 Introduction 21

2.2 Experimental 22

2.2.1 Apparatus 22

2.2.2 Data Analysis 27

2.3 Hydrogen Atom Generation 31

2.3.1 Previously Used Methods 31

2.3.2 193.3 nm Photolysis of N_2O in the Presence of H_2 32

(i) Primary Processes 33

(ii) O^3P Production 34

(iii) H Atom Production and Experimental Conditions 36

(a) $O(^1D)$ Reactions 36

(b) Timescale 38

(c) OH + H_2 Reaction 38

(d) Atom + Radical Reactions 40

(e) Conclusions 43

2.4 Results 44

2.4.1 Experiments at 285K 44

2.4.2 Experiments Above 285K 54

2.5 Fall-off Behaviour of Unimolecular Reactions 58

2.5.1 Models of Fall-off Behaviour 59

2.5.2 Application to H + C_2H_4 70

2.6 Discussion 77

Chapter 3

Direct Observation of Equilibration in the H + C_2H_4 = C_2H_5 System: The Heat of Formation of the Ethyl Radical 86

3.1 Introduction 86

3.2 Experimental 86

3.2.1 193.3 nm Photolysis of Ethylene at Elevated Temperatures 87

3.2.2 Data Analysis 88

3.3 Results and Discussion 95

3.3.1 Experiments 99

3.3.2 Simulations of the Intensity Dependence of k_1 and k_{-1} 103

(i) 800K Simulations 107

(ii) 850K Simulations 111

3.3.3 Calculation of Rate Constants and 113

Thermodynamic Parameters for the
Ethyl Radical
3.3.4 Uncertainties in the Heat of Formation of the Ethyl Radical 119
3.4 Conclusions 122

Chapter 4

The Photolysis of Acetone at 193.3 nm 123

4.1 Introduction 123
4.2 Experimental 129
4.2.1. Apparatus For Laser Flash Photolysis / End Product Analysis Experiments 129
(i) Vacuum Line 129
(ii) Laser 131
(iii) Chromatograph 132
(a) General Description 132
(b) Cell Flushing and Flow Control 133
(c) Columns and Analysis Methods 135
(iv) Photolysis Cell and Housing 136
4.2.2. Calculation of Absolute End Product Concentrations 139
(i) Measurement of Dead Volume 140
(ii) Homogeneity of Photolysis Product Distribution 140
4.2.3. Chemicals 144
4.3 Results and Discussion 146
4.3.1 Experiments at Room Temperature 146
(i) Identification of Photolysis Products 146

(ii) Yield of Acetyl Radicals 149

(iii) Dependence of Products Yields on Laser Intensity, Pressure and the Prescence of Radical Scavengers 153

(a) Ethane and Carbon Monoxide 154

(b) Methyl Ethyl Ketone 159

(c) Methane 162

(d) Ethylene 181

(e) Other Products 189

4.3.2 Experiments at 600K 193

(i) The Thermal Decomposition of Acetone 193

(ii) Product and Photolysis Yields 195

4.4 Summary 206

Chapter Five

The Pyrolysis of Ethane to High Conversions 209

5.1 Introduction 209

5.2 Experimental 212

5.2.1 Jet-Stirred Reactor 212

5.2.2 Temperature Control and Measurement 216

5.2.3 Gases, Flow Control and Calculation of Residence Times 216

5.2.4 Chromatography 218

5.3 Results 219

5.3.1 Ethane Cracking Experiments 219

5.3.2 Ethane / Propylene Co-cracking Experiments 222

5.4 Modelling 223

5.4.1 Computational Details 223

5.4.2 Thermodynamic Calculation of Rate Constants 227

5.4.3 A Simple Model of Ethane Pyrolysis 231

5.4.4 Vinyl and Allyl Radical Reactions 237

5.4.5 Effect of $\Delta H^{o}_{f,298}(C_2H_3)$ on Model 243

5.4.6 Modelling the Propylene Inhibition of Ethane Pyrolysis 252

5.5 Conclusions 257

References

Appendices

Chapter 1

Introduction

1.1 Hydrocarbon Cracking

1.1.1 Introduction

Hydrocarbon cracking is a process of enormous practical importance to the petrochemical industry. It is the method by which the naphtha fraction of crude oil, consisting typically of C_4 - C_{12} saturated, unsaturated and aromatic hydrocarbons is broken down into small, unsaturated hydrocarbons - particularly ethylene - and hydrogen, by passage through large scale cracking furnaces. Significant quantities of methane and smaller amounts of the lower aromatics such as benzene and toluene are also produced. Typical furnace operating conditions are 1100K and 2 atmospheres pressure, with residence times of the order of a second. The major product, ethylene, is a particularly important commercial molecule: it is the chemical basis for the manufacture of a large number of synthetic polymers, examples of which are polyethylene (polythene) and polyvinyl chloride (PVC), and numerous other products such as the antifreeze, ethylene glycol.

The distribution of products from a cracking furnace is complex and depends on the furnace operating conditions and the composition of the naphtha feedstock. As with any commodity, the values of the various cracking products are subject to fluctuations, determined by changes in supply and demand, and the optimum running conditions of a cracking furnace may change accordingly. In particular, it may become worthwhile to recycle some of the less valuable components in order

to improve the yields of more valuable products. Naphtha cracking is a very large scale and, therefore, expensive process. Industrial furnaces are run almost continuously with occasional and costly shutdowns for repair and maintenance and there is little room for experimentation. It would therefore be very useful if a realistic model of the cracking process were available: the effects of altering running conditions such as residence times, temperature and feedstock composition could be examined rapidly and inexpensively by computer simulation. Thus, the value of the products could be optimised without a great deal of trial and error. This kind of approach is particularly appealing as in recent years cracking furnaces have operated with, at best, small profit margins and, because of the large scale involved, very small changes in the value per tonne of the products make enormous differences to the annual profits or losses.

1.1.2 Mechanism

It is believed that gas phase reactions involving free radicals are the most important chemical processes in hydrocarbon cracking. Reactions involving carbon and hydrogen containing radicals can be classified according to the following types:

Initiation	RR'	===> R• + R'•
Decomposition	R•	===> R'• + Unsaturate
Addition	R• + Unsaturate	===> R'•
H-Transfer	R• + R'H	===> RH + R'•
Recombination	R• + R'•	===> RR'
Disproportionation	R• + R'•	===> RH + Unsaturate

Isomerisation R• ===> R'•

The above scheme demonstrates that naphtha cracking is an extremely complicated chemical process, covering a wide range of reaction types, and consequently the detailed modelling of such a system provides a severe test of the current understanding of gas kinetics and of the available experimental information. In principle, all possible unimolecular decompositions of each feedstock and product component must be considered and the reactions of all possible radicals must be allowed for, both with each other and with each molecular component. Given the complex composition of the naphtha feedstock and the consequent large number of possible radical intermediates, the total number of potential reactions is enormous.

Fortunately, however, at the temperatures employed in industrial pyrolysis, saturated hydrocarbon radicals containing more than two carbon atoms and unsaturated hydrocarbon radicals containing more than three carbon atoms are short-lived with respect to decomposition and are therefore unimportant as reactive intermediates. The relatively stable radicals for which detailed kinetic data are required are: H, CH_3, C_2H_5, C_3H_5 and possibly some C_4 allylic radicals and some aromatic radicals. Thus, although the situation is still complicated, the limited number of important radicals considerably simplifies the problem. In addition, it should be possible to estimate the rates of radical reactions with large hydrocarbons fairly accurately from the rates of the corresponding reactions with smaller hydrocarbons using, for example, Evans-Polanyi [1] type relationships between activation energies and bond dissociation energies.

Because of the complex nature of hydrocarbon pyrolysis, it is necessary to design an approach which will produce the maximum amount of useful information. With increasing access to powerful computers and the development of efficient methods for the numerical integration of stiff sets of coupled differential equations [2,3], it is now relatively straightforward to model complex reaction systems and several software packages are available [4-8]. Furthermore, recent developments in sensitivity analysis [9-12] have enabled sensitivity coefficients for reactions in very large systems to be efficiently calculated and have demonstrated its value in determining the most important reactions, or sets of reactions, in otherwise rather opaque systems. The work in Chapter 5 of this thesis shows that many of the reactions of importance in hydrocarbon pyrolysis are both poorly defined experimentally and closely interdependent, so that attempts to extract rate constant information from the results of kinetically complex experiments are subject to a great deal of uncertainty. A sensible approach, therefore, would be to use large scale modelling, coupled with sensitivity analysis, to determine the most important of the inadequately defined rate constants in the cracking scheme. The selected reactions could then be studied as directly as possible, under conditions of temperature and pressure as close to cracker operating conditions as is practically feasible.

The accuracy to which a rate constant must be known depends on the sensitivity of the model predictions to its value. For example, it is demonstrated from the ethane pyrolysis results of Chapter 5 that even small (factor of two) variations in the values of very important reactions such as the abstraction reaction of hydrogen atoms with ethane:

$$H + C_2H_6 \text{ =====> } H_2 + C_2H_5$$

can significantly affect the results of the model and hence very accurate and precise determinations of key rate constants are required.

Although, as discussed in the next section, sensitive and in principle very accurate techniques are available for the measurement of radical reaction rates, much of the published work to date has been performed at or around room temperature. Long extrapolation of low temperature data to pyrolysis conditions can be subject to considerable uncertainty, particularly for reactions which are both pressure and temperature dependent, such as the addition reaction between hydrogen atoms and ethylene:

$$H + C_2H_4 \text{ =====> } C_2H_5$$

It is thus important to measure rate constants under experimental conditions as close to those for which they are required as is possible.

Unfortunately, cracker temperatures, at around 1100K, fall somewhat above the high temperature limits of conventional time-resolved apparatus, although radical reactions have recently been directly studied at temperatures above 1000K [13,14] and Felder et al. [15] have described a flash photolysis / kinetic spectroscopy apparatus capable of measuring atom reaction rates beween 300 and 1900K. Shock tube, or more recently, homogenous laser heating [16], can be used to provide high temperatures. However, a major problem with performing experiments at cracking temperatures is that many of the reactants and products quite naturally pyrolyse under such

conditions and it can often be difficult to measure the rates of isolated reactions.

A suitable compromise would be to measure reaction rates accurately over as wide a range of experimental conditions as possible, using conventional heating methods and then extrapolate to the appropriate cracking conditions. Such an approach would be advantageous in two respects. Firstly, comprehensive data on the rate of an elementary reaction, over a wide range of experimental conditions, would provide a sensitive test of current reaction rate theories. Secondly, if an accurate description of the dependence of the rate of a reaction on temperature and pressure could be developed, it would then be possible to calculate the reaction rate under reasonably proximate experimental conditions.

At the elevated temperatures employed in hydrocarbon cracking, many reactions become effectively reversible. It is often the case that reactions are more easily measured in a single direction, a good example being the ethyl radical recombination reaction and its reverse, the symmetric thermal decomposition of n-butane:

$$C_2H_5 + C_2H_5 \text{ ===== } N\text{-}C_4H_{10}$$

The forward reaction has been accurately measured over a wide range of temperatures using molecular modulation spectroscopy [17], flash photolysis - u.v. absorption [18] and very low pressure pyrolysis [19], whereas it is difficult to measure the reverse reaction in isolation, because of the competing dissociation to produce methyl and n-propyl radicals [20]:

$$N\text{-}C_4H_{10} \text{ ===== } CH_3 + N\text{-}C_3H_7$$

It is often preferable to calculate the rate of a reverse reaction when the rate parameters for the forward reaction and accurate thermodynamic parameters for the species involved are known, rather than rely on an uncertain, indirectly determined value. The thermochemical estimation of rate constants and extrapolation of rate data out of a restricted pressure and temperature range is discussed in more detail in Section 1.3.

1.2 Direct Measurement of Radical Reaction Rates

1.2.1 Radical Sources

Baggott and Pilling [21] have comprehensively reviewed recent developments in the measurement of atom and small radical reaction rates; the purpose of this section is to provide a broad view of the techniques available.

The photolysis of a suitable precursor has been perhaps the most common method of producing free radicals. When radicals are required in low concentrations ($\sim 10^{11} - 10^{12}$ cm^{-3}), for example, when the reactions of the radical with an excess of added substrate are to be studied using a sensitive detection technique, then the choice of precursor is often not crucial, as long as it produces the desired radical and absorbs in the wavelength region of the photolysing radiation. Slagle et al. [22] have studied the $C_2H_3 + O_2$ reaction, using 193.3 nm photolysis of vinyl bromide producing both vinyl radicals and bromine atoms, but because of the very low $[C_2H_3]/[O_2]$ ratios employed (typically 2×10^{-3}), the vinyl radicals were removed exclusively by reaction with oxygen.

The choice of precursor becomes more important when high ($\sim 10^{13}$ - 10^{14} cm^{-3}) radical concentrations are needed, in, for example, studies of radical - radical reactions, where it is highly desirable to employ a symmetrical precursor to ensure that cross combination reactions are unimportant. Tulloch et al. [23] used 1,5-hexadiene as an allyl radical source and azoalkanes have often been employed for the pulsed production of alkyl radicals [24-26], although the use of azoalkanes is restricted to temperatures below 600K by their thermal instability.

Traditionally, inert gas-filled flash lamps have been employed as photolysis sources in the u.v. region, providing high intensity output across a wide spectral range. However, although cut-off filters can be used to restrict the wavelengths output from flash lamps, it can be difficult to ensure that only the precursor is photolysed; in addition, flash durations of the order of microseconds and longer restrict the useful experimental timescale of conventional flash photolysis experiments. Such problems can largely be overcome by the use of rare gas halide excimer lasers, which span much of the u.v. region. Excimer lasers provide well collimated, monochromatic u.v. radiation in short (typicaly 10 ns), high energy pulses and have been employed increasingly as sources of photolysis radiation in recent years [27-30]. Ultraviolet radiation can also be produced at lower intensities by frequency mixing techniques: frequency - quadrupled Nd:YAG radiation at 266 nm has been used to produce $O(^1D)$ atoms from ozone [31] and NH radicals in both their ground ($X^3\Sigma^-$) and first excited ($a^1\Delta$) states from N_2H_4 and NH_3 respectively [32].

Indirect photolytic radical sources suitable for time-resolved work include the pulsed mercury photosensitised decomposition of

hydrogen [33].

Infrared multiphoton dissociation (IRMPD) can be used to provide the equivalent energy of an u.v. photon and is a well established means of producing radical species [34,35]. Furthermore, IRMPD and more recently, ultraviolet multiphoton dissociation (UVMPD) have been used to provide total energies greater than are commonly available from high intensity single photon sources, enabling highly unsaturated and energetic species such as C_2 to be produced [36,37].

Radicals have also been produced for real-time kinetic work by pulsed thermal decomposition techniques. Shock wave heating has been conventionally employed: Skinner and co-workers have formed hydrogen atoms by shock heating of a number of hydrocarbons [38-40] and Frank and Just [41] used the shock-induced decomposition of nitrous oxide in the presence of hydrogen to produce both oxygen and hydrogen atoms. There has recently been interest in the use of pulsed infrared lasers to provide rapid heating of gas mixtures via fast energy transfer from a suitably absorbing bath gas. Smith et al. [42] photolysed a mixture of sulphur hexafluoride, nitrogen, hydrogen peroxide and methane with a pulsed CO_2 laser and were able to study the reaction between methane and hydroxyl radicals, formed by the rapid thermal decomposition of hydrogen peroxide, at temperatures of up to 1400K, above which thermal decomposition of the SF_6 bath gas became important.

Microwave discharge techniques have been frequently used as radical and, more particularly, atom sources in flow tubes [43-46]. Gas mixtures, commonly a diatomic gas diluted with an inert gas, are flowed through a microwave cavity, producing atoms. The atoms can be converted into other radicals by reaction downstream of the

discharge; for example, Park and Gutman [47] produced ethyl radicals by reacting chlorine atoms, formed in a microwave discharge through molecular chlorine, with ethane. Reactant gas is injected into the flow system downstream of the radical-producing zone and a steady concentration profile is set up down the flow tube. Time resolution is achieved by monitoring reactant concentrations as a function of distance down the tube. Flow tube methods are presently restricted to pressures of around 10 Torr or lower, however.

Hydrogen atoms have been produced in a number of studies using the pulsed radiolysis of molecular hydrogen [48-51], although this technique can only be used with hydrogen pressures of several hundred Torr and greater.

1.2.2 Radical Monitoring

A great number of spectroscopic techniques have been employed to monitor the concentrations of atoms and radicals in real-time experiments. The long-established methods of resonance fluorescence and resonance absorption, using microwave-driven resonance lamps as radiation sources, remain the most convenient means of following the reactions of atoms [52-54].

Laser induced fluorescence (LIF) has been widely used to detect a number of small radicals from OH [55] to C_2H_5O [56]. LIF is a very sensitive technique, capable of detecting concentrations as low as $10^6 - 10^7$ cm^{-3} under ideal (i.e. non-kinetic) conditions and has the advantage that, in favourable cases, the reactions of species in well defined vibrational states can be studied [57-59]. The use of LIF is, however, restricted by electronic quenching to pressures of a few

Torr or lower, particularly for the larger radicals and is confined to those radicals which do not strongly predissociate in the upper state.

Many forms of absorption spectroscopy have been used to monitor radical concentrations. A number of radicals exhibit strong u.v. absorption features, allowing their time dependent concentrations to be followed by monitoring the transmission of wavelength selected u.v. radiation from high intensity sources such as xenon arc lamps. The kinetics of CH_3 [26], C_2H_5 [18], CH_3O_2 [60] and CH_3CO [61] radicals, amongst others, have been studied in this way.

Several radicals of interest e.g. $^1CH_2$, NH_2 and HCO display weak or highly structured absorptions in the visible region. The advent of c.w. inert gas ion-pumped dye lasers has facilitated the study of the kinetics of these radicals, particularly in their ground states, which can be now be studied at higher pressures than are practical using LIF [62-64]. The low divergence of laser radiation enables multipass techniques to be routinely employed, greatly increasing the sensitivity of the method. The sensitivity of visible laser absorption spectroscopy can also be enhanced by placing the absorption cell inside the dye laser cavity, as demonstrated by Reilly et al. [65] who employed this method to measure HCO reaction rates.

The use of narrow bandwidth, tunable, infrared radiation from diode lasers has tremendous potential for the study of radical kinetics. Multipass techniques can be employed and specific transient species can be monitored unambiguously, a significant improvement on conventional u.v. absorption techniques, where the absorption features of radicals species frequently overlap. Laguna and Baughcum

[66] measured methyl radical reaction rates by monitoring the absorption of diode laser radiation by the ν_2 mode of the radical. However, very little data employing diode laser absorption monitoring has been published over the last few years; it appears that diode laser systems are not ideally suited to kinetic experiments, where the monitoring wavelength has to be accurately maintained over long periods of time in electrically noisy environments.

Bayes and co-workers [67] and Gutman and co-workers [68] have used photoionisation mass spectrometry (PIMS) to study, in particular, the reactions of organic free radicals with molecular oxygen. The technique is very sensitive, being capable of detecting radical concentrations as low as 10^{11} cm^{-3} and has the advantage that both reactant and product species can be monitored simultaneously, providing information on both the rates and mechanisms of radical reactions. However, PIMS is limited to pressures below a few Torr and timescales of milliseconds or longer.

Magnetic resonance techniques, such as laser magnetic resonance [69] and electron spin resonance [70], are well established techniques for the study of the reactions of small radicals in flow systems at low pressures.

1.3 Extrapolation and Estimation of Rate Constants

Despite the recent advances made in techniques for the study of radical reactions described in the last section, it is often impractical or impossible to measure rate constants under precisely the experimental conditions required for the modelling of complex

systems. Such an approach is particularly difficult at the temperatures encountered in hydrocarbon cracking, as complications due to the thermal decomposition of precursor, reactant or product species are difficult to avoid. A more realistic approach would be to measure the rate constants of important reactions over as wide a range of experimental conditions as possible and subsequently to extrapolate the data to the required experimental region, using computational techniques which are soundly based in theory.

For reactions which are temperature but not pressure dependent, measurement of the reaction rate over a temperature range sufficient to determine Arrhenius parameters for the reaction may be adequate. However, many reactions have been shown to exhibit curved Arrhenius plots when studied over a large temperature range [71,72] and thus extrapolation to high temperatures using low temperature data can lead to serious errors.

The accurate extrapolation of pressure dependent reaction rates presents a very difficult problem: both the limiting low and high pressure rate constants are often temperature dependent and in addition, the form of the pressure dependence between the two limits will be a function of transition state properties, temperature and the nature of the bath gas. The historically much used Lindemann - Hinshelwood (LH) and Rice - Ramspberger - Kassel (RRK) formalisms are now known to provide only a very qualitative description of fall-off behaviour and are hence unsuitable for use as tools for prediction or extrapolation. The most accurate description of fall-off behaviour is provided by master equation methods, coupled with Rice - Ramspberger - Kassel - Marcus (RRKM) calculations, although such techniques are very time consuming - a great disadvantage if a number of reactions

are to be modelled. In a series of recent papers, Troe [73,74] has developed a model, validated by comparison with RRKM and master equation calculations, which accurately describes the pressure dependence of reaction rates in terms of parameters which are readily calculated from a knowledge of reactant and bath gas properties. The method of Troe is discussed in detail in Chapter 2, where it is used to provide parameters for the pressure and temperature dependence of the H + C_2H_4 reaction. Comparison of the model predictions with the high temperature data given in Chapter 3 demonstrate the model's validity and it is used in Chapter 5 to estimate the H + C_2H_4 rate constant at cracker temperatures and an atmosphere pressure.

At sufficiently high temperatures, all chemical reactions become effectively reversible. It is often possible to measure the rate of a reaction much more accurately in one direction. For example, in atom addition / radical decomposition systems such as the H + C_2H_4 === C_2H_5 system, the addition rate constant can often be measured directly whereas the radical decomposition can usually be studied only indirectly. In such circumstances, the rate of the reverse reaction could be calculated from the rate of the forward reaction more accurately than it could be measured, if precise thermodynamic parameters for the species involved were available and hence the thermodynamic equilibrium constant for the reaction was well defined. Even if it were, in principle, possible to measure the rates of both forward and backward reactions accurately, a great deal of effort would be saved if half of the required rate constants could easily be calculated. The thermochemical calculation of reverse rate constants would be particularly valuable in the case of pressure dependent reactions, where the ratio of two reation rates could be evaluated

from the thermodynamics of the reaction and thus the difficult task of extrapolating data to the appropriate experimental conditions would only have to be performed once.

The thermodynamic parameters of hydrocarbon molecules are well known over a wide range of temperatures and have been tabulated by Stull et al. [75]. Although the entropies of alkyl radicals can now be calculated with reasonable accuracy, as discussed below, there is, however, a good deal of uncertainty surrounding the heats of formation of alkyl radicals other than methyl.

Alkyl radical heats of formation have traditionally been measured using radical buffer techniques, largely due to Benson and co-workers [76]. In general, the equilibrium, or approach to equilibrium, in the system:

$$RI + HI \text{ ===== } RH + I_2$$

is observed at temperatures between 500 and 800K. The above equilibrium is known to be established via the free radical mechanism:

$$I_2 + M \text{ ===== } 2I + M$$

$$RI + I \overset{1}{\underset{2}{=====}} R + I_2$$

$$R + HI \overset{3}{\underset{4}{=====}} RH + I$$

Several, apparently reasonable, assumptions about the overall kinetics and the barriers to reactions 2 and 3 are required in order to extract radical heats of formation. The values of $\Delta H_f(R^\bullet)$ so obtained have long been accepted as the best estimates and despite an increasing body of evidence suggesting that the heats of formation

obtained from halogenation experiments could be seriously and systematically in error, McMillen and Golden [77] preferred radical buffer values to those obtained by other methods in their 1982 review. Recently, Tsang has reviewed alkane pyrolysis / radical recombination [78] and radical addition / radical decomposition [79] data and has shown that the alkyl radical heats of formation calculated from the two sets of data were in good agreement and systematically between 2 and 4 $kcalmol^{-1}$ greater than those obtained from radical buffer experiments. It is worth noting that errors of 2 and 4 $kcalmol^{-1}$ in the enthalpy change for a reaction lead to errors of almost a factor of 2.5 and over a factor of 6 respectively in the calculated reverse rate constant at 1100K and greater errors at lower temperatures. The $\Delta H_{f,298}(R^{\bullet})$ values recommended by both Tsang and McMillen and Golden for a number of alkyl radicals are presented for comparison in Table 1.1.

Table 1.1

Comparison of Recommended Alkyl Radical Heats of Formation

$\Delta H^{o}_{f,298}(R^{\bullet})$ in $kcalmol^{-1}$

	C_2H_5	n-C_3H_7	s-C_3H_7	n-C_4H_9	s-C_4H_9
McMillen and Golden [77]	25.9±1	21.0±1	18.2±1	8.7±1	13.0±1
Tsang [78]	28.5±0.5	-	20.3±0.7	12.0±1.0	-
Tsang [79]	-	24.0±0.5	22.3±0.6	11.7±0.7	17.0±0.4

Recent evidence from independent sources [80,81] supports the higher value for ethyl, although Cao and Back [82] have pointed out that much of the controversy surrounding alkyl radical heats of

formation arises from the use of very ambitious error limits, and it is clear that data of high precision are required to resolve the situation. Chapter 3 describes experiments in which the equilibrium constant for the $H + C_2H_4 \text{ ===== } C_2H_5$ system was directly measured, enabling thermodynamic parameters for the ethyl radical to be obtained with much greater precision than has been possible to date.

In order to calculate equilibrium constants, entropies as well as enthalpies of reactions are required. The entropies of hydrocarbon molecules are well known [75]; alkyl radical entropies are, in general, less well known. In principle, reaction entropies can be obtained from the intercepts of plots of $\ln K_p$ vs $1/T$, but large temperature ranges are required to make the extrapolation reliable and the proc edure is complicated, in general, by a dependence of ΔH_r and ΔS_r on temperature. A more satisfactory proc edure is to use Third Law methods, as radical entropies can be accurately calculated from their moments of inertia, masses and vibrational frequencies using statistical mechanics, if these parameters are well determined. Until recently, the best estimates of alkyl radical entropies were those calculated by Purnell and Quinn [83], who estimated the vibrational frequencies of methyl and ethyl radicals; the entropies of larger radicals were calculated by estimation of the differences in entropy between the radicals and their parent alkanes.

Recently, however, Pacansky and co-workers [84-91] have directly observed the infrared spectra of a number of alkyl radicals in argon matrices at around 10K and have extended these observations through ab initio calculations. C-H stretching frequencies α to the radical centre were found to be significantly greater than those observed in alkanes and similar to olefinic C-H stretching frequencies,

suggesting that the carbon radical centre was sp^2 hybridised. The strongest radical i.r. absorption feature was assigned to the pyramidal out-of-plane bending mode of the radical centre, the frequency of which decreased with increasing alkyl substitution at the radical centre from 540 cm^{-1} for the ethyl radical to below 200 cm^{-1} for the t-butyl radical. Other radical frequencies were similar to those found in the parent molecule, apart from one C-H stretch situated on the carbon atom β to the radical centre, which was somewhat reduced in frequency owing to an in-plane interaction between the C-H bond and the p orbital containing the unpaired electron.

Thus, it is now, in general, possible to calculate alkyl radical entropies and heat capacities to high precision; the remaining uncertainties are associated with their heats of formation. The use of Third Law calculation of alkyl radical entropies and heat capacities to extrapolate thermodynamic data to 298K is demonstrated in Chapter 3 for the ethyl radical.

1.4 Aims of This Work

The work presented in this thesis represents part of a programme of experiments designed to measure the rates of elementary radical reactions, which are of both theoretical interest and of central importance in hydrocarbon pyrolysis.

The reaction between hydrogen atoms and ethylene:

$$H + C_2H_4 \underset{k_{-1}}{\overset{k_1}{=====}} C_2H_5 \qquad \text{R1,-1}$$

exemplifies the problems found in the modelling of high temperature systems: it is well into the fall-off region at the temperatures and pressures found in industrial crackers and estimation of its rate, under such conditions, from data obtained at low temperatures is prone to error.

Chapter 2 of this thesis describes the development of the 193.3 nm photolysis of nitrous oxide in the presence of hydrogen as a well defined hydrogen atom source suitable for use in experiments at temperatures up to and beyond 1000K and its use in a study of the addition rate constant, k_1 over a wide range of pressure and temperature. The pressure and temperature dependence of k_1 is analysed using the Troe factorisation method [73,74], enabling its rate under cracking conditions to be calculated more accurately than has been previously possible.

At cracking temperatures, the unimolecular decomposition of the ethyl radical, R_{-1}, is as important as the forward reaction. Calculation of k_{-1} would be relatively simple if accurate thermodynamic parameters were available for the species involved. However, as was discussed in the last section, there has been much recent controversy over alkyl radical heats of formation and the heat of formation of the ethyl radical is subject to considerable uncertainty (± 2 kcalmol^{-1}). Chapter 3 describes experiments at around 800K in which the equilibrium between hydrogen atoms, ethylene and ethyl radicals was observed directly, enabling very accurate thermodynamic parameters for the reaction and hence for the ethyl radical to be evaluated.

The reactions of the methyl radical are of great importance in

hydrocarbon pyrolysis: unlike other saturated carbon containing radicals, methyl radicals are thermally stable at cracker temperatures and build up to high concentrations, playing an important role in propagation and termination steps. The suitability of the acetone molecule as a methyl radical precursor in high temperature experiments, via its photolysis at 193.3 nm, is investigated in Chapter 4.

Chapter 5 desribes end product analysis experiments in which ethane was pyrolysed at temperatures and to conversions similar to those used in industrial furnaces. A detailed model of the kinetics of ethane pyrolysis is developed and the sensitivity of the model predictions to many poorly defined rate constants is demonstrated. On the basis of this work, the further study of a number of reactions is suggested.

Chapter 2

The Reaction of Hydrogen Atoms With Ethylene

2.1 Introduction

Despite the great amount of experimental work performed on the H + C_2H_4 system in the last 25 years [33,49,50,51,53,92-115], much of the published data on the bimolecular rate constant , k_{bi}, is not directly comparable because of the complex dependence of k_{bi} on temperature, pressure and the nature of the bath gas. For example, flow tube measurements [92,93,95,99,103,104,107,108], in which the pressure range covered is restricted to between 0.5 and 25 Torr, are invariably well into the fall-off region at temperatures around and above ambient. Attempts to determine Arrhenius parameters under such conditions are complicated by the dependence of the degree of fall-off at each temperature on both the pressure and bath gas used, and long extrapolation of data to the high pressure limit at a given temperature is difficult and subject to considerable uncertainty. Greater pressure ranges are possible and have been employed in essentially static systems where the atoms are produced photolytically [33,94,96,97,100,102, 104,106,109,112,113]. However, detailed measurements of the pressure dependence of k_{bi} have been restricted to 298K, where two independent determinations of the fall-off curve in He from 5 to several hundred Torr have been published [33,102].

The limiting high pressure rate constant has been the subject of several studies. Flash photolysis of ethylene [102,111], mercury photosensitised decomposition of hydrogen [33,98,100,104,112,113] and

pulsed radiolysis [50,51,53,101,105,112,115] have been used to produce hydrogen atoms which were monitored by resonance fluorescence, or resonance absorption. Two fairly extensive temperature dependences of k_∞ have been published by Lee et al. [111] and Sugawara et al. [51], which together cover the temperature range 193-461K, are in good agreement and quote:

$$k_\infty = (3.67 \pm 0.66)\times10^{-11}\exp(-(1042 \pm 84)/T)$$

and $$k_\infty = (4.70 \pm 0.49)\times10^{-11}\exp(-(1096 \pm 26)/T)$$

respectively, in units of molecule^{-1}cm^{3}s^{-1}. The errors quoted here and elsewhere in this chapter refer to two standard deviations, unless stated otherwise and include a Student's t where possible.

Thus, although the limiting high pressure rate constant appears to be well defined, the available fall-off data applies only to 298K. At the temperatures and pressures applicable to hydrocarbon cracking, the reaction will be significantly into the fall-off region and it is clear that more extensive measurements of the pressure dependence of the bimolecular rate constant are required at temperatures above ambient.

This chapter describes experiments in which the bimolecular rate constant for the reaction of hydrogen atoms with ethylene has been studied as a function of temperature (285-604K) and pressure (50-750 Torr He). Hydrogen atoms were monitored by Lyman α resonance fluorescence and produced using 193.3 nm photolysis of nitrous oxide in the presence of hydrogen, a new method which is shown to provide a clean, well-defined and widely applicable atom source, particularly at temperatures above 400K. Methods of modelling the fall-off behaviour of unimolecular reactions are discussed and the experimental data analysed using the method of Troe, facilitating

comparison of the present data with previously published work and allowing a model to be developed, which can be used to predict the rate constant for the title reaction accurately, under conditions where no experimental data is available.

2.2 Experimental

2.2.1 Apparatus

The apparatus used in this study is shown schematically in Figure 2.1. The detailed design and construction of the apparatus has been presented by Brouard [116] and consequently only a general description is given here.

The multiport photolysis cell was of stainless steel contruction, heated by eight 3/8" 200W Watlow Firerod cartridge heaters rated to 1000K and set into the body of the cell. Each of the ten ports into the cell was water-cooled in series, enabling the 'O' ring mountings for the port windows (Spectrosil quartz for the photolysis beam and magnesium fluoride for the detection axes) to be maintained at around room temperature at all temperatures employed. Heat loss was minimised by surrounding the cell with Kaowool thermal cladding. The temperature in the cell was monitored by two Chromel-Alumel thermocouples situated just above and below the photolysis region, with a quoted accuracy of ± 2.2K below 500K and 0.75% at higher temperatures. The thermocouples were also used as sensors for the in-house temperature controller used to power the cartridge heaters. With this arrangement, a temperature range of 285-1000K is feasible and in practice temperatures of up to 875K have been employed [117].

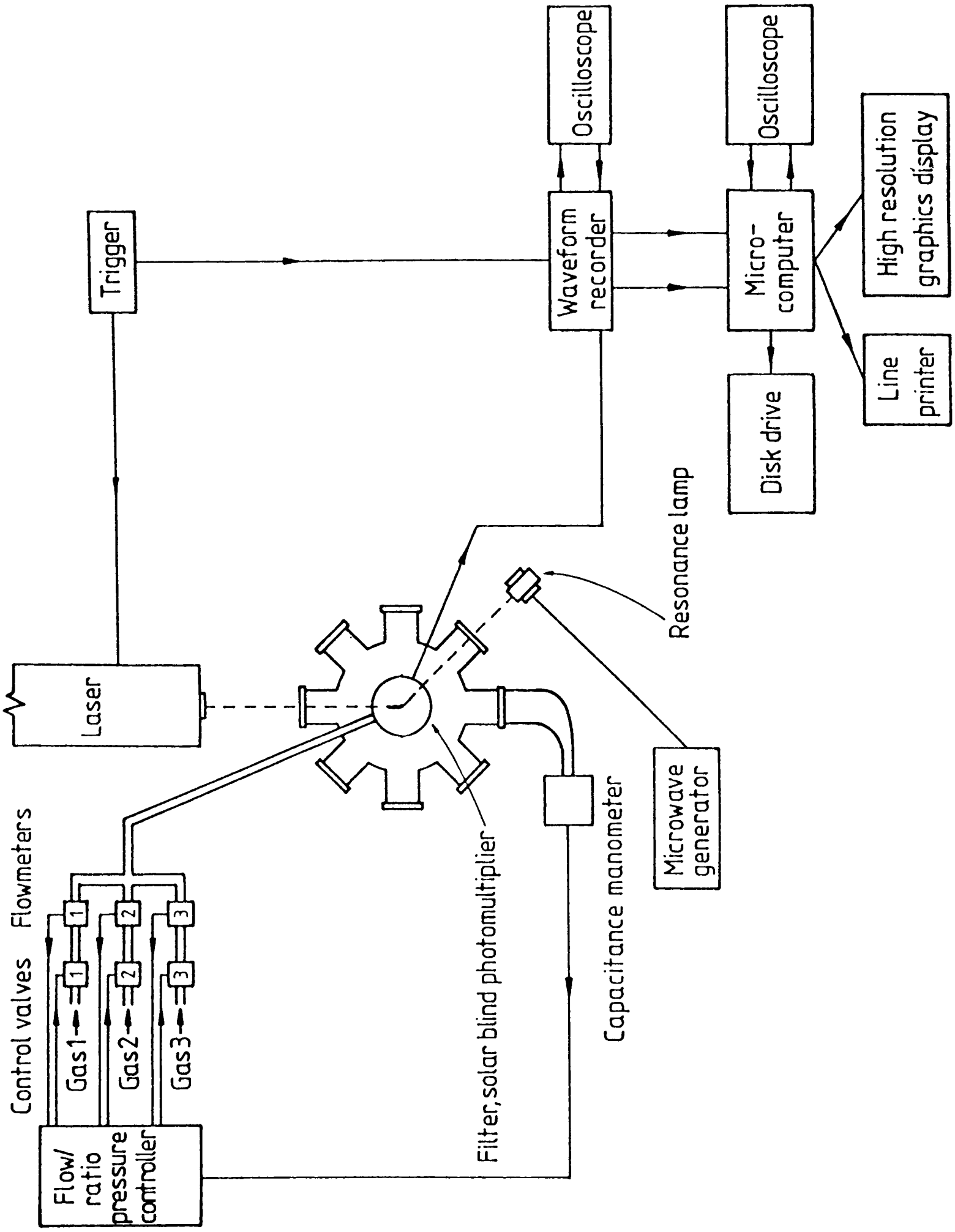

Figure 2.1. Apparatus for Laser Flash Photolysis/ Resonance Fluorescence Experiments (Schematic).

Prior to experiments, the cell was evacuated to below $1x10^{-5}$ Torr as measured on a Penning gauge, using a 4" oil diffusion pump (Edwards 401) backed by a two-stage rotary pump. The pumping system could be isolated from the cell by means of an Edwards butterfly valve. During experiments, the total pressure in the cell was monitored by an MKS capacitance manometer (220 BHS 3A1) and was controlled by a needle valve separating the cell from a second rotary pump.

Gas mixtures were flowed through the cell in a direction perpendicular to the photolysis and detection beam axes. The composition of each mixture was measured and controlled by Tylon (Type FM 360) mass flow meters and valves, and an MKS (Type 260) flow ratio/pressure controller. The flow control valves were enclosed in aluminium foil to eliminate variation in the actual flow through the flowmeters caused by interference from the radio frequency discharge. Calibration of the individual flowmeters was performed using a detergent bubble meter, enabling an accuracy limit of ± 2% to be placed on the substrate concentration for all mixtures.

The gases used in the reaction cell were supplied to the flowmeters either directly from cylinders through Greyhound Oxisorb filters or as mixtures from 5-litre glass bulbs. Ethylene (BDH 99.8%) was purified by extensive freeze-pump-thaw cycles and stored dilute ($\sim$20 Torr in 1000) in argon (BOC zero grade 99.999%). Nitrous oxide (BDH 99.6%) was purified by freeze-pump-thaw cycles and diluted to 50 Torr in 1000 with hydrogen (Matheson preparative grade 99.995%). In experiments where greater $[H_2]/[N_2O]$ ratios were required, further hydrogen (B.O.C. zero grade) was directly supplied to a separate flowmeter. The helium diluent (B.O.C. A grade 99.999%) was taken

directly from a cylinder without further purification. The absence of hydrocarbon impurities in each gas used was checked by gas chromatography, as was the concentration of substrate mixtures.

Hydrogen atoms were generated by photolysis of the nitrous oxide / molecular hydrogen precursor at 193.3 nm with ArF laser radiation from a Lumonics TE861S excimer laser operating at ∿3 Hz. Variation in the laser pulse energy incident on the cell window between 15 and 150 mJ was achieved by placing quartz flats between the laser and the cell. The laser repetition rate was adjusted so that the contents of the reaction volume were completely renewed between each pulse. The beam was passed through a 6mm x 22mm rectangular stop so that only the homogenous central portion was used. After passing into the cell, the laser radiation was defocused into the reaction zone through a 5 cm focal length biconcave quartz lens.

The hydrogen atom concentration in the reaction zone was monitored using Lyman α resonance fluorescence. Exciting radiation at 121.5 nm was produced by a microwave driven (Electromedical Supplies Mk III Microtron 200 power supply) discharge lamp of conventional design [118] mounted externally to the cell. A mixture of 10 Torr H_2 (Matheson preparative grade 99.995%) in 1000 Torr He (B.O.C. A grade 99.999%) was flowed through the lamp at a total pressure of around 1 Torr. Because it was necessary to keep the end window of the lamp as close as possible to the cell window, in order to reduce absorption losses in air, the air-cooled microwave cavity was positioned a few centimetres from the end of the lamp, resulting in a strongly reversed line profile for the Lyman α emission. Although the use of a line reversed lamp results in a somewhat reduced overlap between the Doppler profile of the hydrogen atom absorption in the reaction zone

and the lamp profile, a linear dependence of the fluorescence signal strength on the atom concentration is ensured at atom concentrations of up to $4x10^{12}$ cm^{-3} [102]. The resonance fluorescence radiation was detected at right angles to the plane defined by the resonance lamp and photolysis beam axes with a Thorn EMI solar blind photomultiplier tube (G26L314LF) mounted outside the cell. The gap between the photomultiplier tube and the resonance fluorescence exit window was flushed with dry nitrogen to keep the optical path free from water vapour and oxygen which would otherwise attenuate the signal. Figure 2.2 shows the geometry of the photolysis and detection system.

The analogue voltage output from the photomultiplier was amplified with an in-house variable gain (x10 - x1000) amplifier and then digitised using a Biomation 8100 waveform recorder. The photolysis pulse and recorder sweep were synchronised by means of an adjustable pulse generator, which acted as an external trigger for the laser and armed the waveform recorder. After each collection cycle, the stored trace was transferred to a Research Machines 380Z microcomputer and succesive traces were summed until an acceptable signal-to-noise ratio was acheived. The final decay, typically averaged over 500 laser pulses, was then transferred to floppy disk for subsequent analysis.

2.2.2 Data Analysis

Under conditions where $[C_2H_4]>>[H]$, the hydrogen atoms produced in the initial photolysis decay in an exponential manner according to the scheme:

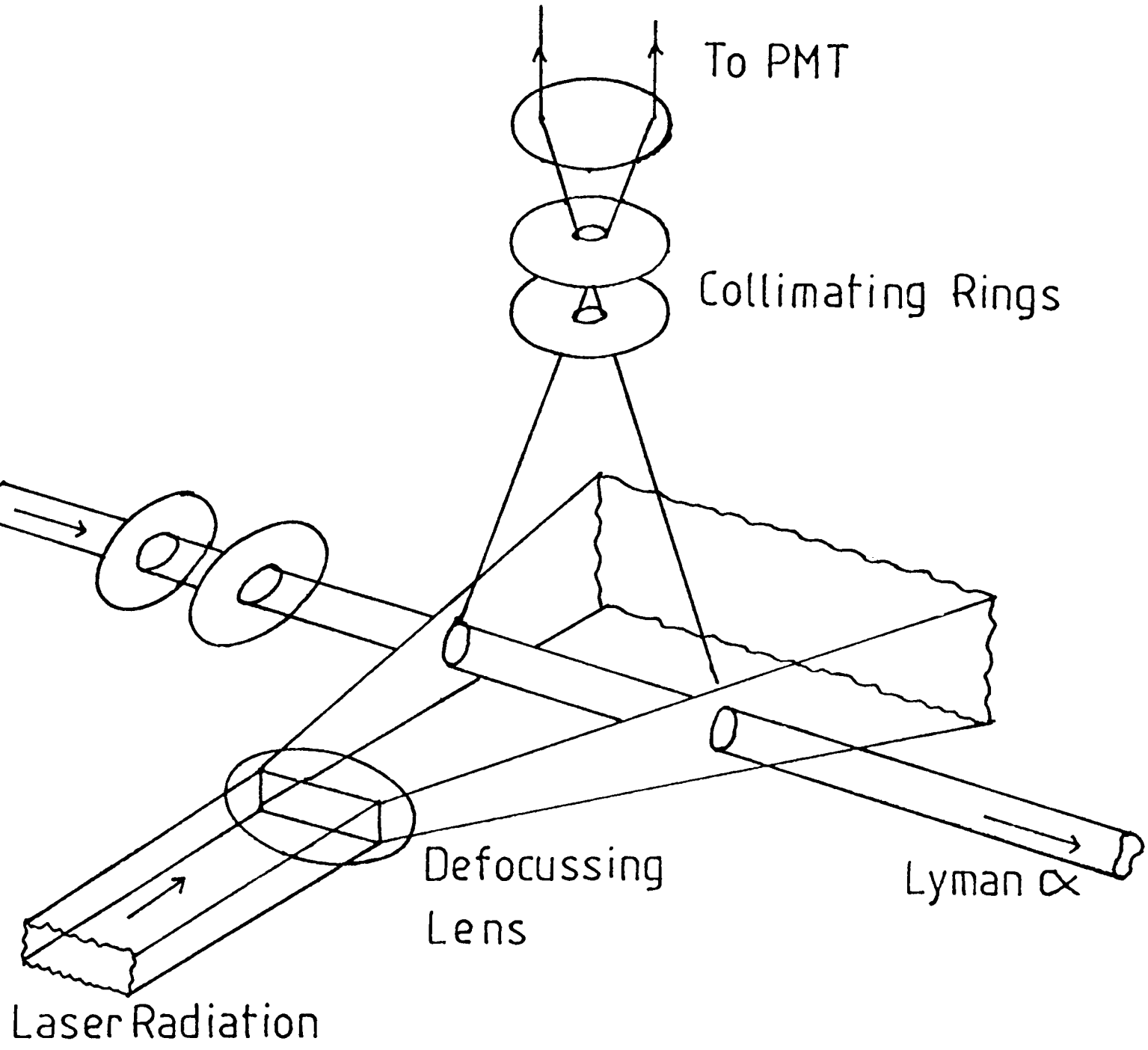

Figure 2.2
Photolysis and Detection Axes (Schematic)

$$H + C_2H_4 \xrightarrow{k_1} C_2H_5 \qquad \text{R2.1}$$

$$H \xrightarrow{k_d} \text{Products} \qquad \text{R2.2}$$

where R2.2 is a small first-order loss process, attributed to diffusion out of the reaction zone. The time-dependent atom concentration is given by:

$$[H] = [H]_o \exp(-k_{app}.t) \qquad \text{E2.1}$$

where $$k_{app} = k_1[C_2H_4] + k_d \qquad \text{E2.2}$$

and $[H]_o$ is the hydrogen atom concentration at t=0. Owing to the linear relationship between atom concentration and signal strength, $[H]_o$ and [H] can be replaced by the corresponding resonance fluorescence signal strengths $[I]_o$ and [I], giving:

$$[I]/[I]_o = \exp(-k_{app}.t) \qquad \text{E2.3}$$

The two unknown parameters, $[I]_o$ and k_{app} were extracted from each decay using a non-linear least-squares fitting routine incorporating the Marquardt algorithm [119].

In order to extract both best fit parameters and their uncertainties from experimental decay traces, one must be able to estimate the uncertainty in each data point so that the fit is properly weighted. In situations where the number of detected events is very small compared with the number of possible events as found, for examples, in photon counting and radioactive decay studies, Poisson statistics apply and the standard deviation for each data point i is given by $N_i^{1/2}$, where N_i is the signal strength at that point. In absorption experiments, on the other hand, where the decay

is usually seen as a small transient change in the signal reaching the detector, the uncertainty in each data point can often be assumed to be constant and calculated from the noise on the pre-trigger baseline.

The present experiments fall between the two limits in that the signal noise was much greater than the baseline noise and although Poisson statistics were not applicable, the absolute scatter on the data decreased with signal strength for a given decay, as can be seen by reference to the residuals in Figure 2.3. Equal weighting of each data point would thus overemphasise the points at the beginning of the trace and could lead to an error in the best fit value of k_{app}. In an attempt to weight the data properly and produce reasonable estimates of the fitted parameter variances, a quadratic fit to the absolute magnitudes of the residuals from an initial unweighted fit was performed and the fitted functional form of the data variance used in a subsequent reanalysis. In practice, only very minor changes in the fitted parameters from the unweighted fit were observed and the chief advantage in using this procedure was that it provided a good estimate of the sample variance, s^2, and hence realistic parameter uncertainties.

A problem with this method of weighting the data is that the uncertainty in each data point is estimated from the scatter of the data about a close approximation to the final fitted decay and consequently, the reduced χ^2 test for goodness of fit is not valid. A discussion of further statistical tests for goodness of fit is given in Chapter 3; for the present experiments, where a single exponential decay was expected, visual examination of the residuals was found to be sufficient to determine whether distortion of the

decay from the exponential form was appreciable.

2.3 Hydrogen Atom Generation

2.3.1 Previously Used Methods

In order to study the time-resolved kinetics of hydrogen atoms, a suitable pulsed method of producing the atoms must be developed. Although the shock wave induced decomposition of nitrous oxide in the presence of hydrogen [41] and pulsed radiolysis [50,51] have been used as hydrogen atom sources for time-resolved kinetic studies, the most convenient and widely used methods of radical generation in recent years have involved the pulsed photolysis of a suitable radical precursor. There are several factors which determine the suitability of any precursor as a photolytic source of radicals. The precursor should ideally:

(1) Photolyse at the wavelengths to be used.

(2) Be thermally stable and chemically inert with respect to the radicals produced, unless the substrate is itself the radical source.

(3) Provide a clean source of radicals. The products of the photolysis must be well defined and must not complicate the kinetics of the reaction to be studied.

and (4) Produce radicals on a timescale which is fast with respect to the kinetics to be studied.

Finding a clean source of hydrogen atoms for kinetic work is notoriously difficult as methods analogous to those used for other radicals are often impractical. The direct photolysis of molecular hydrogen, which would be the simplest and best-defined photolytic

source is not possible because the wavelengths required lie in the vacuum ultraviolet. The use of diimine, HNNH, analogous to the azoalkanes much employed in studies of alkyl radical kinetics is difficult, owing to the instability of the precursor and although several precursors such as formaldehyde could be photolysed to produce hydrogen atoms, there is invariably a concomitant production of a second radical which could affect the kinetics of real time experiments and which would certainly complicate any mechanistic studies. Ethylene has been used at wavelengths below 185 nm [102], where the photolysis is known to be clean, hydrogen atoms being the only radical products of the photolysis [120], although the use of a radical precursor which is itself reactive towards the radicals produced limits the generality of the method. The flash lamp photolysis of water at wavelengths around 170 nm provides a clean source of hydrogen atoms and hydroxyl radicals [121,122], but the use of flash lamps suffers from the disadvantages of broad band photolysis and photolysis pulse durations of the order of several microseconds. Such disadvantages can be largely overcome by the use of an excimer laser as the photolysis light source: excimer lasers provide monochromatic u.v. radiation in short (10 ns), high intensity (MW) pulses. The next section describes the use of 193.3 nm photolysis of nitrous oxide in the presence of molecular hydrogen as a well defined and widely applicable hydrogen atom source.

2.3.2 193.3 nm Photolysis of N_2O in the Presence of H_2

Hydrogen atoms can be generated via the 193.3 nm photolysis of nitrous oxide in the presence of molecular hydrogen according to the

scheme:

$$N_2O \xrightarrow[193.3\ nm]{h\nu} O(^1D) + N_2$$

$$O(^1D) + H_2 \text{ =====> } OH + H$$

$$OH + H_2 \text{ =====> } H_2O + H$$

$$OH + \text{Olefin} \text{ =====> Products}$$

The individual processes involved and the experimental conditions under which the system provides a clean hydrogen atom source are discussed in more detail below.

(i) Primary Processes

The second electronic absorption band of nitrous oxide, corresponding to the $A\ ^1\Delta \leftarrow\!\!\!\!= X\ ^1\Sigma^+$ transition, peaks at 180.6 nm and has an absorption coefficient of 1.1×10^{-19} molecule^{-1}cm^2 at 193.3 nm [123]. The energetically possible products at 193.3 nm are shown in Table 2.1.

Table 2.1

Energetically Possible Products of the Photolysis of N_2O at 193.3 nm

Products	Threshold /(nm)	Quantum Yield
$X^1\Sigma^+g\ N_2 + O(^3P)$	741.5	< 0.03
$X^1\Sigma^+g\ N_2 + O(^1D)$	340.7	> 0.95
$X^1\Sigma^+g\ N_2 + O(^1S)$	211.5	-
$X^2\Pi\ NO + N(^4S)$	251.9	< 0.02

Preston and Barr [124], using heavy metal atom resonance lamps

at 184.9, 213.9 and 228.8 nm, photolysed N_2O in the presence of isotopically labelled NO and showed that the quantum yield for N atom production was less than 0.017, as no $^{29}N_2$ was produced from the reaction $N + {}^{15}NO \Longrightarrow {}^{29}N_2 + O$. In a series of end product analysis experiments, Cvetanovic [125-127] showed that the excited oxygen atoms produced in the photolysis of N_2O at 184.9 nm exhibit the same relative quenching rates as those produced by photolysis of N_2O at 213.9 nm and NO_2 at 228.8 nm where production of O^1S was not energetically possible, providing very strong indirect evidence for O^1D as the only excited oxygen atoms produced in the photolysis of N_2O at wavelengths close to 193.3 nm. In the same series of experiments, Cvetanovic also showed that the quantum yield for O^3P production at 184.9 nm was <0.03, giving a quantum yield for the spin-allowed process:

$$N_2O \xrightarrow[193.3\ nm]{h\nu} N_2(X^1\Sigma^+g) + O(^1D)$$

of 0.95 or greater at room temperature.

(ii) O^3P Production

It is important to demonstrate the absence of O^3P atoms in the current photolysis system, as ground state oxygen atoms are known to react with ethylene with a rate constant similar to that for the reaction of hydrogen atoms with ethylene [128], producing a complex intermediate which can decompose to produce significant yields of hydrogen atoms, even at pressures as great as 760 Torr N_2 [129]. O^3P atoms in the photolysis system would therefore produce hydrogen atoms on a timescale comparable with that of their removal by reaction with

ethylene, resulting in a distortion of the hydrogen atom decay profiles.

The reaction between $O(^1D)$ atoms and molecular hydrogen is known to proceed rapidly, with a temperature-independent rate constant of 1.25×10^{-10} molecule^{-1}cm^{3}s^{-1} [130] and to produce hydroxyl radicals and hydrogen atoms via R2.3 with a yield of > 0.95 at room temperature [30].

$$O(^1D) + H_2 \text{ =====> } OH + H \qquad \text{R2.3}$$
$$\text{=====> } O(^3P) + H_2$$

Although only very small amounts of $O(^3P)$ could thus be produced at room temperature, from either the primary photodissociation (see above), or from the reaction between $O(^1D)$ atoms and hydrogen, it is not possible to exclude the production of $O(^3P)$ at higher temperatures. Using the current apparatus, however, McOwan [117] has studied the 193.3 nm photolysis of nitrous oxide in the presence of hydrogen, but in the absence of a reactive substrate, at temperatures up to 800K. The presence of $O(^3P)$ atoms would be indicated by an increase in signal after the photolysis pulse because of hydrogen atoms produced in the relatively slow reaction:

$$O(^3P) + H_2 \text{ =====> } H_2O + H$$

No such build-up in signal with time was observed. The hydrogen atom resonance fluorescence signal decayed slowly and monotonically after the laser pulse. The pressure and temperature dependence of the rate of this slow decay was entirely compatible with hydrogen atom loss by diffusion out of the monitoring zone and it may be assumed, therefore, that $O(^3P)$ atoms are not produced in significant

quantities under the present experimental conditions.

(iii) H Atom Production and Experimental Conditions

The use of an indirect hydrogen atom source places restrictions on the experimental conditions under which the system can be employed. For the present experiments, the concentrations of the gases in the reaction zone were chosen so that hydrogen atoms were produced rapidly with respect to the rate of their removal by reaction with the olefin substrate and so that the reactions of other species did not complicate the hydrogen atom kinetics. A detailed discussion of the factors which limit the applicability of the $N_2O/ArF/H_2$ system is given below.

(a) $O(^1D)$ Reactions

Although $O(^1D)$ atoms react rapidly with molecular hydrogen, as described above, they also react rapidly with N_2O with a rate constant of $1.2x10^{-10}$ $molecule^{-1}cm^3s^{-1}$ [131] and a branching ratio between R2.4 and R2.5 of 1:1.6 [132].

$$O(^1D) + N_2O \text{ =====> } N_2 + O_2 \qquad \text{R2.4}$$

$$\text{=====> } 2NO \qquad \text{R2.5}$$

Nitrous oxide was supplied to the reaction vessel as a 1:20 mixture in hydrogen. As discussed below, additional hydrogen was employed at temperatures above ambient, increasing the $[H_2]/[N_2O]$ ratio still further.

Although there appears to be no published data on the gas phase reaction between $O(^1D)$ atoms and ethylene:

$$O(^1D) + C_2H_4 \text{ =====> Products} \qquad \text{R2.6}$$

De More [133] studied the reaction in liquid argon at 87K and estimated $k_{2.3}/k_{2.6} = 2.6$. For experiments at 400K and above, the ratio $[H_2]/[C_2H_4]$ was such that R2.6 was negligible. At the highest ethylene concentrations at 285K, however, the $[H_2]/[C_2H_4]$ ratio was 10 and 25% of the $O(^1D)$ atoms could have reacted with the olefin. R2.6 would only affect the results of the present experiments if it produced ground state oxygen atoms in significant quantities (see (iii) above). De More found that R2.6 proceeded via both addition to the olefinic double bond and insertion into the C-H bonds of ethylene, with $k_{C=C}/k_{C-H} \curvearrowright 5$.

$$O(^1D) + C_2H_4 \text{ =====> } \underset{\diagdown O \diagup}{CH_2\text{-}CH_2}{}^* \text{ =====> } \underset{\diagdown O \diagup}{CH_2\text{-}CH_2}, \; CH_3CHO$$

$$\text{=====> } HO\text{-}CH{=}CH_2{}^* \text{ =====> } CH_3CHO$$

Although collisional stabilisation of the products of R2.6 will be much less efficient in the gas phase than in liquid argon, it is extremely unlikely that $O(^3P)$ atoms would be produced by their dissociation. Other radical products of R2.6 would merely increase the overall radical concentration at short times and would not affect the hydrogen atom kinetics, as discussed in detail in (d) below. In addition, R2.6 was shown to be unimportant experimentally: plots of the apparent first-order rate constant for removal of hydrogen atoms against $[C_2H_4]$ at 285K and a given pressure were highly linear from low ethylene concentrations, where $[C_2H_4]/[H_2] \curvearrowright 0.015$ and R2.6 was negligible, to the highest ethylene concentrations, where R2.6 might account for 25% of the $O(^1D)$ removal, indicating that R2.6 did not

significantly affect the hydrogen atom kinetics.

$O(^1D)$ is rapidly quenched to $O(^3P)$ by the heavier rare gases, but the quenching rate constant decreases rapidly with decreasing atomic number and Husain has placed an upper limit on the quenching rate constant for reaction with helium of $7x10^{-16}$ $molecule^{-1}cm^3s^{-1}$ [134].

The $N_2O/ArF/H_2$ system with $[H_2]/[N_2O] > 20$, $[H_2]/[C_2H_4] > 20$ and $[H_2]/[He] > 1.4x10^{-4}$ thus provides a clean source of hydrogen atoms and hydroxyl radicals.

(b) Timescale

The rate of hydrogen atom production via R2.3 was required to be on a timescale which was short with respect to the fastest H + olefin rate to be measured. Owing to radio frequency noise and scattered light from the excimer laser, the fastest pseudo first-order rate constant which could be reliably measured was around 2000 s^{-1}, placing a lower limit of $\sim 2x10^{14}$ $moleculecm^{-3}$ on $[H_2]$ and an upper limit of $\sim 2.7x10^{15}$ $moleculecm^{-3}$ on $[C_2H_4]$ at 285K. In practice, the lower limit on $[H_2]$ was determined by the requirement that the reaction between $O(^1D)$ atoms and ethylene be slow with respect to that between $O(^1D)$ atoms and hydrogen.

(c) OH + H_2 Reaction

The presence of hydroxyl radicals in the reaction system provides perhaps the most severe restrictions on the range of conditions which may be used. In the present system, hydroxyl radicals can react with either molecular hydrogen or the olefin:

$$OH + H_2 \quad =====> H_2O + H \qquad R2.7$$

$$OH + C_2H_4 \quad =====> \text{Products} \qquad R2.8$$

Both reactions have been directly studied [132,135] and have rate constants given by:

$$k_{2.7} = 4.12\times10^{-19}T^{2.44}\exp(-1281/T)$$

and $$k^{\infty}2.8 = 3.3\times10^{-12}\exp(320/T) \text{ molecule}^{-1}\text{cm}^3\text{s}^{-1}$$

where $k^{\infty}2.8$ refers to the limiting high pressure rate constant. R2.8 is mechanistically complex, as discussed below and is subject to some fall-off under the present experimental conditions, so that the above expression represents an upper limit. In order to avoid complication of the present kinetic scheme by hydrogen atoms produced via R2.7, one must ensure that the rate of removal of hydroxyl radicals by reaction with either C_2H_4 or H_2 is fast with respect to rate of removal of hydrogen atoms by reaction with C_2H_4. In the first case, no H atoms would be produced via R2.7, whereas in the second case, all the hydroxyl radicals present would be rapidly converted to hydrogen atoms before the atoms had begun to appreciably decay by reaction with ethylene. The advantage of the second method is that the hydrogen atom concentration would be doubled for the same overall radical concentration, allowing experiments to be performed at lower total radical concentrations.

Table 2.2 shows the bimolecular rate constants $k_{2.7}$ and $k_{2.8}$, in units of $\text{molecule}^{-1}\text{cm}^3\text{s}^{-1}$, over the temperature range 300 - 600K. Also shown is the partial pressure of H_2 required to make $k_{2.7}[H_2] = 2\times10^4\ s^{-1}$, a factor of 10 faster than the fastest H + olefin rate to be measured.

Table 2.2

Rate Contants for the Reactions of Hydroxyl Radicals With Ethylene and Hydrogen from 300-600K

Temperature/K	$k_{2.7}$	$k_{2.8}$	$[H_2]$/Torr
300	6.4×10^{-15}	9.7×10^{-12}	97.4
400	3.7×10^{-14}	7.4×10^{-12}	22.4
500	1.2×10^{-13}	6.3×10^{-12}	8.5
600	2.9×10^{-13}	5.7×10^{-12}	4.2

Below 400K , the rate of $k_{2.7}$ is such that many tens of Torr of H_2 would be required to achieve rapid conversion of OH to H. Large partial pressures of H_2 are undesirable for two reasons. Firstly, the partial pressure of H_2 should be kept small with respect to the total system pressure otherwise large and possibly non-quantitative corrections would have to be made to account for the presence of a second bath gas. Secondly, it is known [136] that hydrogen efficiently quenches Lyman α resonance fluorescence, with a quenching half pressure of 7.6 Torr at room temperature. Consequently, conversion of OH to H via R2.7 was not practical at temperatures below 400K and the H_2 concentration was kept at around 1 Torr for low temperature experiments, so that hydroxyl radicals reacted exclusively with ethylene by addition. The effect of this reaction in the present experiments is discussed in detail below.

(d) Atom + Radical Reactions

At temperatures of 400K and above, concentrations of hydrogen were chosen so that only hydrogen atoms reacted with the olefin

substrate, resulting in a very clean hydrogen atom source. However, hydrogen atoms are converted into ethyl radicals by reaction with ethylene, and the possibility of secondary hydrogen atom + alkyl radical reactions places an upper limit on the initial atom concentrations and hence nitrous oxide concentrations which could be used. A calculation of the initial atom concentration in the reaction zone for a particular [N_2O] and laser pulse energy is given in Appendix 1.

For experiments at 285K, the hydroxyl radicals formed in R2.3 reacted with ethylene rather than with molecular hydrogen. Zellner and Lorentz [135] studied the temperature and pressure dependence of $k_{2.8}$ from 296-524K and 4-130 mbar Ar and observed the negative temperature dependence for the limiting high pressure rate constant given in the previous section. It is believed that the reaction proceeds according to the scheme:

$$OH + C_2H_4 \;===\; C_2H_4OH^* \;\Longrightarrow\; C_2H_5O$$

$$\Big\Vert \quad k_M[M]$$

$$\Downarrow$$

$$C_2H_4OH$$

$$C_2H_5O \;\Longrightarrow\; (1-\alpha)(CH_3CHO + H) + \alpha(CH_2O + CH3)$$

Bartels et al. [137] studied the reaction at 296K and 2.7 mbar He and observed significant rearrangement and subsequent dissociation of the excited adduct, with α = 0.36. Thus, at low pressures, hydroxyl radicals would react with ethylene to produce hydrogen atoms which could interfere with the present experiments. However, Zellner has shown that the fraction of hydroxyl radicals converted to hydrogen atoms is 0.045 at 25 Torr and 0.03 at 50 Torr. As all the present

experiments were performed at 50 Torr and above, it is expected that the contribution to the H atom signal from atoms generated via R2.8 was negligible. Furthermore, $k_{2.8}$ is a factor of 10 greater than the rate constant for the corresponding H atom addition at 285K and the production of H atoms via R2.8 would be on a much faster timescale than that of the reaction to be measured. Thus, if all the hydroxyl radicals produced could be made to react with ethylene, then their effect would merely be to increase the total radical concentration, and the atom decay traces would be affected only under conditions of high initial radical concentrations.

At 285K there is a factor of $\sim$100 between the rate constant for reaction of hydrogen atoms with ethylene and that for reaction with the ethyl radical adduct of R2.1. For the lowest ethylene concentrations of $\sim 3\times10^{14}$ moleculecm^{-3}, atom-radical reactions could thus become significant at the 15% level for initial O(^{1}D) concentrations as low as 2.5×10^{11} atomcm^{-3}. In practice, the lower limit on [N_2O] was determined by signal intensity requirements and experiments at 285K were performed with [N_2O] $\sim 1\times10^{15}$ moleculecm^{-3} and initial O(^{1}D) concentrations of $\sim 5\times10^{11}$ atomcm^{-3} and consequently, the effects of secondary reactions had to be allowed for at this temperature. At the higher temperatures, lower initial atom concentrations could be employed, and the effects of secondary reactions were found to be minimal.

The problem of secondary reactions was investigated experimentally and, as will be shown later, the effect of any small contribution to the hydrogen atom decay from secondary reactions could be removed by working at constant laser energy, and extracting the bimolecular rate constant from plots of the pseudo first-order

rate constant, k_{app}, against $[C_2H_4]$.

(e) Conclusions

At 400K and above, the $N_2O/ArF/H_2$ system provides a very clean source of hydrogen atoms, suitable for both time-resolved and end product analysis work, two atoms being produced for each photon absorbed. The thermal stability of N_2O and H_2, together with the very low reactivity of N_2O towards hydrogen atoms and hydroxyl radicals [138,139], would allow this method of hydrogen atom generation to be used at temperatures up to and beyond 1000K.

Below 400K, it was not practical, in the present experiments, to use sufficiently high hydrogen concentrations to make the production of hydrogen atoms by the reaction of hydroxyl radicals with hydrogen, R2.7, rapid with respect to the rate of their removal by reaction with the olefin. Under such conditions, hydrogen atoms could be produced by R2.7 on a the timescale of the reaction to be measured, unless the hydroxyl radicals were removed by another route. At temperatures of 300K and below, however, the reaction of hydroxyl radicals with ethylene is at least an order of magnitude faster than the corresponding hydrogen atom reaction, resulting in rapid removal of OH, so that the hydrogen atom kinetics would not be affected by the presence of hydroxyl radicals.

Typical reactant and precursor concentrations used in experiments at 285K, 400 and 604K are given in Table 2.3.

Table 2.3

Typical Experimental Concentrations For The

$H + C_2H_4$ System

Temperature/K	$[C_2H_4]$	$[N_2O]$	$[H_2]$	$[H]_o$
285	$1x10^{15}$	$1x10^{15}$	$2x10^{16}$	$5x10^{11}$
400	$5x10^{14}$	$7x10^{14}$	$4x10^{17}$	$1x10^{12}$
604	$4x10^{14}$	$5x10^{14}$	$6x10^{16}$	$5x10^{11}$

(concentrations in atom/moleculecm^{-3})

2.4 Results

Experiments were performed at temperatures of 285, 400, 511 and 604K and total pressures of between 50 and 750 Torr He. At 285K, the "low temperature" method of atom generation was employed. At 400K and above, the "high temperature" method was used.

2.4.1 Experiments at 285K

Experiments at 285K were performed at total pressures of 50, 100, 200 and 400 Torr He and ethylene concentrations of between $3x10^{14}$ and $2.2x10^{15}$ moleculecm^{-3}. At each pressure, the bimolecular rate constant was obtained from the slope of a straight line plot of the pseudo first-order rate, k_{app}, vs. $[C_2H_4]$.

The intercepts of such plots are usually ascribed to diffusion of the atoms out of the monitoring zone. As will be described below, however, the intercepts in the present experiments were often substantially bigger than the measured diffusional loss, because of

the effects of atom + radical reactions and comparison of the experimental intercept with the measured diffusional loss rate provided a check on the importance of secondary reactions. The rate of diffusional loss of hydrogen atoms could be measured by photolysing the N_2O/H_2 precursor mixture in the absence of ethylene. Table 2.4 shows the pressure and temperature dependence of the hydrogen atom diffusional loss rates in units of s^{-1}, as measured for the present experimental arrangement by Brouard [116]. It can be seen that k_d increases sensibly with temperature and decreasing pressure. Brouard has shown that, if the geometry of the detection optics is accounted for, the measured loss rates can be accurately reproduced using calculated diffusion coefficients for hydrogen atoms in helium.

Table 2.4

Hydrogen Atom Diffusional Loss Rates k_d/s^{-1} as a Function of Pressure and Temperature

Temperature/K	401	500	600
Pressure/Torr He			
25	176	244	-
50	120	138	-
100	66	70	121
200	42	52	76

Initially, experiments were performed at a total pressure of 100 Torr He in order to characterise the system. A typical decay trace together with the residuals from a single exponential fit to the decay is shown in Figure 2.3. It was found that at a fixed N_2O concentration of 1.0×10^{15} moleculecm^{-3}, the values of k_{app} obtained at fixed $[C_2H_4]$ depended somewhat (± 10%) upon the laser pulse energy

Figure 2.3. Hydrogen Atom Decay Trace at 285K. Pressure 100 Torr He, Laser Pulse Energy 58 mJ, Concentrations in moleculecm^{-3} :$[C_2H_4]$ = $1.55x10^{15}$, $[N_2O]$ = $1.0x10^{15}$, $[H_2]$ = $2.0x10^{16}$, $[H]_o$ ~ $5x10^{11}$. Points Weighted by a Quadratic Fit to the Absolute Magnitudes of the Residuals From an Initially Unweighted Fit.

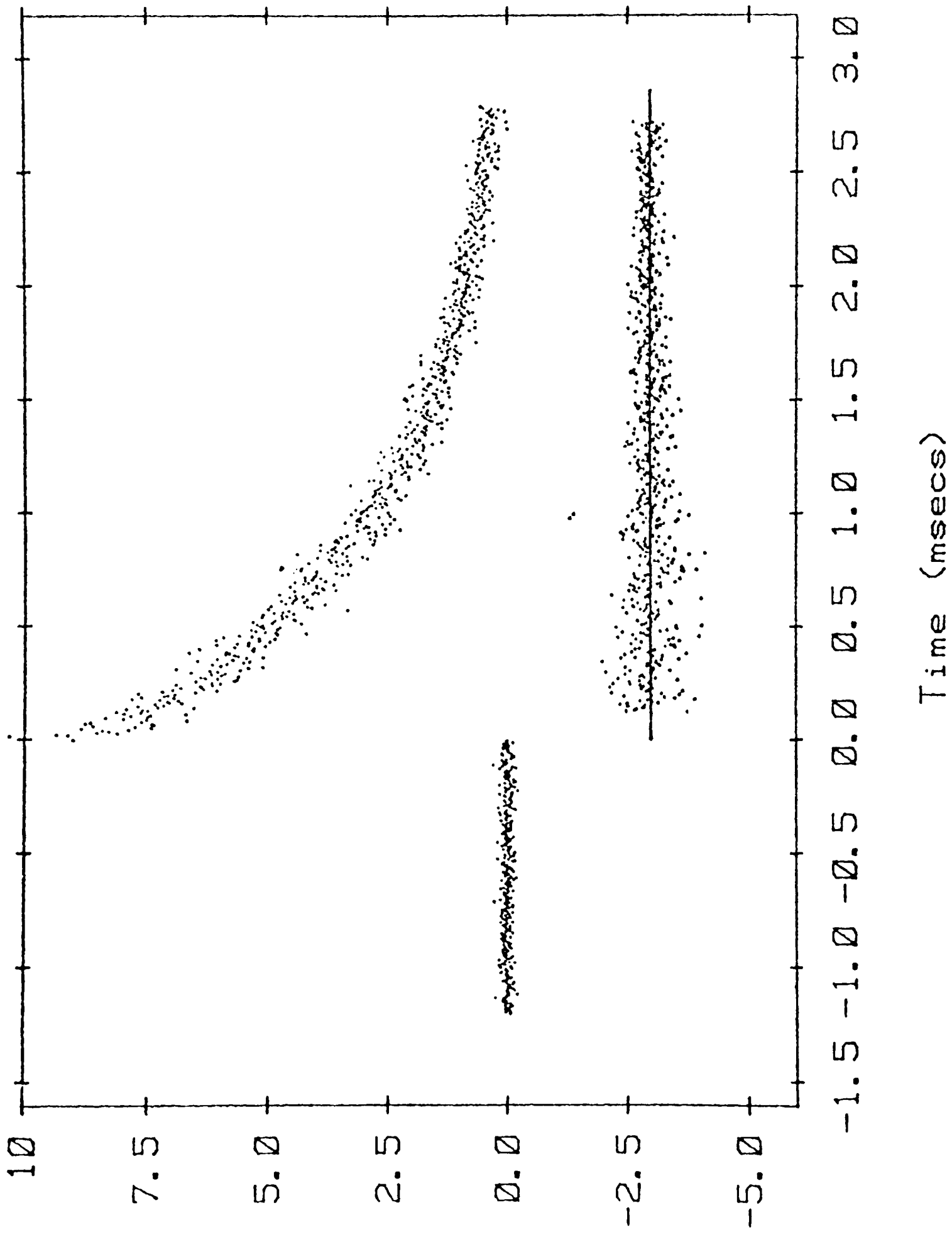

used and the state of the optical components in the path of the laser radiation. In addition, the $[C_2H_4]=0$ intercepts of the k_{app} vs. $[C_2H_4]$ plots were around 100 s^{-1}, substantially greater than expected from the diffusional loss of $\sim$50 s^{-1}. These results indicate that secondary reactions were not negligible. An approximate calculation, given in Appendix 1, sets an upper limit of $5.5x10^{11}$ cm^{-3} on the initial $O(^1D)$ concentration for a laser pulse energy of 60 mJ. Assuming a rate constant of $1x10^{-10}$ $molecule^{-1}cm^3s^{-1}$ for the reaction of hydrogen atoms with C_2H_5 and C_2H_4OH and a total radical concentration of $\sim 1x10^{12}$ cm^{-3} near the end of the decay, then the apparent first-order atom decay rate might be increased by 100 s^{-1} at long times which could lead to non-exponential behaviour.

Simulations were perfomed using the numerical integration package FACSIMILE [4], in which the effect of secondary reactions on the bimolecular rate constant obtained from a linear plot of k_{app} vs. $[C_2H_4]$ was explored. Hydrogen atom decay profiles were generated according to the following scheme (rate constants are in $molecule^{-1}cm^3s^{-1}$)

H	+ C_2H_4	==> C_2H_5	$7.5x10^{-13}$	This Work
OH	+ C_2H_4	==> C_2H_4OH	$7.0x10^{-12}$	[135]
H	+ C_2H_5	==> CH_3 + CH_3	$1.0x10^{-10}$	Estimate
H	+ C_2H_4OH	==> PROD1	$1.0x10^{-10}$	"
OH	+ C_2H_4OH	==> PROD2	$1.0x10^{-10}$	"
OH	+ C_2H_5	==> PROD3	$1.0x10^{-10}$	"
H	+ CH_3	==> CH_4	$2.8x10^{-11}$	[116]
C_2H_5	+ C_2H_5	==> C_4H_{10}	$2.1x10^{-11}$	[18]
C_2H_5	+ C_2H_4OH	==> PROD4	$3.0x10^{-11}$	Estimate

$C_2H_5 + CH_3$	==> C_3H_8	$5.8x10^{-11}$	Mean Value Rule
$C_2H_4OH + C_2H_4OH$	==> PROD5	$3.0x10^{-11}$	Estimate
$C_2H_4OH + CH_3$	==> PROD6	$3.0x10^{-11}$	"
$CH_3 + CH_3$	==> C_2H_6	$4.0x10^{-11}$	[26]
$OH + H_2$	==> $H_2O + H$	$6.5x10^{-15}$	[132]

The initial hydrogen atom concentration, $[H]_o$ ($=[OH]_o$) was varied between $4x10^{11}$ and $1.6x10^{12}$ atomcm^{-3} for ethylene concentrations between $5x10^{13}$ and $2x10^{15}$ moleculecm^{-3}. The generated decay traces were analysed using a linear least-squares fitting routine, according to the simple first-order scheme:

$$H + C_2H_4 \xrightarrow{k_{app}} C_2H_5$$

The simulated k_{app} vs. $[C_2H_4]$ plots are shown in Figure 2.4. In all cases, examination of the residuals to the fit showed that the decay profiles exhibited negligible deviation from first-order behaviour. The effect of secondary reactions at a fixed $[H]_o$ was to increase the apparent rate constant by an essentially fixed amount, independent of $[C_2H_4]$, for ethylene concentrations greater than $2x10^{14}$ moleculecm^{-3}. At lower concentrations, the plots were curved, giving rise to an increased apparent bimolecular rate constant. Also shown in Figure 2.4 are linear fits to the simulated data over the experimental range of $[C_2H_4]$ ($3x10^{14} < [C_2H_4] < 2x10^{15}$ moleculecm^{-3}). For initial atom concentrations as high as $1.6x10^{12}$ cm^{-3}, the second order rate constants returned from these k_{app} vs. $[C_2H_4]$ fits differed by less than 6% from the value of k_1 input to the simulations. The simulations suggest, therefore, that the effect of atom + radical reactions can be eliminated by working at fixed laser energy and

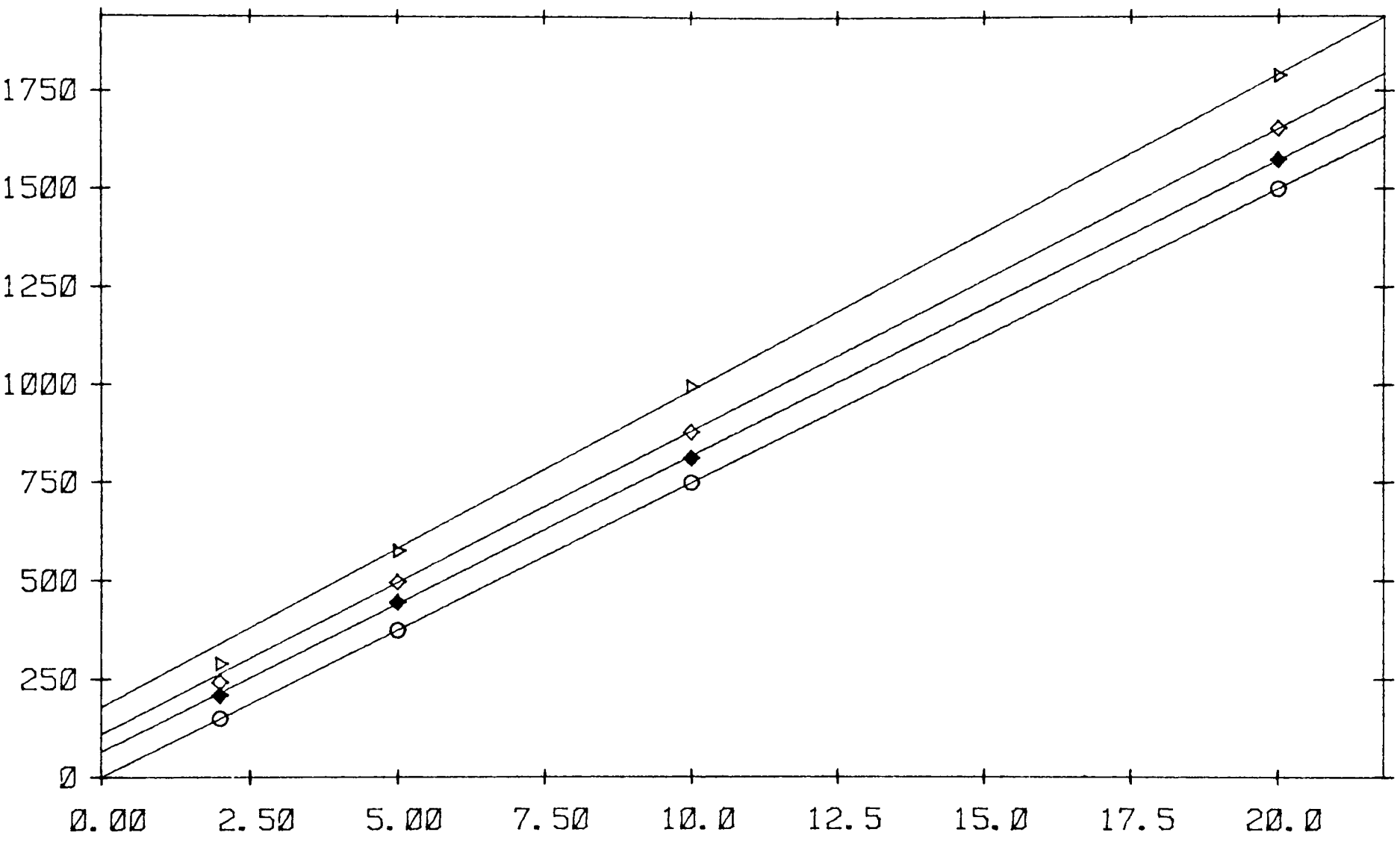

Figure 2.4. Simulated k_{app} vs $[C_2H_4]$ Plots. $[H]_o$ =

o 0, ◆ 4.0×10^{11}, ◇ 7.5×10^{11}, ▷ 1.6×10^{12} cm^{-3}.

$[C_2H_4]$ > $3x10^{14}$ moleculecm^{-3}. Under these conditions, with $[H]_o$ ($=[OH]_o$) < 10^{12} moleculecm^{-3}, the error introduced into k_{bi} is expected to be negligible.

Experiments were then performed at a fixed laser pulse energy of 58 mJ, which gave rise to a linear plot of k_{app} vs. $[C_2H_4]$ with very little scatter, as shown in Figure 2.5.

In order to check this procedure, a series of experiments was performed, in which the initial atom concentration was systematically varied. k_{app} was measured (i) vs. $[C_2H_4]$ as a function of $[N_2O]$, at a fixed laser pulse energy and (ii) as a function of laser pulse energy, at fixed $[N_2O]$ and $[C_2H_4]$. The results of the $[N_2O]$ dependence are summarised in Table 2.5. In fitting the k_{app} vs. $[C_2H_4]$ plots, each value of k_{app} was weighted with the inverse of its variance, as determined by the analysis program. The errors quoted in Table 2.5 refer to 95.45% confidence limits, including a Student's t, where the largest of the internal and external † errors in each fit was taken. The initial atom concentrations in Table 2.5 were estimates, based on the calculation given in Appendix 1. The four values of the bimolecular rate constant so obtained show no dependence on initial atom concentration and the intercepts at $[C_2H_4]$=0 increase with $[H]_o$, as predicted by the simulations.

† The parameter errors calculated when fitting a set of data to a functional form can be estimated either from the uncertainties in the data points input to the fitting procedure - internal errors, or the actual scatter of the data about the fit - external errors.

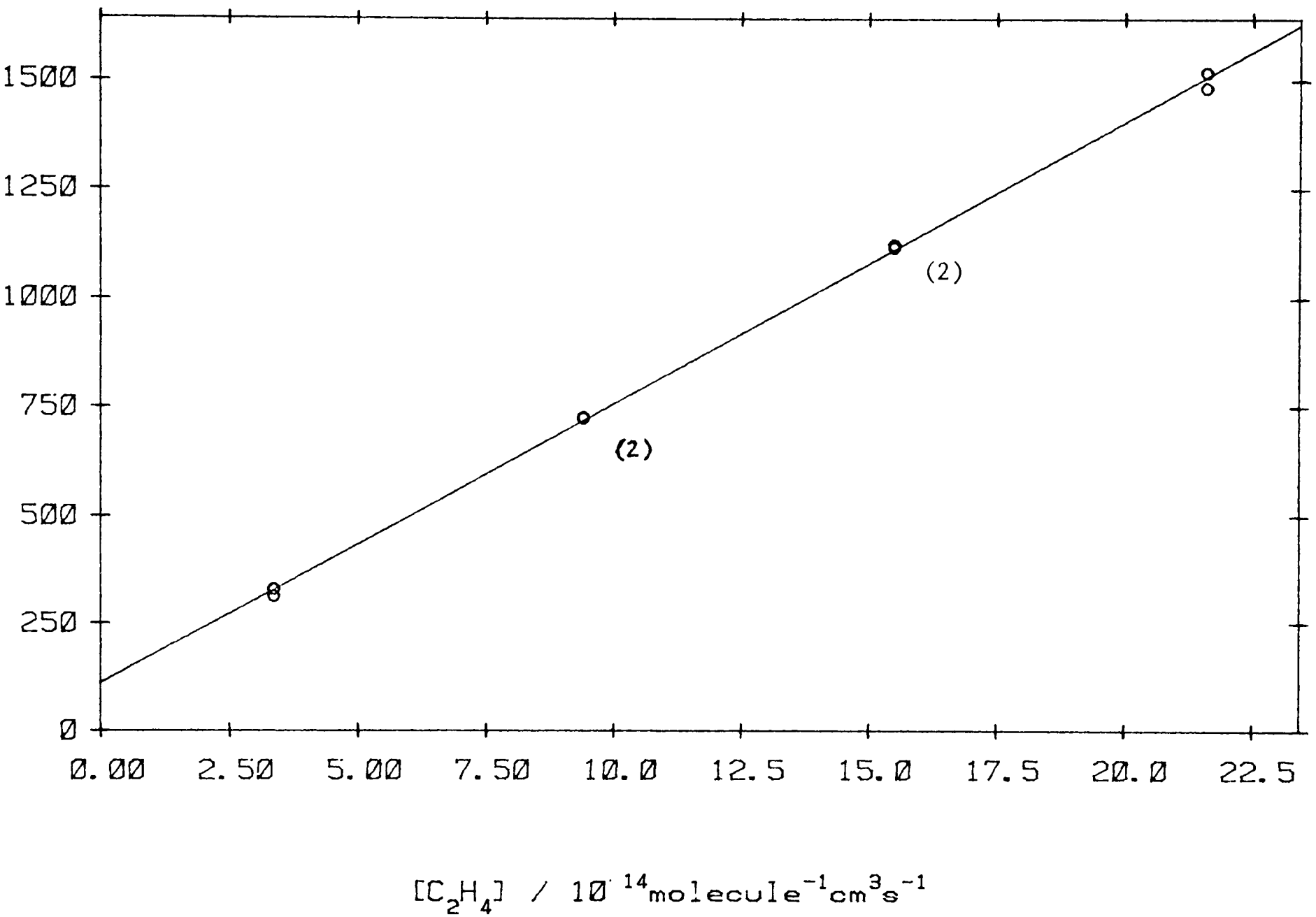

Figure 2.5. Experimental k_{app} vs $[C_2H_4]$ Plot at Fixed Laser Energy. I = 58 mJ, Pressure 100 Torr He.

Table 2.5

The Dependence of k_{app} on $[H]_o$ at 285K

$[N_2O]$ /10^{-15} moleculecm^{-3}	$[H]_o$/ 10^{11}cm^{-3}	k_{app} /10^{-13} molecule^{-1}cm^{3}s^{-1}	Number of Expts.	Intercept /s^{-1}
.25	1.25	6.86±0.72	6	52.2±39.6
.50	2.5	6.76±0.47	7	75.8±52.7
1.0	5.0	6.98±0.24	14	113.2±30.6
2.0	10.0	6.79±0.36	10	144.5±45.5

The effect of laser energy on k_{app} for $[C_2H_4]$ = 6.59x10^{14} moleculecm^{-3} and $[N_2O]$ = 1.0x10^{15} moleculecm^{-3} is shown in Figure 2.6. A linear extrapolation to I=0 gives a first-order decay rate in the absence of secondary reactions of 449 ± 24 s^{-1}, which, after correcting for a diffusional loss of 50 s^{-1}, corresponds to a bimolecular rate constant of (6.05 ± 0.32) molecule^{-1}cm^{3}s^{-1}, in reasonable agreement with the value of (6.95 ± 0.24) molecule^{-1}cm^{3}s^{-1} obtained from the k_{app} vs. $[C_2H_4]$ plot of Figure 2.5.

The bimolecular rate constants at 50, 100, 200 and 400 Torr He obtained from the slope of k_{app} vs. $[C_2H_4]$ plots, using $[N_2O]$ = 1.0x10^{15} moleculecm^{-3} and a fixed laser pulse energy of 58 mJ, are given in Table 2.6.

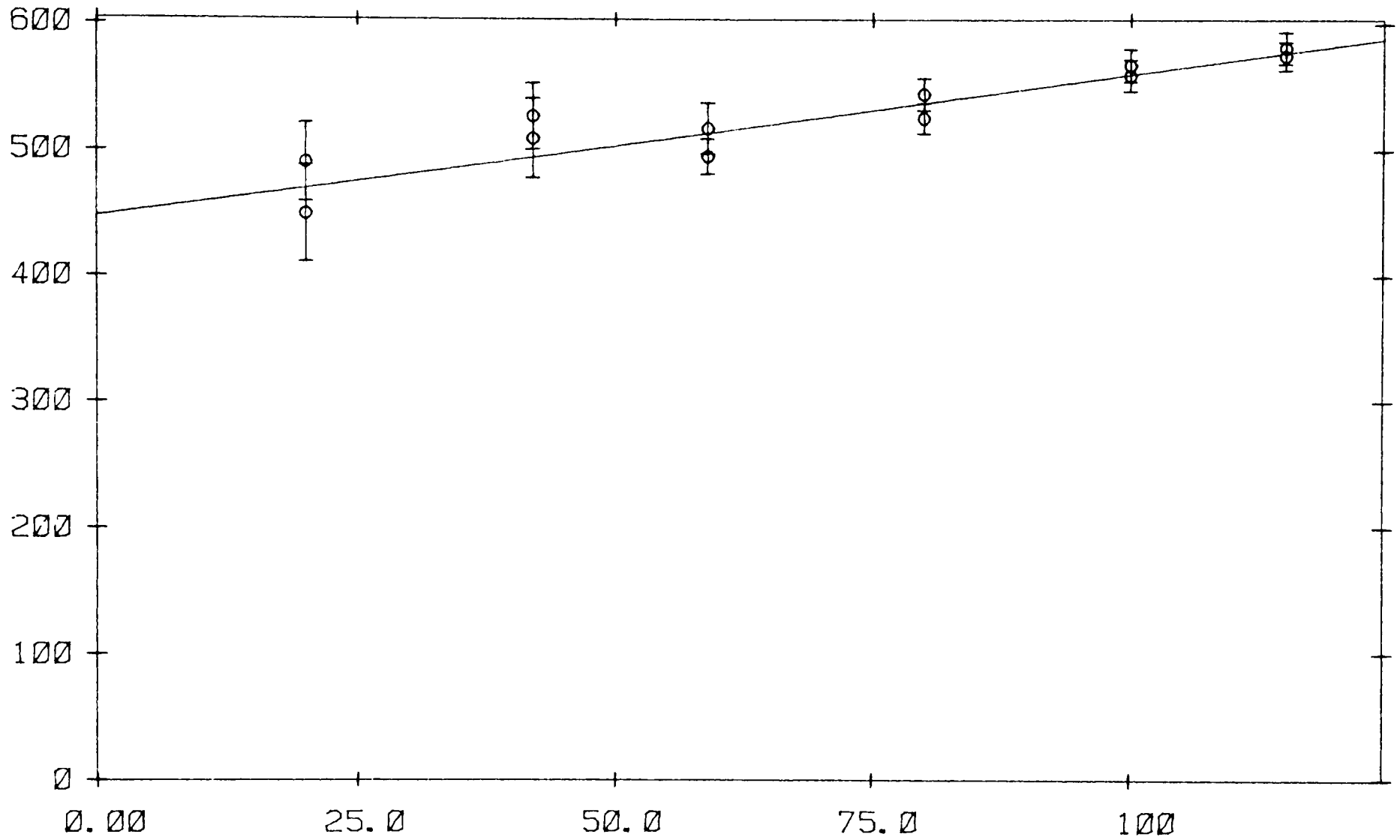

Figure 2.6. Effect of Laser Energy on k_{app} at 285K. Pressure 100 Torr He, $[C_2H_4] = 6.59 \times 10^{14}$, $[N_2O] = 1.0 \times 10^{15}$ moleculecm^{-3}, errors 2σ.

Table 2.6

The Pressure Dependance of the H + C_2H_4 Rate Constant at 285K

Pressure Torr He	Number of Experiments	k_{bi} /10^{-13} $molecule^{-1}cm^3s^{-1}$
50	13	6.01 ± 0.29
100	14	6.98 ± 0.24
200	11	7.54 ± 0.20
400	12	7.79 ± 0.47

2.4.2 Experiments Above 285K

Fall-off curves were obtained at temperatures of 400, 511 and 604K using the "high temperature" method of atom generation. A laser pulse energy of 58 mJ was employed throughout. At each pressure, a fixed N_2O concentration of between 2.4 - $8.3x10^{14}$ $moleculecm^{-3}$ was used. It was possible to work at lower precursor concentrations than were used at 285K, because of a combination of the greater efficiency of the atom generation system at the higher temperatures and the lower ethylene concentrations used: ethylene absorbs strongly at 121.5 nm [140], as was demonstrated by a reduction of the resonance fluorescence intensity at $t \sim 0$ with increasing $[C_2H_4]$ at all temperatures. The molecular hydrogen partial pressures used at each temperature, together with the corresponding first-order rate of conversion of OH into H via R2.7 are given in Table 2.7.

Table 2.7

Molecular Hydrogen Partial Pressures Used in Experiments at Elevated Temperatures

Temperature/K	Hydrogen Pressure/Torr	$k_{2.7}[H_2]/s^{-1}$
400	17.8	1.6×10^4
511	6.9 (50 Torr total)	1.8×10^4
	13.3 (100 Torr total)	1.8×10^4
604	4.0	2.0×10^4

In order to check that sufficient H_2 was present to make R2.7 rapid with respect to the H + C_2H_4 rates to be measured, experiments were performed at each temperature and pressure in which hydrogen atoms were generated in the absence of ethylene. The traces obtained showed no sign of a build-up in atom concentration even on the shortest timescale used experimentally (4 ms) and could be described by a slow first-order diffusional decay. The first-order diffusional loss rates were absorbed in, and in fact made up virtually all of, the intercepts of the constant laser energy k_{app} vs. $[C_2H_4]$ plots. In addition, the apparent rate constants at fixed ethylene concentrations were much less sensitive to laser pulse energy and the condition of the photolysis path optics. These two observations suggested that the effects of secondary reactions were negligible for experiments above 285K. The dependence of the first-order rate constant on laser pulse energy, measured at 500K, $[C_2H_4] = 1.51 \times 10^{14}$ moleculecm^{-3} and $[N_2O] = 2.2 \times 10^{14}$ moleculecm^{-3}, is shown in Figure 2.7. The observed insensitivity of k_{app} to variations in laser pulse energy was partly because of the low atom concentrations employed and

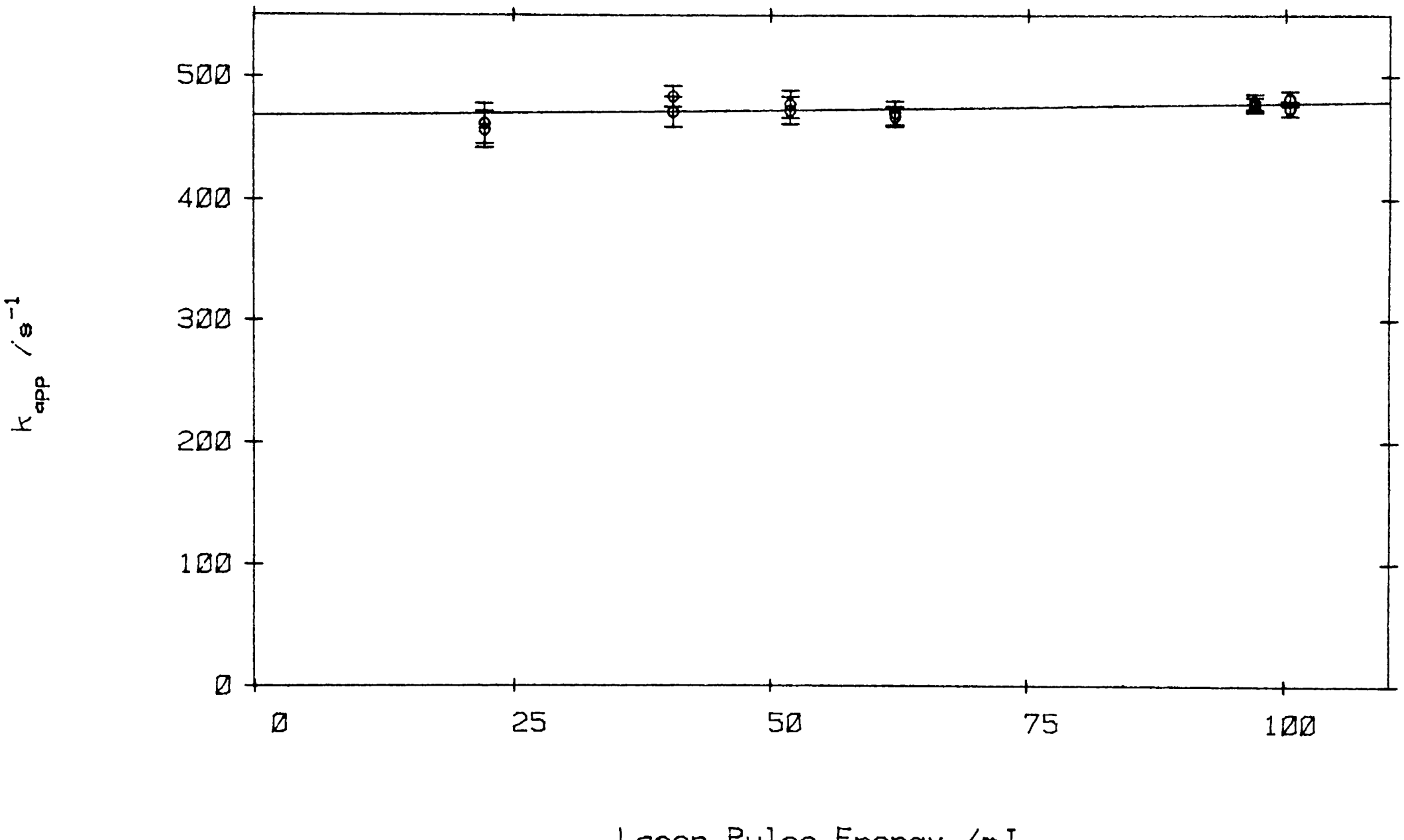

Figure 2.7. Effect of Laser Energy on k_{app} at 500K. Pressure 500K, $[C_2H_4]$ = $1.81x10^{14}$, $[N_2O]$ = $2.2x10^{14}$ $moleculecm^{-3}$, errors 2σ.

partly because ethyl radicals were produced on the same timescale as that of the atom + olefin reaction itself. At 285K, where the addition of OH to C_2H_4 is a factor of ten faster than the corresponding hydrogen atom reaction, half of the carbon-containing radicals were produced at t=0.

The bimolecular rate contants, obtained as a function of overall pressure at 400, 511 and 604K, are given in Table 2.8.

Table 2.8

$H + C_2H_4$ Bimolecular Rate Constants at 400, 511 and 604K

Temperature/K	P/Torr	$k_{bi} \times 10^{12}$	N_o of Expts
400	100	1.33±0.12	8
	200	1.79±0.22	8
	400	2.08±0.09	8
	600	2.11±0.25	8
511	50	1.64±0.13	12
	100	2.04±0.10	15
	200	2.46±0.08	8
	400	2.92±0.18	12
	700	3.57±0.23	12
604	50	1.62±0.10	12
	100	2.15±0.12	10
	200	2.83±0.09	8
	400	3.53±0.19	10
	600	4.38±0.14	11

(Errors refer to 95.45% confidence limits, k_{bi} in molecule^{-1}cm^{3}s^{-1}).

The values of k_{app} for all experiments in this study are listed in Appendix 2.

2.5 Fall-off Behaviour of Unimolecular Reactions

The data presented in the preceeding sections show a complex dependence on both temperature and pressure. Although the H + C_2H_4

reaction has been the subject of a large number of investigations, much of the data is not directly comparable, owing to the different conditions used. Two direct studies of the temperature dependence of the limiting high pressure rate constant have been performed [51,111] and are in good agreement. Extrapolation of the data in this study to the high pressure limit at each temperature would allow a direct comparison with these previous studies. Furthermore, if the fall-off behaviour of the $H + C_2H_4$ reaction could be expressed in terms of simple parameters, then extrapolation would be possible, to conditions of practical interest in, for example, hydrocarbon cracking, where pressures of 2 Atm and temperatures of 1100K are typical.

The next section briefly summarises the commonly used methods, based on theories of unimolecular reactions, which have been used to model fall-off behaviour and to extrapolate data to the low and high pressure limits. The method recently developed by Troe [73,74], which provides a computationally simple yet accurate description of fall-off behaviour, is described in more detail; its application to the present data is discussed in Section 2.5.2.

2.5.1 Models of Fall-off Behaviour

The principle of microscopic reversibility links the rate constant for a bimolecular addition reaction to that for the corresponding unimolecular dissociation via the equilibrium constant, K_C. The pressure behaviour of an addition reaction is hence identical to that of the reverse dissociation and can thus be modelled in terms of unimolecular reaction rate theory.

The Lindemann-Hinshelwood (LH) model [141], upon which current statistical theories of unimolecular reactions are based, assumes the scheme:

$$A + M \overset{k_1}{\Longrightarrow} A^* + M \qquad \text{Collisional Activation}$$

$$A^* + M \overset{k_2}{\Longrightarrow} A + M \qquad \text{Collisional Deactivation}$$

$$A^* \overset{k_3}{\Longrightarrow} \text{Products} \qquad \text{Reaction}$$

The overall rate of reaction, k_{uni} ($=-(1/[A])d[A]/dt$), is given by:

$$k_{uni} = k_1k_3[M]/(k_2[M] + k_3) \qquad \text{E2.4}$$

and the limiting low and high pressure rate constants k_o and k_∞ by:

$$k_o = k_1[M] \qquad \text{E2.5}$$

and

$$k_\infty = k_1k_3/k_2 \qquad \text{E2.6}$$

Inverting E2.4 gives:

$$1/k_{uni} = 1/k_\infty + 1/k_1[M] \qquad \text{E2.7}$$

allowing k_∞ to be extracted, in principle, from a plot of $1/k_{uni}$ vs. 1/Pressure. Unfortunately, such plots invariably show significant curvature, which the simple LH model cannot reproduce, and lead to a serious underestimate of k_∞.

The theory of Rice, Ramspberger and Kassel (RRK) [141] has been much used in the past to model the fall-off behaviour of unimolecular reactions. The chief difference between the RRK and LH approaches is that RRK theory allows for an energy-dependent dissociation rate constant $k_3(E)$. In the widely used classical formalism of RRK theory,

$k_3(E)$ is related to the probability that one of S harmonic oscillators contains at least the critical energy of reaction, E_o, out of a total energy E, by the expression:

$$k_3(E) = A(1-E_o/E)^{S-1} \qquad \text{E2.8}$$

Use of the classical Hinshelwood expression for k_1 leads to the Kassel integral form of the reduced fall-off curve:

$$k_{uni}/k_\infty = 1/(S-1)! \int_{x=0}^{x=\infty} \frac{x^{S-1}\exp(-x)dx}{1 + (A/k_2[M])(x/(x + B))} \qquad \text{E2.9}$$

where $B=E_o/kT$ and A is the experimental high-pressure pre-exponential factor. Although widely used because of its comparative simplicity, this description of fall off behaviour usually requires the number of oscillators, s, to be around half the number of normal modes in the molecule, in order to reproduce the experimental fall-off curve. This reduction in the number of "active" modes was originally taken to be indicative of inefficient intramolecular energy transfer, but is now known to be caused by the classical approximations used. Furthermore, RRK theory gives rise to fall-off curves which are generally broader than those observed experimentally [73], thus limiting its usefulness even as an empirical method of extrapolation.

Rabinovitch and coworkers [142] developed an empirical method of extrapolating fall-off data to the high pressure limit which retains the computational simplicity of the LH model. It was shown, by evaluating the Slater expression for k_{uni}/k_∞, that for a molecule with a given number of oscillators, n, there was a given value of q which would linearise a plot of $1/k_{uni}$ vs. P^{-q}. Typically, q would be around 0.5 (for n=18) and would increase with molecular complexity. It was suggested that q could be chosen empirically, using the

linearity of a plot of k_{uni} vs. P^{-q} as the criterion for determining the best value. Figure 2.8. shows the result of variation in q on such plots for the present data at 511K. It is clear that the extrapolated value of k_∞ is very sensitive to the chosen value of q and that the optimum value of q is not well determined by the data. Furthermore, it was shown in the original work that the best value of q depended on the range of k_{uni}/k_∞ covered and on the method of weighting the data, and that the data needed to be close to k_∞ for the extrapolation to be reliable. This method of extrapolation is thus inaccurate in all but the most favourable circumstances.

The statistical theory of Rice, Ramspberger, Kassel and Marcus (RRKM) [141] has been used extensively in modelling unimolecular reactions. The reaction scheme used is an extension of the RRK scheme and includes an intermediate activated complex between energised molecules and products:

$$A + M \underset{k_2}{\overset{dk_1(E^* \Longrightarrow E^* + dE^*)}{\rightleftharpoons}} A^*(E^* \Longrightarrow E^* + dE^*) + M$$

$$A^*(E^*) \xrightarrow{k_a(E^*)} A^\dagger \xrightarrow{k^\dagger} \text{Products}$$

Activated Complex

A quasi-equilibrium in one direction is assumed between A^* and $A^\dagger$. k_1 and $k_a(E^*)$ are calculated using the methods of quantum statistical mechanics, in contrast to the classical methods of the LH and RRK theories. The overall rate of reaction is found by integration over all energy states:

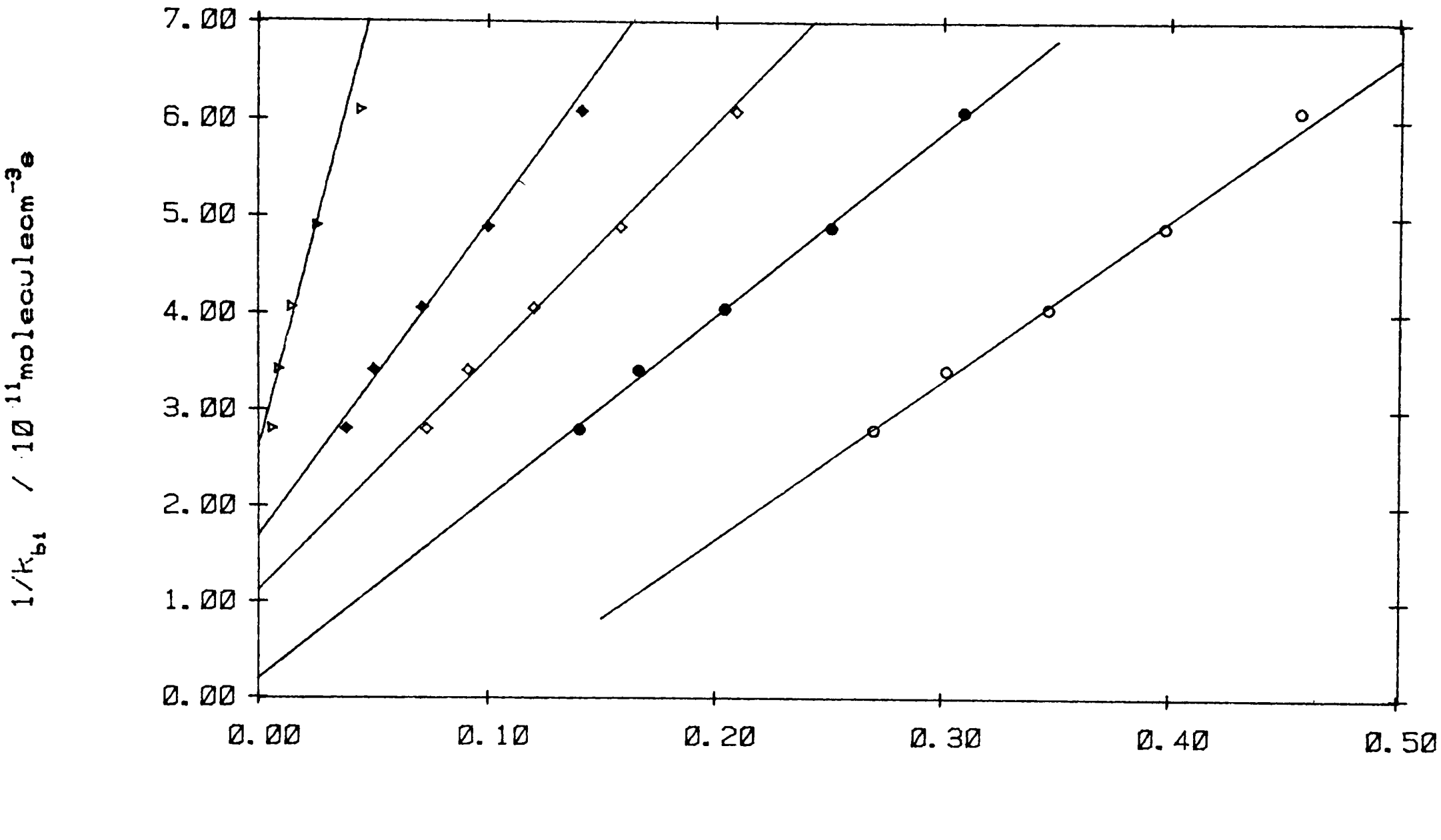

Figure 2.8. Plot of $1/k_{bi}$ vs $1/P^q$ for 511K data.

q = o 0.2, ● 0.3, ◇ 0.4, ◆ 0.5, ▷ 0.8.

$$k_{uni} = \int_{E^*=E_0}^{E^*=\infty} \frac{k_a(E^*)dk_1(E^*==>E^*+dE^*)/k_2}{1 + k_a(E^*)/k_2[M]} \qquad \text{E2.10}$$

Evaluation of $k_a(E^*)$ requires a knowledge of the structure and vibrational frequencies of the activated complex, the position of which is determined by the minimum sum of states criterion [143]. The approach generally adopted is to adjust the frequencies and geometry of the activated complex so that the theoretical and experimental values of k_∞ agree. Once the properties of the activated complex have been determined, fall-off curves can be constructed using E2.10. The RRKM theory thus requires a knowledge of the limiting high pressure rate constant to define the activated complex for the reaction and it is therefore necessary to employ an iterative approach to fit the data and to determine the limiting low and high pressure rate constants. Furthermore, the RRKM treatment sets the rate of deactivation of energised molecules equal to the collision number, Z, as in the LH and RRK models, and uses the strong collision assumption, whereby the energy states of the molecule before and after each collision are assumed to be uncorrelated. Inefficient collisions, in which the energised molecule is not wholly deactivated, can be allowed for in part by replacing the collision number Z by βZ, where β is the collision efficiency of the bath gas. This approach still retains some of the characteristics of the strong collision assumption, however.

The effect of weak collisions on the pressure dependence of unimolecular reactions can be examined using the master equation approach, due largely to Rabinovitch and co-workers [144].

Correlation of energy states before and after each collision is allowed for by assuming a specific probability for the energy transferred. A master equation, which consists of a set of coupled differential equations describing the time evolution of each energy state, is solved using RRKM-type calculations to evaluate the rate of product formation from each energy state. The use of master equations is very time-consuming and although it is perhaps necessary for systems involving photo- or chemical activation, work on thermal systems has shown that a full master equation treatment is usually unnecessary, in that the effect of weak collisions can be adequately described in a semi-empirical fashion.

In a series of recent papers, Troe [73,74,145] has developed a semi-empirical model, validated by RRKM and master equation calculations, describing the deviation of fall-off behaviour from the simple LH model in terms of parameters which can be readily calculated from the molecular properties of the system under study. Such an approach is of great value in the development of complex kinetic models, enabling the pressure dependence of a reaction rate to be described as a relatively simple function of molecular parameters, thereby allowing extrapolation of data out of a neccesarily restricted experimental range without recourse to involved and detailed calculation. The method of Troe has been used successfully in a number of studies [26,29,81,146,147] and is outlined below.

The simple Lindemann-Hinshelwood expression for the pressure dependence of a unimolecular reaction E2.4 can be rewritten as a function of the reduced pressure scale k_o/k_∞.

$$k_{uni}/k_\infty = (k_o/k_\infty)/(1+k_o/k_\infty) \qquad \text{E2.11}$$

This expression is set equal to the "Lindemann-Hinshelwood factor", $F_{LH}(k_o/k_\infty)$ in the Troe formalism. Since experimental fall-off curves are invariably broader than predicted by E2.11, because of both the inadequacies of the LH model of strong collision behaviour and the effects of weak collisions, the overall pressure dependent rate constant is written as:

$$k/k_\infty = F_{LH}(k_o/k_\infty)F^{SC}(k_o/k_\infty)F^{WC}(k_o/k_\infty) \qquad \text{E2.12}$$

$F^{SC}(k_o/k_\infty)$ is a strong collision broadening factor describing the difference between LH fall-off curves and exact strong collision RRKM calculations. $F^{WC}(k_o/k_\infty)$ allows for the effects of weak collisions, as determined by a comparison of strong collision RRKM and full master equation calculations.

The values of F^{SC} calculated for a large number of systems were found to be roughly symmetrical about, and show the maximum deviation from unity at, the centre of the fall-off curve (k_o/k_∞ =1), on a doubly reduced plot of k/k_∞ vs. k_o/k_∞. The broadening factor in the centre of the fall-off curve, F^{SC}cent, is expressed in terms of the Kassel parameters S and B. Evaluation of the classical Kassel integral E2.9 for k_o/k_∞ = 1 as a function of S and B allowed an empirical expression for F^{SC}cent to be developed:

$$-\log F^{SC}\text{cent} = (1.06\log S)^{2.2}/(1+C_1 S^{C}2) \qquad \text{E2.13}$$

where $$C_1 = 0.10\exp(2.5/B - 0.22B - 6\times10^{-10}B^6) \qquad \text{E2.14}$$

and $$C_2 = 1.9 + 4.6\times10^{-5}B^{2.8} \qquad \text{E2.15}$$

Discrepancies between the values of F^{SC}cent calculated in this way

and RRKM calculations, were partly resolved by replacing S and B with the modified Kassel parameters S_K and B_K:

$$S_K = 1 + U^{\dagger}VIB/kT \qquad E2.16$$

$$B_K = ((S_K-1)/(S-1)).((E_O + a(E_O)E_Z)/kT) \qquad E2.17$$

Where $U^{\dagger}VIB$ is the internal vibrational energy of the transition state, $a(E_O)$ the Whitten-Rabinovitch correction to the density of states and E_Z the zero point energy of the molecule. The forms of S_K and B_K were chosen so as to reproduce the limiting low and high pressure results of the more accurate quantum RRK model, whilst retaining the convenient form of the reduced fall-off curve, as developed from the classical RRK model. A further improvement in agreement between RRKM theory and this empirical model was found by replacing B_K with a slightly modified parameter, B_T:

$$B_T = B_K((S_K-1)/(S-1))^{0.6} \qquad E2.18$$

The chief difficulty in evaluating $F^{SC}cent$ lies in the the calculation of S_K, as a knowledge of the vibrational frequencies of the transition state is required:

$$S_K = 1 + U^{\dagger}VIB/kT = 1 + \sum_{i=1}^{s-1} \frac{h\nu_i^{\dagger}/kT}{\exp(h\nu_i^{\dagger}/kT)-1} + R/2 \qquad E2.19$$

where $\nu_i^{\dagger}$ are the transition state frequencies and R is the number of free internal rotors in the transition state. If it is not known, the frequency pattern of the activated complex can be chosen, as in RRKM calculations, so as to reproduce the limiting high pressure rate constant, although the empirical method then offers no real advantage

in terms of computational simplicity over a full RRKM calculation, in that an iterative approach is required to determine k_∞ and k_o. However, S_K can be calculated approximately using the molecular vibrational frequencies:

$$S_K \curvearrowright S_{eff} + \Delta s \qquad \text{E2.20}$$

where
$$S_{eff} = \sum_{i=1}^{s-1} \frac{h\nu_i/kT}{\exp(h\nu_i/kT)-1} \qquad \text{E2.21}$$

and $1 < \Delta s < 2$

The pressure dependence of F^{SC} is allowed for using the expression:

$$\log F^{SC} = \frac{\log F^{SC}_{cent}}{1 + ((\log(k_o/k_\infty) + a)/(N^{SC} \pm \Delta N^{SC}))^2} \qquad \text{E2.22}$$

where the positive sign refers to $k_o/k_\infty > 1$ and the negative sign to $k_o/k_\infty < 1$. The width of the dependence about $k_o/k_\infty = 1$ is described by N^{SC}:

$$N^{SC} \curvearrowright 0.75 - 1.27 \log F^{SC}_{cent} \qquad \text{E2.23}$$

and its asymmetry by a and ΔN^{SC}, which are given by:

$$a = -0.12 \qquad \text{E2.24}$$

and
$$\Delta N^{SC} \curvearrowright 0.1 + 0.6 \log F^{SC}_{cent} \qquad \text{E2.25}$$

The effect of weak collisions on the fall-off behaviour of unimolecular reactions is represented by the factor F^{WC} in E2.12. By solution of the master equation for a number of molecular systems using k(E)'s calculated by RRKM methods and an exponential model of

collisional transition probabilities, it was shown that the effect of weak collisions could be expressed empirically in terms of β_c (a collision efficiency), S_K, $F^{SC}cent$ and F_E, a quantity which describes the energy dependence of the density of states of the molecule above E_o. F_E can be approximately calculated using:

$$F_E = \sum_{j=0}^{n} (n/(n-j))(kT/(E_o+a(E_o)E_z) \qquad \text{E2.26}$$

where $n = s-1+r/2$.

s = number of oscillators.

and r = number of free internal rotations in the molecule

β_c is defined using the limiting low pressure rate constant, k_o [74]:

$$k_o = \beta_c(Z[M]/Q) \int_{E=E_o} \rho(E)\exp(-E/kT)dE \qquad \text{E2.27}$$

Troe has shown that for temperatures below 1000K and molecules containing fewer than 10 atoms, β_c can be related to the average energy transferred in a deactivating collision, $<\Delta E_{down}>$ and F_E by the expression:

$$\beta_c = (<\Delta E_{down}>/(<\Delta E_{down}> + F_E kT))^2 \qquad \text{E2.28}$$

The overall weak collision broadening factor F^{WC} is expressed in a form similar to that for F^{SC}:

$$F_{WC}(k_o/k_\infty) = \frac{\log F^{WC}cent}{1+((\log(k_o/k_\infty)+c)/(N^{WC}-d\log(k_o/k_\infty)+c))^2} \qquad \text{E2.29}$$

where

$$\log F^{WC}_{cent} = (0.16\log\beta_c + 0.04(\log\beta_c)^2)(1+(\log F_E)^{2.2}) \quad \text{E2.30}$$

$$N^{WC} = 1-(0.086S_K+1.7)\log F^{SC}_{cent}-0.3\log\ \beta_c \quad \text{E2.31}$$

$$c = 1.5(\log F^{SC}_{cent})^2(1-0.5\log\ \beta_c) \quad \text{E2.32}$$

$$\text{and} \quad d = -0.03S_K + 0.45(1-\exp(-0.3S_K)) \quad \text{E2.33}$$

To summarise, the currently available and realistic methods for the analysis of fall-off data are :

(i) RRKM calculations, using a collision efficiency β_c.

(ii) Troe method.

and (iii) RRKM plus master equation calculations.

Of the three, method (i) may not be accurate enough owing to its use of the strong collision assumption, and a full master equation calculation (iii) is probably not justified. The method of Troe, however, allows for the effects of weak collisions and is relatively easy to apply. The analysis of the present data using the Troe factorisation method is discussed below.

2.5.2 Application to H + C_2H_4

The fall-off data at each temperature was analysed by incorporating the method of Troe, described in the previous section, into a non-linear least-squares analysis program which, for a given set of fall-off data, returned best fit values for k_∞ and k_O. The parameters for the H + C_2H_4 system, used in the Troe analysis below and in the calculations described in Chapter 3, are given in Table 2.9.

Table 2.9

Input Parameters For Troe Analysis of

$H + C_2H_4$ Fall-Off Data

	Ethyl Radical	Ethylene	Activated Complex
	[89,90,148]	[149,150]	[151]
Vibrational Frequencies /cm^{-1}	3112	3104.9	3036
	3033	3102.5	3009
	2987	3026.4	2955
	2920	3021	2944
	2842	1630	1504
	1462*	1443.5	1446
	1440	1342.2	1218
	1427*	1220	1185
	1366	1023	944
	1175	949.3	938
	1138	939.6	869
	948*	826.0	821
	713*		399
	540		369
External	24.5		20.35
Moments of Inertia	22.8		16.84
/$amuA^2$	4.9		3.46
Internal Moment of Inertia /$amuA^2$	1.12		
Symmetry Numbers	6		4

0K Threshold to Ethyl Radical Decomposition [151]: 38.0 $kcalmol^{-1}$

$\langle \Delta E_{down} \rangle$: 285 cm^{-1}

(Ethyl radical frequencies marked * were calculated [90]).

The vibrational frequencies of the ethyl radical are taken from the work of Pacansky et al.. Ten of the fourteen vibrational frequencies were directly measured with the radical trapped in an argon matrix at 10K [89]. The four unobserved frequencies are taken from ab initio calculations by Pacansky and Schraeder [90], who were also able to reproduce the observed frequencies in all cases. Both experimental [87] and theoretical [148] work has demonstrated the absence of a significant barrier to internal rotation in the ethyl radical and free internal rotation is thus assumed.

Although S_K could be calculated approximately from the molecular vibrational frequencies using equations E2.20 and E2.21, Hase has shown [151] that the available high pressure data for both the bimolecular addition of hydrogen atoms to ethylene and the unimolecular dissociation of the ethyl radical can be reproduced by RRKM theory using the transition state frequencies given in Table 2.9. The assumption of a fixed transition state in this system has been shown to be valid, by variational RRKM calculations which predict only a slight variation in the position of the activated complex for energies up to 35 $kcalmol^{-1}$ above threshold [152]. Furthermore, classical trajectory calculations have shown that recrossing of the dividing surface between reactants and products is negligible and thus RRKM theory should provide a good model for the reaction [153].

The value of $\langle\Delta E_{down}\rangle$ is assumed temperature-independent [154] and calculated from E2.28 using a value of 0.28 for the collision efficiency of He relative to an assumed unit efficiency for SF_6, as determined in a study of the relative collision efficiencies of various bath gases in the H + C_2H_4 system at room temperature and

total pressures of between 1 and 25 Torr [33]. The collision efficiency of H_2 was similarly measured and found to be 0.1. As will be demonstrated later, the values of k_∞ and $k_O/[M]$ returned from the fitting procedure were very insensitive to variations in β_c and the exact value of $\langle\Delta E_{down}\rangle$ is not critical. Combining the relative collision efficiencies of He and H_2 with the corresponding relative collision diameters and average molecular speeds, enables a value of 0.51 to be calculated for the effective pressure of H_2 relative to He in the H + C_2H_4 system. In fitting the data, the presence of small but non-negligible partial pressures of hydrogen were allowed for by reducing the total pressure of the system by 0.49 times the hydrogen partial pressure at each temperature. Although this procedure is only approximate, the correction was very small: at 400K, where the greatest hydrogen partial pressures were employed, the effect of correcting for the presence of hydrogen in this manner altered the fitted values of the limiting low and high pressure rate constants by +4.9% and -1.7% respectively.

The fitted values of k_∞ and $k_O/[M]$ together with the calculated values of S_K and β_c at each temperature are shown in Table 2.10. Figure 2.9 shows the fitted fall-off curves at each temperature together with the experimental data.

Figure 2.9 Fitted Fall-Off Curves, all Temperatures.

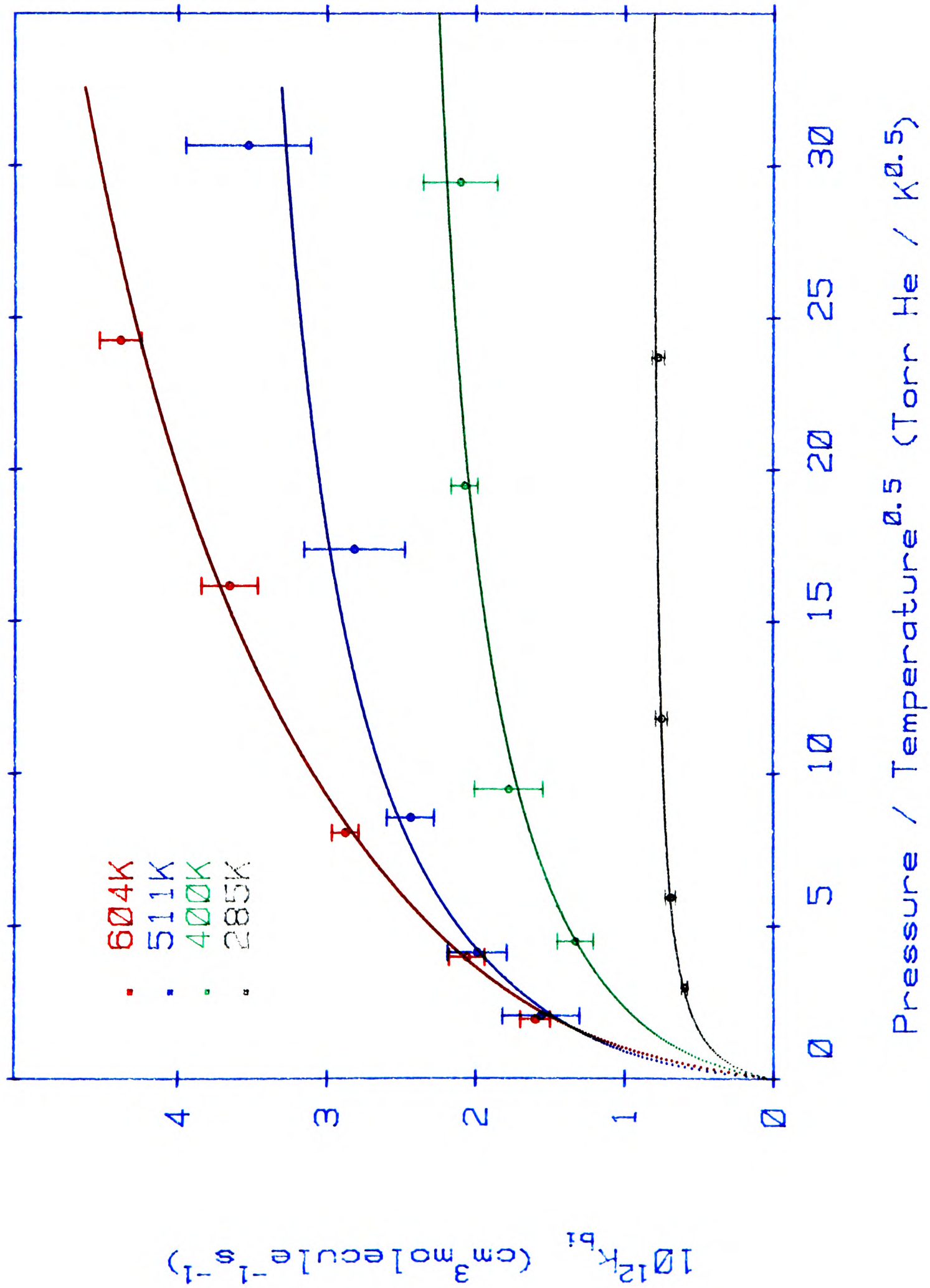

Table 2.10

Fitted Values of k_∞ and $k_O/[M]$ Using Troe Procedure

T/K	$k_\infty/10^{-13}$ molec^{-1}cm^{3}s^{-1}	$k_O/[M]\ /10^{-30}$ molec^{-2}cm^{6}s^{-1}	β_C	S_K
285	8.54±0.44	1.99±0.48	0.29	1.89
400	28.3±3.0	2.44±0.86	0.20	2.64
511	42.7±6.6	6.35±2.42	0.14	3.38
604	76.9±7.4	5.36±0.84	0.11	3.96

The quoted uncertainties refer to two standard deviations, as returned from the fitting program and reflect the experimental uncertainties of the rate constants put into the fitting procedure, rather than the inherent accuracy of the method. In order to assess the accuracy to which k_∞ and $k_O/[M]$ can be determined within the framework of the model, uncertainties in the chosen input parameters β_C and S_K must be taken into account.

For the data at 604K, where the experimental results are furthest into the fall-off region and the fitted value of k_∞ is hence most sensitive to the chosen values of the collisional energy transfer parameter, a variation of β_C by almost an order of magnitude above and below the estimated value of 0.11, produced a corresponding variation in the fitted values of k_∞ and $k_O/[M]$ of only ±5% and ±10% respectively, without significantly affecting the goodness of the fit. Attempts to treat β_C as an adjustable parameter in the fitting procedure were unsuccesful, further demonstrating the insensitivity of the shape of the calculated fall-off curve to variations in β_C. Thus, uncertainties in energy transfer parameters have no significant

effect on $k_o/[M]$, k_∞, or the predicted values of k_{bi} over the experimental temperature and pressure range.

A second uncertainty in the model input parameters arises because the values used for S_K were calculated from the transition state frequencies of Hase. Comparison of the values of S_K calculated at each temperature using the transition state frequencies and those calculated using the molecular frequencies and the relationship E2.2,0 showed that the approximate relationship $1 < \Delta s < 2$ was satisfied, although the exact value of Δs was found to be temperature-dependent, varying from 0.99 at 285K to 1.42 at 604K. The effect of varying Δs between the limits of the approximate formula E2.20 was invesigated at each temperature. In all cases, increasing S_K increased both $k_o/[M]$ and k_∞ because of the corresponding broadening of the fitted fall-off curve. The effect on k_∞ was found to be small, increasing from 5.0% at 285K to 12.2% at 604K. However, the fitted values of $k_o/[M]$ were very sensitive to the chosen value of S_K, an increase in Δs from 1 to 2 producing a 95% increase in $k_o/[M]$ at 285K, although this effect was reduced to 51% at 604K where the data are closer to the third order region. The greater sensitivity of $k_o/[M]$ over k_∞ to the model parameters is not unexpected as the data is closer to the high pressure limit than to the third order low pressure region at all temperatures studied.

The intrinsic accuracy of the extrapolation procedure is difficult to quantify and will be dependent on the distance of the available data from its low and high pressure limits. Troe has shown [74] that, given the values of k_∞ and $k_o/[M]$ for a series of molecules, the simplified procedure of the preceeding section reproduces numerically exact RRKM and master equation calculations to

20% or better, although it is unclear whether this represents a limit on the accuracy of the reverse process: that of extrapolating fall-off data to the low and high pressure limits. Given the uncertainties in the extrapolation method and the model parameters employed therein, it seems reasonable to assume that the true value of k_∞ lies within ±20% of the value quoted in Table 2.10 at 604K, although k_∞ will be better defined at the lower temperatures. The sensitivity of the fitted values of $k_O/[M]$ to the model parameters suggest that $k_O/[M]$ is determined to no better than a factor of two at 285K, although this uncertainty will probably be reduced at higher temperatures.

2.6 Discussion

A comparison of the present extrapolated values of k_∞ and the data of Lee and Sugawara is shown in Figure 2.10. Also shown in Figure 2.10 is a best-fit straight line to all three sets of data giving:

$$k_\infty = (4.39 \pm 0.56)\times10^{-11}\exp(-(1087 \pm 36)/T) \quad \text{molecule}^{-1}\text{cm}^3\text{s}^{-1} \quad \text{E2.34}$$

It can be seen that the extrapolated values of the current study are well within ±20% of the values predicted by the best fit plot. Given that the highest pressure rate constant measured at 604K is less than 60% of the extrapolated k_∞, the agreement between the present data and that of Lee and Sugawara is satisfactory and the method of extrapolation to k_∞ appears to be valid. In particular, the use of values of S_K calculated from the transition state of Hase

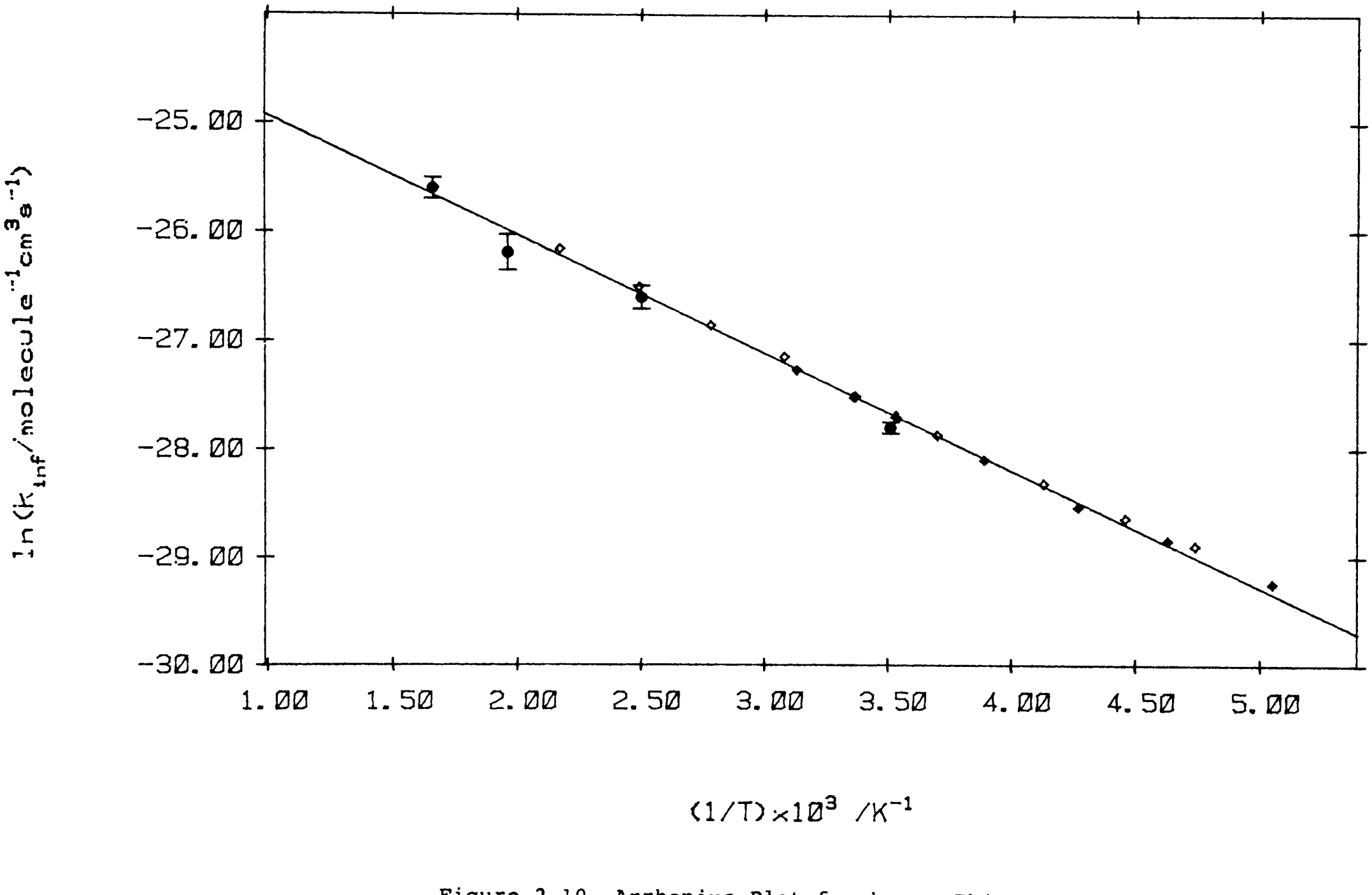

Figure 2.10. Arrhenius Plot for k_∞. ● This Work, 2σ Errors, ◆ Lee et al. [111], ◇ Sugawara et al. [51].

quantitatively reproduces the broadening of the fall-off with increasing temperature over the range 285 - 604K and should allow accurate prediction of the fall-off behaviour at higher temperatures.

Hase [151] has suggested that tunneling might be important in the H + C_2H_4 reaction and although the Arrhenius fit to the data in Figure 2.10 is very good, it is possible that the fit slightly underestimates the true rate constant at the lowest temperatures. The effect of tunneling on a reaction rate may be calculated using the Wigner tunneling correction, W(T), which is expressed in terms of an imaginary vibrational frequency for the reaction coordinate [155]:

$$W(T) = 1 + (h\nu/kT)^2/24 \qquad E2.35$$

Using the imaginary frequency of 546i cm^{-1} calculated by Hase, the tunneling correction factor varies from 1.64 at 200K to 1.07 at 600K. Dividing each experimental high pressure rate constant by W(T) and refitting to an Arrhenius expression gives:

$$k_\infty/W(T) = (5.39 \pm 0.68)x10^{-11}\exp(-(1227 \pm 36)/T) \qquad E2.36$$

$$\text{molecule}^{-1}\text{cm}^3\text{s}^{-1}$$

As might be expected, allowing for the effects of tunneling resulted in a slight increase in both the Arrhenius A factor and the activation energy for the reaction. The correlation coefficient for the linear fit was not, however, significantly increased by the tunneling correction and deviations from the experimental expression, E2.34, will be unimportant except at very low temperatures.

In order to be able to calculate the value of k_{bi} at a given pressure and temperature using the method of Troe, the temperature dependences of both k_∞ and $k_O/[M]$ are required, together with the

collisional energy transfer parameter for the appropriate bath gas, $\langle\Delta E_{down}\rangle$. The limiting low pressure third order rate constant can be written [141]:

$$k_o(T) = [M]\beta_c Z_{LJ}(Q^*/Q)\exp(-E_o/RT) \qquad E2.37$$

where, if angular momentum constraints are neglected, Q^* and Q are the total partition functions for the molecule relative to $E=E_o$ and $E=0$ respectively, Z_{LJ} the Lennard-Jones collision number and E_o the critical energy requirement for the reaction. The relatively weak temperature dependences of β_c and Z_{LJ} are in opposite directions and so mutually-cancelling to a large extent. This effect, coupled with the weak temperature dependence of Q^*/Q, causes an experimental Arrhenius-type expression to be often adequate. Figure 2.11 shows an Arrhenius fit to the present data which gives:

$$k_o/[M] = (1.39\pm0.76)\times10^{-29}\exp(-(569\pm220)/T) \qquad E2.38$$
$$\text{/molecule}^{-2}\text{cm}^6\text{s}^{-1}$$

The large scatter about the best fit line is presumably a consequence of the large uncertainties in the extrapolated values of $k_o/[M]$. However, the low pressure activation energy is sensibly below the high pressure value, as predicted by unimolecular reaction rate theory and although the fitted Arrhenius expression must be regarded as only an approximate representation, it should reproduce $k_o/[M]$ to within a factor of two for the purposes of the model because of its relatively small dependence on temperature.

No published determinations of $k_o/[M]$ for the addition reaction are available for comparison with the present data. The pressure dependence of the thermal dissociation of the ethyl radical has, however, been studied between 673 and 773K by Loucks and Laidler

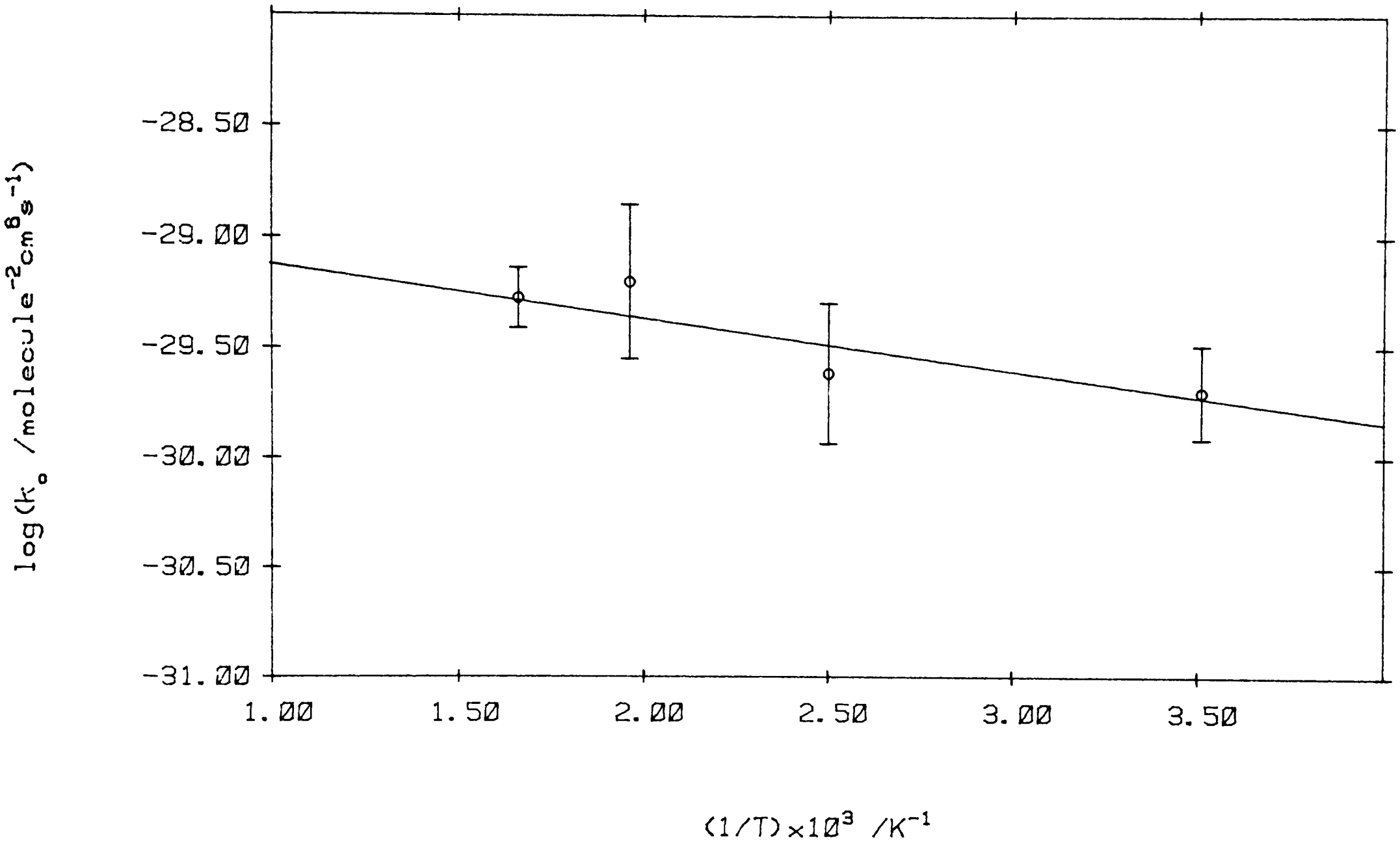

Figure 2.11. Arrhenius Plot for k_o. Errors 2σ.

[156] and between 913 and 999K by Lin and Back [157]. Loucks and Laidler evaluated the limiting low pressure rate constant for the dissociation from the slope of a Lindemann plot at each temperature, resulting in the Arrhenius expression $k_o/[M] = 1.1x10^{-6}exp(-31800calmol^{-1}/RT)$ $molecule^{-1}cm^3s^{-1}$, while Lin and Back extrapolated their data to the low and high pressure limits using a simplified RRK expression for the fall-off curve and obtained $k_o/[M] = 3x10^{-6}exp(-32400calmol^{-1}/RT)$ $molecule^{-1}cm^3s^{-1}$. An average of the two determinations gives $k_o/[M] = 4.5x10^{-30}$ $molecule^{-1}cm^3s^{-1}$ for the dissociation at 298K. Using the thermodynamic parameters obtained in Chapter 3, the equilibrium constant for the H + C_2H_4 == C_2H_5 system is calculated to be 490 $molecule^{-1}cm^3$ at 298K, which, when combined with the average value for the limiting low pressure rate constant, gives a value for the limiting low pressure addition rate constant of $2.2x10^{-27}$ $molecule^{-2}cm^6s^{-1}$, more than three orders of magnitude greater than that obtained from the present study.

This severe discrepancy presumably arises from the different methods of extrapolation used. As discussed in Section 2.5.1, the RRK and Lindemann-Hinshelwood theories provide only a very qualitative description of the shape of a unimolecular fall-off curve, and although the k vs. P expressions in each case may reproduce the data reasonably well, the limiting rate constants so obtained may be seriously in error. The expression for $k_o/[M]$ obtained in this study will thus provide a much better estimate of the true value of $k_o/[M]$ at a given temperature. Moreover, errors in the extrapolated values of $k_o/[M]$ caused by inadequacies in the method of extrapolation used in the present work, should not cause serious errors in the the values of $k_{bi}(P,T)$ predicted by the same model, as long as the

predicted values of k_{bi}/k_∞ are not far removed from the present experimental range.

In principle, k_{bi} can now be calculated using the method of Troe at any helium pressure and system temperature. Fall-off curves in other bath gases are readily calculated by substituting the appropriate value of $\langle\Delta E_{down}\rangle$ in the expression for β_c, E2.28 and modifying E2.38 to take into account changes in β_c and Z_{LJ}.

The pressure dependence of k_{bi} at 298K and in a helium diluent has been the subject of a number of studies by Braun and coworkers [94,102] and Michael and coworkers [33,93,104]. Figure 2.12 shows the predicted fall-off curve at 298K, together with the most recent data from both groups. It can be seen that the calculated fall-off curve agrees reasonably well (±25%) with the somewhat scattered experimental data at all pressures.

A further comparison between experimental and calculated values of k_{bi} may be made using the data of the following chapter, in which the value of k_{bi} is determined at a total pressure of 200 Torr He and temperatures of 775, 800 and 825K. The predicted and observed values of k_{bi} are in good agreement and are given in Table 2.11.

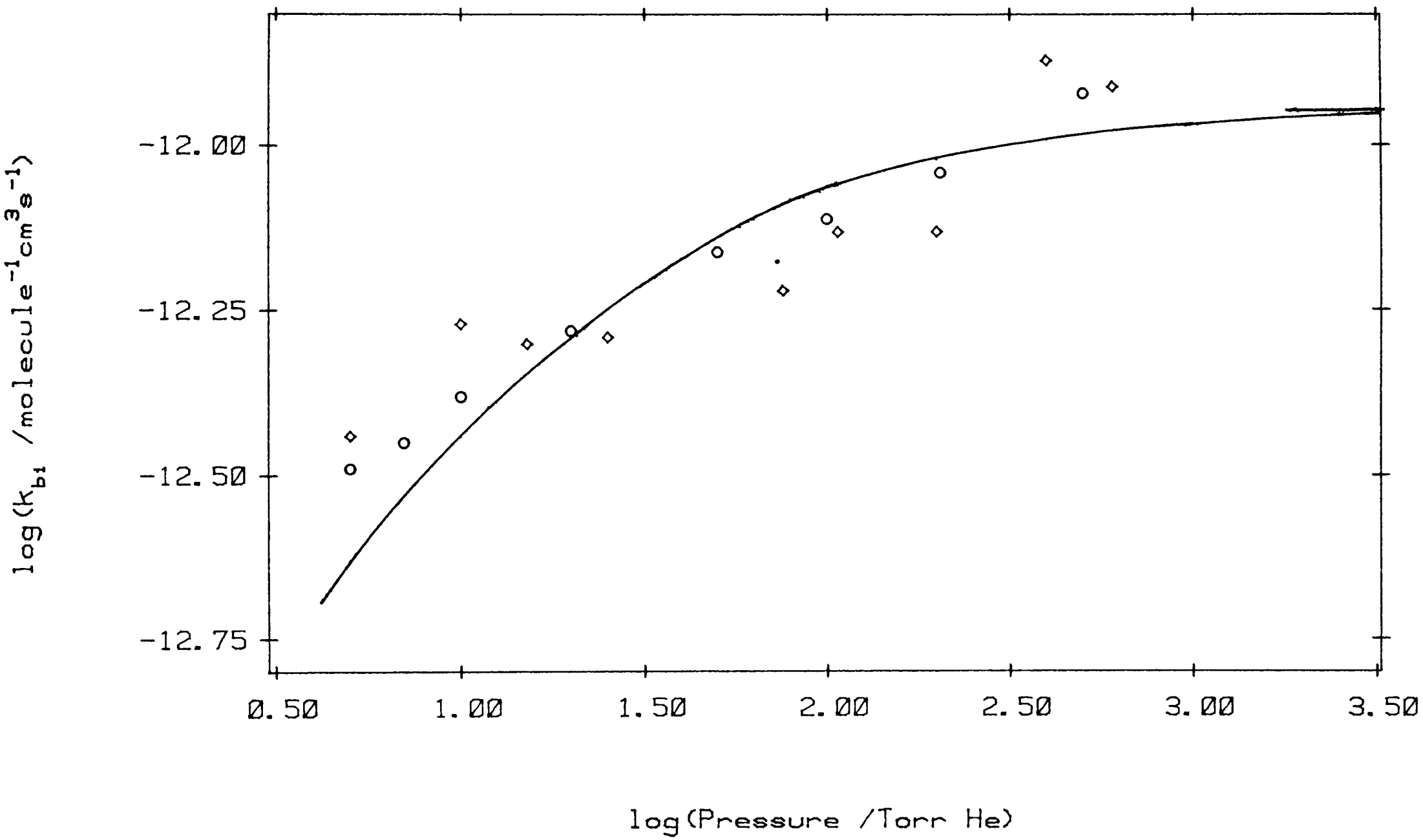

Figure 2.12. Comparison of Model Fall-Off Predictions With Published Data at 298K. o Braun et al. [102], ◇ Michael et al. [33].

Table 2.11

Comparison of Calculated and Experimental Values of k_{bi} at Around 800K

Temperature/K	$k_{bi}/10^{-12}$molecule^{-1}cm^{3}s^{-1}	
	Calculated	Experimental
825	2.74	2.82
800	2.76	2.97
775	2.69	3.53

The present model should thus be able to calculate k_{bi} over a wide range of temperatures and pressures with an accuracy of approximately ±25% at pressures where k_{bi} is predicted to be greater than 20% of k_∞. For lower values of k_{bi}/k_∞, the predictions of the model are less accurate because of the uncertainty in $k_o/[M]$ and an accuracy of no better than a factor of two is expected. The use of the present model in estimating values of k_{bi} under conditions appropriate to industrial pyrolysis is discussed in Chapter 6.

Chapter 3

Direct Observation of Equilibration in the H + C_2H_4 = C_2H_5 System: The Heat of Formation of the Ethyl Radical

3.1 Introduction

For many years, the heat of formation of the ethyl radical has been accepted to be around 26 kcalmol^{-1}, as determined by halogenation experiments [76]. Recently, however, this value has frequently been questioned. Parkes and Quinn [17] reported that their rate constant for ethyl radical recombination, directly measured over a wide temperature range using molecular modulation spectroscopy, was only compatible with the data available on the pyrolysis of n-butane, if a heat of formation greater than 26 kcalmol^{-1} was used. Work by Golden [19], using very low pressure pyrolysis to measure the ethyl radical recombination rate, supported this observation. Castelhano et al. [80], using the radical buffer method in solution, found $\Delta H^{o}f,298(C_2H_5)$ = 28.0±1.0 kcalmol^{-1}. This value was taken by Hase and used to model the data available on the H + C_2H_4 == C_2H_5 system with a single RRKM transition state [151], thereby removing a long standing inconsistency between the high pressure forward and reverse rate data. Cao and Back [82] recently reviewed the pyrolysis data available on the heat of formation of the ethyl radical and the H + C_2H_6 == H_2 + C_2H_5 system in particular. It was concluded that the evidence pointed overwhelmingly towards a higher heat of formation of around 28 kcalmol^{-1}, although they were unable to define an optimum value. In a recent study of the non-stationary-state pyrolysis of

ethane, Pacey and Wimalasena [81] indirectly measured the rates of ethyl radical recombination and decomposition at 900K and calculated values for $\Delta H^{o}f,298(C_2H_5)$ from previously published data on the corresponding reverse reactions, giving an average value of 28.69 $kcalmol^{-1}$. It is worth noting that an error of 2 $kcalmol^{-1}$ in the enthalpy change for a reaction leads to an error of nearly a factor of three in the calculated reverse rate constant at 1000K and a factor of almost thirty at 300K.

This chapter describes experiments in which equilibrium in the H + C_2H_4 == C_2H_5 system was directly observed at temperatures of around 800K, using Lyman α resonance fluorescence to monitor the hydrogen atom concentration in real time. The forward and backward rate constants were evaluated simultaneously by analysis of the decay traces obtained, thereby removing some of the potential systematic errors which could arise from the separate study of the two reactions. Cao and Back pointed out that although the data on the H + C_2H_6 == H_2 + C_2H_5 equilibrium was in general agreement, their own value for the C_2H_5 + H_2 rate constant was anomalous, illustrating the limitations of using two separately determined rate constants to define an equilibrium constant.

3.2 Experimental

The apparatus used in this study was described in Chapter 2. Different methods of hydrogen atom generation and data analysis were employed, as described below.

3.2.1 193.3 nm Photolysis of Ethylene at Elevated Temperatures

The absorption cross section of ethylene at 193.3 nm and ambient temperatures is too small to allow the production of concentrations of hydrogen atoms which were detectable using the present apparatus (>$5x10^{10}$ atomcm^{-3}). It was found at temperatures above 700K, however, that detectable concentrations of hydrogen atoms could be generated photolytically in the absence of the nitrous oxide/hydrogen precursor, using ethylene concentrations appropriate to kinetic measurements ([C_2H_4] $\sim 2.5x10^{14}$ moleculecm^{-3}). This increase in absorption cross section at 193.3 nm with temperature, can be understood in terms of the vibrational structure of the room temperature v.u.v. absorption spectrum of ethylene in the region around 190 nm, shown in Figure 3.1 [158].

Mulliken [159] has performed calculations on the vibrational structure of the π^*--π (A^1B_{1u}--X^1A_g) transition in ethylene, using the predictions of molecular orbital theory. The ground (N) and excited (V) state energies are shown as a function of the twist angle between the two methylene groups in Figure 3.2. The (0,0) transition lies around 265 nm but is extremely weak because of the large change in twisting angle involved. At shorter wavelengths, the Franck-Condon overlap between the ground and excited state wavefunctions rises with increasing twisting excitation of the upper state and thus, a progression due to the excited state twisting mode, ν'_4, is expected. A further complication arises, owing to the strong coupling between the twisting and C-C (ν_2) stretching modes in both states. For the twisted configuration, the π^* and π molecular orbitals are

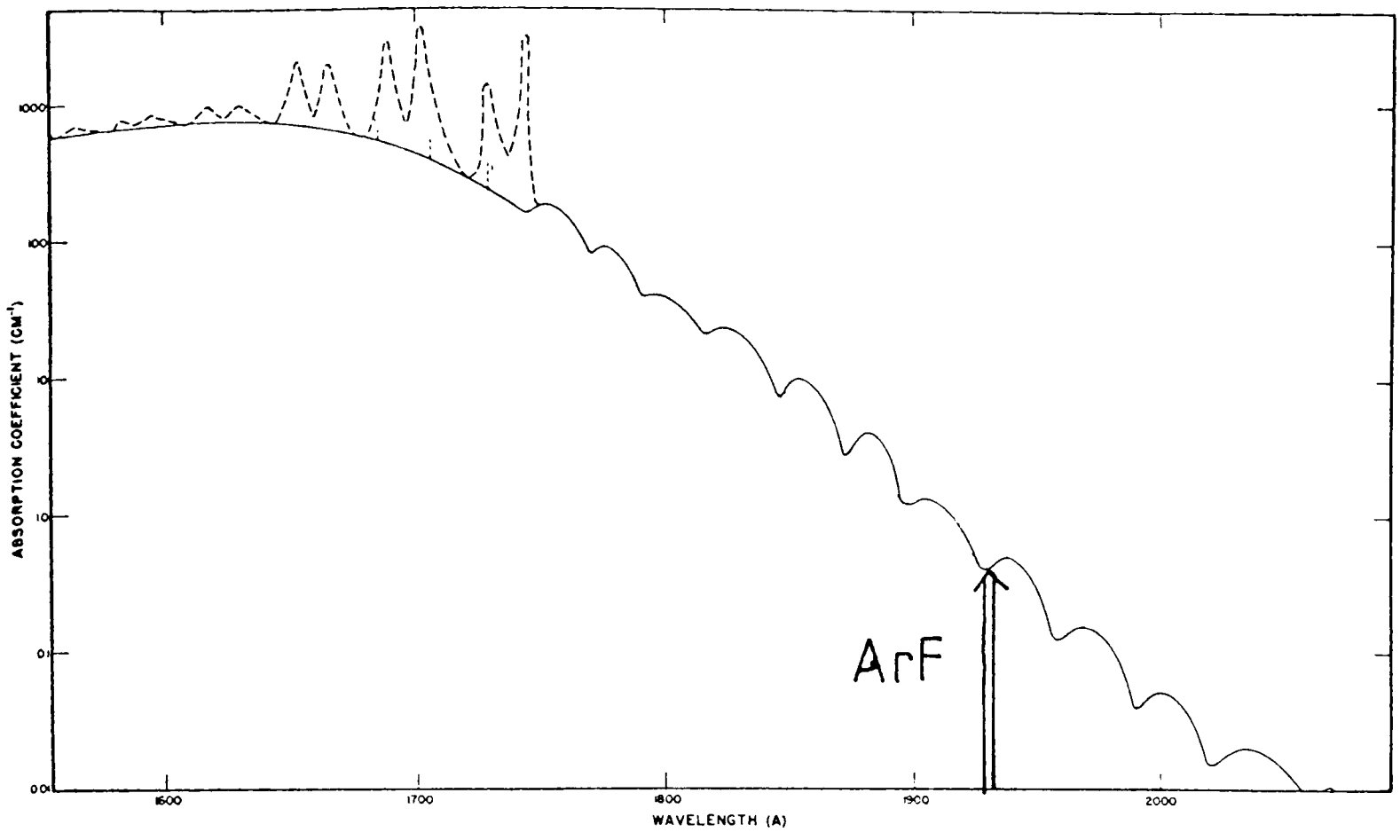

Figure 3.1. Ethylene Absorption Spectrum 155.5 - 205.0 nm.

Figure 3.2. Energy of Ethylene Π and Π^* States as a Function of Twist Angle, θ. The arrows demonstrate how the vertical excitation energy is reduced with excitation of the molecular twisting mode.

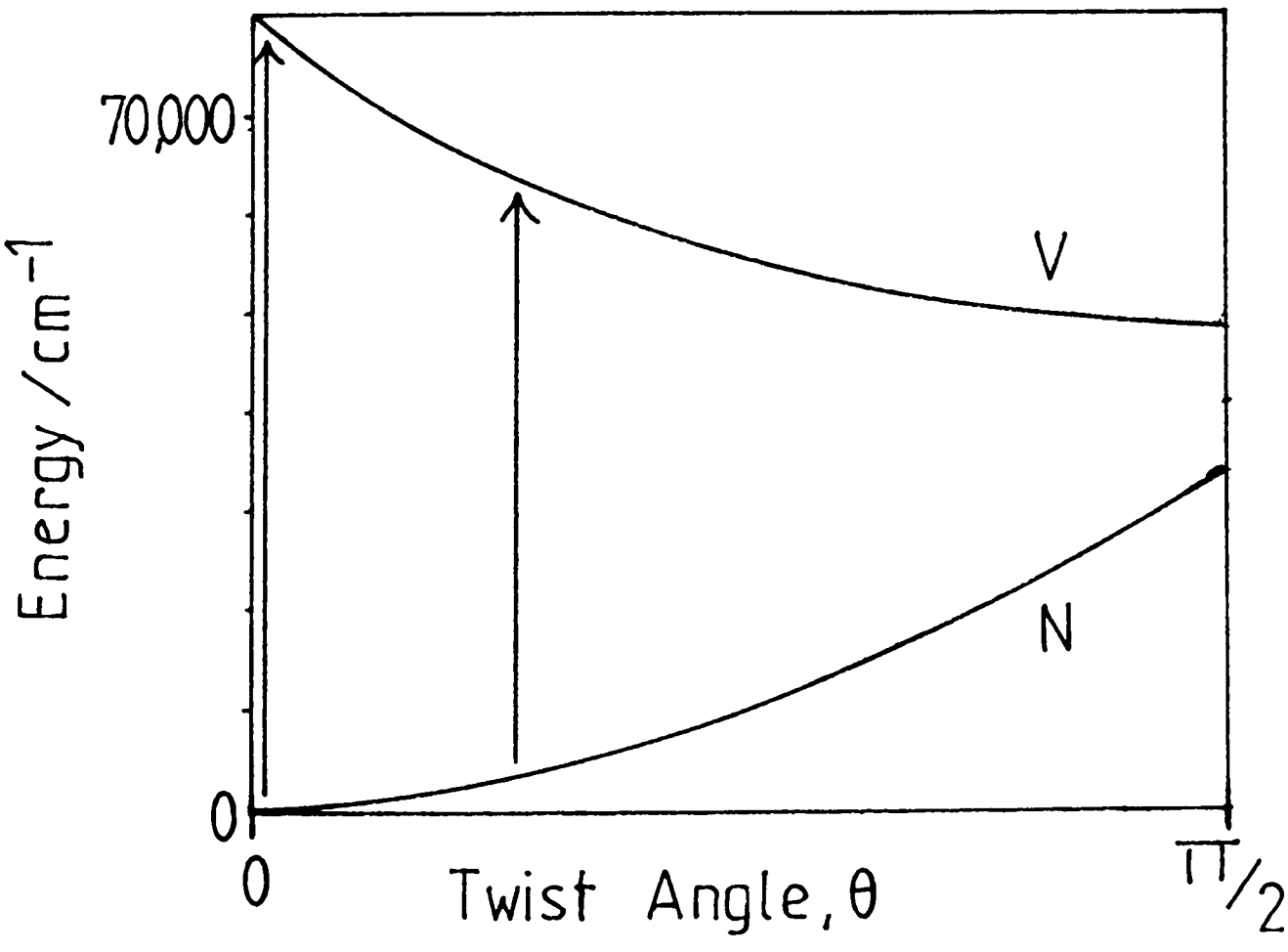

essentially non-bonding in character, resulting in nearly equal C-C bond lengths for the upper and lower states. For the planar configuration, however, the π^* and π molecular orbitals are antibonding and bonding respectively, giving rise to a large increase in the equilibrium C-C bond length between the ground and excited states. Mulliken modelled the vibrational structure in the long wavelength tail of the v.u.v. spectra of both C_2H_4 and C_2D_4, in terms of a progression in both the $\nu'2$ and $\nu'4$ modes and found good agreement with experiment.

Excitation of the ground state ν_2 and ν_4 modes will reduce the energy gap between the ground state molecule for a given (ν'_2,ν'_4) upper state vibronic level and will also shift the Franck-Condon envelope to lower energy, as shown in Figure 3.2, giving rise to an increased extinction coefficient at longer wavelengths. The increase in the absorption coefficient of ethylene at 193.3 nm with increasing temperature can thus be rationalised in terms of an increasing thermal population of the ground state ν_2 and ν_4 modes, resulting in an increased Franck-Condon overlap between the ground and electronic states at lower energies and a corresponding red shift in the v.u.v. absorption spectrum.

The absolute concentrations of hydrogen atoms generated by the direct photolysis of ethylene at elevated temperatures could not be accurately calculated, as the temperature dependence of its absorption cross section at 193.3 nm is not known. However, a comparison of the resonance fluorescence signal achieved when using $N_2O/H_2/He$ mixtures as the hydrogen atom precursor and that found using direct photolysis of ethylene, indicated that the ratio $[H]_o/[C_2H_4]$ varied between $1x10^{-3}$ and $1x10^{-2}$ over the intensity

ranges covered at 800K. This proceedure was only approximate, but allowed an upper limit of $4x10^{12}$ cm^{-3} to be placed on the maximum hydrogen atom concentration employed, corresponding to experiments performed at the highest laser energies and with the largest ethylene concentrations used. The vast majority of experiments were performed at much lower hydrogen atom concentrations, thus ensuring linearity between resonance fluorescence signal and hydrogen atom concentration at all times, with the line-reversed resonance lamp used [102].

The photolysis of ethylene at wavelengths around 180 nm is thought to proceed according to the scheme:

$$C_2H_4 \quad =====> \quad C_2H_2 + H_2 \qquad \text{P3.1}$$

$$C_2H_4 \quad =====> \quad C_2H_3^* + H \qquad \text{P3.2}$$

$$C_2H_3^* + M \quad =====> \quad C_2H_3 + M \qquad \text{P3.2a}$$

$$C_2H_3^* \quad =====> \quad C_2H_2 + H \qquad \text{P3.2b}$$

$$C_2H_4 \quad =====> \quad C_2H_2 + 2H \qquad \text{P3.3}$$

Back and Griffiths [120] used high intensity flash lamps with a broad spectral range (155 - 190 nm) and showed that no stable vinyl radicals were produced at pressures of around 1 Torr, in agreement with earlier work at 147 nm [160]. A mechanism involving processes P3.1 and P3.2 was proposed. Products due to the formation of vinyl radicals were observed on addition of 300 Torr N_2, in yields which indicated that 12% of the excited radicals, produced by the loss of a hydrogen atom from ethylene (P3.2), were stabilised. However, further increases in the quenching gas pressure resulted in only a marginal increase in the yield of vinyl radical products. This observation suggests that a photolysis channel was present (P3.3), by which acetylene and hydrogen atoms were produced directly and not via a

vibrationally excited vinyl intermediate. Furthermore, experiments by Borrell et al [161], employing low intensity photolysis with mercury lamps at 184.9 nm, showed that the vinyl radical yield was independent of pressure between 46 and 532 Torr, demonstrating that all the excited vinyl radicals, capable of being collisionally stabilised, were stabilised above 50 Torr. The quantum yields for the three primary processes were found to be 0.68, 0.20 and 0.16 for channels P3.1, P3.2 and P3.3 respectively.

The presence of vinyl radicals in the reaction system could have two complicating effects on the hydrogen atom decay. Firstly, if the rate of dissociation of the thermalised vinyl radicals was similar to the rate of removal of hydrogen atoms by reaction with ethylene (i.e. a few milliseconds), then the atom decay traces would contain a component which increased with time. The rate constant for the thermal decomposition of C_2H_3 was estimated from the limiting high pressure rate constant for the addition of hydrogen atoms to acetylene [162] and thermodynamic parameters for the hydrogen atom [163], acetylene [75] and the vinyl radical. The vinyl radical heat of formation is subject to a great deal of uncertainty, as is discussed in detail in Chapter 5. Recently, Ayranchi and Back [164] have obtained $\Delta H^{O}f(C_2H_3)$ = 63.4±2 $kcalmol^{-1}$, which is in serious disagreement with the value of 70.4±2 $kcalmol^{-1}$ favoured in the review by McMillen and Golden [77]. These two disparate estimates, combined with the limiting high pressure rate of the addition reaction and estimates of the entropy and heat capacity for vinyl taken from Benson [163], result in values of 1.2 and 87 s^{-1} respectively for the limiting high pressure rate of vinyl dissociation at 800K. As was demonstrated in Chapter 2, the rate

constant for the H + C_2H_4 reaction is at least a factor of four below its high pressure limit at 800K and 200 Torr He and it would be surprising if the vinyl dissociation rate were not still further into the fall-off region. The thermal dissociation of vinyl radicals is thus expected to be slow on the timescale of the present experiments and should not affect the hydrogen atom kinetics.

The second complication, which might be caused by the presence of vinyl radicals, arises from possible secondary reactions such as:

$$H + C_2H_3 \quad =====> \quad C_2H_4$$

$$C_2H_5 + C_2H_3 \quad =====> \quad 1\text{-}C_4H_8$$

which could affect the hydrogen atom decay at high radical concentrations.

In order to establish whether vinyl radicals were present in the photolysis system, a brief series of end product analysis experiments was performed, using the apparatus described in Chapter 4. Mixtures containing 1 Torr of ethylene in 200 Torr of helium were photolysed at 193.3 nm and at a temperature of 750K, the temperature limit of the end product analysis apparatus. Pulse energies of 35 mJ were employed and the beam was not defocused into the cell, so that the conditions of the time-resolved experiment were reproduced as closely as possible. Because of the low absorption cross section of the ethylene molecule at 193.3 nm, 100 laser pulses were required to obtain significant amounts of hydrocarbon products. Product analysis was performed by gas chromatography, employing a 2m n-octane/Porasil-C column and flame ionisation detection.

In principle, the relative amounts of saturated and unsaturated products would enable the relative importance of photolysis channels

P3.2a and P3.2b to be determined according to the simple scheme:

$$H + C_2H_4 \quad =====> \quad C_2H_5$$

$$C_2H_5 + C_2H_5 \quad =====> \quad N\text{-}C_4H_{10} \ , \ C_2H_4 + C_2H_6$$

$$C_2H_5 + C_2H_3 \quad =====> \quad 1\text{-}C_4H_8 \ , \ C_2H_4 + C_2H_4$$

$$C_2H_3 + C_2H_3 \quad =====> \quad 1,3\text{-}C_4H_6$$

Whence:

$$([H]/[C2H3])_o = \frac{2([N\text{-}C_4H_{10}]+[C_2H_6]) + [1\text{-}C_4H_8]}{2[1,3\text{-}C_4H_6] + [1\text{-}C_4H_8]}$$

Apart from acetylene, which was the most abundant component, the identified hydocarbon products were $N\text{-}C_4H_{10}$, C_2H_6, $1\text{-}C_4H_8$ and $1,3\text{-}C_4H_6$ in the ratios 2.28 : 0.79 : 0.25 : 0.23 . Analysis as above, gives $([H]/[C_2H_3])_o = 9.0$

However, the photolysis also produced compounds with retention times corresponding to C6 unsaturated hydrocarbons and with a total carbon yield approximately equal to the sum of the 1-butene and 1,3-butadiene products. Furthermore, the yields of 1-butene and 1,3-butadiene were approximately equal suggesting that the reaction scheme was complicated by the addition of vinyl radicals to ethylene. Possible reactions include:

$$C_2H_3 + C_2H_4 \quad =====> \quad C_4H_7^*$$

$$C_4H_7^* + M \quad =====> \quad C_4H_7 + M$$

$$C_4H_7^* \quad =====> \quad 1,3\text{-}C_4H_6 + H$$

$$C_4H_7 + C_2H_3 \ , \ C_2H_5 \quad =====> \quad C6 \text{ Products}$$

If one assumes that each C6 product contained one vinyl and one ethyl radical and that each 1,3-butadiene molecule arose from the addition of vinyl radicals to ethylene, then $([H]/[C_2H_3])_o = 6.6$.

Analysis of the data of Borrell et al. gives $([H]/[C_2H_3])_o$ = 3.5, suggesting that the fraction of thermalised vinyl radicals was substantially reduced under the conditions employed in this work. A direct comparison of the two results is difficult, owing to the different conditions employed, although the extra 14.25 $kcalmol^{-1}$ of thermal energy available at 750K more than makes up for the 6.7 $kcalmol^{-1}$ loss in photon energy from 184.9 to 193.3 nm and a decrease in the fraction of stabilised vinyl radicals is therefore not unreasonable.

The direct photolysis of ethylene at 193.3 nm and 750K is thus a fairly clean source of hydrogen atoms. An upper limit of 0.2 can be placed on the ratio of vinyl radical concentration to hydrogen atom concentration at t=0, under conditions appropriate to our kinetic measurements. As will be demonstrated later, any small contribution to the hydrogen atom decay from vinyl radical reactions can be completely removed by extrapolation to zero laser intensity.

3.2.2 Data Analysis

Under conditions where radical - radical reactions are unimportant i.e. $[C_2H_4] >> [H]_o$, hydrogen atoms formed in the initial photolysis are removed according to the simple scheme:

$$H + C_2H_4 \xrightarrow{k_1} C_2H_5 \qquad \text{R3.1}$$

$$C_2H_5 \xrightarrow{k_{-1}} C_2H_4 + H \qquad \text{R3.2}$$

$$H \xrightarrow{k_d} \text{Products} \qquad \text{R3.3}$$

where R3.3 is a first-order loss process, attributed to diffusion out of the monitoring zone.

The rate of ethyl radical diffusion was calculated to be a factor of seven slower than hydrogen atom diffusion under the conditions of the present experiments and was thus assumed to be unimportant. Solution of this set of first-order differential equations results in a biexponential time-dependent hydrogen atom concentration:

$$[H]/[H]_o = A\exp(\lambda_+ t) + B\exp(\lambda_- t) \qquad E3.1$$

where $[H]_o$ is the hydrogen atom concentration at t=0,

$$A = \frac{(k_1[C_2H_4] + k_d + \lambda_-)}{(\lambda_- - \lambda_+)} \qquad E3.2$$

$$B = \frac{(k_1[C_2H_4] + k_d + \lambda_+)}{(\lambda_+ - \lambda_-)} \qquad E3.3$$

$$\text{and} \quad \lambda\pm = (-b\pm(b^2 - 4c)^{1/2})/2 \qquad E3.4$$

$$\text{where} \quad b = k_1[C_2H_4] + k_{-1} + k_d \qquad E3.5$$

$$\text{and} \quad c = k_{-1}k_d \qquad E3.6$$

k_d was determined separately by generating hydrogen atoms in the absence of ethylene using mixtures of nitrous oxide and hydrogen, as described in Chapter 2. As the resonance fluorescence signal obtained was linear in hydrogen atom concentration, $[H]/[H]_o$ can be replaced by the ratio of the resonance fluorescence intensities at t=t and t=0, I(t) and I(0):

$$I(t)/I(0) = A\exp(\lambda_+ t) + B\exp(\lambda_- t) \qquad E3.7$$

Equations E3.2 - E3.7 were incorporated into a non-linear least-squares analysis program, which returned the best fit values

and variances of k_1, k_{-1} and I(0), for each decay trace. Typical analyses were perfomed over 5 ms using 700 data points from each trace. The first ~~7~~5 μs of each decay was discarded, because of a distortion in the decay at short times caused by a combination of radio frequency noise and scattered light from the excimer laser.

In contrast to the decays obtained at lower temperatures, fitting to the high temperature traces produced residuals which were approximately constant in magnitude with time, as can be seen from Figure 3.3. This change in behaviour can be attributed to the non-zero concentrations of hydrogen atom at long reaction times in the high temperature experiments.

Each data point was consequently given an equal variance (σ_i^2 = constant) in the analysis. As there was no realistic method of determining the statistical variance of the data, either before each experiment, or from the pre-trigger baseline, the variance of each data point was set to unity.

Non-linear least-squares analysis estimates the variance of each fitted parameter, k_j, from the corresponding element of the curvature matrix ε_{jj} [119]:

$$\sigma_j^2 = \varepsilon_{jj}$$

and determines the goodness of fit of the chosen function to the data from the closeness of the reduced χ^2 parameter to unity:

$$\text{Reduced } \chi^2 = \chi^2/(N-n-1) = \sum_{i=1}^{N} \frac{(1/\sigma_i^2)(y(i)-yfit(i))^2}{(N-n-1)}$$

where N is the number of data points and n the number of fitted

parameters. However, for these methods to provide meaningful results, the internal errors of the data points must be well defined, and the reduced χ^2 test was thus not applicable to the present data.

Realistic estimates of the external uncertainty in the data points were obtained from the observed variance of the data, s^2, about the fitted decay:

$$s^2 = \sum_{i=1}^{N} (y(i)-yfit(i))^2/(N - n - 1)$$

and the parameter errors calculated from:

$$\sigma_j^2 = s^2 \varepsilon_{jj}$$

That is, the external scatter of the data was used to calculate the uncertainties in the fitted parameters. The experimental signal-to-noise ratio for each decay trace, S/N, could be calculated from s, which is the root mean square of the scatter:

$$S/N = I(0)/s$$

As the reduced χ^2 test is meaningless when the variance of the data points is estimated from the scatter of the data about the fit itself, the goodness of fit of each decay was tested using two further statistics. The correlation index, CORI, is given by [4]:

$$CORI = \sum_{i=1}^{N} \frac{(y(i)-yfit(i))}{\sqrt{\chi^2(\sigma_i=1)}}$$

and tests whether the residuals are one-sided. Data with residuals

equally scattered about zero will produce |CORI| < 1. The autocorrelation index, AUCO is a measure of any systematic fluctuations in the residuals:

$$AUCO = \sum_{i=2}^{N} \frac{(y(i)-yfit(i))(y(i-1)-yfit(i-1))}{\chi^2(\sigma_i=1)}$$

The absence of any systematic trends in the residuals is indicated if $|AUCO| < (N-1)^{1/2}/N$ [4]. This autocorrelation test proved to be at least as sensitive to non-randomness in the residuals as a direct visual observation of the fit and enabled unsupervised batches of analyses to be reliably undertaken.

3.3 Results and Discussion

3.3.1 Experiments

Laser flash photolysis/resonance fluorescence experiments were performed at temperatures of 775, 800, 825 and 850K. The total pressure in each experiment was 200 Torr He, representing a compromise between the quenching of the resonance fluorescence signal with increasing bath gas pressure and a desire to limit the first-order diffusional loss rate to around 100 s^{-1}. At each temperature, the diffusional loss was measured with a precision of approximately 10% (2σ), using mixtures of nitrous oxide and hydrogen as the hydrogen atom source. The first-order loss rates so obtained are shown in Table 3.1.

Table 3.1

H Atom Diffusional Loss Rates in Equilibration Experiments

T/K	k_d/s^{-1}
775	70±3
800	90±9
825	108±14
850	78±4

Although the loss rates quoted in Table 3.1 do not exhibit the expected $T^{-1/2}$ dependence, they were invariant over the course of each set of experiments and thus provided a good estimate of the rate of first-order hydrogen atom loss in each case. The greater than expected increase in k_d with temperature up to 825K and the decrease between 825 and 850K, could be explained if there was some non-systematic reactive loss term, in addition to diffusive loss. These experiments were the first to be performed at temperatures above 600K using this apparatus and it is possible that chemical species, which were reactive towards hydrogen atoms, were degassing from the walls of the cell as the temperature was initially increased, but were mostly removed by the time the experiments at 850K were performed. Subsequent experiments at similar temperatures [165], produced diffusional loss rates in line with the value of k_d at 850K and which exhibited the expected $T^{-1/2}$ dependence, supporting this mechanism. The introduction of a very small additional first-order loss term does not, however, affect the analysis, as long as the total first-order loss rate is known. The very small errors in the fitted parameters, which would be introduced if k_d were in error

by up to 10%, are discussed in Section 3.3.4.

The ethylene concentration (typically $4x10^{14}$ moleculecm^{-3}) was varied at each temperature by at least a factor of two, in order to determine whether there was any systematic dependence of K_p on the partial pressure of ethylene, caused by complicating reactions such as the abstraction reaction of hydrogen atoms with ethylene. Because the absolute initial radical concentrations were only approximately known, a laser intensity dependence was performed at each temperature and ethylene concentration. The laser pulse energy, I, was variable over an order of magnitude (15 - 150 mJ).

A typical decay trace, together with the residuals from a non-linear least-squares fit, is shown in Figure 3.3. The decay is clearly not a single exponential, in contrast to the lower temperature work (see Figure 2.3). The signal does not achieve an equilibrium level, because the first-order loss term was not negligible on the millisecond timescale of the experiment.

It was found that the values of k_1 and k_{-1} obtained at each ethylene concentration depended somewhat on the laser intensity used. In all cases, both k_1 and k_{-1} decreased with I, the effect being greatest for k_{-1} and increasing with temperature. At 825K, k_{-1} decreased by 30% over the experimental range of laser intensities, compared to a 15% decrease in k_1 over the same range. The experimental values of k_{-1} and k_1 depended only very weakly on I at 775K.

At 775, 800 and 825K, the plots of k vs. I appeared to be linear and for a given temperature, the linearly extrapolated values of k_{-1} and k_{bi} ($=k_1/[C_2H_4]$) at I=0 showed no systematic dependence on $[C_2H_4]$. At 850K, however, although the k_{-1} plot appeared linear, the

Figure 3.3. Experimental Hydrogen Atom Decay Trace at 825K. Laser Pulse Energy 127 mJ, $[C_2H_4]$ = 1.90×10^{14} $molecule cm^{-3}$.

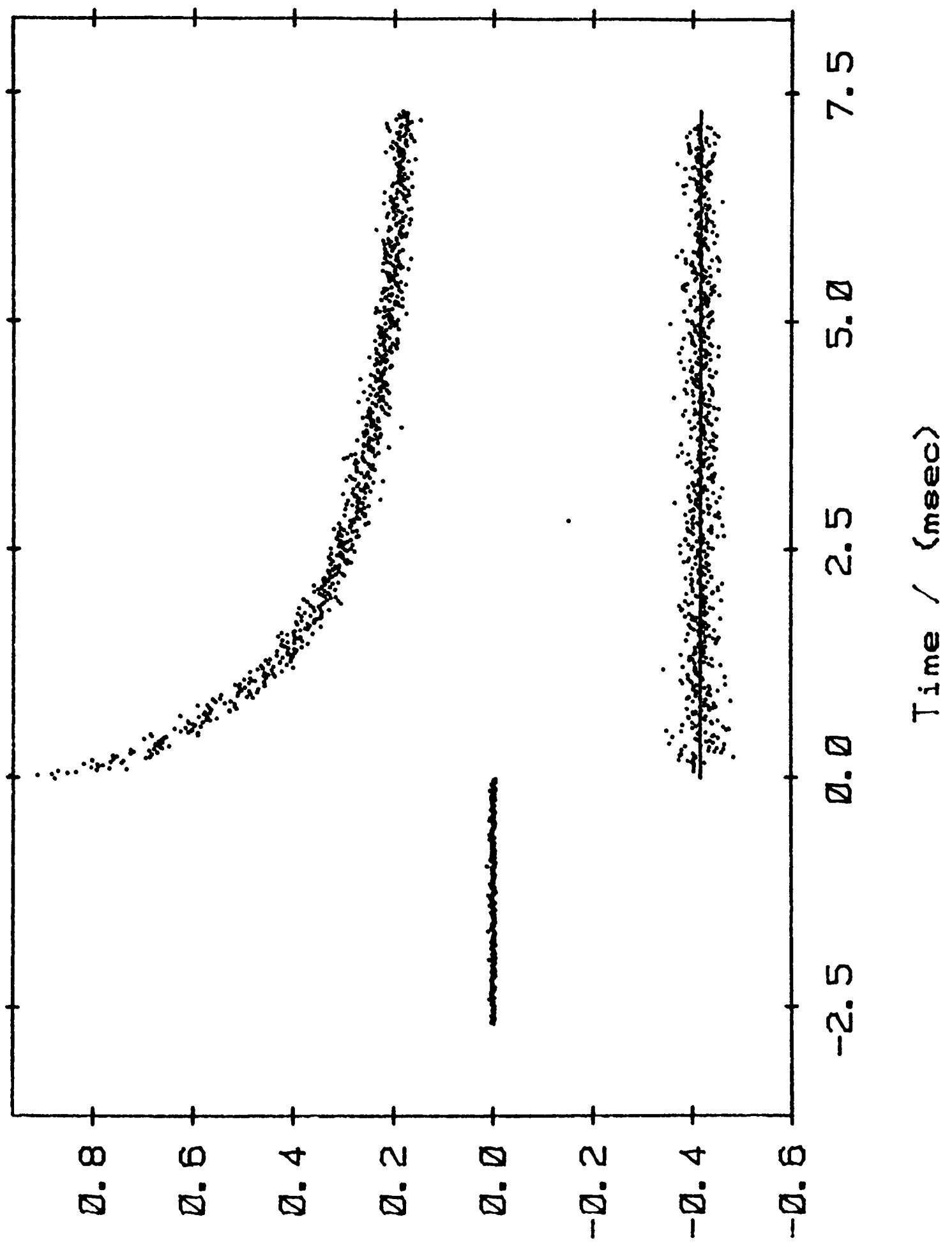

data were much more scattered than at the lower temperatures and k_{bi} displayed an obviously non-linear I dependence. Typical experimental intensity dependences for k_{bi} and k_{-1} at 825 and 850K are shown in Figures 3.4-6. As both k_{bi} and k_{-1} displayed a negative dependence on I, their ratio, K_c, was only slightly dependent on laser energy, as is shown in Figure 3.7 for data at 825K.

The values of k_1 and k_{-1} from each experiment in this study, are listed in Appendix 3.

3.3.2 Simulations of the Intensity Dependence of k_1 and k_{-1}

The dependence of both k_1 and k_{-1} on laser intensity clearly show that secondary reactions were not negligible under the experimental conditions employed. Extrapolation to I=0 was necessary, in order to extract the true equilibrium constant for the system at each temperature. Although the k vs. I plots appeared to be resonably linear at the lower temperatures, simulations were performed to determine whether the experimentally observed dependences could be reproduced by the inclusion of radical-radical reactions and if so, the best means of extracting the true values of k_1 and k_{-1} from the data. The following radical-radical reactions were added to the simple kinetic scheme of Section 3.2.2. Rate constants are in molecule^{-1} cm^3 s^{-1}.

$H + C_2H_5 \Longrightarrow CH_3 + CH_3$	1×10^{-10}	Estimate
$C_2H_5 + C_2H_5 \Longrightarrow N\text{-}C_4H_{10}$,	2×10^{-11}	[18]
$C_2H_6 + C_2H_4$		
$C_2H_5 + CH_3 \Longrightarrow C_3H_8$,	5×10^{-11}	[18],[26],

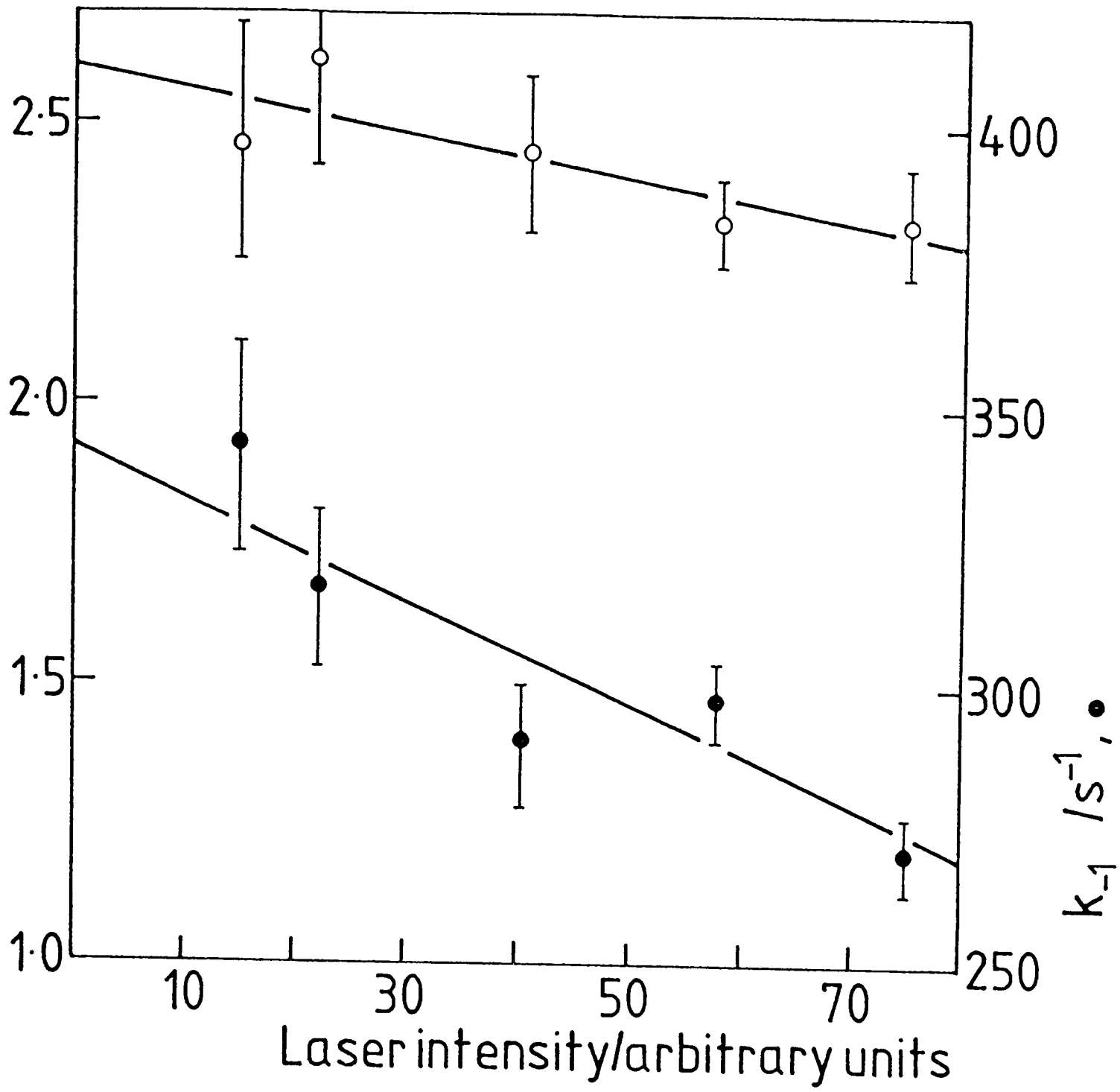

Figure 3.4. Experimental Dependence of k_{bi} and k_{-1} on Laser Pulse Energy at 825K. $[C_2H_4]$ = 3.83x10^{14} moleculecm^{-3}.

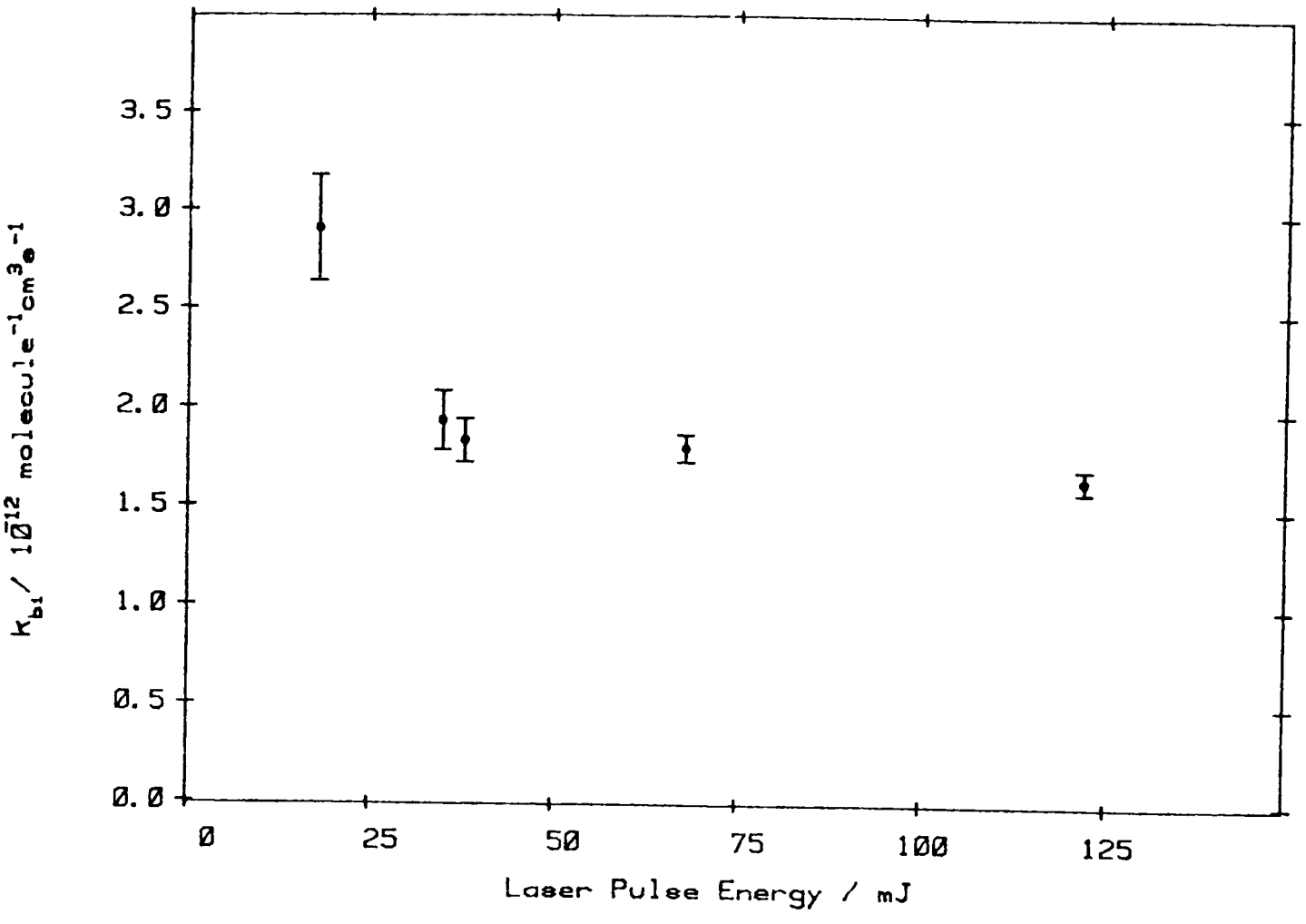

Figure 3.5. Experimental Dependence of k_{bi} on Laser Pulse Energy at 850K. $[C_2H_4]$ = 2.80×10^{14} moleculecm^{-3}.

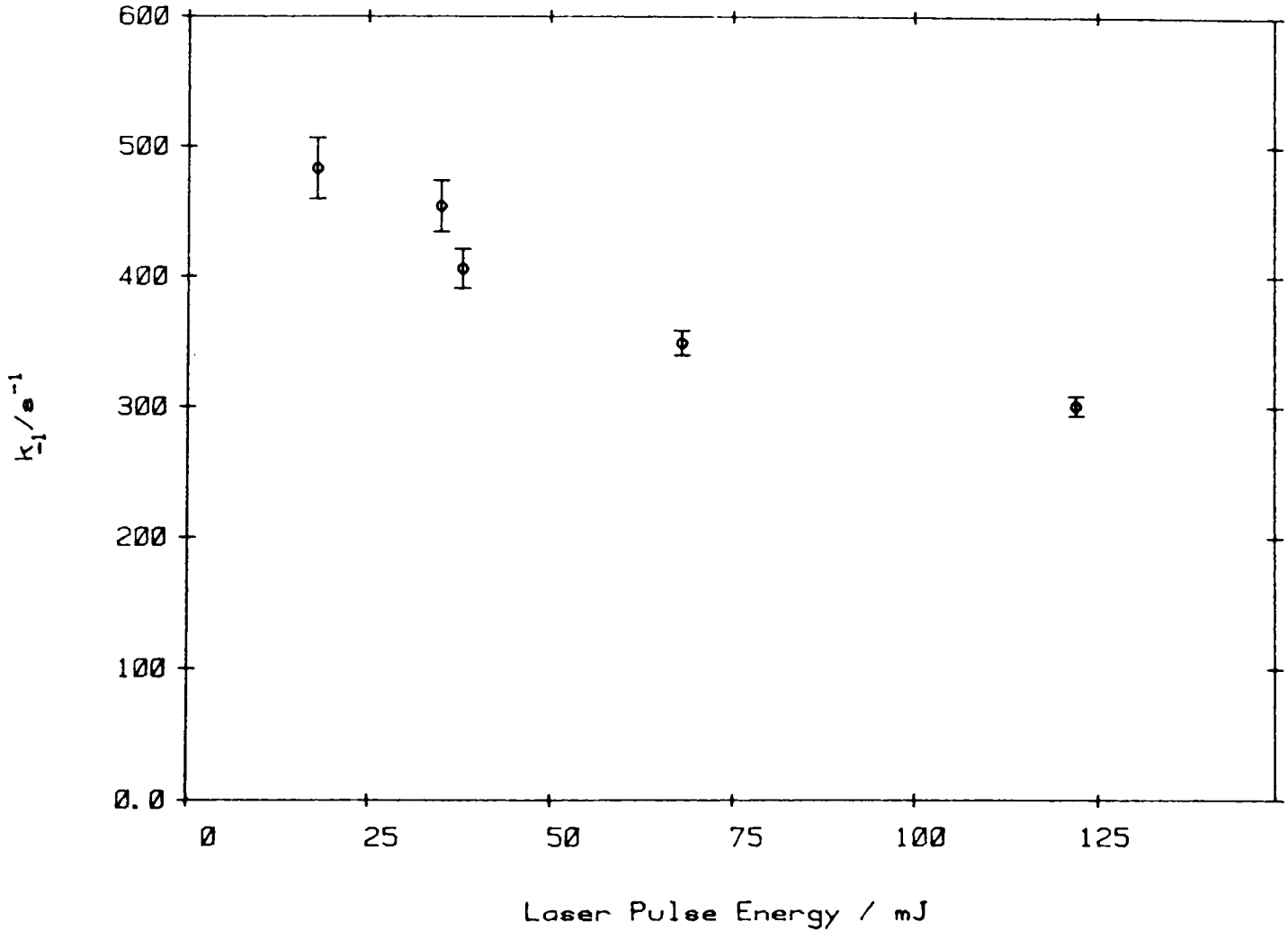

Figure 3.6. Experimental Dependence of k_{-1} on Laser Pulse Energy at 850K. $[C_2H_4]$ = 2.80×10^{14} moleculecm^{-3}.

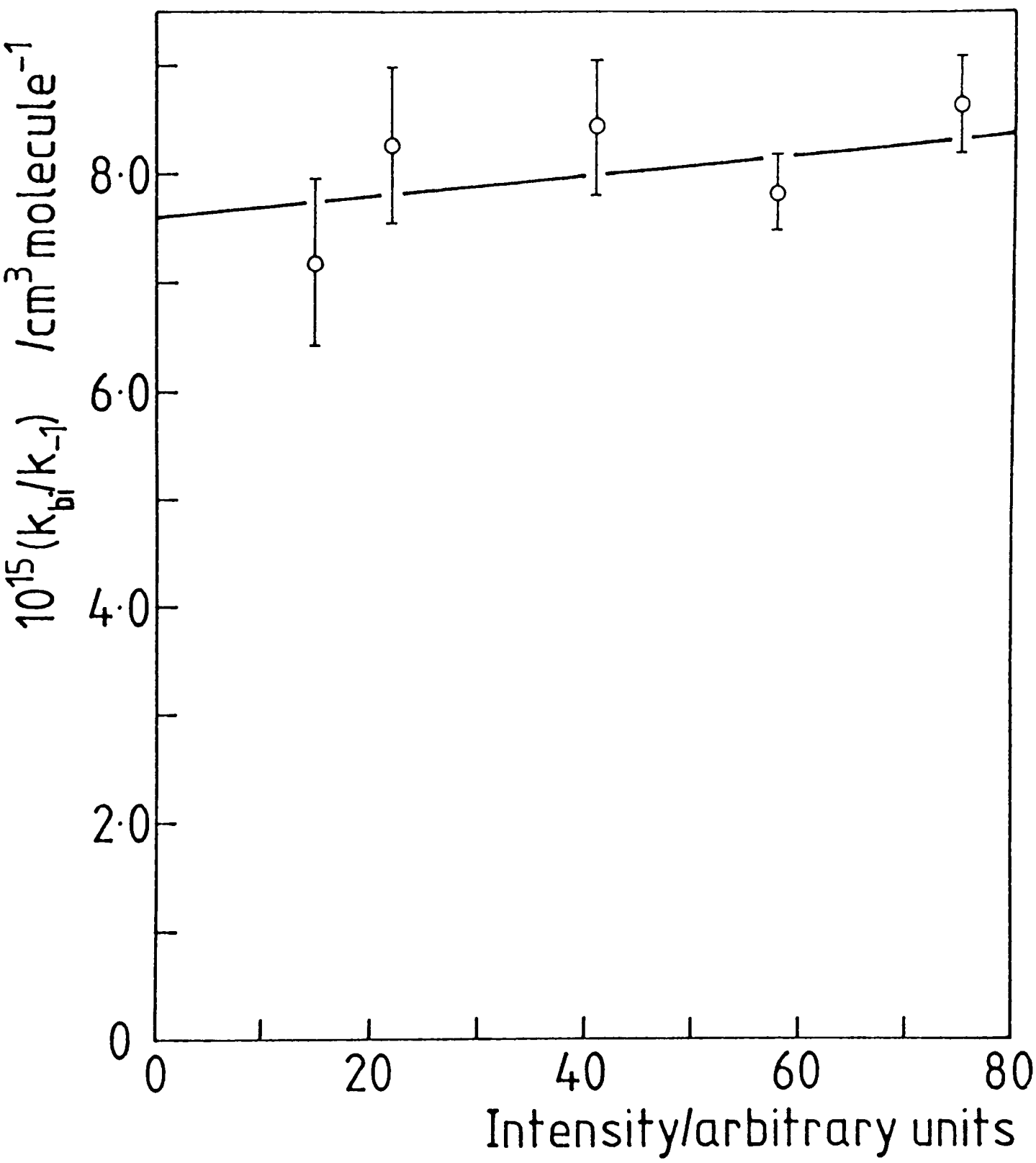

Figure 3.7. Experimental Dependence of K_c on Laser Pulse Energy at 825K. $[C_2H_4]$ = 3.83x10^{14} moleculecm^{-3}.

		$CH_4 + C_2H_4$		Mean Value Rule
$CH_3 + H$	=====>	CH_4	$1x10^{-12}$	[165]

An estimate of the rate of the reaction of hydrogen atoms with ethyl radicals, greater than the value of $6x10^{-11}$ molecule^{-1}cm^{3}s^{-1} obtained by Kurylo et al. [102], was used and it was assumed that there was no stabilisation of the excited ethane intermediate, in order to provide an upper estimate of the effect of this reaction.

The corresponding non-analytic decay traces were generated using the numerical integration package FACSIMILE [4]. Simulations were performed for temperatures of 800 and 850K, using the same timescale, diffusional loss rate and number of data points as employed in the experimental work. Bimolecular addition and unimolecular decomposition rate constants were taken from a linear extrapolation of the experimental I dependences to I=0. Initial hydrogen atom concentrations were varied from $5x10^{10}$ to $1.6x10^{12}$ atomcm^{-3}. The generated, smooth curves were transferred to floppy disk, and were analysed using the experimental data analysis program.

(i) 800K Simulations

Simulations using $k_{bi} = 3x10^{-12}$ molecule^{-1}cm^{3}s^{-1} and $k_{-1} = 170$ s^{-1} reproduced the observed decrease in both k_1 and k_{-1} with I and the greater sensitvity of k_{-1} to I, as shown in Figure 3.8. The form of the intensity dependence of k_{-1} was slightly curved in each case, with the curvature becoming more apparent as $[H]_o$ increased. The addition of normally-distributed random noise [166] to the smooth traces, using average experimental signal to noise ratios of 30:1 and then reanalysing the traces, produced intensity dependences which

Figure 3.8. Simulated Dependence of k_{bi} and k_{-1} on Initial Hydrogen Atom Concentration at 800K. k_{bi} = $3x10^{-12}$ molecule^{-1}cm^{3}s^{-1}, k_{-1} = 170 s^{-1}, k_d = 108 s^{-1} $[C_2H_4]$ = $5.2x10^{14}$ moleculecm^{-3}. o, Δ $[C_2H_3]_o$ = 0; ●, ▲ $[C_2H_3]_o$ = $[H]_o$; ■, x k_4 = $3.0x10^{-13}$ molecule^{-1}cm^{3}s^{-1}.

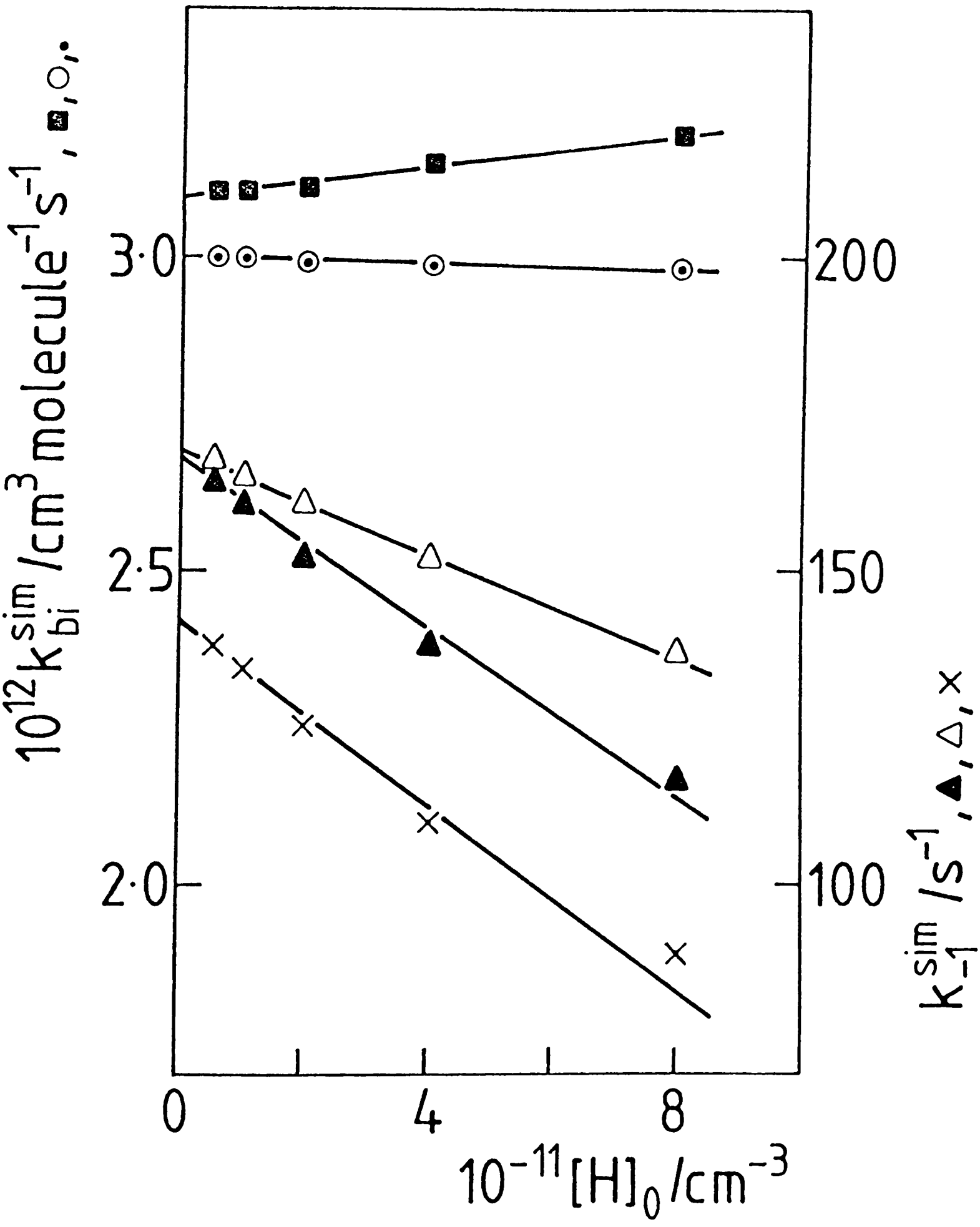

were very similar to those observed experimentally. In all cases, the small scatter in the fitted values of k_1 and k_{-1} caused by the addition of the noise, completely masked any slight curvature in the form of the intensity dependences. The plots of k vs. I then extrapolated linearly back to the original values used to generate the decays, within the external errors of the linear fit. A comparison of the F-test [119] values for linear and quadratic fits to the simulated intensity dependences, showed that the use of further terms in the fitting function did not significantly improve the fit. Furthermore, although fitting to the smooth generated decays produced fits which were slightly distorted at high $[H]_o$, because of the deviation of the decays from a truly biexponential form, the inclusion of noise into the decay traces completely masked any such distortion of the fit, as determined by the AUCO parameter, in accordance with the random residuals observed experimentally, even at the highest laser intensities. It was concluded, therefore, that, provided the reaction scheme employed in the simulations is realistic, a linear extrapolation to I=0 gives accurate values of k_1 and k_{-1}, as long as $[H]_o$ is not too large.

The effect of the presence of vinyl radicals in the reaction system was investigated by including an initial vinyl radical concentration equal to the initial hydrogen atom concentration and the extra reactions below. Estimated rate constants are in $molecule^{-1}cm^3s^{-1}$.

$H + C_2H_3 \Longrightarrow C_2H_4$	1.0×10^{-10}	Estimate
$C_2H_5 + C_2H_3 \Longrightarrow 1\text{-}C_4H_8$,	5.0×10^{-11}	[18],
$C_2H_4 + C_2H_4$		Mean Value Rule

$CH_3 + C_2H_3 \Longrightarrow C_3H_6$	7.5×10^{-11}	[18],[26],MVR
$C_2H_3 + C_2H_3 \Longrightarrow 1,3\text{-}C_4H_6$	2.0×10^{-11}	Estimate

A 15% increase in the slope of k_{-1} vs. I resulted, but the essentially linear nature of the plots and the values obtained by extrapolation were unaffected. The slight dependence of k_1 on I was unchanged. As the initial vinyl concentration was shown experimentally to be less than a fifth of the initial hydrogen atom concentration by the end product analysis experiments described in Section 3.2.1, the presence of vinyl radicals in the reaction system will have only a very minor effect on the decay traces obtained and will have no effect on the validity of the extrapolation to zero intensity.

The abstraction reaction of hydrogen atoms with ethylene:

$$H + C_2H_4 \Longrightarrow H_2 + C_2H_3 \qquad R3.4$$

provides a further potential complication to the kinetic scheme. The few studies made of this reaction [167-172] have been either very indirect, or at temperatures far removed from the present conditions. Estimates of k_4^{800K} range from 2.4×10^{-12} to 4.8×10^{-15} molecule^{-1}cm^{3}s^{-1}. As the magnitude of k_4 was thus essentially undetermined under the present conditions, it was important to investigate its likely effect on the experimentally determined rate constants. Simulations were performed in which k_4 was set to $0.1k_{bi}$, corresponding to $k_4^{800} \sim 3 \times 10^{-13}$ molecule^{-1}cm^{3}s^{-1}. As can be seen from Figure 3.8, the presence of an abstraction channel causes the k vs. I plots to extrapolate back to values of k_1 and particularly k_{-1}, which are significantly in error: k_1 is overestimated and k_{-1} is underestimated, resulting in an artificially high value of K_c

($=k_{bi}/k_{-1}$). If k_4 were important, the first-order loss term would be expected to increase linearly with $[C_2H_4]$ giving extrapolated rate constants, k_{-1} and k_{bi}, which were dependent on $[C_2H_4]$.

(ii) 850K Simulations

Rate constants of $3x10^{-12}$ molecule^{-1}cm^{3}s^{-1}, 600 s^{-1} and 78.5 s^{-1} were used for k_{bi}, k_{-1} and k_d to simulate the I dependences of k_{bi} and k_{-1} at 850K. To reiterate, the values of k_{-1} obtained from experiments at 850K decreased more steeply with I than they did at lower temperatures, although the dependence were approximately linear. The experimental values of k_1, however, were non-linear in I.

The simulated I dependences, shown in Figures 3.9 and 3.10 for $[C_2H_4] = 2.8x10^{14}$ molecule^{-1}cm^3, were in broad agreement with the experimental behaviour, in that k_{-1} displayed a steeper dependence on I than at 800K, with little curvature and that plots of k_{bi} vs. I were curved. Given also that the experimental range of $[H]_o/[C_2H_4]$ would rise with increasing temperature, because of the positive temperature dependence of $\varepsilon_{193.3}(C_2H_4)$, the experimentally observed non-linearity of k_{bi} vs. I plots at 850K is not unexpected. Unfortunately, the exact form of the variation of k_{bi} with laser intensity is dependent upon the somewhat uncertain values chosen for the radical-radical reactions and the range of $[H]_o/[C_2H_4]$ covered. It was, therefore, not possible to develop an accurate method of extracting the zero intensity values of k_{bi} from the curved intensity dependences.

It was concluded that, although the experimental behaviour at 850K was qualitatively reproduced, it was not possible to extrapolate both k_{bi} and k_{-1} to zero intensity as accurately as was possible at

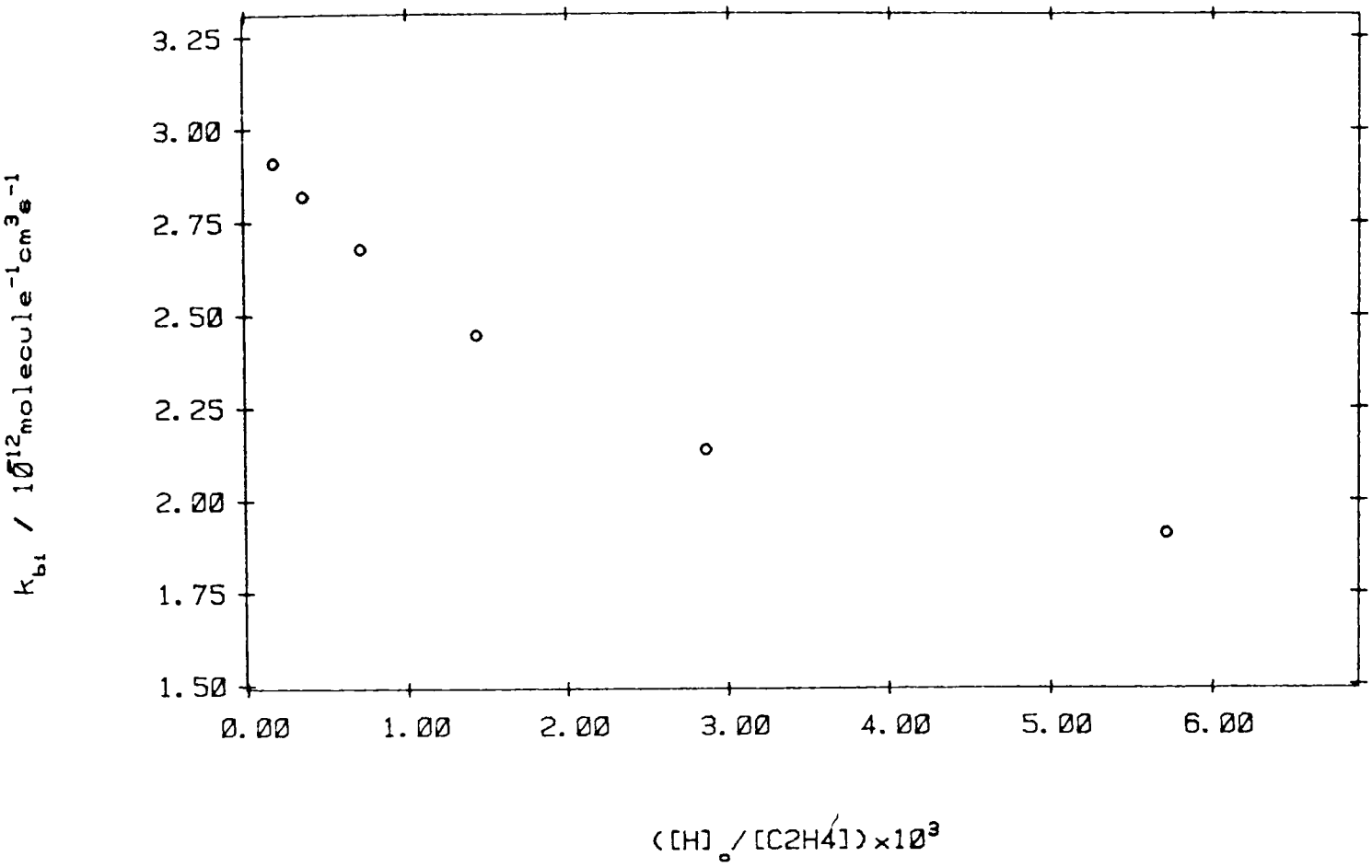

Figure 3.9. Simulated Dependence of k_{bi} on Initial Hydrogen Atom Concentration at 850K. k_{bi} = 3.0x10^{-12} molecule^{-1}cm^{3}s^{-1}, k_{-1} = 600 s^{-1}, k_d = 78.5 s^{-1}, [C_2H_4] = 2.80x10^{14} moleculecm^{-3}.

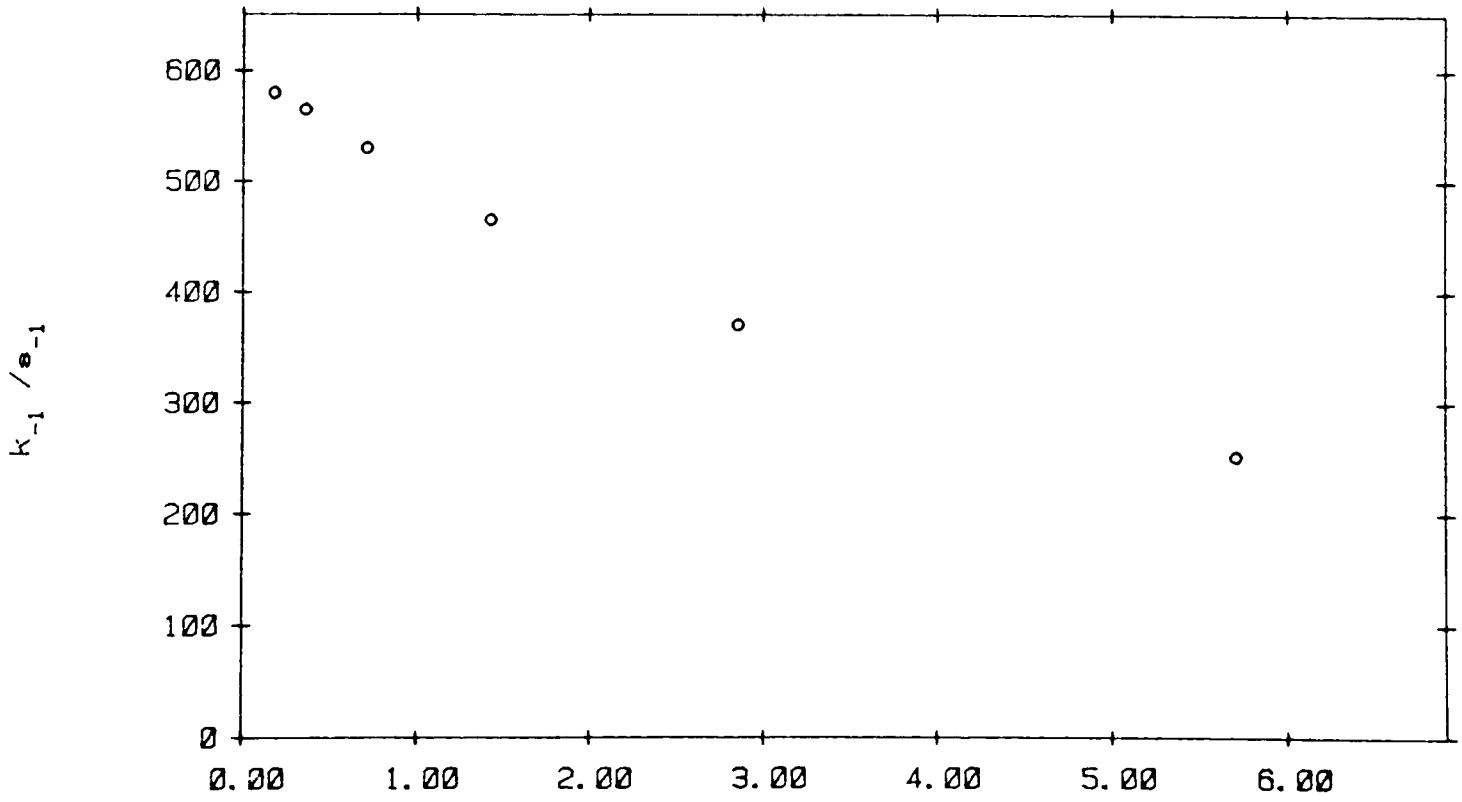

Figure 3.10. Simulated Dependence of k_{-1} on Initial Hydrogen Atom Concentration at 850K. k_{bi} = 3.0x10^{-12} molecule^{-1}cm^{3}s^{-1}, k_{-1} 600 s^{-1}, k_d = 78.5 s^{-1}, [C_2H_4] = 2.80x10^{14} moleculecm^{-3}.

the lower temperatures.

3.3.3 Calculation of Rate Constants and Thermodynamic Parameters

As the simulated k vs. I plots depended somewhat upon the temperature, the timescale and the ethylene concentration used, a linear extrapolation to I=0 was made for every value of $[C_2H_4]$ at each temperature, over the range 775 - 825K. Each determination of k_1 and k_{-1} was weighted in the linear plots by the reciprocal of its statistical variance, as determined by the analysis program. Table 3.2 shows the values of k_{-1} and k_{bi} obtained between 775 and 825K. The data obtained at 850K was not used in the calculation of $k_{bi}(T)$ and $k_{-1}(T)$ because of the uncertainty in extrapolating to I=0 at this temperature.

Table 3.2

Extrapolated Values of k_{bi} and k_{-1}

T/K	$[C_2H_4]/10^{14}$ moleculecm^{-3}	$k_{bi}/10^{-12}$ molecule^{-1}cm^{3}s^{-1}	k_{-1}/s^{-1}
775	1.90	2.74±1.38	103.4±61.2
	2.50	3.64±0.18	91.6±5.3
	5.00	3.31±0.28	92.1±3.4
800	2.60	2.90±0.18	151.5±21.4
	5.20	2.98±0.24	171.7±30.5
825	1.90	2.93±0.20	381.4±23.4
	3.83	2.59±0.26	342.3±42.1
	6.45	2.86±0.23	362.0±31.9

The uncertainties quoted here and elsewhere in this chapter, refer to 95.45% confidence limits, using the largest of the external and internal errors for each fit and include a Student's t, where possible. No systematic variation of the estimates of k_{-1} and k_{bi} with ethylene concentration is apparent, confirming that the abstraction reaction R3.4 is unimportant in this study.

The free energy change accompanying a chemical reaction is related to the equilibrium constant via:

$$\Delta G^{O}_{T} = -RT\ln K_p$$

and to the enthalpy and entropy changes for the reaction by:

$$\Delta G^{O}_{T} = \Delta H^{O}_{T} - T\Delta S^{O}_{T}$$

$\Delta H^{O}T$ and $\Delta S^{O}T$ are related to the standard enthalpy

and entropy changes by the expressions:

$$\Delta H^{\circ}_{T} = \Delta H^{\circ}_{298} + \int_{T=298}^{T} \Delta C_p(T)dT$$

and

$$\Delta S^{\circ}_{T} = \Delta S^{\circ}_{298} + \int_{T=298}^{T} \Delta C_p(T)d\ln T$$

where $\Delta C_p(T)$ is the temperature dependent change in heat capacity for the reaction. In principle, both the standard enthalpy and entropy changes for a given chemical reaction can be extracted from the temperature dependence of the equilibrium constant using the expression:

$$-\Delta H^{\circ}_{298}/T + \Delta S^{\circ}_{298} = R\ln K_p - \int_{T=298}^{T} \Delta C_p(T)d\ln T + (1/T)\int_{T=298}^{T} \Delta C_p dT \quad E3.8$$

The narrow temperature range covered in the experiments and the long extrapolation to 298 K, precluded the reliable estimation of both $\Delta H^{\circ}298$ and $\Delta S^{\circ}298$ from the data. However, the molecular parameters of both C_2H_4 and C_2H_5 are well defined, as is discussed in Section 2.5.2, enabling the standard entropy change for the reaction to be calculated to high precision. The absolute entropy of one mole of gas contained in a fixed volume, V, is given by:

$$S = R[\ln q_{tot} + T(d\ln q_{tot}/dT)_V - (\ln N - 1)]$$

where for standard states, V is the volume occupied by one mole of gas at 1 atmosphere pressure and temperature T, N is Avogadro's constant and q_{tot} is the total partition function for all degrees of freedom:

$$q_{tot} = q_{trans} \cdot q_{rot} \cdot q_{introt} \cdot q_{vib} \cdot q_{el}$$

The appropriate expressions, used to calculate q_{tot}, are shown in Table 3.3 [173].

Table 3.3

Formulae Used To Calculate Absolute Entropies

Partition Function	Formula	$T(d\ln q/dT)_V$
Translational	$1.54x10^{22} m^{3/2} T^{5/2}$	3/2
Rotational	$0.0148(I_a I_b I_c/\sigma^2)^{1/2} T^{3/2}$	3/2
Internal Rotational	$0.360(IT/\sigma^2)^{1/2}$	1/2
Vibrational	$(1 - e^{-xi})^{-1}$	x_i/e^{xi-1}
Electronic	1 for molecule, 2 for radical	0

Temperatures are in K, masses in a.m.u and moments of inertia in a.m.u.A^2. $x_i = h\nu_i/kT$. Table 3.4 shows the calculated entropies for H, C_2H_4 and C_2H_5 at 298K. The values recommended by Benson [163] are shown for comparison.

Table 3.4

Calculated Values of S^{O}_{298} ($calmol^{-1}K^{-1}$)

Species	S^{O}_{298} (Calc.)	S^{O}_{298} (Benson)
H	27.35	27.4
C_2H_4	52.35	52.4
C_2H_5	59.15	58.0

Although the values of $S^{O}298$ for H and C_2H_4 calculated here are in good agreement with those recommended by Benson, the value for C_2H_5 is significantly different. The thermodynamic parameters for H and C_2H_4 are well-known and provide a check on the method of calculation used. The discrepancy between the two values for C_2H_5 arises chiefly from the different treatments of the ethyl internal rotation used. Benson assumed a barrier to internal rotation similar to that for CH_3NH_2 (2 $kcalmol^{-1}$) and estimated the entropy of C_2H_5 from that of CH_3NH_2, after correcting for changes in electronic degeneracy and symmetry number. Free internal rotation was assumed for the purposes of this study, on the basis of experimental and theoretical studies, as is discussed above.

The standard entropy change for the forward reaction, k_1, is calculated to be -20.57 $calmol^{-1}K^{-1}$. The heat capacity change for the reaction at constant pressure, ΔC_p, was calculated as a function of temperature at 50K intervals from 300K to 1000K, assuming classical heat capacities for translation, rotation and free internal rotation. Vibrational heat capacities for C_2H_4 and C_2H_5 were calculated using the formula:

$$C_{vib} = R \sum x_i^2 e^{xi}/(e^{xi} - 1)^2$$

A plot of C_{vib} against temperature was linear, with a correlation coefficient of 0.995. $\Delta C_p(T)$ was replaced by:

$$\Delta C_p(T) = -3.59 + 2.01(T/1000)\ calmol^{-1}K^{-1}$$

in E3.8 and $\Delta H^O 298$ calculated for each value of $K_p(T)$. $\Delta H^O f,298(C_2H_5)$ was calculated from $\Delta H^O 298$ and the published [174,175] standard heats of formation of H and C_2H_4 (52.07 and 12.54 $kcalmol^{-1}$ respectively). The eight separate determinations of the standard heat of formation of the ethyl radical are presented in Table 3.5.

Table 3.5

Calculated Values of $\Delta H^O_{f,298}(C_2H_5)$

T/K	$[C_2H_4]/10^{14}$ moleculecm^{-3}	$\Delta H^O_{f,298}(C_2H_5)$ /kcalmol^{-1}
775	1.90	28.81±1.20
	2.50	28.19±0.12
	5.00	28.35±0.14
800	2.60	28.16±0.24
	5.20	28.35±0.30
825	1.90	28.56±0.26
	3.83	28.57±0.26
	6.45	28.51±0.20

The quoted 95.45% confidence limits were calculated from the statistical uncertainties in k_1 and k_{-1} using the method of propagation of errors. A weighted mean of the values listed in Table 3.5 gives:

$$\Delta H^{o}_{f,298}(C_2H_5) = (28.36\pm0.08)\ \text{kcalmol}^{-1}.$$

3.3.4 Uncertainties in the Heat of Formation of the Ethyl Radical

The errors quoted in Tables 3.2 and 3.5 refer only to the random errors derived directly from the data analysis. They include no estimates of possible systematic errors, although all eight determinations lie within the statistical error of their weighted mean at the 95.45% confidence level. There are several possible sources of systematic error which could reduce the accuracy of the calculated values of $\Delta H^{o}f,298(C_2H_5)$.

(i) Although the temperature of the system was uniform over the reaction region and was stable to within ±2K during each set of experiments, the quoted absolute accuracy of the thermocouples used was ±4K over the experimental temperature range. As K_p is a strong function of temperature, a small systematic error in T would give rise to a relatively large error in K_p. From the experimental dependence of $\ln K_p$ on 1/T and the quoted uncertainty in T, the corresponding 2σ uncertainty in the heat of formation of the ethyl radical is calculated to be ±0.36 kcalmol^{-1}.

(ii) The concentration of C_2H_4 in the system is subject to uncertainties caused by the measurement of the system pressure and temperature, and in the calibrations of the flow meters. Estimates of these potential errors are 1%, 0.5% and 2% respectively, giving rise to a potential 2σ error of ±0.07 kcalmol^{-1} in $\Delta H^{o}f,298(C_2H_5)$.

(iii) Any error in the calculated standard entropy and heat capacity changes for the reaction would be almost directly reflected in the value of $\Delta H^{o}f,298(C_2H_5)$ obtained. As the vibrational frequencies of ethylene are well known, the uncertainties in the vibrational frequencies of the ethyl radical determine the accuracy to which $\Delta S^{o}298$ and $\Delta C_p(T)$ can be calculated. The ethyl radical vibrational frequencies used in the present calculation are taken from the work of Pacansky et al. [90], as discussed in Chapter 2 and are listed in Table 2.9. It is of note that the two low frequency rocking modes (at 713 and 948 cm^{-1}) are calculated, rather than directly measured and are hence subject to uncertainty. Hase [151] used an earlier set of frequencies calculated by Pacansky and Dupuis [89] to estimate the missing frequencies. The only significant differences between the frequency set used by Hase and that used in these calculations are due to these two lowest, unobserved frequencies, set by Hase to 802 and 1186 cm^{-1} respectively. Calculation of the standard entropy of the ethyl radical with the frequency set employed by Hase gives $S^{o}298(C_2H_5)$ = 59.00 $calmol^{-1}K^{-1}$ and the expression for $\Delta C_p(T)$:

$$\Delta C_p(T) = -4.18 + 2.42(T/1000)\ calmol^{-1}K^{-1}$$

The corresponding value of $\Delta H^{o}f,298(C_2H_5)$ is calculated to be 28.12 $kcalmol^{-1}$, or 0.24 $kcalmol^{-1}$ smaller than calculated previously, demonstrating the sensitivity of the calculated value of $\Delta H^{o}f,298(C_2H_5)$ to changes in the molecular parameters of the ethyl radical. It is, perhaps, of interest that the changes in $S^{o}298(C_2H_5)$ and $\Delta C_p(T)$ contribute equally to the overall change in $\Delta H^{o}f,298$, because of the long extrapolation to 298K.

Very recently, Melius and Wagner [176] calculated the vibrational frequencies of the ethyl radical, using detailed ab initio calculations (HF/6-31G) and obtained frequencies which were significantly different from those quoted by Pacansky. The most important differences concern the two lowest frequency modes, where Melius and Wagner calculate 414 and 778 cm^{-1}, compared with the values of 540 and 713 cm^{-1} obtained by Pacansky [90]. It should be noted, however, that although the higher frequency was calculated in both cases, the lower frequency, corresponding to the umbrella mode at the radical centre, was observed as the strongest radical i.r. absorption feature by Pacansky and is unlikely to be significantly in error. The remaining error thus lies in the value of the second lowest frequency. Increasing this frequency from 713 cm^{-1} to 778 cm^{-1} alters $\Delta H^{o}f,298(C_2H_5)$ by only 0.1 $kcalmol^{-1}$.

It is difficult to quantify the uncertainty in $\Delta H^{o}f,298(C_2H_5)$ caused by the use of calculated frequencies, as the actual uncertainty in each calculated frequency is not known. An estimate of such errors will not be included in the final uncertainty for the ethyl radical heat of formation, but a change of up to 0.1 $kcalmol^{-1}$ might be necessary, if better ethyl radical frequencies were to become available.

(iv) The first-order diffusional loss term was determined in separate experiments with a precision of around 10%. Any error in k_d will be reflected in the value of k_{-1} returned from the analysis program and will have the greatest effect on K_p when k_{-1} is smallest i.e. at 775K. Changing the input k_d by 10% from 70 s^{-1} at 775K alters K_p by 2.6%, giving rise to a maximum 2σ uncertainty in $\Delta H^{o}f,298(C_2H_5)$ of

± 0.05 kcalmol^{-1}.

(v) The simulations in Section 3.2.2 show that the effect of the abstraction reaction R3.4 would be to introduce a further first-order loss term which increased with $[C_2H_4]$. This additional term would produce a systematic dependence of k_{bi}, k_{-1} and K_p on ethylene concentration. No systematic dependence of K_p or the two rate constants on $[C_2H_4]$ was observed at any temperature, indicating that R3.4 plays a negligible part in the overall kinetics.

The major, quantifiable, systematic error in the calculation of the heat of formation of the ethyl radical thus arises from a small uncertainty in the absolute temperature measurement. Combining internal and external errors using:

$$\sigma^2_{TOT} = \sigma^2_{INT} + \sigma^2_{EXT}$$

gives:

$$\Delta H^{O}_{f,298}(C_2H_5) = (28.36 \pm 0.40)$$

3.4 Conclusions

The equilibrium constant for the H + C_2H_4 == C_2H_5 system has been directly measured between 775 and 825K and at a total pressure of 200 Torr He. The standard heat of formation of the ethyl radical has been evaluated from the enthalpy change for the reaction at the experimental temperatures, using the known molecular properties of the species involved in the equilibrium. A weighted average of the eight separate determinations gives $\Delta H^{O}f,298(C_2H_5) = (28.36 \pm 0.40)$

$kcalmol^{-1}$, where the errors refer to 95.45% confidence limits and take into account both the data variance and estimates of potential systematic errors. The value of the ethyl radical heat of formation so obtained is much more precisely determined than has previously been possible and confirms that the long-accepted value of 26 $kcalmol^{-1}$, as determined by halogenation experiments, is in serious error.

Chapter Four

The Photolysis of Acetone at 193.3 nm

4.1 Introduction

A knowledge of the gas-phase reactions of the methyl radical is central to an understanding of the mechanisms of hydrocarbon pyrolysis: its thermal stability at cracking temperatures leads to high steady-state concentrations of the radical and it consequently plays an important part in chain propagation and termination steps. A clean methyl radical source, suitable for pulsed laser photolysis, would enable its reaction rates to be directly measured using transient ultraviolet [177] or infrared [66] absorption spectroscopy.

The flash photolysis of azomethane, using radiation in both the near [61] and far [178] ultraviolet, is known to provide a clean source of methyl radicals and has been frequently employed, although the use of azomethane as a radical precursor is limited, by its low thermal stability, to temperatures below 600K. Other possible methyl radical precursors such as acetaldehyde and the methyl halides suffer, at the high concentrations ($\sim 10^{14}$ cm^{-3}) employed in recombination studies, from potential problems caused by the unavoidable production of a second radical in the photolysis.

The acetone molecule would seem to be a promising methyl radical source: it is readily available, easily handled, thermally stable to well above 600K for residence times of several seconds, as typically found in flash photolysis experiments, and absorbs ultraviolet radiation above its dissociation threshold in a region which is accessible by pulsed laser sources.

The photochemistry and photophysics of the acetone molecule,

excited via its first absorption band (π^*<--n_o) which peaks around 280 nm (ε_{max} ~14 $M^{-1}cm^{-1}$), has been much studied [179-181], at wavelengths both above and below its dissociation limit. It is known that the primary dissociative process at wavelengths above 280 nm produces methyl and acetyl radicals:

$$CH_3COCH_3 \xrightarrow[\lambda>280\ nm]{h\nu} CH_3 + CH_3CO$$

Flash photolysis of acetone at λ>280 nm has been used as a source of both acetyl and methyl radicals for kinetic measurements [182], although the presence of a second radical in similar concentration limits the usefulness of the system as a methyl radical source.

The yield of acetyl radicals, as determined from quantum yields for carbon monoxide, or for biacetyl formed in the recombination reaction:

$$CH_3CO + CH_3CO \Longrightarrow (CH_3CO)_2$$

decreases with increasing temperature, owing to the thermal decomposition of the radical, and reactions involving the acetyl radical were found to be insignificant above 423K in end product analysis experiments employing low intensity, steady state photolysis, with λ>280 nm [183,184]. However, the thermal dissociation of acetyl radicals could complicate the methyl radical kinetics on the much shorter (μs - ms) timescale of flash photolysis / kinetic spectroscopy experiments.

The acetyl radical yield also decreases with decreasing wavelength below 280 nm, a consequence either of the increased dissociation of vibrationally excited acetyl radicals produced in the

initial photolysis step, or of the emergence of a second photolysis channel at higher energies which directly produces carbon monoxide:

$$CH_3COCH_3 \text{ =====> } CH_3 + CO + CH_3$$

Gandini and Hackett [180] found that the quantum yield of carbon monoxide production in the region 280 - 255 nm was unaffected by the presence of several hundred Torr of an inert bath gas and concluded that the direct route to carbon monoxide production was most likely, although they were unable to rule out the possibility of rapid predissociation from a low-lying excited electronic state of the acetyl radical.

No evidence for the presence of acetyl radicals has been found in the photolysis products of acetone excited via its second absorption band around 200 nm [185-187], although the single recent study performed in this wavelength region [187] employed a low intensity light source and the presence of short-lived acetyl radicals would not have been detected. The quantum yields for carbon monoxide and ethane production were found to be around unity, with very small yields of minor products attributed to high energy photolysis routes such as:

$$CH_3COCH_3 \text{ =====> } H + CH_2COCH_3$$

Such evidence suggests that the photolysis of acetone in this wavelength region, using a high intensity light source such as an excimer laser operating on the ArF transition at 193.3 nm, could provide a very clean methyl radical source for use in direct reaction rate measurements.

The second electronic absorption band of acetone [188], which

starts at 51270 cm^{-1} and exhibits a short progression in the ν_4' methyl deformation mode [189] is shown in Figure 4.1. It is thought that this band corresponds to the 3s <-- n_o Rydberg transition, as demonstrated by a broadening of its vibrational features at high pressures [190]. However, although all structure is lost, the band does not completely disappear in condensed phases and it is possible that a weaker underlying continuum corresponding to a s^* <-- n_o valence shell excitation is present [189]. As can be seen from Figure 4.1, 193.3 nm radiation at 51733 cm^{-1} lies in the region of low absorption between the first two features of the band, with $\varepsilon_{193.3} \sim$ 700 $M^{-1}cm^{-1}$.

Some of the thermodynamically possible photolysis products at 193.3 nm (147.8 $kcalmol^{-1}$), together with their corresponding excess energies are shown in Table 4.1.

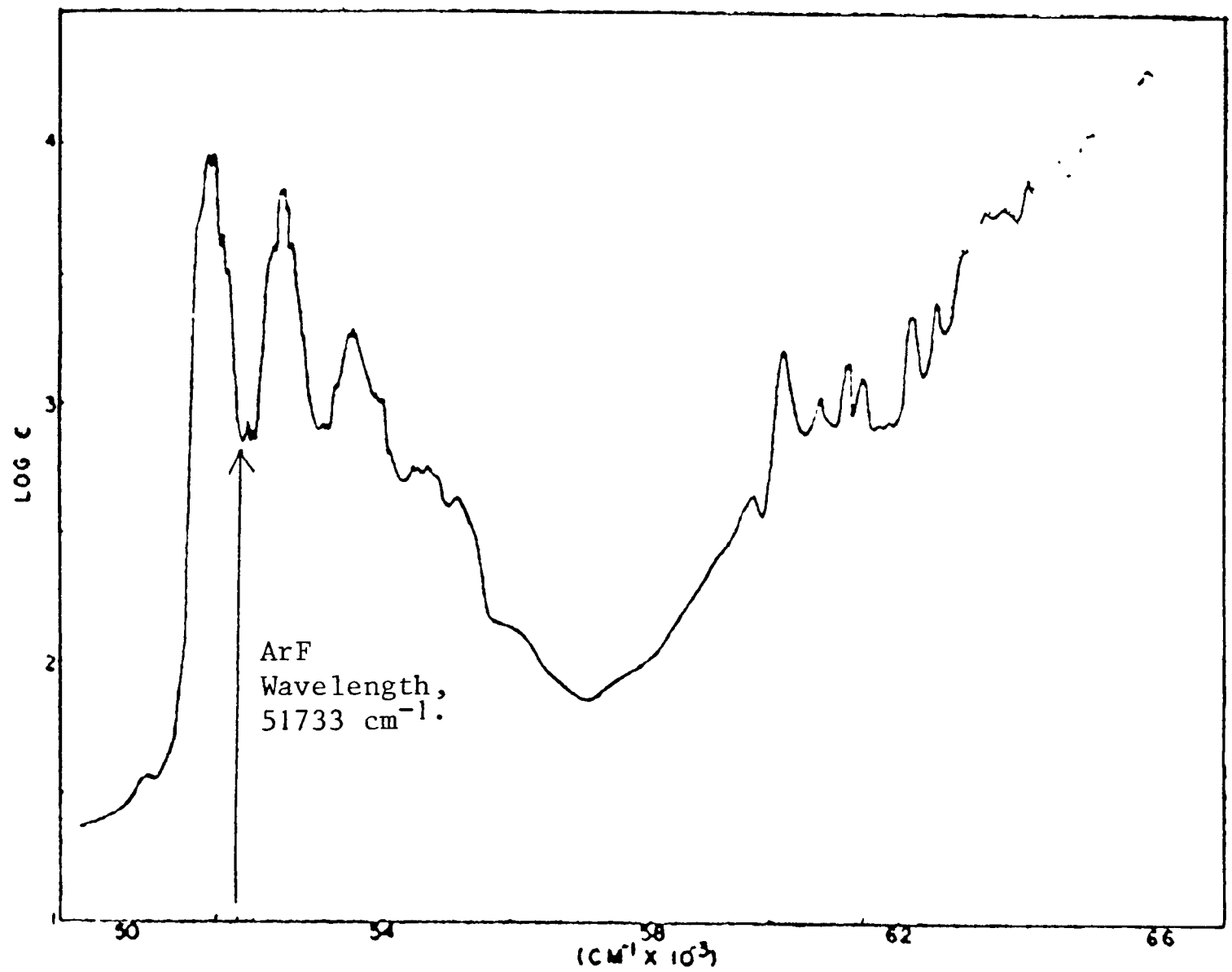

Figure 4.1. Absorption Spectrum of Acetone 40,000-67,000 cm^{-1}.

Table 4.1

Thermodynamically Possible Products From The 193.3 nm Photolysis Of Acetone [163]

Products	Excess Energy /kcalmol^{-1}
$CH_3 + CH_3CO$	66.7
$CH_3 + CO + CH_3$	53.9
$CH_3COCH_2 + H$	47.2
$CH_3 + CH_2CO + H$	21.2
$CH_4 + CH_2CO$	125.6
$CH_2CCH_2 + H_2O$	108.2
$CH_3CCH + H_2O$	109.8
$C_2H_4 + CO + H_2O$	110.2
$C_3H_6 + O\ (^3P)$	31.9
$C_{H4} + {}^3CH_2 + CO$	54.6
$C_2H_6 + CO$	142.9
$CH_3COCH + H_2$	55.4

Although there are a large number of energetically possible primary photolysis products, not all of which are shown in Table 4.1, many will not be produced, because of the presence of large barriers to dissociation and complex rearrangement.

The succeeding sections of this chapter describe the apparatus used, and the laser flash photolysis / end product analysis experiments performed, to determine the photolysis channels which are operating at the ArF excimer wavelength and the suitability of acetone as a methyl radical precursor in laser flash photolysis /

kinetic spectroscopy experiments.

4.2 Experimental

4.2.1. Apparatus For Laser Flash Photolysis / End Product Analysis Studies

The apparatus used in this study is shown schematically in Figure 4.2. Gas mixtures, made up on an all-glass vacuum line were transferred to a quartz cell housed in a stainless steel heating block and photolysed with defocused u.v. radiation from an excimer laser. After photolysis, the entire contents of the cell were transferred to a gas chromatograph for analysis. Transfer of the sample mixture between vacuum line, cell and chromatograph was controlled by two six-port stainless steel valves. A more detailed description of the individual sections of the apparatus is given below.

(i) Vacuum Line

The vacuum line was of conventional all-glass design and capable of achieving pressures of 10^{-5} Torr, as measured on a Penning gauge, by means of a 1" water-cooled oil diffusion pump (Edwards) backed by a two stage rotary pump (Metrovac). Young's greaseless taps and 'O' ring joints were used in the parts of the line which came into contact with gas mixtures. Gases were introduced into the line from cylinders via Swagelok connections to nylon tubing and stored in removable 2 litre bulbs. When large quantities of diluent gases were required, they were supplied directly from cylinders through Oxisorb

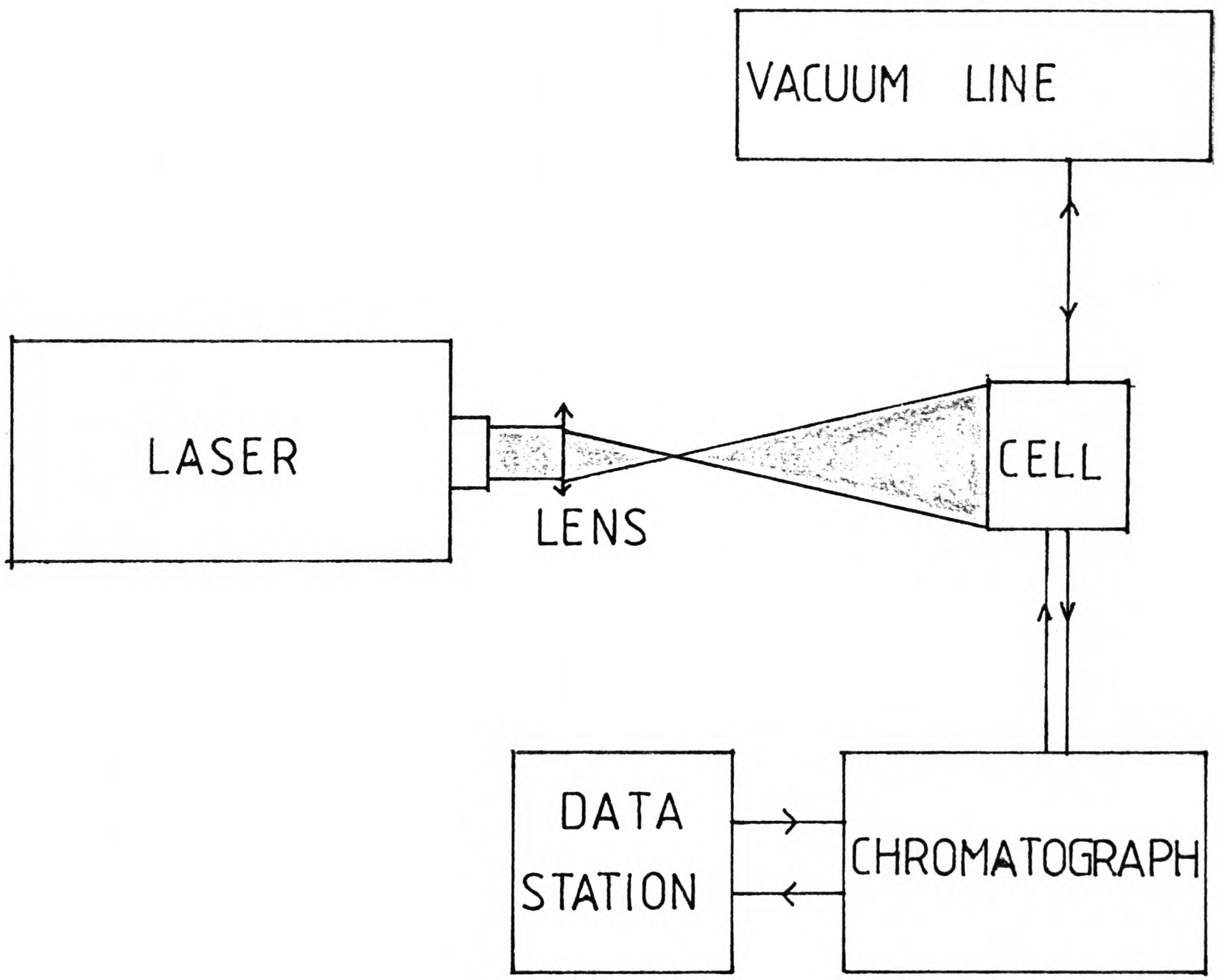

Figure 4.2
Flash Photolysis / End Product Analysis Apparatus (Schematic).

filters. Sample mixtures were made up in a 0.5 litre mixing vessel containing a magnetic stirrer, which enabled homogeneous samples to be prepared in a few minutes. The vacuum line was connected to the photolysis cell via a stainless steel six-port valve and 0.085" i.d. stainless steel tubing.

(ii) Laser

A spark-gap-triggered, discharge-pumped Oxford Lasers KX2 excimer laser, operating on the ArF transition at 193.3 nm with a bandwidth of $\sim$0.2 nm, was used as the photolysis light source in this study. An operating mixture of 9 Torr F_2, 150 Torr Ar and 20 p.s.i.g. He was employed and pulse energies of up to 100 mJ, as measured on a Gentec ED500 Joulemeter, were possible at a repetition rate of 0.5-1.0 Hz. Variation in pulse energy was achieved by inserting quartz flats in the beam path. The cavity gases were recirculated through a liquid-nitrogen-cooled trap using a Compton D657 compressor fitted with a PTFE diaphragm. In this way, absorbing impurities, which would otherwise build up in the cavity over the course of a few minutes operation and significantly reduce the output power, could be selectively trapped out and the useful lifetime of a single laser fill extended from $\sim$30 minutes to over 3 hours. Prior to use, the laser cavity was evacuated to below 0.15 Torr, initially through a soda lime trap to remove residual F_2, with a Speedivac rotary pump. The rectangular (5 cm x 1 cm) beam was defocused through a 9 cm focal length biconvex Spectrosil quartz lens, so as to fill the cylindrical body of the photolysis cell completely.

(iii) Chromatograph

(a) General Description

A commercial Varian Vista 44 system, consisting of a Vista 4600 gas chromatograph and a CDS401 data processing and control station, was employed for chromatographic analyses. The chromatograph incorporated both a flame ionisation detector (FID) and a thermal conductivity detector (TCD); the two detectors could be used separately or in series. For the majority of analyses, flame ionisation detection alone was employed because of its greater sensitivity towards hydrocarbons, although some experiments were performed using both detection methods when analysis of carbon monoxide, which has a negligible FID response, was required. Instrumental parameters during the course of an analysis were controlled from the CDS401 data station, which also performed peak identification and integration. Data processing facilities included the storage and subsequent subtraction of baseline shifts caused by temperature programming, and the digital recording of chromatograms on floppy disk, enabling data analysis to be optimised without the need to re-run the chromatogram repeatedly. Data processing and chromatograph operating parameters for a given analysis could be stored on disk. During the course of an analysis, the instrumental conditions and current operating parameters could be monitored, and, if required, altered, via the interactive real-time status page of the CDS401.

(b) Cell Flushing and Flow Control

The chromatograph was connected to the photolysis cell via two stainless steel six-port valves (Valco), as shown schematically in Figure 4.3. In configuration A, the cell was connected to the vacuum line for evacuation and introduction of gas mixtures, and the helium carrier gas fed directly into the column through flow controller 1, which was set to give a flow of approximately 35 sccm min^{-1}. Before each analysis, the transfer line was flushed out with carrier gas by opening the needle valve ($N^{\cdot}$) for a few minutes. In order to transfer the cell contents to the column, the valves were switched to configuration B, in which the carrier gas was routed into the cell, where it pressurised the sample gas and forced it through the transfer line onto the column. Flow controller 2 was set so as to match the maximum cell pressure to that at the head of the column in configuration A, thereby minimising flow disturbances when the valves were returned to configuration A on completion of the transfer. Similarly, the bleed on the column valve was adjusted so as to maintain the carrier gas head pressure at its normal operating value. The valves were pneumatically driven by compressed nitrogen, the flow of which was controlled from the data station by means of solenoid-based actuators.

Despite the high flushing efficiency of the cell design, described below, the time taken to flush out the cell volume effectively, was long compared to the peak widths expected and typical differences in retention times between adjacent peaks, resulting in significant peak tailing and overlap. A procedure was developed in which the column was wrapped in woven glass fibre tape

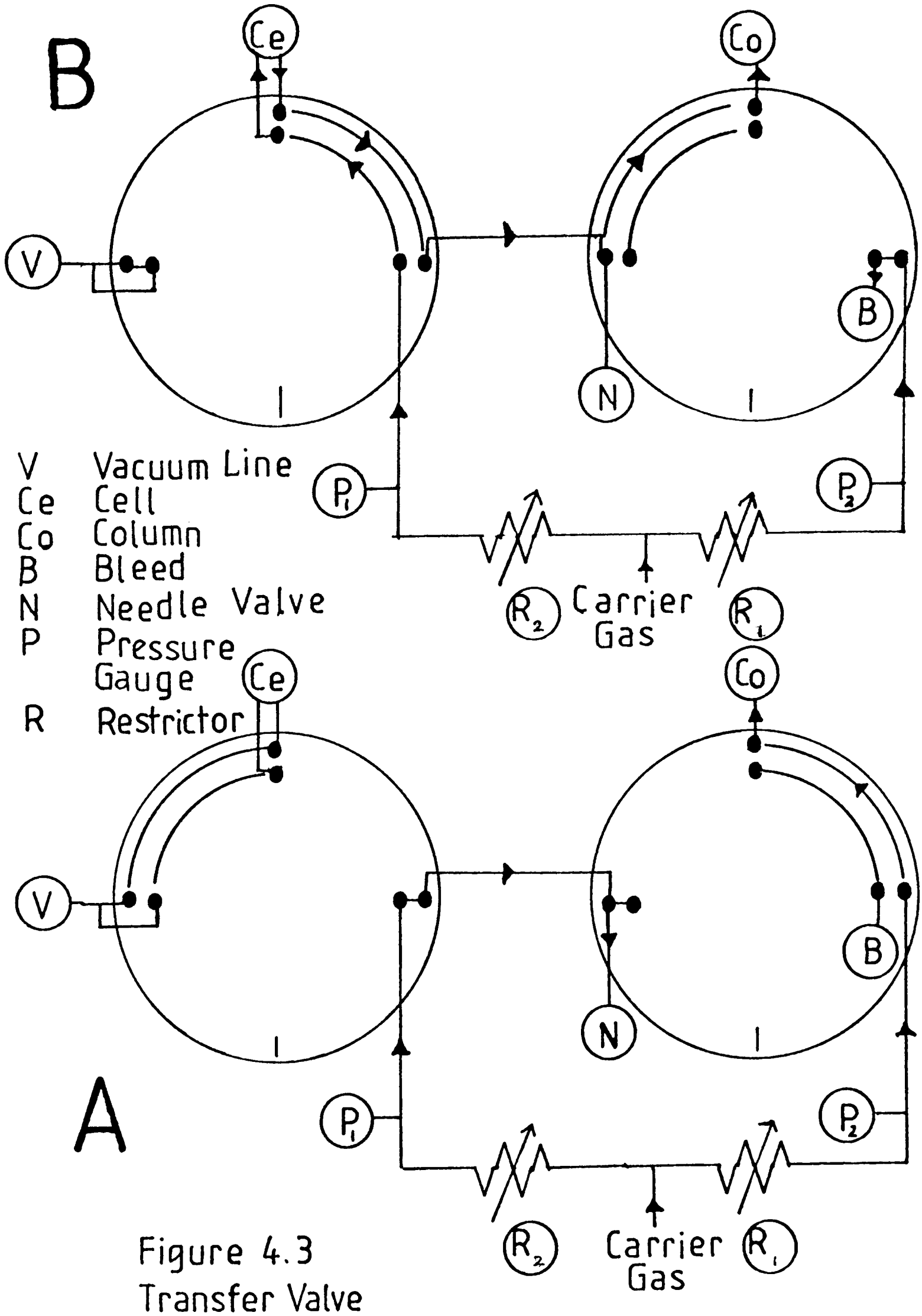

Figure 4.3
Transfer Valve
Configurations

and cooled in liquid nitrogen for the flushing period. Once the valves had been switched back, the liquid nitrogen Dewar was removed and the cell allowed to warm up to the ambient oven temperature. It was found that the process of cooling the column to 77 K effectively trapped the sample (including volatile components such as CO and Ar) in the first few column centimetres, resulting in sharp, well-separated peaks. Improved absolute separation of rapidly eluting components was also noticed because of the insulating nature of the glass fibre tape, which slowed the warming up of the column from 77K to 303K once the liquid nitrogen was removed, thereby providing a few minutes' sub-ambient operation.

(c) Columns and Analysis Methods

The various columns used in this work were all home-made by filling chromatographic quality 0.085" i.d. stainless steel tubing (Greyhound) with commercial column packing materials. Settling of the column packing was achieved by attaching a water pump to one end of the column through a glass fibre plug and causing the length of the column to vibrate by means of a file. Once packed, the open end was sealed with a second glass fibre plug, and the column formed into a 1" diameter spiral, which would fit into a small liquid nitrogen Dewar, and wound in glass fibre tape.

For end product analysis work, a 12' column of Chromosorb 102 60/80 mesh packing material was used. This particular column material was chosen for its ability to elute both hydrocarbons and oxygenated compounds with good separation [191]. In experiments where FID detection alone was employed, the column was held at 303K for seven minutes after the gas sample had been transferred, then temperature

programmed up to 443K in two stages: from 303 to 423K at 5Kmin^{-1} and from 423 to 443Kat 1Kmin^{-1}. When TCD detection of carbon monoxide was required, the column was kept at 263K in a methanol / ice bath for the initial isothermal period in order to achieve adequate separation between the carbon monoxide peak and a peak caused by an air impurity introduced during the switching of the valves. A listing of the analysis method used is given in Appendix 4.

(iv) Photolysis Cell and Housing

The cell was made entirely of Spectrosil quartz, which does not appreciably attenuate radiation at wavelengths above 190 nm and of a construction, shown in Figure 4.4, based on a design by Braun [192], which enabled its entire contents to be rapidly and efficiently flushed out into the chromatographic detection system, providing greater sensitivity than offered by conventional sampling techniques. Carrier gas was fed into the annular ring at one end of the cell, from which it flowed evenly into the main cell body through a narrow ($\sim$1 mm) circular gap between the end window and the cylindrical cell body. The pressurised cell contents were forced out through a similar arrangement at the other end of the cell. Although ideal plug-flow conditions were by no means achieved using this design, it was found that > 99% of a rapidly eluting hydrocarbon sample was flushed out of a total cell volume of 41.7 cm^3, at a flow rate of 35 sccm's, in eight minutes, representing a considerable improvement on the the 15 minutes flushing time required for 99% elution of a cell of volume 27.9 cm^3, in which the cell arms fed directly into the cell body [193].

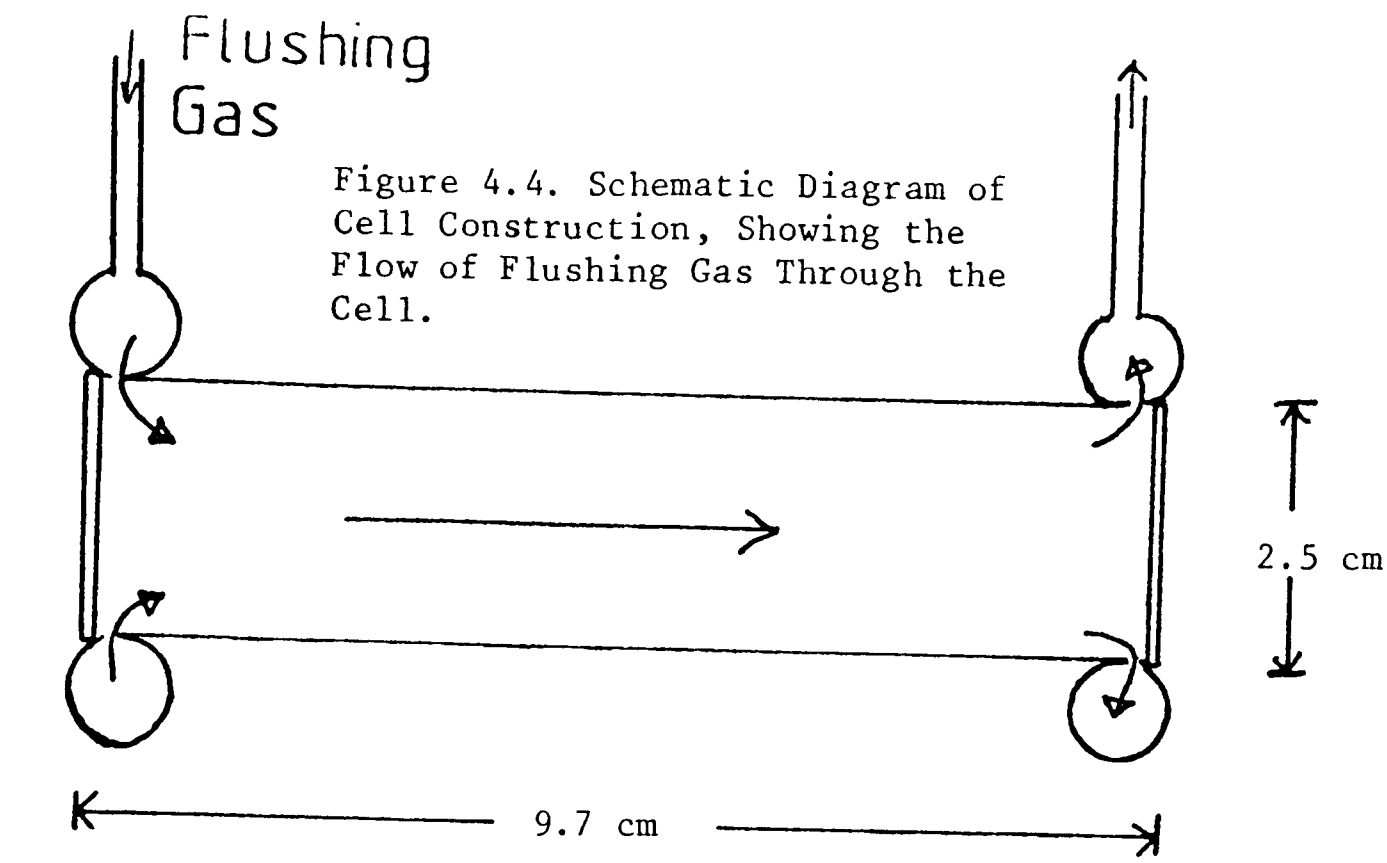

Figure 4.4. Schematic Diagram of Cell Construction, Showing the Flow of Flushing Gas Through the Cell.

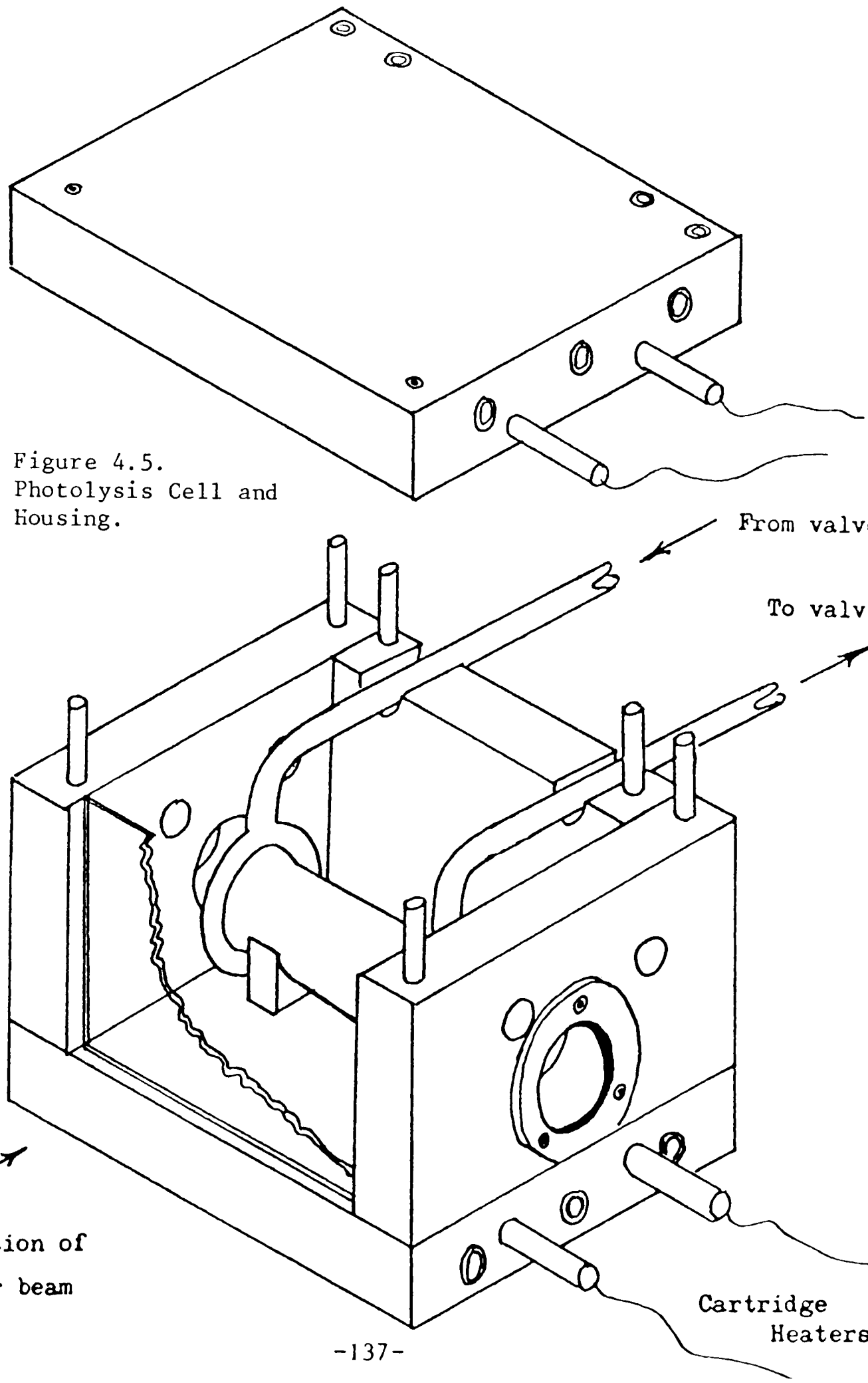

Figure 4.5.
Photolysis Cell and Housing.

The cell was mounted in a stainless steel housing, heated by four 270 W cartridge heaters (Genisto Ltd.) powered by an in-house temperature controller. The temperature inside the housing was monitored by a Chromel-Alumel thermocouple, which also acted as a sensor for the temperature controller. Laser radiation reached the cell through a Spectrosil quartz plate mounted in the front of the housing. The arrangement of the cell and housing is shown in Figure 4.5. Thermal insulation, provided by 0.5" Zircon board and covering all but the region of the quartz plate required to pass the excimer radiation, enabled temperatures of up to 750K to be attained. As one side of the cell housing contained a poorly-conducting quartz plate, temperature gradients were unavoidable and at 600K, there was a 10K drop in temperature across the the cell, although the uncertainty in the overall cell temperature was reduced at lower temperatures.

In order to test the sensitivity of the method and place product concentrations on an absolute scale, extensive calibrations were performed in which quantitative amounts of accurately made up mixtures of C_1 - C_4 hydrocarbons diluted to $\sim$1 in 1000 with Ar were analysed. In all cases, plots of detector response against hydrocarbon partial pressure were highly linear (±2%) and passed through the origin. The measured hydrocarbon response factors (hydrocarbon partial pressure / detector counts) were invariant over the course of many months and independent of column. FID responses for both saturated and unsaturated hydrocarbons are known to be [194] proportional to the number of carbon atoms in the molecule; it is thought that the major current-carrying species in the flame ionization of hydrocarbons is HCO^+, formed in the high temperature reaction $CH + O \Longrightarrow HCO^+ + e^-$. Calibrations using several

independently made up mixtures gave relative response factors which never varied by more than ±5% from that expected on the basis of carbon number. Ketones are known to display a sensitivity equal to the corresponding hydrocarbon with one fewer carbon atoms, the carbonyl group having a negligible contribution to the overall signal. Calibrations for acetone were in agreement with this observation: its response factor was very close to that for C_2 hydrocarbons. The close agreement between the expected and observed relative response factors for a wide range of molecules demonstrated that the method of sample transfer was equally efficient for all compounds of interest. Tests showed that C_3 hydrocarbon concentrations as low as 0.002 mTorr (equivalent to 2.6×10^{12} molecules in the cell) could be detected and absolute hydrocarbon partial pressures of 0.1 mTorr and greater could be measured with an accuracy of ±5% or better. Calibrations using the TCD showed that thermal conductivity detection was approximately a factor of 100 less sensitive than flame ionisation detection for hydrocarbons.

4.2.2. Calculation of Absolute End Product Concentrations

One of the primary intended uses of the present apparatus is to determine the suitability of a series of molecules as radical sources for real time kinetic studies. In order to be able to work backwards from end product yields to intial radical concentrations, thereby allowing any proposed photolysis mechanism to be tested by numerical integration, it is often important to know the absolute end product concentrations, particularly under conditions where initially high radical concentrations decay by second-order processes, as commonly

found in flash photolysis experiments.

Although the relative concentrations of photolysis products in the reaction cell were readily calculated from their relative FID response factors and peak areas, calculation of absolute product concentrations was not so straightforward because of the presence of non-negligible dead volume - regions of the cell which are not photolysed, and potential inhomogeneity in the initial radical concentrations.

(i) Measurement of Dead Volume

The incoming laser radiation was defocused so as to irradiate the main cell body and annular end rings (see Figure 4.4), but not the cell arms. The volumes of the the irradiated (V_x) and non-irradiated (V_y) sections of the cell were measured by titration with water from a burette, taking care to remove trapped air bubbles from the end rings, giving $V_x = 32.7 \pm 0.2$ and $V_y = 8.7 \pm 0.2$.

In practice, the chromatograph was programmed with response factors referring to calibration mixtures, which necessarily filled the whole cell. Concentrations of end products in the photolysed regions of the cell were calculated by multiplying the output concentrations by a factor of $((V_x + V_y)/V_x)$ (=1.27).

(ii) Homogeneity of Photolysis Product Distribution

Although the ratio of photolysed to non-photolysed cell volume was well defined for the present apparatus, as described above, and average end product concentrations in the photolysed volume could be readily calculated, any modelling of a photolysis system would be

considerably complicated if significant concentration gradients were present across the photolysed volume. Such gradients could be caused by inhomogeneity in the photolysis beam or its non-uniform transmission into various parts of the cell.

Before each series of experiments, the laser beam profile was examined and adjusted if necessary to produce an even, rectangular beam shape. Precursor absorbance was kept down to below $\sim$0.2 to ensure an approximately linear absorption in light intensity as the beam passed through the cell.

The light intensity experienced in the complex end sections of the cell was almost certainly slightly different to that found in the main cell body and would have had a poorly defined spatial distribution. Calculations showed, however, that the annular cell end sections comprised at most 10% of the total photolysed volume and it was assumed that the overall effect on the measured average concentrations was small.

The cylindrical profile of the main cell body seen by the incoming laser radiation would also create a non-uniform light intensity distribution inside the cell, because of the dependence of the transmission of radiation through a dielectric boundary on the angle of incidence [195] :

$$T_{par} = \frac{(n_r\cos(a_r)/n_i\cos(a_i))}{(2\sin(a_r)\cos(a_i)/(\sin(a_i+a_r)\cos(a_i-a_r))^2}$$

$$T_{per} = \frac{(n_r\cos(a_r)/n_i\cos(a_i))}{(2\sin(a_r)\cos(a_i)/\sin(a_i+a_r))^2}$$

where T_{par} and T_{per} are the transmittances for radiation polarised

parallel and perpendicular to the plane of incidence, a_i and a_r are the angles of incidence and refraction and n_i and n_r are the refractive indices of the incident and refractive media. Figure 4.6 shows the situation where a parallel beam of radiation is incident upon a cylindrical vessel. For an essentially superradiant excimer laser, the output laser radiation will be unpolarised and it is assumed that the overall transmission is given by $(T_{par} + T_{per})/2$. For a thin-walled vessel, the angle of incidence at the second boundary is approximately equal to the angle of refraction from the first boundary and the transmittance at the second boundary is calculated by interchanging n_i and a_i for n_r and a_r in the above equations.

The calculated variation in transmitted light intensity with vertical distance from the cylindrical axis of a quartz vessel ($n \sim 1.6$ at 193.3 nm) is shown in Figure 4.7. A significant fall off in transmission is observed for $X > 0.8R$, leading to a reduction in light intensity in the upper and lower extremities of the cell. However, less than 10% of the irradiated cell volume is contained in the region where $X > 0.8R$ and the average light intensity will be very close to that seen at $X = 0$. The second curve in Figure 4.7 shows the average transmittance of a beam of width 2X, centred on the cylindrical axis, as a function of beam width, obtained by convoluting the transmittance at each X with the corresponding cell depth $2(R^2-x^2)^{1/2}$. The average transmittance calculated in this way was 0.876 for a beam completely filling the cell, only 2% less than the value of 0.896 expected for a narrow beam incident upon the centre of the cell and any inhomogeneity in the light intensity seen by the sample caused by the cylindrical cell profile was thus assumed

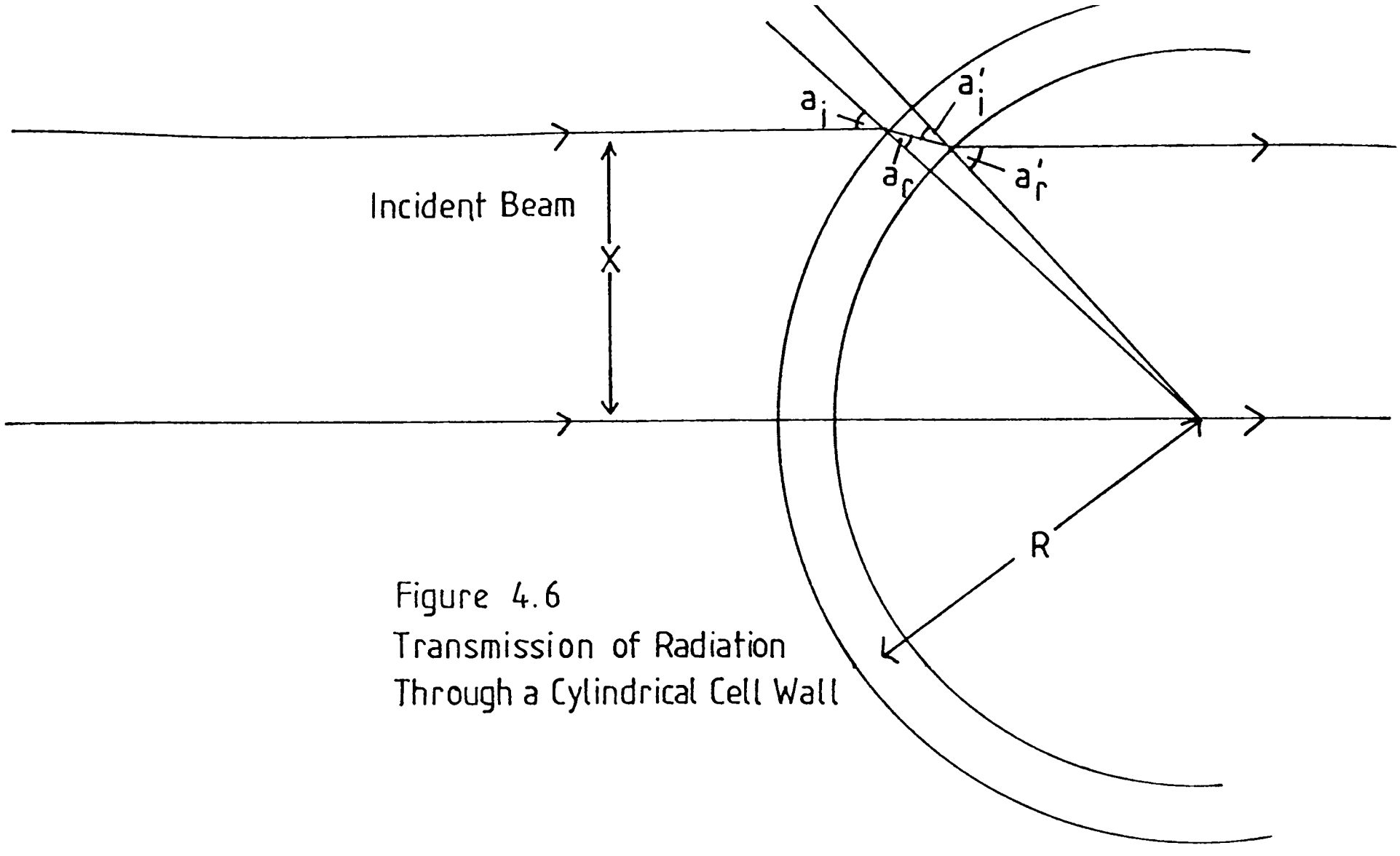

Figure 4.6
Transmission of Radiation
Through a Cylindrical Cell Wall

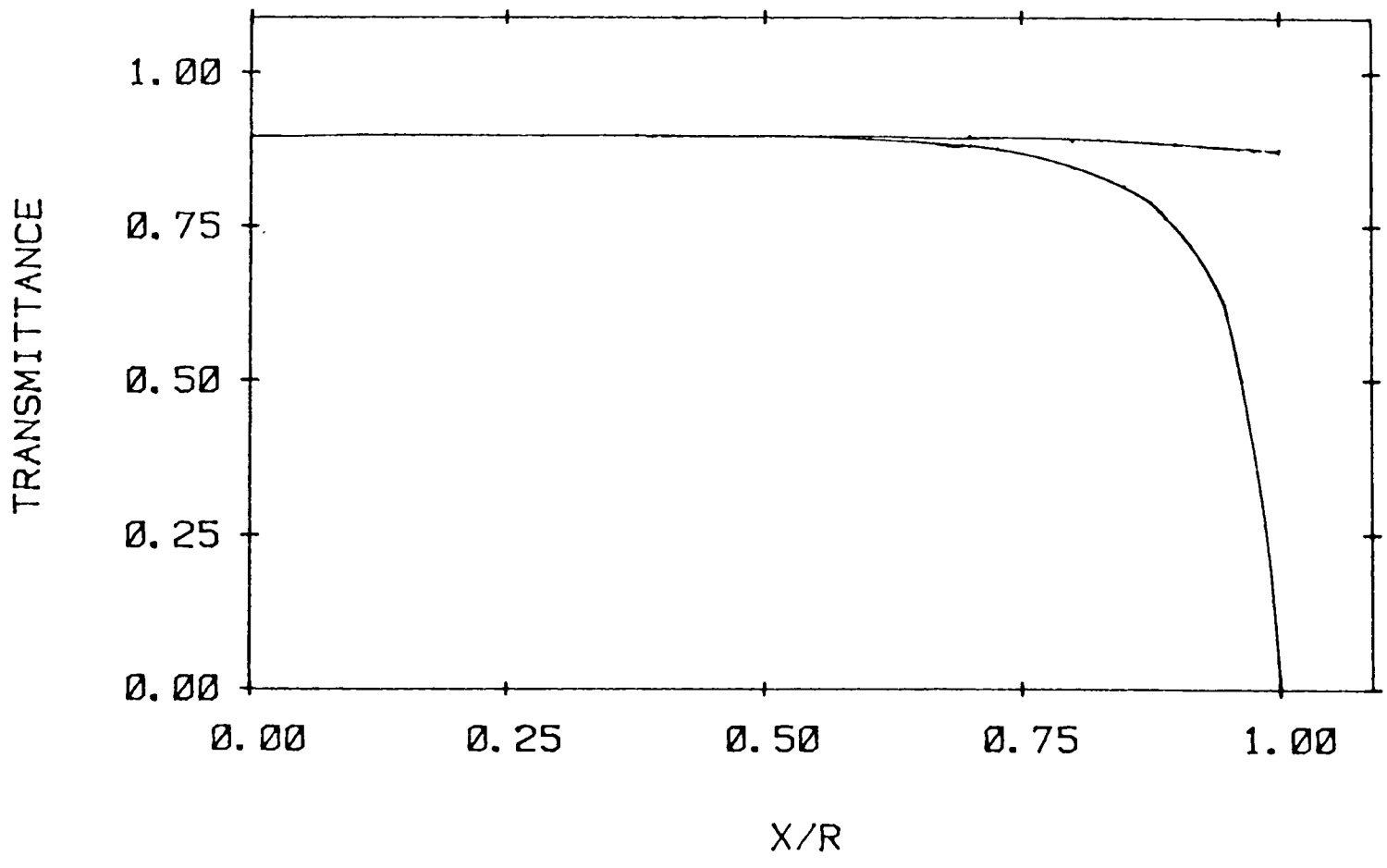

Figure 4.7. Transmission of Laser Radiation Through the Cell Wall.

Lower Curve: transmission of radiation as a function of distance from the cylindrical cell axis, X/R.

Upper Curve: volume-averaged transmission vs. X/R.

to be negligible.

4.2.3. Chemicals

	Chemical	Supplier	Grade
Laser			
Gas Mix	Fluorine	B.O.C	5% in helium
	Argon	B.O.C	Zero
	Helium	B.O.C	A
Spark Gap	Air	B.O.C	
Chromatograph			
Carrier Gas	Helium	B.O.C	A
	Passed through molecular sieve MS5A trap in liquid nitrogen to remove methane impurity.		
FID	Air	B.O.C	
	Hydrogen	B.O.C	
Valves	Nitrogen	B.O.C	Oxygen free
Calibrants	Methane	Matheson	U.H.P
	Ethylene	Matheson	99.7%
	Ethane	Matheson	C.P.
	Propylene	B.D.H	99%
	Propane	Matheson	C.P.
	n-Butane	Matheson	C.P.
	Allene	K and K	99%
	Carbon Monoxide	Matheson	C.P.
	MEK	Aldrich	99.9%
	Biacetyl	Aldrich	99.9%

Experimental

Acetone	B.D.H	Aristar 99.8%

Purified by extensive freeze-pump-thaw cycles. Detectable impurities 1.3×10^{-6}% C_2H_6, 5×10^{-7}% MEK and 7×10^{-7}% CH_4.

Ethylene	Matheson	99.7%

Volatile impurities removed by freeze-pump -thaw cycles. Methane impurity removed by trap-to-trap distillation from n-propanol/ liquid nitrogen slush bath to liquid nitrogen. Only remaining detectable impurity 3.6×10^{-6}% ethane.

Nitric oxide	B.D.H	99%

Other nitrogen oxides and air removed by trap-to-trap distillation from isopentane/ liquid nitrogen slush bath to liquid nitrogen until white in colour.

Helium	B.O.C.	A

Supplied to the line through an Oxisorb filter to reduce oxygen to below 1 p.p.m..

4.3 Results and Discussion

4.3.1 Experiments at Room Temperature

(i) Identification of Photolysis Products

Initial experiments were performed with 1 Torr of acetone at a total pressure of 330 Torr He and laser pulse energies of between 10 and 100 mJ, corresponding to photolysis fluxes of 0.38 - 3.8 $mJcm^{-2}$ incident upon the photolysed regions of the cell. Identified products were ethane, carbon monoxide, methane, methyl ethyl ketone (MEK), ethylene, allene and propane in approximate ratios:

100 : 100 : 4.5 : 2.5 : 0.15 : 0.07 : 0.03

A typical chromatograph trace is shown in Figure 4.8.

The presence of equal amounts of ethane and carbon monoxide, together with the low yields of other products, shows that by far the most important primary process in the photolysis of acetone at 193.3 nm is the dissociation to produce carbon monoxide, and two methyl radicals; ethane is produced by the recombination of two methyl radicals:

$$CH_3COCH_3 \xrightarrow[193.3\ nm]{h\nu} CH_3 + CO + CH_3 \qquad P1$$

$$CH_3 + CH_3 \longrightarrow C_2H_6 \qquad R1$$

Although the ethane product was present in sufficiently large quantities to be reliably detected in single shot experiments, it was necessary to perform multi-shot (typically 10 shots) experiments in order to produce accurately detectable concentrations of the minor products and carbon monoxide. None of the detected products absorb

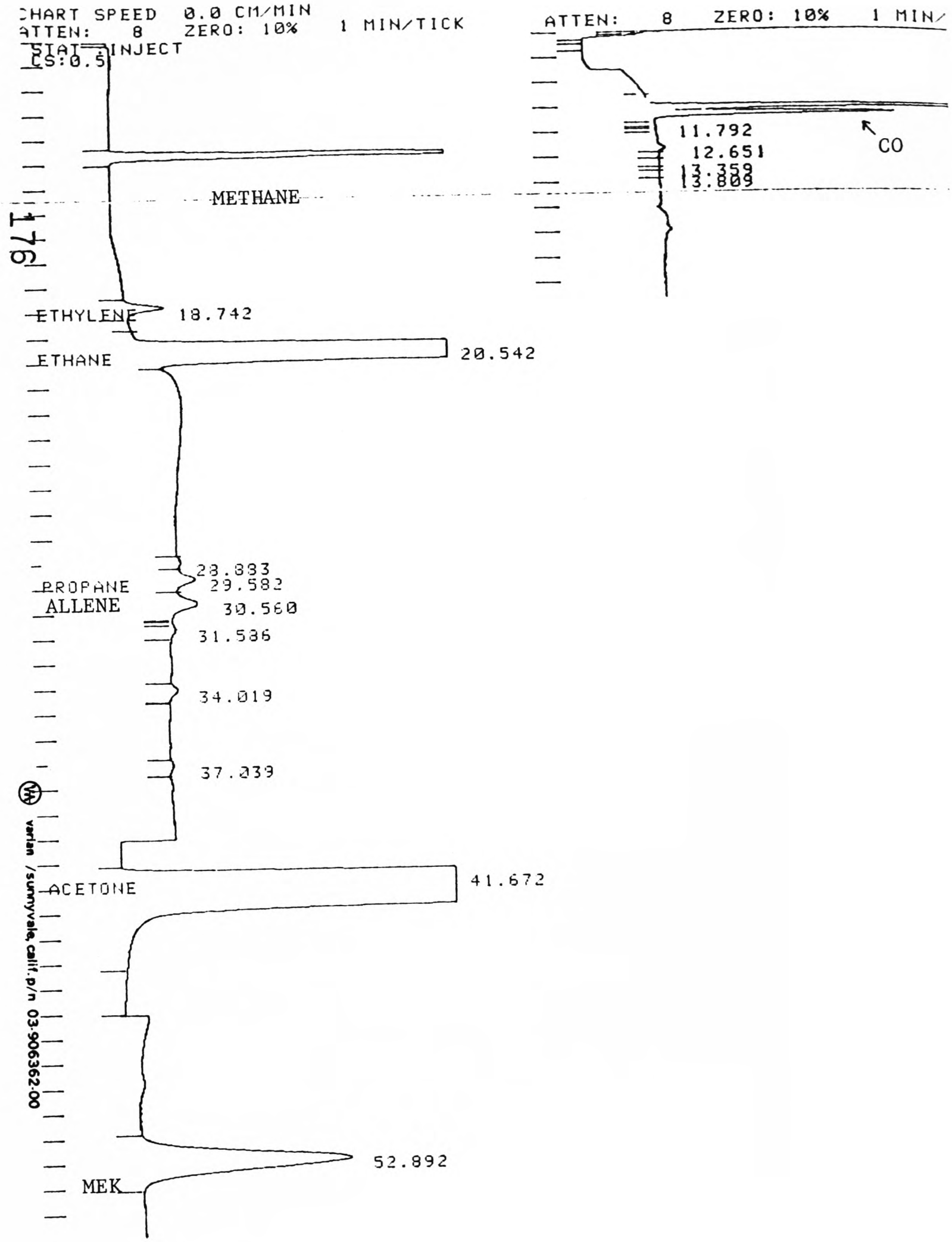

Figure 4.8. Typical Experimental Chromatograph, Showing Both FID and TCD Traces. Experimental Conditions: 300K, 500 Torr He, 1 Torr Acetone, 7 Laser Shots at 70 mJ.

significantly at 193.3 nm and no effects arising from secondary reactions were noticed : plots of product yields vs number of shots at a given intensity were found to be linear for all products, as can be inferred from the plots of product yields vs intensity shown in later sections for experiments at all pressures, which contain data obtained with varying numbers of laser shots.

Because of the large [precursor]/[product] ratios caused by the low extinction coefficient of acetone at 193.3 nm, it was not possible to correlate precursor depletion with product formation and thereby check for undetected photolysis routes.

A simple photolysis scheme consistent with the major (>1%) detected products would be:

CH_3COCH_3	====> $CH_3 + CO + CH_3$	P1
CH_3COCH_3	====> $CH_3COCH_2 + H$	P2
$CH_3 + CH_3$	====> C_2H_6	R1
$CH_3 + H$	====> CH_4	R2
$CH_3 + CH_3COCH_2$	====> MEK	R3

whence the hydrogen atoms and acetonyl radicals produced via the minor photolysis channel P2 react exclusively with methyl radicals which are present in approximately x50 greater concentration. Although large precursor concentrations were used, it is known that the abstraction reactions of hydrogen atoms and methyl radicals with acetone are extremely slow at room temperature [196,197]. Calculated pseudo-first-order rates for the disappearance of hydrogen atoms and methyl radicals by reaction with 1 Torr of acetone at 300K are 2 and $2x10^{-3}$ s^{-1} respectively, several orders of magnitude slower than the corresponding calculated rates of disappearance by radical - radical

reactions, taking a typical initial methyl radical concentration of $1x10^{14}$ moleculecm^{-3}. Although no data are available for the addition of hydrogen atoms to the carbonyl double bond in acetone, Batt and Mowat [198] have calculated the rate of addition of methyl radicals to acetone from the measured Arrhenius parameters for the thermal decomposition of the t-butoxy radical and estimate that the reaction is at least an order of magnitude slower than the corresponding abstraction at all temperatures.

(ii) Yield of Acetyl Radicals

Very low yields of acetyl radicals in the present system were suggested by the equal concentrations of the ethane and carbon monoxide products, in contrast to the corresponding near u.v. photolysis where significant yields of acetyl radicals are produced. However, the experimental ratio $[C_2H_6]/[CO]$ showed considerable scatter (±20%), because of the difficulty in measuring mTorr quantities of carbon monoxide using a TCD and it was only realistically possible to conclude that the initial acetyl concentration was small (< 10%) with respect to the initial methyl radical concentration. Furthermore, small quantities of acetyl radicals generated in the initial photolysis would be expected to regenerate the precursor via reaction with methyl radicals:

$$CH_3CO + CH_3 \text{ ====> } CH_3COCH_3$$

and would therefore not be detected. Larger inital acetyl radical concentrations would also produce biacetyl by self recombination:

$$CH_3CO + CH_3CO \text{ ====> } (CH_3CO)_2$$

Calibration showed that biacetyl was not separated from MEK on the Chromosorb 102 column and an independent check on the absence of acetyl radicals was necessary to ensure that the measured MEK yields were reliable.

The acetyl radical exhibits a broad absorption in the far ultraviolet, peaking around 210 nm where $\sigma = 1.4 \times 10^{-17}$ molecule^{-1}cm^{2} [199] and which has been used to monitor acetyl concentrations in molecular modulation [61,199] and flash photolysis / kinetic spectroscopy [182] experiments.

In an attempt to observe acetyl radicals in the present photolysis system, a series of experiments was performed using a laser flash photolysis / time resolved u.v. absorption apparatus developed in this laboratory, a detailed description of which is given in the thesis of Smith [193]. Briefly, acetone / helium mixtures at a total pressure of 330 Torr and an acetone partial pressure of 1 Torr were slowly flowed through a cylindrical quartz cell at 300K and photolysed by defocused 193.3 nm radiation from a Lumonics TE861-S excimer laser operating at 0.5 Hz. Radical concentrations were monitored on a 4 ms timescale by following the time resolved transmission of collimated u.v. radiation from a high pressure xenon arc lamp through the cell and a calibrated monochromator onto a photomultiplier. Signal averaging of the amplified and digitised traces was employed, typically over 256 laser pulses. The temperature, pressure, acetone concentration and initial methyl radical concentration were such that the conditions of the end product experiments were closely reproduced.

Initially, the monochromator was set to the sharp methyl radical

absorption at 216.36 nm ($\sigma(CH_3)$ = $4.1x10^{-17}$ $molecule^{-1}cm^2$, 0.6 nm bandpass [26]). Excellent methyl radical signals were achieved, with very good signal to noise ratios, as shown in Figure 4.9. Analysis of the methyl radical decay traces so obtained, according to the simple second-order scheme:

$$CH_3 + CH_3 \text{ =====> } C_2H_6 \qquad \text{R1}$$

returned values of k_1 which were in excellent agreement with values obtained using azomethane as the methyl radical precursor [26]. The u.v. photolysis of azomethane is known to be a clean source of methyl radicals [178] and has been used as such in several studies of methyl radical kinetics [177,26,29].

Subsequent attempts to detect acetyl radicals by absorption at 223 nm ($\sigma_{223}(CH_3CO)$ = $1x10^{-17}$ $molecule^{-1}cm^2$ [199]) under identical experimental conditions were unsuccessful. Any change in absorption after the laser pulse was well within the experimental noise, as shown in Figure 4.10, allowing an upper limit of $1x10^{-2}$ to be placed on the $[CH_3CO]/[CH_3]$ ratio at t=0.

It is therefore concluded that acetyl radicals play no significant part in the photolysis of acetone at 193.3 nm. Even if the upper limit set on $([CH_3CO]/[CH_3])_{t=0}$ were realised, the acetyl radicals formed in such small quantities would react with a very small fraction of the methyl radicals present to regenerate the precursor, and would not appreciably affect the methyl radical kinetics. The photolysis of acetone in the far u.v. thus provides a much cleaner methyl radical source than photolysis in the near u.v., where acetyl radicals are produced in yields comparable to those of methyl radicals.

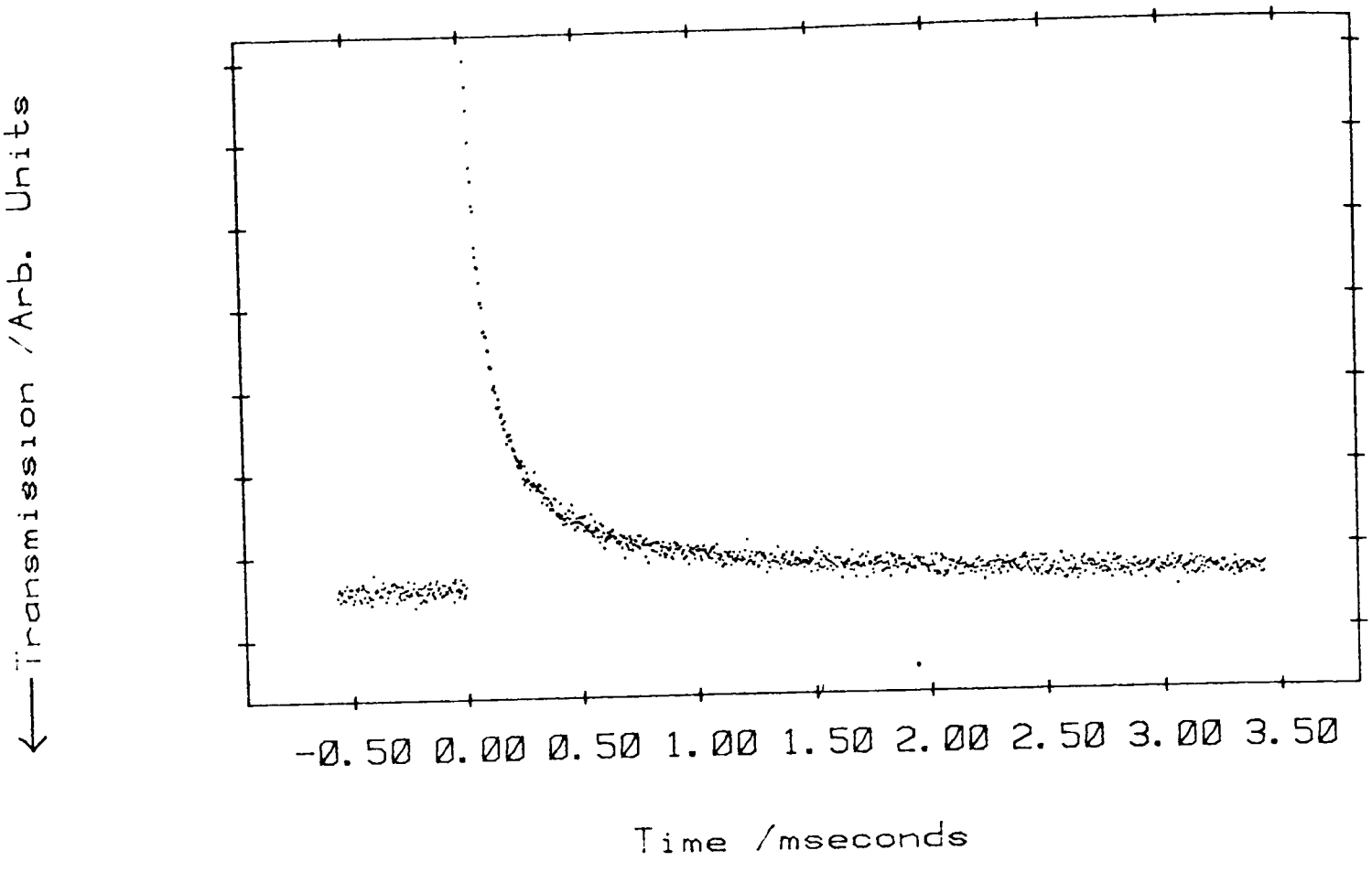

Figure 4.9. Time-Resolved Absorption at 216.36 nm, Following 193.3 nm Photolysis. Non-linear least-squares analysis of the second-order methyl radical decay gives $k_1/\sigma = 3.15 \times 10^6$ cms^{-1}.

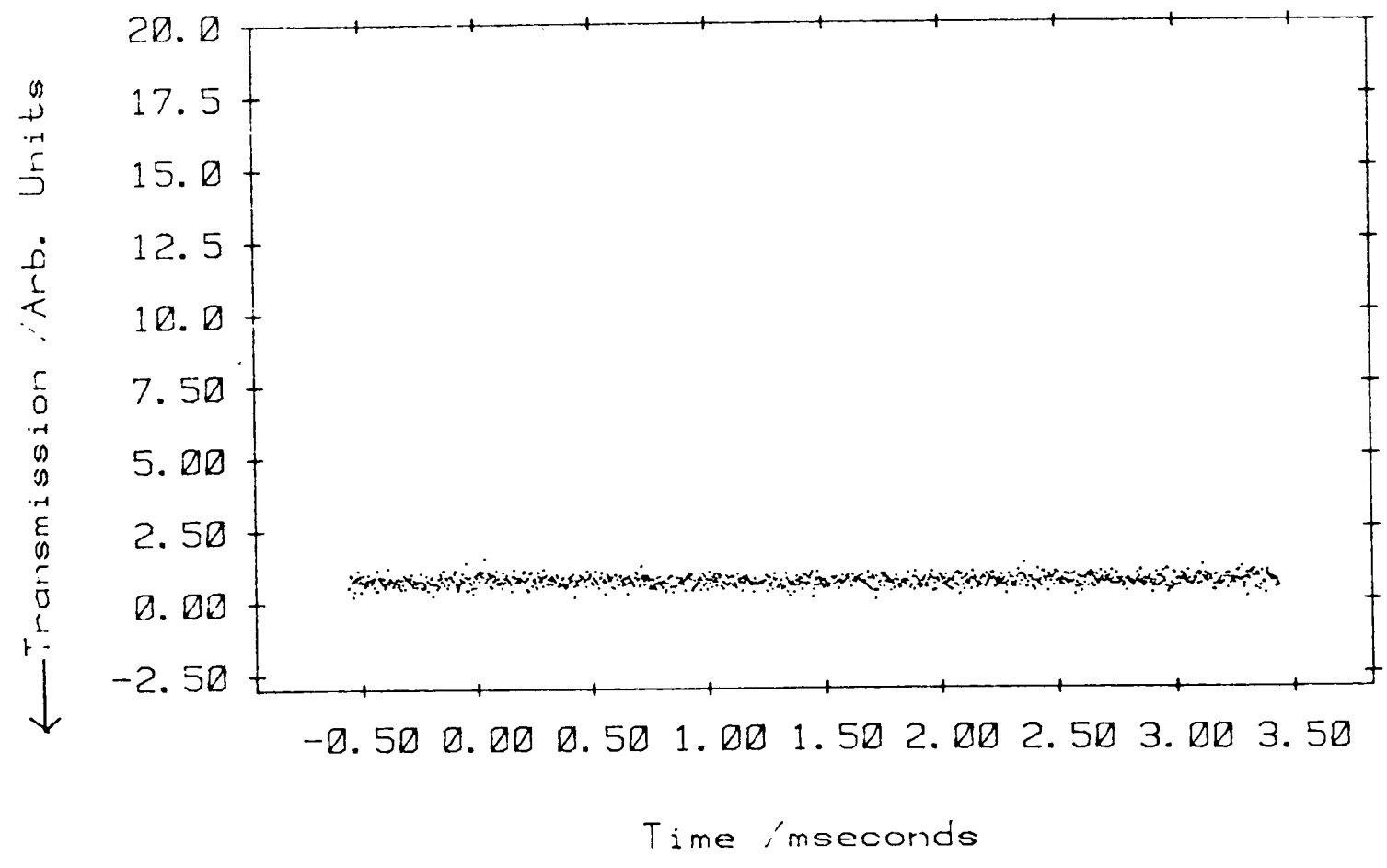

Figure 4.10. Time-Resolved Absorption at 223 nm, Following 193.3 nm Photolysis of Acetone.

(iii) Dependence of Product Yields on Laser Intensity, Pressure and the Presence of Radical Scavengers

As demonstrated above, by far the most important primary process in the photodissociation of acetone at 193.3 nm is that producing methyl radicals and carbon monoxide, resulting in the major products ethane and carbon monoxide. Additional products were observed, however, in much smaller yields, presumably arising from minor photolysis channels. In order to elucidate the mechanism by which minor products were formed, the dependences of product yields on pressure, temperature, laser intensity and the presence of the radical scavengers ethylene and nitric oxide were systematically studied.

Further end product analysis experiments were performed in which product yields were measured as a function of laser energy, I, for total pressures of 10, 40 and 500 Torr He. Experiments typically employed 10 laser shots and 1 Torr of acetone, although experiments at 10 Torr employed 20 laser shots and acetone partial pressures of 0.25 Torr, and the acetone partial pressure was varied from 0.53 to 2.56 Torr at 500 Torr. In addition, ethylene and nitric oxide were employed as scavengers for hydrogen atoms and methyl radicals respectively. Ethylene scavenging experiments were performed at a total pressure of 500 Torr He with a fixed laser energy of 80±5 mJ. Nitric oxide scavenging experiments were performed at total pressures of 10 and 500 Torr He with fixed laser energies of 95±6 mJ (10 Torr) and 80±5 mJ (500 Torr).

(a) Ethane and Carbon Monoxide

The yield of ethane per Torr of precursor and at a fixed laser energy, I, was found to be independent of total pressure and varied linearly with both laser energy and acetone partial pressure. The dependence of the ethane yield on I for all pressures is shown in Figure 4.11. In each case the ethane yield has been scaled to refer to 1 Torr of acetone and 10 laser shots. Also shown is a best fit straight line to the data, which gave $[C_2H_6]$/mTorr = $(4.2\pm0.3)\times10^{-2}$I/mJ - (0.03 ± 0.01), or $F_{300K} = (4.2\pm0.3)\times10^{-5}$I/mJ, where F_{300K} is the fraction of the precursor removed per laser shot. The error limits quoted here and elsewhere in this chapter refer to two standard deviations unless otherwise stated.

The ratio of carbon monoxide to ethane was close to unity at the three highest pressures; it was not possible to measure the carbon monoxide yield quantitatively at 10 Torr because the overall product yields were approximately a factor of two down on the yields at higher pressures, owing to the factor of four reduction in the acetone partial pressure and the use of only twice the number of laser shots. Figure 4.12 shows a plot of $[CO]/[C_2H_6]$ at a total presure of 330 Torr He. The average values of $[CO]/[C_2H_6]$ at 40, 330 and 500 Torr were 1.29±0.28, 1.01±0.26 and 1.00±0.28 respectively. A value of slightly greater than unity is expected on the basis of the simple photolysis scheme outlined in the last section as a few percent of the methyl radicals produced in the initial photolysis would react with hydrogen atoms or acetonyl radicals.

The ethane yield was independent of up to 10 Torr of added ethylene, a consequence of the very slow rate of addition of methyl

Figure 4.11. Ethane Yield vs. Laser Pulse Intensity for Experiments at 300K, all Pressures. The yields are scaled to refer to 10 laser shots, with 1 Torr of acetone, but are not corrected for dead volume. Multiply by 1.27 to calculate the real ethane partial pressure in the photolysed region of the cell.

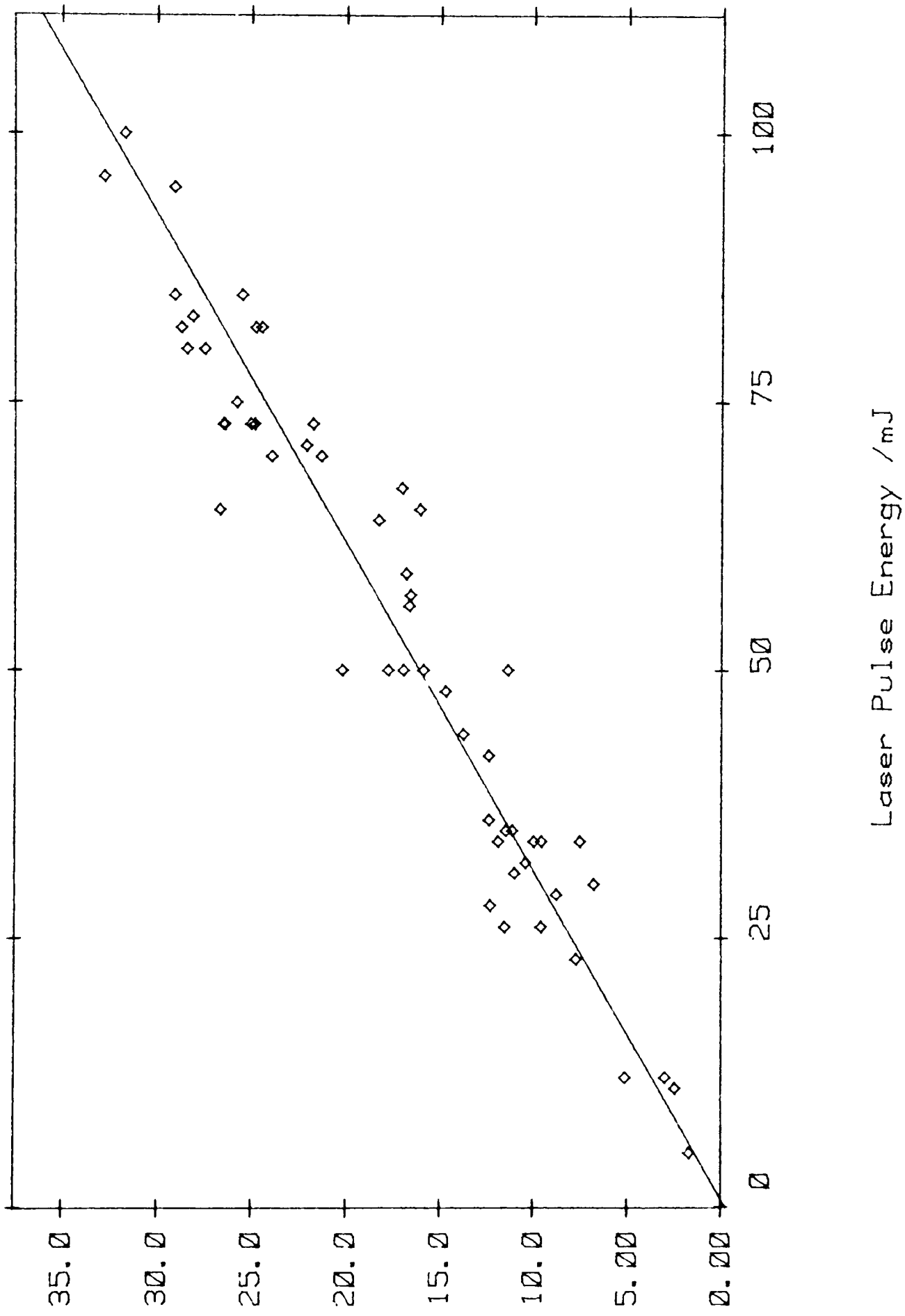

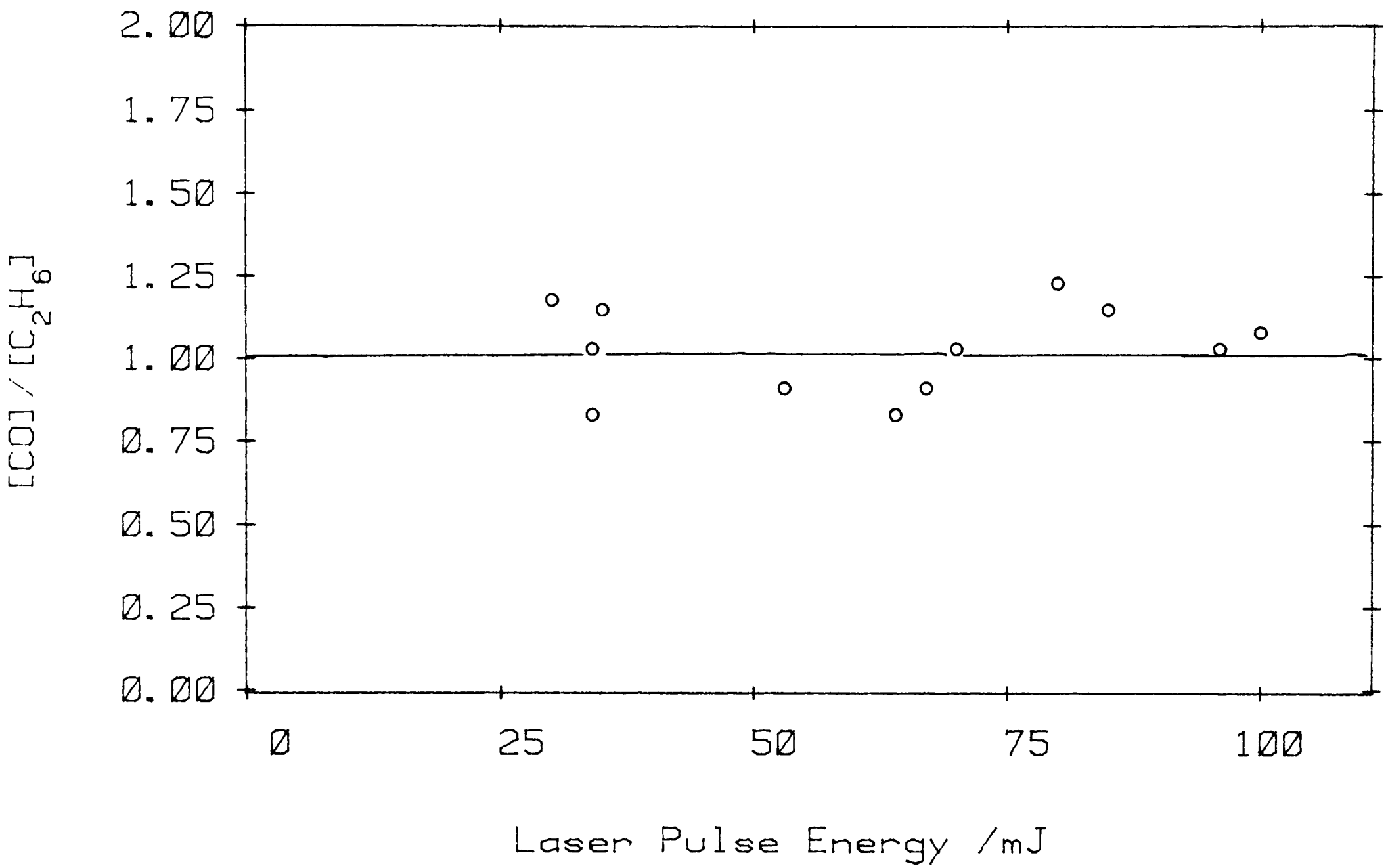

Figure 4.12. Ratio of Carbon Monoxide to Ethane vs. Laser Pulse Energy. 300K, Total Pressure 330 Torr He.

radicals to ethylene at room temperature, but was very sensitive to the presence of nitric oxide, which reacts rapidly with methyl radicals to give a stable recombination product:

$$CH_3 + NO \xrightarrow{k_s} CH_3NO$$

The dependence of the yield of ethane, relative to that found in the absence of nitric oxide, on [NO] at 10 and 500 Torr total pressure is shown in Figure 4.13. The effect of nitric oxide can be seen to be less pronounced at the lower pressure, because of the greater pressure dependence of k_s relative to k_1. Assuming that methyl radicals are removed either by self-recombination or reaction with nitric oxide, then the ethane end product yield is given by:

$$[C_2H_6] = [CH_3]_o/2 - (k_s[NO]/2k_1)\ln(1 + (2k_1[CH_3]_o/k_s[NO]))$$

where $[CH_3]_o$ is the initial methyl radical concentration. Using values of $[CH_3]_o$ calculated from the unscavenged data of Figure 4.11, the value of $k_s/2k_1$ was varied at each pressure to give the best agreement between the observed and calculated ethane yields. The resulting best fit curves are also shown in Figure 4.13. Using the accurately known rate constants for k_1 [26], k_s was calculated to be 6.9×10^{-13} molecule^{-1}cm^{3}s^{-1} at 10 Torr He and 4.2×10^{-12} molecule^{-1}cm^{3}s^{-1} at 500 Torr, in reasonable agreement with values of 6.0×10^{-13} and 6.1×10^{-12} recently determined in this laboratory by direct measurement [200]. In the present system, ethane thus appears to be entirely produced by methyl radical recombination, although the data of Figure 4.13 cannot exclude a small (< 2%) contribution from a molecular elimination channel.

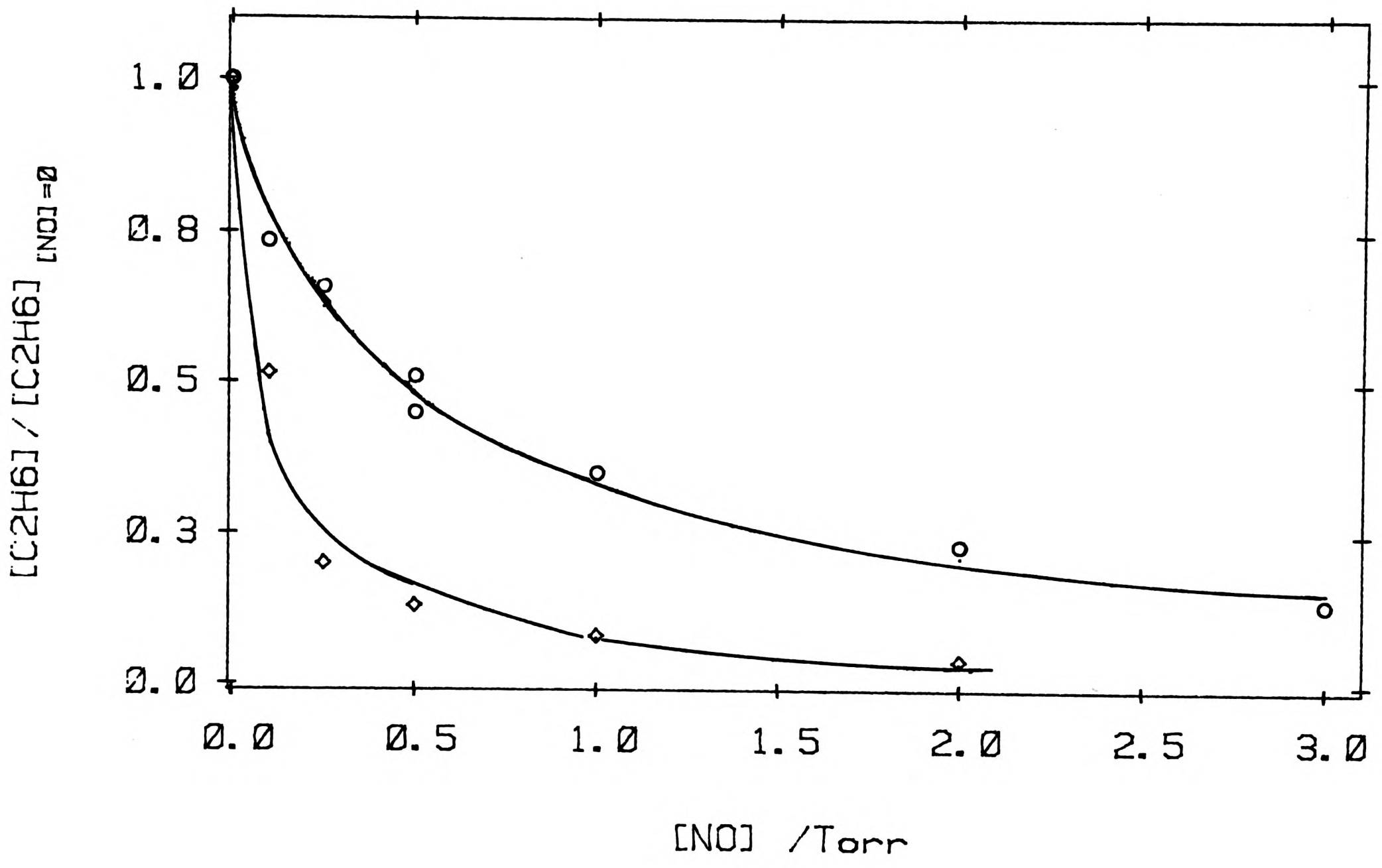

Figure 4.13. Dependence of Ethane Yield on the Concentration of Nitric Oxide. ◇500 Torr, o 10 Torr. Solid lines represent best fits to the data, assuming that methyl radicals are removed by recombination or reaction with NO (see text).

(b) Methyl Ethyl Ketone

The observed yield of MEK relative to ethane, R_{MEK}, where $R_X = ([X]/[C_2H_6])x100$, was independent of laser intensity and acetone partial pressure, but increased with total pressure, as shown in Figure 4.14. R_{MEK} was unaffected by the presence of ethylene, but was reduced to zero by small pressures of nitric oxide, indicating that MEK was produced via radical intermediates; the recombination reaction between methyl and acetonyl radicals must be the major route to MEK:

$$CH_3 + CH_3COCH_2 \text{ =====> } CH_3COC_2H_5 \qquad R3$$

with acetonyl radicals produced via the minor photolysis channel P2:

$$CH_3COCH_3 \xrightarrow[193.3\ nm]{h\nu} CH_3COCH_2 + H \qquad P2$$

The average values of R_{MEK} at each pressure are given in Table 4.2.

Table 4.2

Yields of Methyl Ethyl Ketone Relative to Ethane at 300K

Pressure/Torr	R_{MEK}
500	2.71 ± 0.44
330	2.43 ± 0.26
40	1.58 ± 0.58
10	0.82 ± 0.22

An increase in R_{MEK} with total pressure can be qualitatively explained by a more efficient stabilisation of the vibrationally

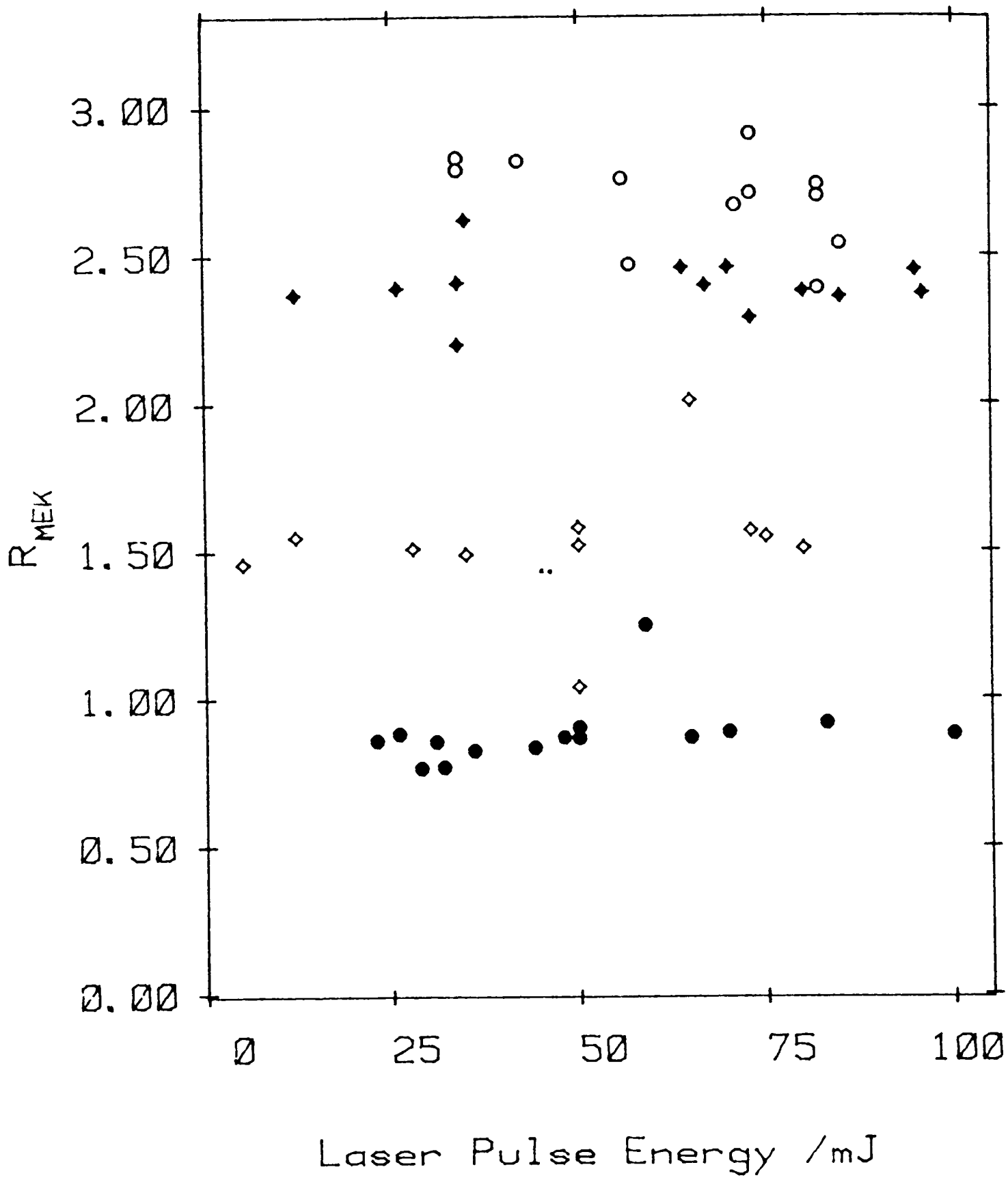

Figure 4.14. Dependence of R_{MEK} on Total Pressure and Laser Pulse Energy at 300K. ● 10 Torr, ◇ 40 Torr, ◆ 330 Torr, o 500 Torr

excited acetonyl radicals produced in the initial photolysis. The 47.1 $kcalmol^{-1}$ excess energy for photolysis channel P2 is sufficient to enable further dissociation of the acetonyl radical to occur, giving ketene, which would not be detected by gas chromatography, and a methyl radical:

$$CH_3COCH_3 \xrightarrow[193.3\ nm]{h\nu} H + CH_3COCH_2^* \xrightarrow{} CH_2CO + CH_3 + H$$

$$CH_3COCH_2^* \xrightarrow{M} H + CH_3COCH_2 \quad (S)$$

Ketene produced by the thermal decomposition of acetonyl radicals has been observed in both the pyrolysis [201] and high temperature near u.v. photolysis [202] of acetone. In the latter case, the dependence of the yield of ketene on temperature enabled an upper estimate of 41 $kcalmol^{-1}$ to be made for the activation energy of the decomposition.

Assuming that all thermalised acetonyl radicals react with methyl radicals to produce MEK, then extrapolation of R_{MEK} to its high pressure limit would enable the yield of photolysis channel P2 to be determined. Troe has shown [203] that for systems involving chemical or photochemical activation, the fractional yield of the stabilised product S/(S + D) can be closely approximated by:

$$S/(S+D) = k(E)/(k(E) + \gamma_c Z_{LJ}[M])$$

where k(E) is the RRKM dissociation rate constant for the energised species evaluated for an activation energy E, $Z_{LJ}[M]$ the Lennard-Jones collision rate and γ_c a collisional efficiency parameter for the system in question. Using the above expression:

$$1/R_{MEK} = 1/R^{\infty}_{MEK} + k(E)/(R^{\infty}_{MEK}\gamma_C Z_{LJ}[M])$$

where R^{∞}_{MEK} is the limiting high pressure value of R_{MEK}. A plot of $1/R_{MEK}$ against 1/Pressure is shown in Figure 4.15, together with a best fit straight line to the data, which gives $R^{\infty}_{MEK} = 2.65 \pm 0.52$.

In conclusion, methyl ethyl ketone is formed by a radical mechanism, its yield increasing with increasing total system pressure to a high pressure limit of around 3% of the ethane yield. This increase with pressure can be ascribed to an increasing stabilisation of the vibrationally excited acetonyl radical produced via the minor photolysis channel P2. The exact value of the limiting high pressure value of R_{MEK}, R^{∞}_{MEK} is however revised slightly to 3.05 ± 0.60 after the detailed consideration of the reaction scheme in (c) below.

(c) Methane

It was demonstrated in the previous section that acetonyl radicals are formed via a minor photolysis channel, which presumably also produces hydrogen atoms. One possible route to methane would then involve the reaction between hydrogen atoms and methyl radicals:

$$CH_3 + H \text{ =====> } CH_4 \qquad R2$$

R_{CH4} ($=[CH_4]x100/[C_2H_6]$) was independent of laser energy, within experimental uncertainty, but increased with pressure, as shown in Figure 4.16. The average values of R_{CH4} at each pressure are given in

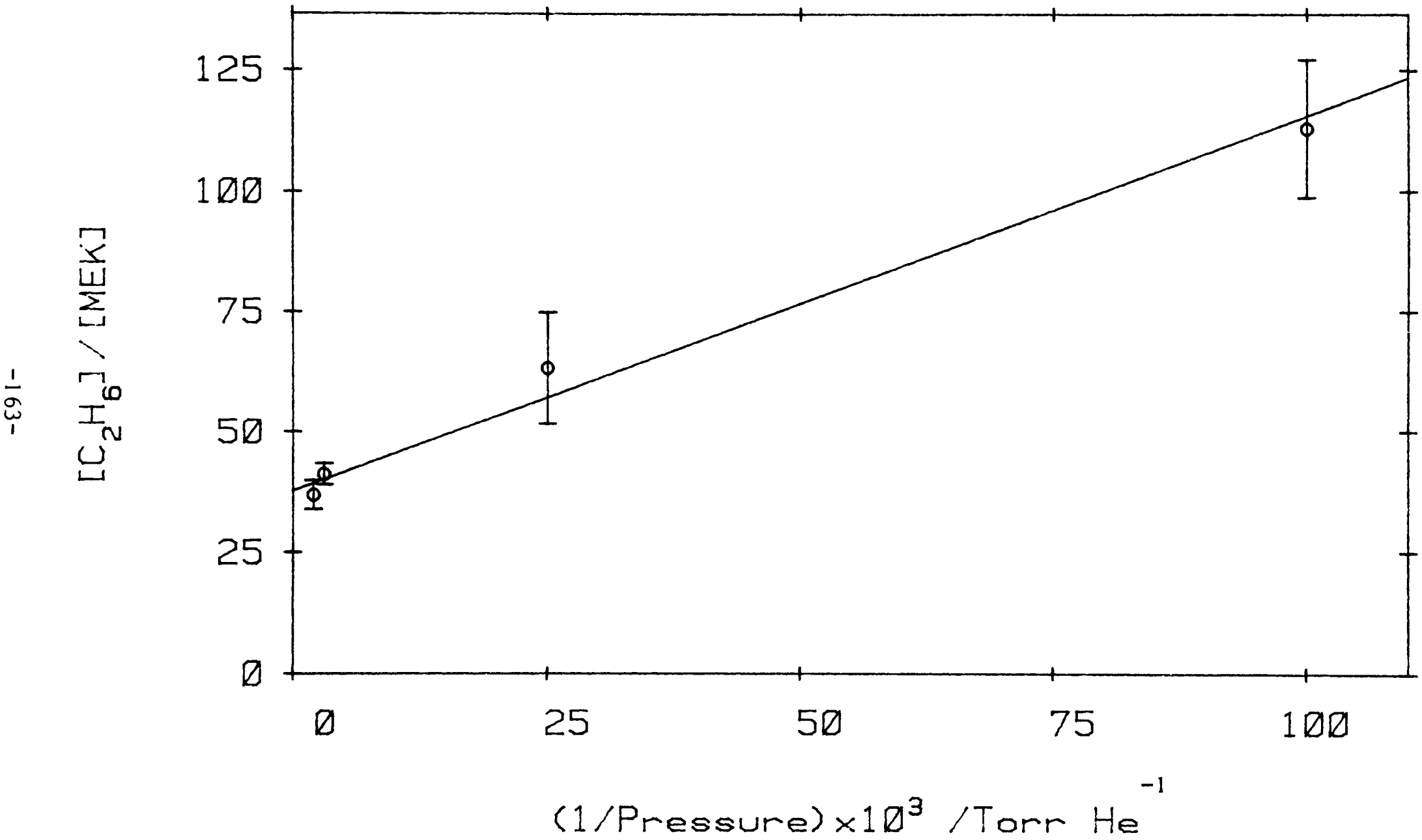

Figure 4.15. Plot of $1/R_{MEK}$ vs. 1/Pressure to Determine the Limiting High Pressure Value of R_{MEK}.

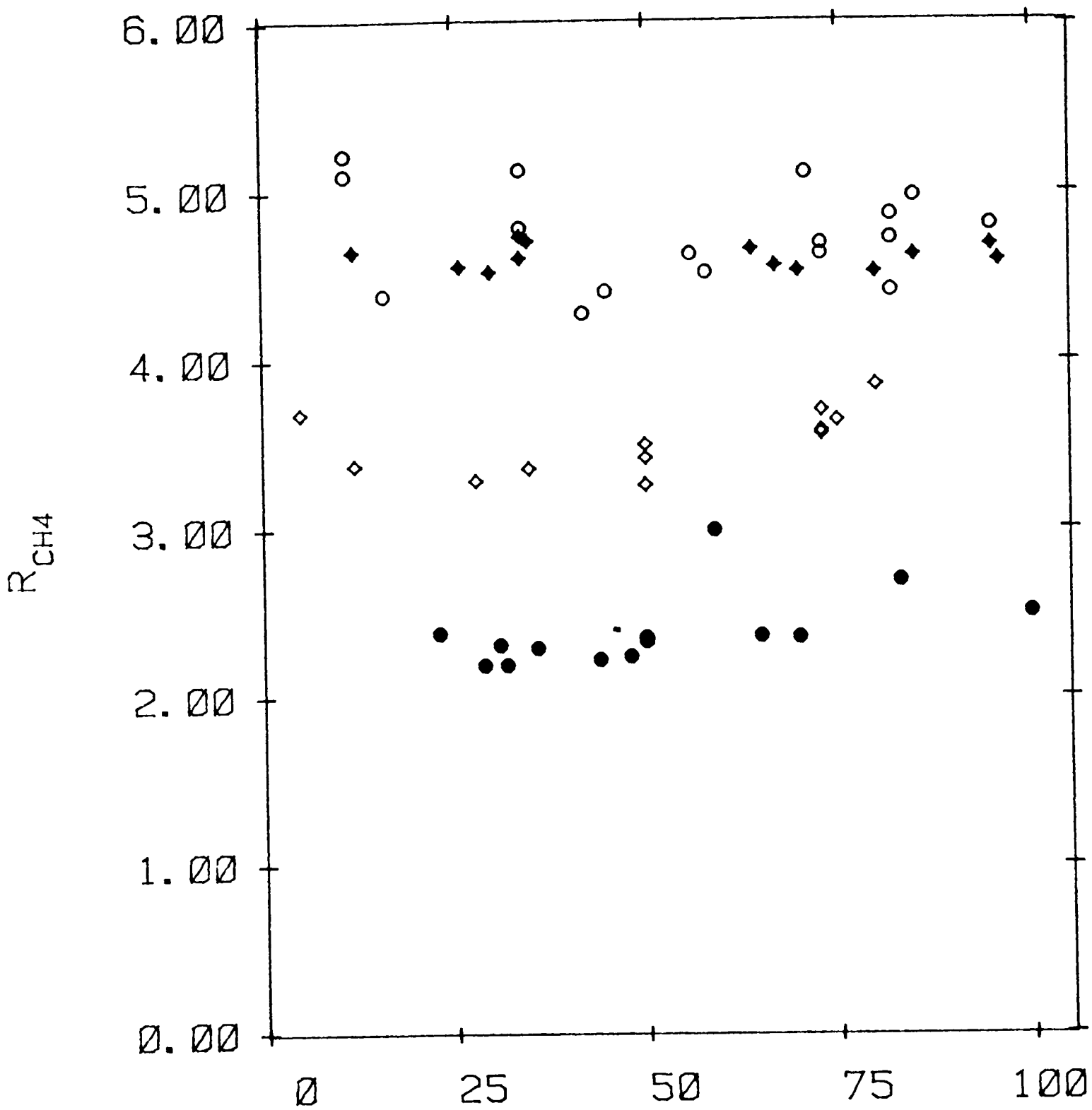

Figure 4.16. Dependence of R_{CH4} on Total Pressure and Laser Pulse Energy at 300K. ● 10 Torr, ◇ 40 Torr, ◆ 330 Torr, o 500 Torr.

Table 4.3.

Table 4.3

Average Values of R_{CH4} as a Function of Total Pressure

Pressure/Torr He	R_{CH4}
10	2.29 ± 0.18
40	3.54 ± 0.38
330	4.43 ± 0.44
500	4.87 ± 0.80

If the reaction between methyl radicals and hydrogen atoms were the sole route to methane and all the hydrogen atoms produced via P2 were to react with methyl radicals to form methane, then R_{CH4} would be expected to be pressure independent and equal to the limiting high pressure value of R_{MEK}. At all but the lowest pressure, however, R_{CH4} was significantly greater than 2.65, suggesting that there were either further sources of hydrogen atoms, or alternative pathways for methane production. Addition of ethylene to the present photolysis mixtures provided a method for determining the absolute yield of hydrogen atoms: hydrogen atoms would react with ethylene by addition to form ethyl radicals, which would react further to produce propane under the conditions of excess methyl radicals found in the present experiments, resulting in a reduction of R_{CH4} and a corresponding increase in R_{C3H8} with increasing $[C_2H_4]$. Similarly, the yield of methane at high $[C_2H_4]$, where methane production by R2 should be negligible, would enable the fraction of methane produced by routes not involving hydrogen atoms to be quantified.

Figure 4.17 shows the dependence of R_{CH4}, R_{C3H8} and $R_{CH4} + R_{C3H8}$

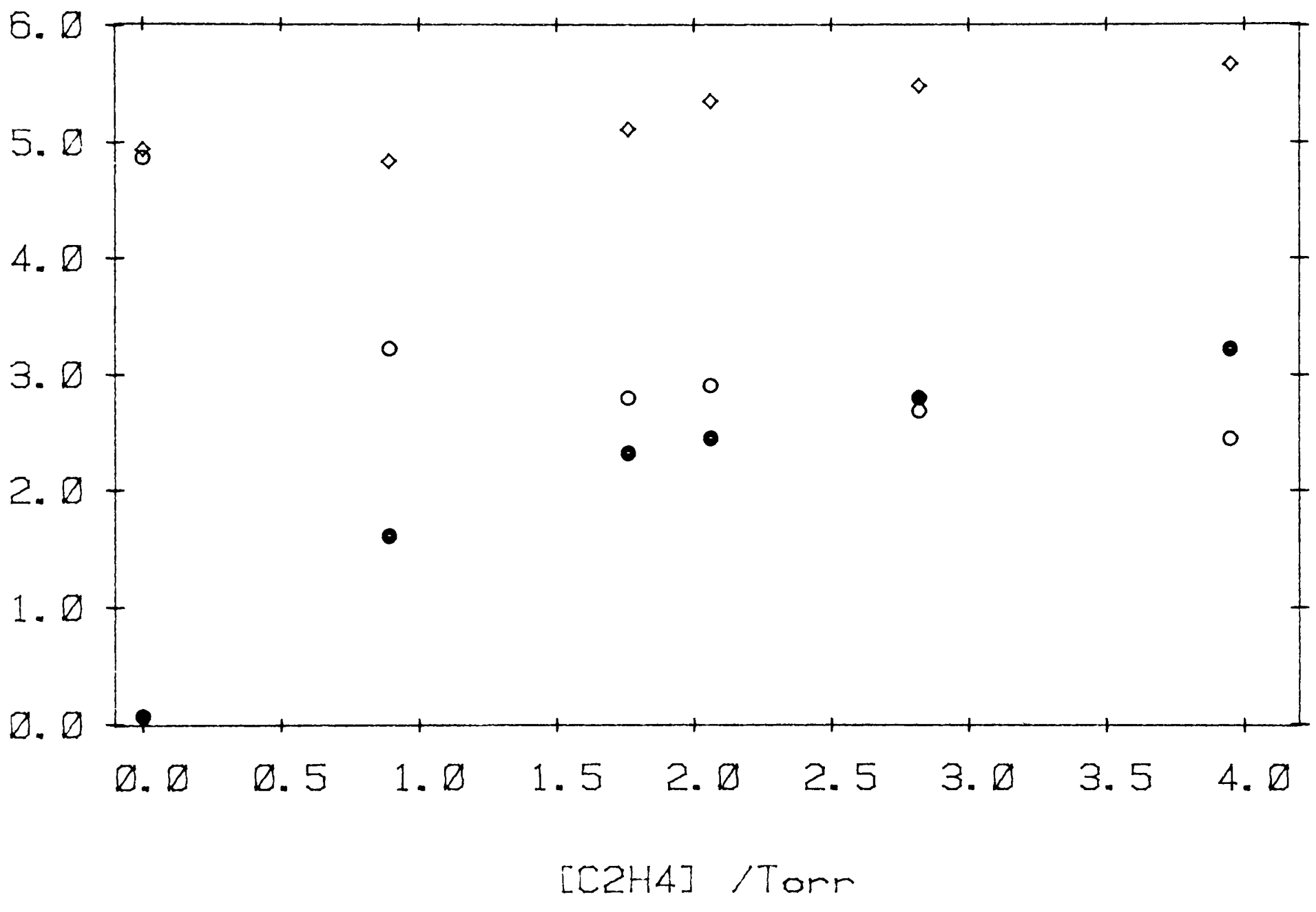

Figure 4.17. Dependence of Product Yields on $[C_2H_4]$, 300K.

Pressure 500 Torr He, I = 80 mJ. • R_{C3H8}, o R_{CH4}, ◇ $R_{C3H8}+R_{CH4}$.

on ethylene partial pressure, for experiments performed at 500 Torr He with a laser pulse energy of 80±5 mJ.

As expected, an increase in R_{C3H8} and a decrease in R_{CH4} with increasing $[C_2H_4]$ was observed. Furthermore, R_{CH4} clearly does not tend to zero at high $[C_2H_4]$, demonstrating that there must be a route to methane which does not involve hydrogen atoms. The yields of hydrogen atoms R_H and non-scavengable methane R_{CH4o} were extracted from the observed values of R_{CH4} and R_{C3H8} by means of the parameter fitting facility of the numerical integration package FACSIMILE [4], using the kinetic scheme shown below.

Reaction	Rate Constant/ $molecule^{-1}cm^3s^{-1}$	Reference
$CH_3 + CH_3 \; ===> \; C_2H_6$	$5.9x10^{-11}$	[26]
$CH_3 + H \; ===> \; CH_4$	$1.85x10^{-10}$	[116]
$CH_3 + C_2H_5 \; ===> \; C_3H_8$	$7.0x10^{-11}$	Mean Value Rule
$H + C_2H_4 \; ===> \; C_2H_5$	$9.4x10^{-13}$	Chapter 2

Initial concentrations were taken as:-

$[CH_3]_{t=o} = 2.13x10^{14}$ cm^3 (from average of ethane yields)

$[H]_{t=o} = [C_3H_8] + (1 - \beta)[CH_4]$

$[CH_4]_{t=o} = \beta[CH_4]$

where β is the fraction of methane not produced via R2. All end products concentrations were calculated per laser shot and corrected for dead volume, as described earlier in the chapter. Values of β were obtained for each experiment. R_{CH4o} displayed no systematic dependence on $[C_2H_4]$; an average of six determinations gave R_{CH4o} = 1.60±0.18.

It can be seen from Figure 4.17 that $R_{CH4} + R_{C3H8}$ increased

slightly with [C_2H_4], an increase caused by a small yield of hydrogen atoms from the photolysis of ethylene, as confirmed by the presence of very small quantities of propylene at high [C_2H_4], formed by the reaction between methyl radicals and vinyl radicals, which are a minor product of the ethylene photolysis. A detailed discussion of the ArF photolysis of ethylene is given in Chapter 3. Thus, the effect of a small amount of ethylene photolysis would be to increase the yield of hydrogen atoms slightly with increasing [C_2H_4] and introduce vinyl radicals into the system. The additional hydrogen atoms would be observed under the present conditions as a small increase in RCH_4 + RC_3H_8 and vinyl radicals would produce propylene by recombination with methyl radicals. It was not possible to detect the expected acetylene photolysis product, as it was not separated from ethylene on the Chromosorb 102 column. The presence of a minor additional source of hydrogen atoms does not, however, affect the analysis for R_{CH4O}, as $[H]_O$ was calculated explicitly from the observed yields of methane and propane in each experiment.

Non-scavengable methane has been observed in the photolysis of acetone by Lin and Ausloos [204] at 147 nm, where it was attributed to a molecular elimination channel on the basis of isotopic labelling studies:

$$CH_3COCH_3 \text{ =====> } CH_4 + CH_2CO \qquad P3$$

and at 184.9 nm by Potzinger and von Bunau [187], who postulated that it was formed by abstraction of hydrogen atoms from acetone by vibrationally hot methyl radicals:

$$CH_3^* + CH_3COCH_3 \text{ =====> } CH_4 + CH_2COCH_3$$

In the present experiments, radical - bath gas collision rates were at least three orders of magnitude greater than the fastest radical-radical reaction rates and it is thus expected that radical - radical reactions involved encounters between thermalised radicals. It is known, however, that helium is a very inefficient collision partner for the vibrational relaxation of methyl radicals. Callear and Van den Bergh [205] estimated that 500 collisions between vibrationally excited methyl radicals, formed in the flash photolysis of dimethyl mercury, and helium atoms, were required to thermalise the methyl radicals at room temperature. It is thus likely that collisions between vibrationally excited methyl radicals and precursor molecules occurred at all pressures employed, although the hot radical reaction would have to be at least three orders of magnitude faster than the equivalent thermal reaction at 300K if significant quantities of methane were to be produced in this way. In addition, the ethylene scavenging experiments from which R_{CH4o} was determined employed ethylene concentrations up to four times greater than the acetone concentration. Although the lowest ethylene vibrational frequency is for the ν_{10} mode at 826.0 cm^{-1} and V-V transfer between methyl radicals and ethylene would not be expected to be very efficient, some change in the degree of vibrational

excitation of methyl radicals in collision with acetone molecules might be expected over the experimental range of $[C_2H_4]$; no systematic change in R_{CH4O} with $[C_2H_4]$ was observed, however.

Sulphur hexafluoride is known to quench vibrationally excited methyl radicals very efficiently [205], as might be expected from the near resonance between the lowest energy methyl radical frequency at 606 cm^{-1} and the sulphur hexafluoride ν_{10} mode at 616 cm^{-1}. The addition of 10 Torr of SF_6 to a photolysis mixture of 1 Torr acetone in 500 Torr He produced no significant change in R_{CH4}, demonstrating that hot methyl radical reactions were not important in the present experiments, at least at the higher pressures employed.

The most probable route to non-scavengeable methane would therefore appear to be the molecular elimination channel P3. It also seems likely that the pressure independent yield of non-scavengeable methane observed by Potzinger and von Bunau arose from a molecular elimination and was not the product of hot methyl radical reactions, as suggested by the authors.

A discrepancy was noticed, however, between the molecular methane yields obtained from the ethylene scavenging experiments and the methane yields obseved in the nitric oxide scavenging experiments. The yields of methane relative to the yield of ethane found in the absence of nitric oxide are shown as a function of [NO] in Figure 4.18. Also shown are the methane yields obtained by numerical integration of the reaction scheme below.

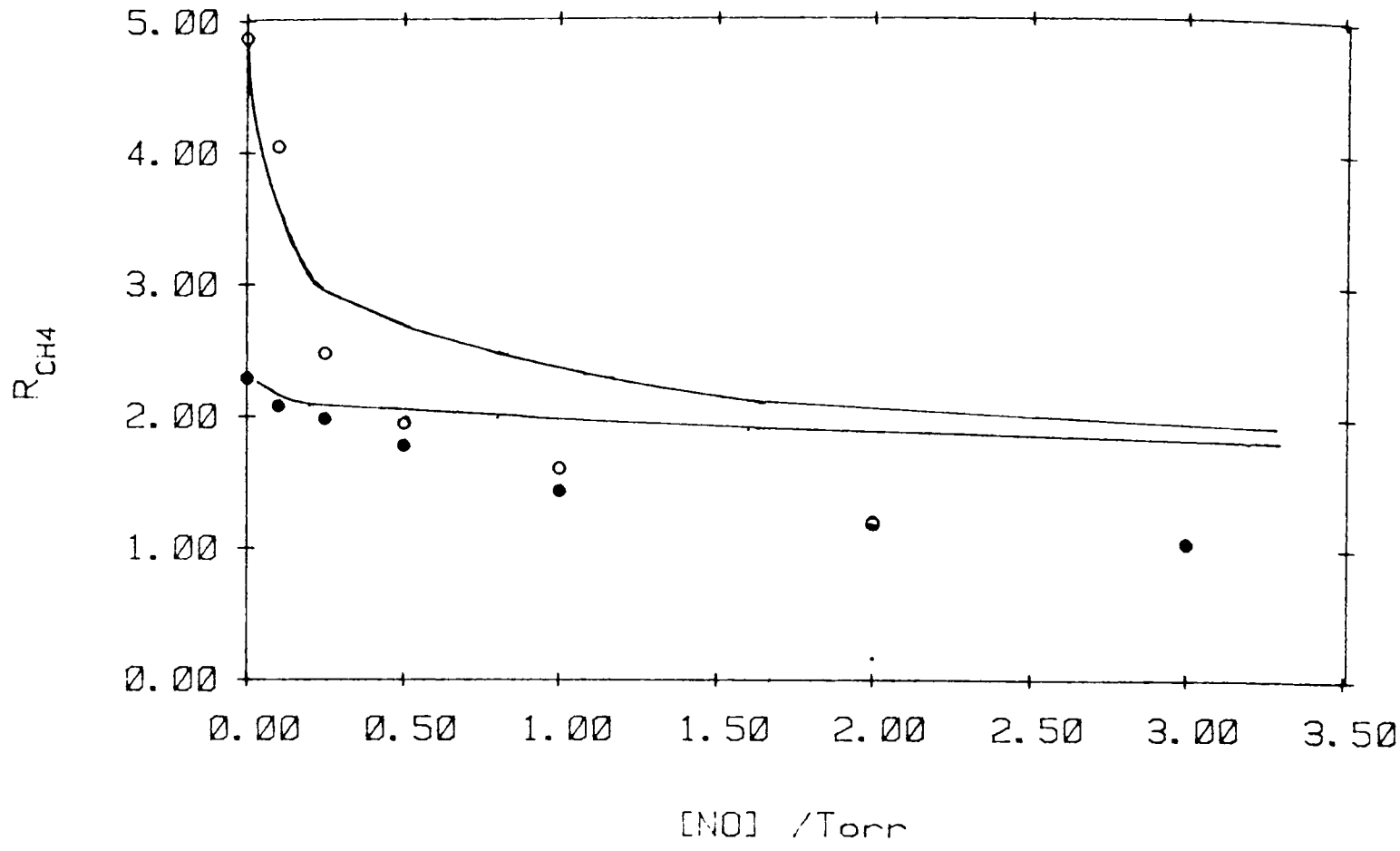

Figure 4.18. Dependence of R_{CH4} on Nitric Oxide Concentration, 300K. Total Pressure: o 10 Torr He, o 500 Torr He. The solid lines show the simulated behaviour, without allowance for electronic quenching by NO.

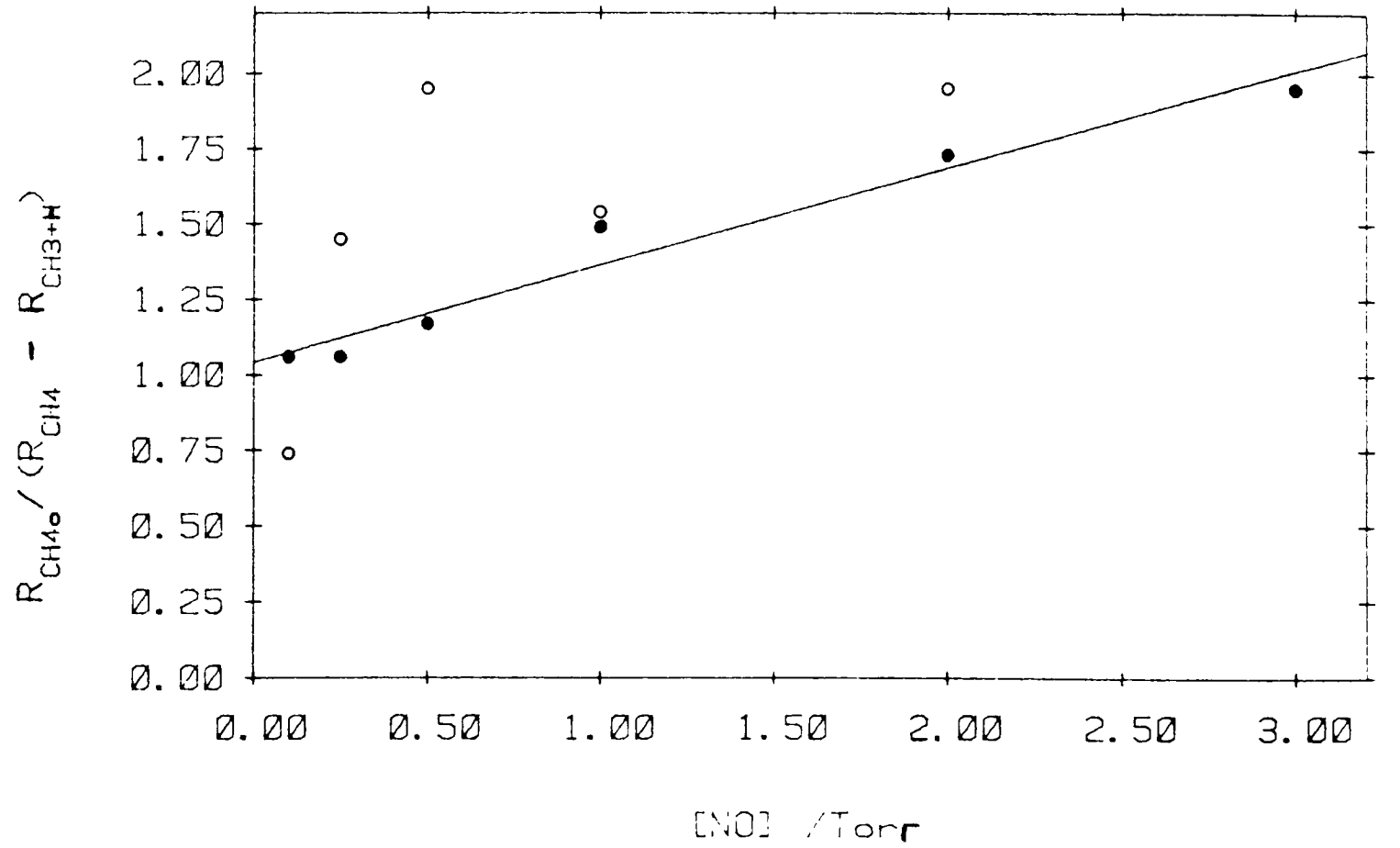

Figure 4.19. Stern-Volmer Plot for the Quenching of the Molecular Methane-Producing Channel, P3, by NO. o 10 Torr total pressure, o 500 Torr total pressure. The straight line represents a best fit to the 10 Torr data.

Reaction	Rate constant/ molecule^{-1}cm^{3}s^{-1}		Reference
	10 Torr	500 Torr	
$CH_3 + CH_3 \Longrightarrow C_2H_6$	5.2×10^{-11}	5.9×10^{-11}	[26]
$CH_3 + H \Longrightarrow CH_4$	7.5×10^{-12}	1.85×10^{-10}	[116]
$CH_3 + NO \Longrightarrow CH_3NO$	6.9×10^{-13}	6.1×10^{-12}	[200]
$H + NO \Longrightarrow HNO$	1.4×10^{-14}	6.9×10^{-13}	[206]

Initial concentrations were taken as:

$[CH_3] = 2.10\times10^{14}$cm^3 (500 Torr)

$= 2.45\times10^{14}$cm^3 (10 Torr)

$[H] = 1.4\times10^{-2}[CH_3]$

$[CH_4] = 0.8\times10^{-2}[CH_3]$

It can be seen that at both pressures, R_{CH4} falls somewhat below the expected value of R_{CH4o} at high [NO]. Such a discrepancy could arise if there was a further route to methane other than those already postulated and which was slowly removed by the addition of nitric oxide. Reactions involving hydrogen atoms are excluded by the constancy of R_{CH4o} measured over a wide range of $[C_2H_4]$ in the ethylene scavenging experiments. The only methyl radical reaction which occurs on a similar timescale to CH_3 + NO other than that with hydrogen atoms, R2, is the recombination reaction R1, which is known to produce only ethane molecules even at temperatures as high as 4800K [207].

A second possibility is that the channel producing molecular methane, P3, is quenched by nitric oxide:

$$CH_3COCH_3 \xrightarrow[193.3\ nm]{h\nu} CH_3COCH_3^*$$

$$CH_3COCH_3^* \quad =====> CH_4 + CH_2CO$$

$$CH_3COCH_3^* + NO \quad =====> \text{Products}$$

One possible mechanism for the quenching of electronically excited acetone by nitric oxide would involve the direct transfer of electronic energy from acetone to nitric oxide. Nitric oxide is known to be an efficient electronic quencher: Callear and Wood [208] observed rapid electronic transfer between ground state nitric oxide and nitrogen molecules in the $A^3\Sigma^+u$ state, by following the time-resolved NO γ band emission. A quenching rate constant of $(5.45\pm0.30)x10^{-11}$ molecule^{-1}cm^{3}s^{-1} was obtained. The γ band of nitric oxide, corresponding to the $A^2\Sigma$ <=== $X^2\Pi$ transition begins at around 230 nm, the first three lines of the vibrational progression lying below 193.3 nm.

If the molecular methane forming channel were electronically quenched by nitric oxide, then it might be expected that Stern-Volmer kinetics would apply to the quenching. Figure 4.19 shows a plot of $R_{CH4o}/(R_{CH4}-R_{CH3+H})$ vs [NO], where R_{CH3+H} is the simulated contribution to R_{CH4} from the H + CH_3 reaction (taken from Figure 4.18), R_{CH4o} is the molecular component of the methane yield in the absence of nitric oxide (=1.60) and R_{CH4} is the experimental methane yield in the nitric oxide scavenging experiments, relative to the ethane yield expected in the absence of nitric oxide. The data at 10 Torr can be seen to follow Stern-Volmer kinetics quite well, a linear fit to the data giving $k_q/k_d = (1.0\pm0.2)x10^{-17}$ molecule^{-1}cm^3. Although the data at 500 Torr is in reasonable agreement with the 10 Torr data at high [NO], it is very scattered at low [NO]. However, at low nitric oxide concentrations, the contribution to R_{CH4} from the H

+ CH_3 reaction is of the same order as R_{CH4O} and any deficiencies in the concentrations and rate constants used in the simulations would be expected to introduce large errors in R_{CH4}-R_{CH3+H} so that the scatter is not unexpected. The decrease in R_{CH4} with [NO] is thus largely consistent with an electronic quenching mechanism.

It might be expected that electronic quenching could affect the analysis, in Section 4.3.1(ii)(a), of the reduction in ethane yield caused by the reaction of methyl radicals with nitric oxide. However, the Stern-Volmer plot results in a quenching half pressure of around 3 Torr of nitric oxide, much greater than the partial pressure of nitric oxide required to reduce the observed ethane yield by the same amount, even at 10 Torr total pressure, where the CH_3 + NO reaction is slowest. Electronic quenching would thus only affect the observed ethane yields if the primary photodissociation channel P1 were much more rapidly quenched than that producing molecular methane, P4.

To summarise, the experimental dependece of R_{CH4} on the presence of radical scavengers suggests that methane was produced by two mechanisms. Experiments using ethylene as a hydrogen atom scavenger demonstrated that significant yields of hydrogen atoms were produced in the photolysis and the decrease in R_{CH4} with [C_2H_4] indicated that a large fraction of the methane yield at 500 Torr was formed by the reaction between hydrogen atoms and methyl radicals. The yield of methane was not reduced to zero at high [C_2H_4], however, demonstrating that some methane was produced by a mechanism not involving hydrogen atoms. R_{CH4} was reduced much more slowly by the presence of nitric oxide than would be expected if reactions of methyl radicals with species other than hydrogen atoms were the source of the additional methane, suggesting a direct molecular

elimination process as a second route to methane production.

In an attempt to model the observed pressure dependence of R_{CH4} and test the validity of the postulated photolysis mechanism, numerical simulations were performed using the reaction scheme below.

$CH_3 + CH_3$	=====> C_2H_6	R1
$CH_3 + H$	=====> CH_4	R2
$CH_3 + CH_2COCH_3$	=====> MEK	R3
$H + CH_2COCH_3$	=====> CH_3COCH_3	R4
$2\ CH_2COCH_3$	=====> $(CH_3COCH_2)_2$	R5

Initial methyl concentrations were calculated from the fitted dependence of $[C_2H_6]$ on I shown in Figure 4.11 and varied from $2.1x10^{13}$ cm^3 to $1.68x10^{14}$ cm^3, corresponding to an experimental laser intensity range of 10 to 80 $mJpulse^{-1}$. Initial hydrogen atom and acetonyl radical concentrations were set equal to $1.3x10^{-2}[CH_3]_{t=o}$ and $1.3x10^{-2}(1-\alpha)[CH_3]_{t=o}$ respectively, where α is the fraction of acetonyl radicals which decompose at a given pressure, calculated from the fit to the data in Figure 4.15. The simulations were allowed to run up to a reaction time of 1 second, after which no further significant changes in radical concentrations were found. Table 4.4 lists the rate constants used.

Table 4.3.4

Rate Constants Used in Simulations of Product Pressure Dependence at 300K

Reaction	Rate Constant/ 10^{-11}molecule^{-1}cm^{3}s^{-1}				Reference
	10	40	330	500 Torr	
R1	5.22	5.57	5.88	5.90	[26]
R2	0.75	2.8	14.7	18.5	[116]
R3	5.96	6.15	6.32	6.33	Mean value rule
R4	10.0	10.0	10.0	10.0	Estimate
R5	1.7	1.7	1.7	1.7	Value for nC_3H_7 [25]

The simulated values of R_{CH4} were independent of initial radical concentrations at all pressures and decreased from very close to 2.67, the value which would be achieved if all the hydrogen atoms were to react with methyl radicals, at 500 Torr, to 1.02 at 10 Torr. This decrease in R_{CH4} with pressure was the result of the varying relative magnitudes of k_1 and k_2: at 500 Torr $k_2 = 3.1k_1$ and hydrogen atoms reacted faster with methyl radicals than the methyl radicals were removed by self-recombination, whereas at 10 Torr $k_2 = 0.14k_1$ and a significant fraction of the hydrogen atoms were left over after the other radicals had decayed away. Hydrogen atoms which do not react by recombination with other radicals are presumably removed by diffusion to and recombination on the walls of the cell, as reaction with the precursor or self-recombination will be very slow under the present conditions. An approximate upper limit for diffusion of the atoms to the walls of the cell can be calculated at each pressure

from the appropriate diffusion constant for hydrogen atoms in helium, D, and the weighted average distance of uniformly produced atoms from the walls of the cell, x (=R/3). An average time taken to diffuse to the cell walls, can be obtained from the two dimensional diffusion expression:

$$t = x^2/2D$$

The calculated values of D and rate of first-order loss by diffusion to the cell walls at each experimental pressure, taking the radius of the cell to be 1.25 cm, are summarised in Table 4.3.5, together with the corresponding rate of first-order loss by reaction with an initial methyl concentration of $1x10^{14} cm^3$ (~50 mJ).

Table 4.5

Comparison of Rates of Hydrogen Atom Loss By Diffusion and Reaction With Methyl Radicals

Pressure/Torr	10	40	330	500
D/cm^2s^{-1}	119	30	3.6	2.4
k_{wall}/s^{-1}	1351	345	40	27
$k_2[CH_3]_{t=o}/s^{-1}$	750	2800	14700	18500

It can be seen that diffusion to the walls of the cell could dominate the hydrogen atom kinetics at the lower pressures, especially as methyl radicals are rapidly removed by R1. Table 4.6 shows the simulated values of R_{MEK} and R_{CH4} as a function of pressure at laser energies of 10 and 80 mJ, after inclusion of the first-order wall loss process:

$$H \xrightarrow{k_w} \text{wall}$$

in the reaction scheme. Values of k_w were taken from Table 4.5. Alsc shown are the values of R_{MEK} which would result if all the acetonyl radicals formed MEK by reaction with methyl radicals.

Table 4.6

Simulated Values Of R_{CH4} and R_{MEK} as a Function of Pressure and Laser Energy

Pressure/ Torr	R_{CH4}		R_{MEK}		Maximum R_{MEK}
	10 mJ	80 mJ	10 mJ	80 mJ	
500	2.60	2.63	2.29	2.29	2.67
330	2.53	2.61	2.07	2.07	2.40
40	0.87	1.45	1.40	1.38	1.60
10	0.15	0.38	0.73	0.72	0.80

Again the simulated values of R_{CH4} were very close to the upper limit of 2.67 and virtually independent of intensity at the two higher pressures. Diffusion to the cell walls becomes comparable to methane formation at 40 Torr and is the major process at 10 Torr. No significant increase in R_{CH4} is expected over the experimental intensity range at 10 Torr and the predicted increase in R_{CH4} at 40 Torr is well within the 2σ errors of the experimental average. Close examination of the data at 40 Torr shows that R_{CH4} does increase systematically with I_j apart from values obtained at low laser intensities (<10 mJ), where the very low methane yields result in fairly uncertain (±10%) values of R_{CH4}.

The simulated values of R_{MEK} show no dependence on I, as

observed experimentally, but are significantly less than the values expected if R3 was the only reactive route for acetonyl radicals at all pressures, the shortfall decreasing slightly from 14.2% to 10.0% at 10 Torr. The self-recombination reaction R5 was found to be the only significant route to removal of acetonyl radicals other than R3; under all conditions less than 3% of acetonyl radicals were predicted to react with hydrogen atoms.

Assuming that the fraction of acetonyl radicals not observed as MEK is constant within the precision of the experimental averages, then the extrapolated value of R^{∞}_{MEK} will be approximately 87% of the true value. Correction in this manner gave:

$$R^{\infty}_{MEK} = 3.05 \pm 0.60$$

A further consequence of the experimental underestimate of the yield of photolysis channel P2 is that the initial yield of hydrogen atoms is similarly underestimated. As the simulations show that R_{CH4} does not change appreciably over the experimental range of I, then the simulated values of R_{CH4} may be scaled by 3.05/2.65 for comparison with experimental values. The scaled simulated values of R_{CH4}, for an average laser energy of 45 mJ, both with and without the calculated wall loss process, plus 1.60 to allow for molecular methane production, as was discussed earlier in this section, are

presented along with the experimental averages in Table 4.7.

Table 4.7

Comparison of Simulated and Observed

Methane Yields at 300K

Pressure/ Torr He	R_{CH4} (Experimental)	R_{CH4} Simulated (with wall loss)	R_{CH4} Simulated (no wall loss)
500	4.87 ± 0.80	4.59	4.64
330	4.51 ± 0.44	4.51	4.63
40	3.54 ± 0.38	2.94	4.03
10	2.29 ± 0.18	1.85	2.77

The experimental and simulated values are in good agreement at the two highest pressures where hydrogen atom loss by diffusion to the walls of the cell is unimportant. At the lower pressures, the simulated values of R_{CH4} bracket the experimental values. Reducing k_w by a factor of two would bring the simulated and experimental values of R_{CH4} into agreement at all pressures, within experimental error.

In summary, methane is produced in two ways: by a direct molecular elimination from the excited molecule (P3), and by recombination of methyl radicals and hydrogen atoms formed via photolysis channel P2. Scavenging experiments allowed discrimination between the two mechanisms. Simulations, including limiting values for the rate of hydrogen atom loss at the walls of the cell, completely reproduced the observed experimental behaviour, with R_{CH4o} = 1.60 and R^{∞}_{MEK} = 3.05.

(d) Ethylene

The yield of the minor product ethylene was independent of pressure and acetone concentration, but dependent on laser energy, unlike all other product yields. R_{C2H4} increased from $\sim$0.2 at 25 mJ to $\sim$0.35 at 80 mJ. Figure 4.20 shows the absolute yield of ethylene as a function of laser intensity for all pressures studied. In each case the absolute yield has been scaled to refer to a 10 shot experiment with 1 Torr of precursor.

A non-linear dependence of a product yield on I can arise in two ways. Firstly, if the product was formed in a process which was second-order in overall radical concentration and which was in competition with a first-order process, then the yield of the second-order process would increase with I. The identical dependences of the scaled yields of ethylene on I at 10 Torr, where the acetone partial pressure was 0.25 Torr and at other pressures, where 1 Torr of precursor was employed and initial radical concentrations hence a factor of four greater for a given I, show that such a mechanism is not operating in the present experiments, unless the first-order process involved reaction with acetone. As was discussed in Section 4.3.1.(i), the reactions of hydrogen atoms and methyl radicals with acetone are negligibly slow at 300K under the present experimental conditions.

A second possibility is that ethylene arises out of a multiphoton process. Given that the laser light is defocused into the photolysis cell, resulting in photon densities of $\sim 1 \times 10^{15}$ cm^{-2} or power densities of $\sim$0.1 $MWcm^{-2}$ in a 10 ns pulse, it is unlikely that a coherent multiphoton process is occurring to a measurable extent

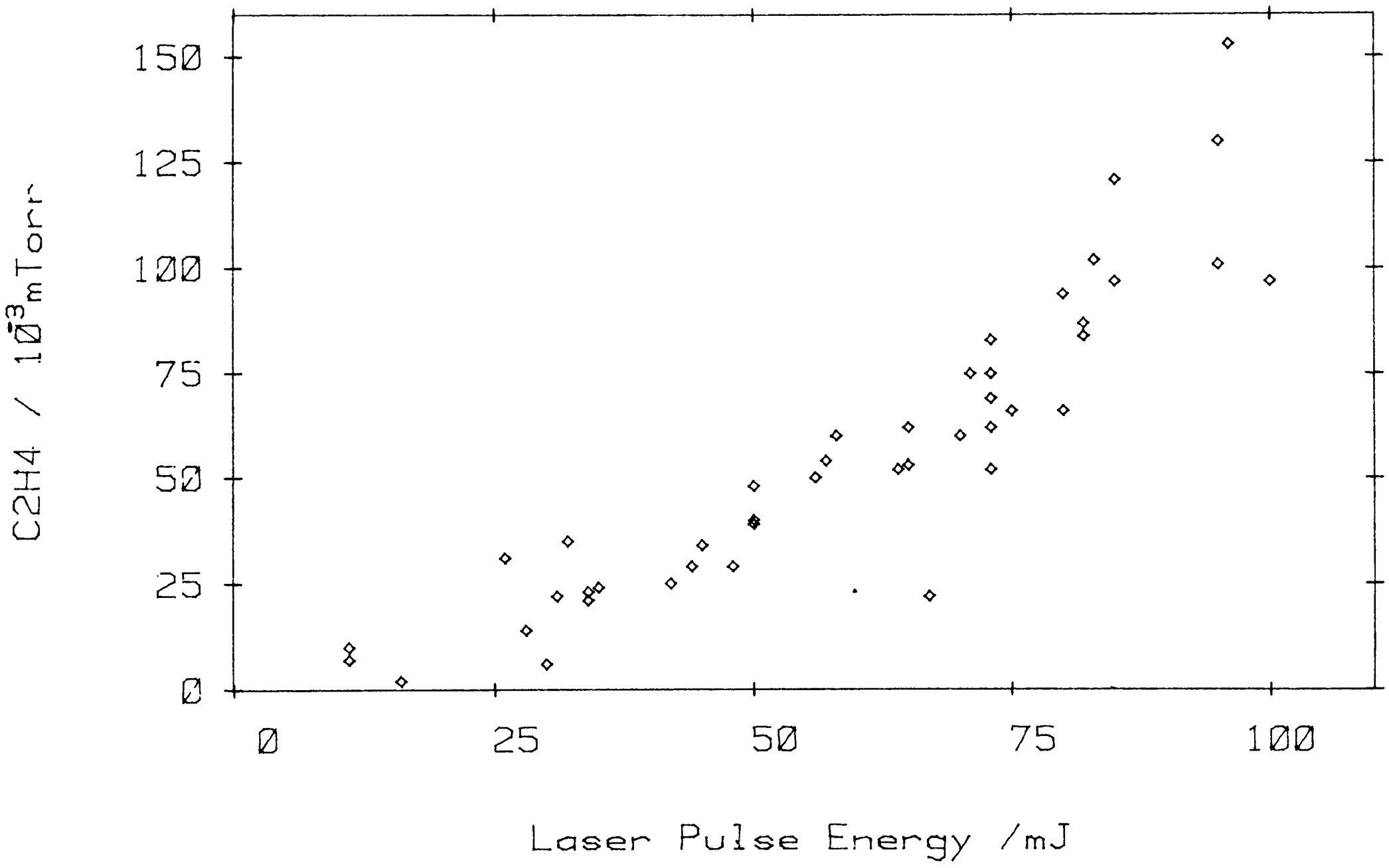

Figure 4.20. Dependence of Ethylene Yield on Laser Pulse Energy, 300K, all Pressures. Yields are scaled to refer to 10 laser shots and 1 Torr acetone. Multiply by 1.27 to correct for dead volume.

and the sequential absorption of further 193.3 nm photons by a real excited state or a photolysis product is much more probable. Ethylene has been observed at high intensities in both the 193.3 nm [178] and broad-band flash-lamp photolysis of azomethane [209]. It was suggested that the mechanism of ethylene production involved the absorption of a second photon by methyl radicals generated in the initial part of the photolysis pulse to produce singlet methylene, which was rapidly quenched by the noble gas buffer to the triplet ground state [34] and which reacted in turn with methyl radicals [210] to generate ethylene and hydrogen atoms.

$$CH_3N_2CH_3 \xrightarrow{h\nu} CH_3 + N_2 + CH_3$$

$$CH_3 \xrightarrow{h\nu} {}^1CH_2 + H$$

$${}^1CH_2 + He \longrightarrow {}^3CH_2$$

$${}^3CH_2 + CH_3 \longrightarrow C_2H_4 + H$$

The ground state methyl radical displays a strongly predissociated absorption band at 216.36 nm, assigned to the (0-0) transition of the B $^2A_1'$ <=== X^2A_2'' band [211]. Transitions with $\Delta v_2 > 2$ are very weak, indicating that the equilibrium structures of the ground and excited states are similar. Transitions with Δv_2 odd are absent, as the radical is planar in both states, with D_{3h} symmetry: the ν_2 out-of-plane bending mode is antisymmetric with respect to some elements of the D_{3h} point group and consequently only transitions with Δv_2 even are allowed. Thus, only transitions with $\Delta v_2 = 0, \pm 2$ are predicted to have appreciable intensities. Yamada et al. [212] showed that the ν_2 mode has a strong negative anharmonicity, caused by ν_2-induced mixing between the ground (X) and

first excited (B) electronic states. The effect of this perturbation on the vibrational levels of the B state was not, however, investigated and the exact dependence of the transition energy on the ν_2 quantum number is therefore uncertain. It is, however, clear that the transition with $\Delta\nu_2 = 0$ will move to shorter wavelengths with increasing vibrational excitation, because of the large increase in the frequency of the ν_2 mode from the ground (606 cm^{-1}) to the B (1360 cm^{-1}) state and highly vibrationally excited methyl radicals should be expected to absorb at 193.3 nm.

Vibrationally excited methyl radicals have been observed in the photolysis of azomethane at 193.3 nm [26], the flash lamp photolysis of dimethyl mercury [205] and the photodissociation of methyl iodide at 266 nm [212]. In the latter case, a population inversion in the ν_2 mode was observed. Excitation of the methyl radical out-of-plane bending mode is likely to occur in all photodissociations producing methyl radicals, owing to the change in methyl radical geometry from a bent to a planar configuration along the reaction coordinate, suggesting that this mechanism of methylene production could be generally applicable to high intensity photodissociations around 200 nm, where methyl radicals are produced on timescales comparable to the duration of the photolysis light pulse.

An order of magnitude estimate of the dissociation rate of excited acetone molecules produced by the absorption of a single 193.3 nm photon can be made using the RRK formula for k(E) (E2.8), the 81.3 $kcalmol^{-1}$ threshold for C-C bond cleavage (see Table 4.1) and the 147.8 $kcalmol^{-1}$ available from the 193.3 nm photon. Assuming an A factor of 10^{14} - 10^{15} s^{-1} and s=12 gives an estimate for the lifetime of the excited acetone molecule with respect to dissociation

of between 0.064 and 0.64 ns, which is short compared to the excimer laser pulse duration of 10 ns in the present experiments.

Support for this mechanism of ethylene production is found in the observation that much greater ethylene yields were found in the flash lamp photolysis of azomethane [209] than in the corresponding ArF excimer photolysis [178]. The much broader spectral range generated by flash lamps would result in the possibility of absorption of further photons by methyl radicals from a wide range of vibrational levels in the electronic ground state. In addition, the flash lamp pulse duration was around 5 μs compared to the 10 ns for pulses from an excimer laser and the rapidly equilibrating radicals would be exposed to photolysis radiation for a much longer period of time.

Further evidence for the presence of methylene in the 193.3 nm photolysis of acetone at high intensities is provided by the work of Nagata et al. [214], who monitored $X^2\Pi$ <=== $A^2\Delta$ emission from electronically excited CH radicals, produced by a three photon process in the photolysis of several methyl radical precursors, including acetone, using focused 193.3 nm radiation. The CH A state rotational distributions were found to be bimodal and virtually independent of precursor; it was hence concluded that CH $A^2\Delta$ radicals were produced by two mechanisms, both of which involved absorption of a second photon by methyl radicals produced in the initial photolysis step.

$$CH_3R \xrightarrow{h\nu} CH_3 + R \qquad CH_3R \xrightarrow{h\nu} CH_3 + R$$

$$CH_3 \xrightarrow{h\nu} CH_2 + H \qquad \text{and} \qquad CH_3 \xrightarrow{2h\nu} CH\ (A\,^2\Delta) + 2H$$

$$CH_2 \xrightarrow{h\nu} CH\ (A^2\Delta) + H$$

In order to increase the range of intensities covered in the present study, an experiment was performed at 330 Torr He and a laser energy of 85 mJ, but without the defocusing lens in place. It is estimated that the laser intensity in the irradiated rectangular section of the main cell body was increased by approximately a factor of 11 in this way. R_{C2H4} was found to be increased by a factor of 13, from 0.35 to 4.55, providing strong evidence for the existence of a two photon mechanism for ethylene production. Furthermore, R_{CH4} was also increased from 4.4 to 13.9, demonstrating a significant increase in the yield of hydrogen atoms. The above mechanism predicts that two hydrogen atoms would be produced for each ethylene molecule observed. Assuming that all the hydrogen atoms react with methyl radicals to form methane, then the increase in R_{CH4} should be equal to twice the increase in R_{C2H4}, as approximately observed.

It must be emphasised that methylene consitutes only a very minor fraction of the radical products at the present low intensities and will not affect the suitability of acetone as a methyl radical precursor in flash photolysis / kinetic spectroscopy experiments. However the presence of methylene provides a route for hydrogen atom production on a timescale similar to that for their removal by reaction with methyl radicals and could be a problem in experiments designed to monitor the decay of hydrogen atoms by reaction with an excess of methyl radicals, as are described later in this chapter, especially at the higher (x15) intensities employed in those experiments.

If all the observed ethylene were produced by the two photon mechanism, then the addition of nitric oxide would be expected to

reduce R_{C2H4} rapidly to zero. A rapid decrease of R_{C2H4} with increasing [NO] was indeed observed, but as shown in Figure 4.21, the ethylene yield did not go to zero at high [NO] and R_{C2H4} appeared to reach a stationary value at both 10 and 500 Torr corresponding to 25-30% of the value expected in the absence of nitric oxide. Non-scavengeable ethylene has been observed in the photolysis of acetone at 147 nm [204], where isotopic labelling studies showed that the ethylene produced in the presence of a nitric oxide scavenger was the result of a molecular elimination. It was suggested that the molecular elimination proceeded via the 1,1 elimination of a hydrogen molecule, followed by rapid rearrangement and dissociation of the carbene so formed:

$$CH_3COCH_3 \xrightarrow{h\nu} CH_3COCH^* + H_2 \Longrightarrow C_2H_4 + CO + H_2 \quad P4$$

Given the scatter in the present observed ethylene yields, it is entirely possible that some of the ethylene was produced by such a single photon process. If both one- and two- photon process were occurring, then R_{C2H4} would be expected to vary as a + bI. A linear fit to R_{C2H4} against I for the unscavenged experiments gave R_{C2H4} = $(0.11\pm0.06) + (2.6\pm0.5)\times10^{-3}I$, where the gradient and intercept of the fit refer to the yields of molecular ethylene and ethylene produced via the photolysis of methyl radicals. From the fit to R_{C2H4}, the yield of molecular ethylene is calculated to be 32% of the total at 90 mJ, close to the value observed in the nitric oxide scavenging experiments.

It is expected that the hydrogen atoms produced via the photolysis of methyl radicals will contribute to the observed methane yield at high pressures where diffusion to the walls of the cell is

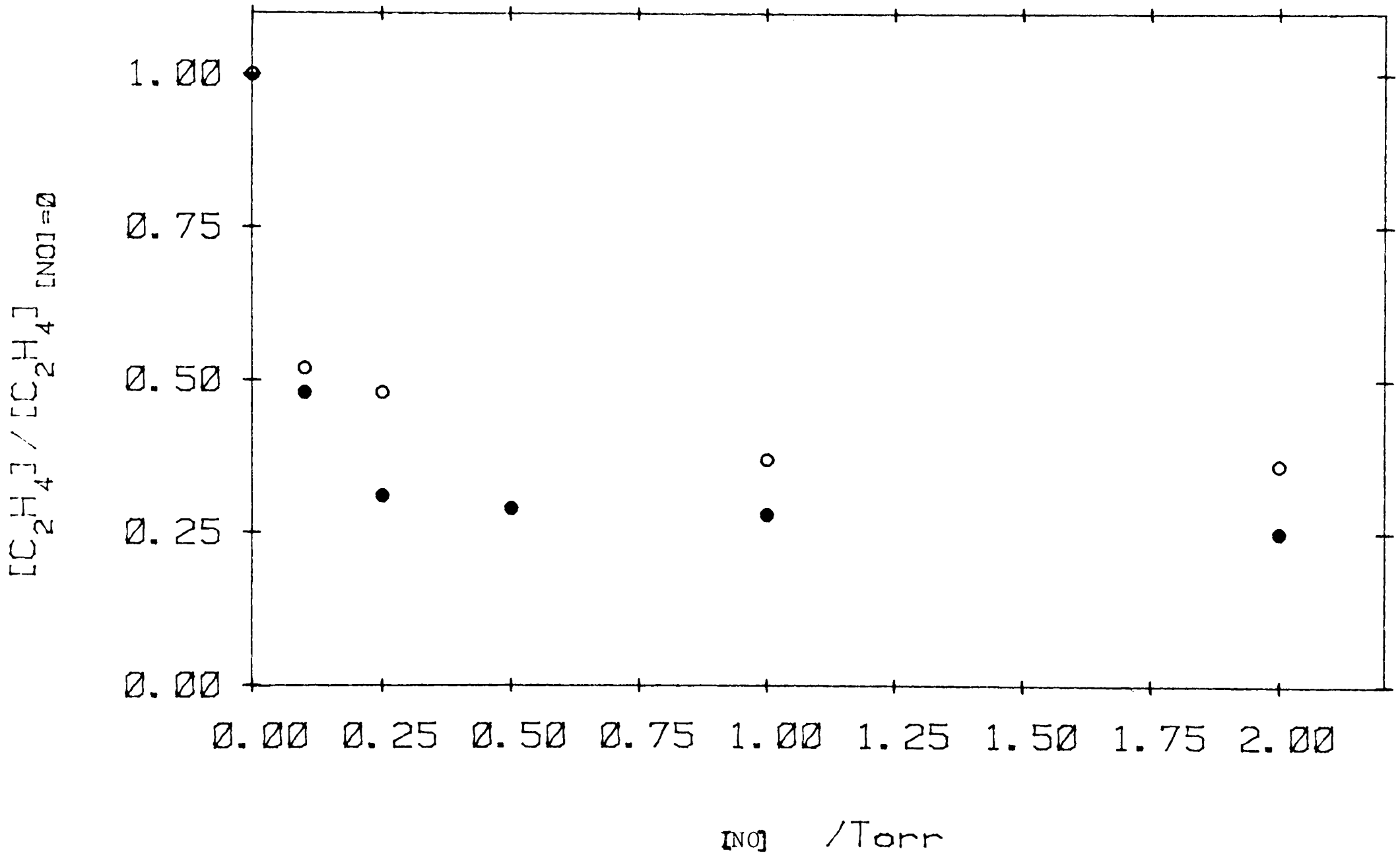

Figure 4.21. Dependence of Ethylene Yield on [NO], 300K.

● 10 Torr, I = 95mJ; o 500 Torr, I = 80 mJ.

not the dominant pathway for hydrogen atom removal and result in a increase in R_{CH4} with I. However, the increase in hydrogen atom yield R_H and hence R_{CH4} is calculated to be 0.42 over the range 10 - 90 mJ, which is well within the 95% confidence limits on $\langle R_{CH4} \rangle$ at the two highest pressures and which would therefore not easily be detected.

(e) Other Products

The only other significant observed end products were found to elute from the column at times corresponding to allene and propane. Both products displayed no dependence on total pressure and a linear dependence on laser energy. Plots of absolute allene and propane yields against I for experiments at all pressures, scaled to 1 Torr acetone and 10 laser shots, are shown in Figures 4.22 and 4.23. The slopes of the best fit straight lines in Figures 4.22 and 4.33 give $R_{C3H4} = 0.17 \pm 0.03$ and $R_{C3H8} = 0.09 \pm 0.02$.

Both allene (1.5%) and propane (0.3%) have been observed in the 147 nm photolysis of acetone [204]. Experiments at that wavelength using nitric oxide as a radical scavenger showed that although propane was formed via a radical mechanism, allene was a primary photolysis product, as was a similar quantity of methyl acetylene, which could not be separated from acetone using the present analysis.

$$CH_3COCH_3 \xrightarrow[193.3\ nm]{h\nu} C_3H_4 + "H_2O" \qquad P5$$

It was not possible to determine the effect of the nitric oxide scavenger on the yields of propane and allene in the present study, because of a baseline distortion which occurred at their expected

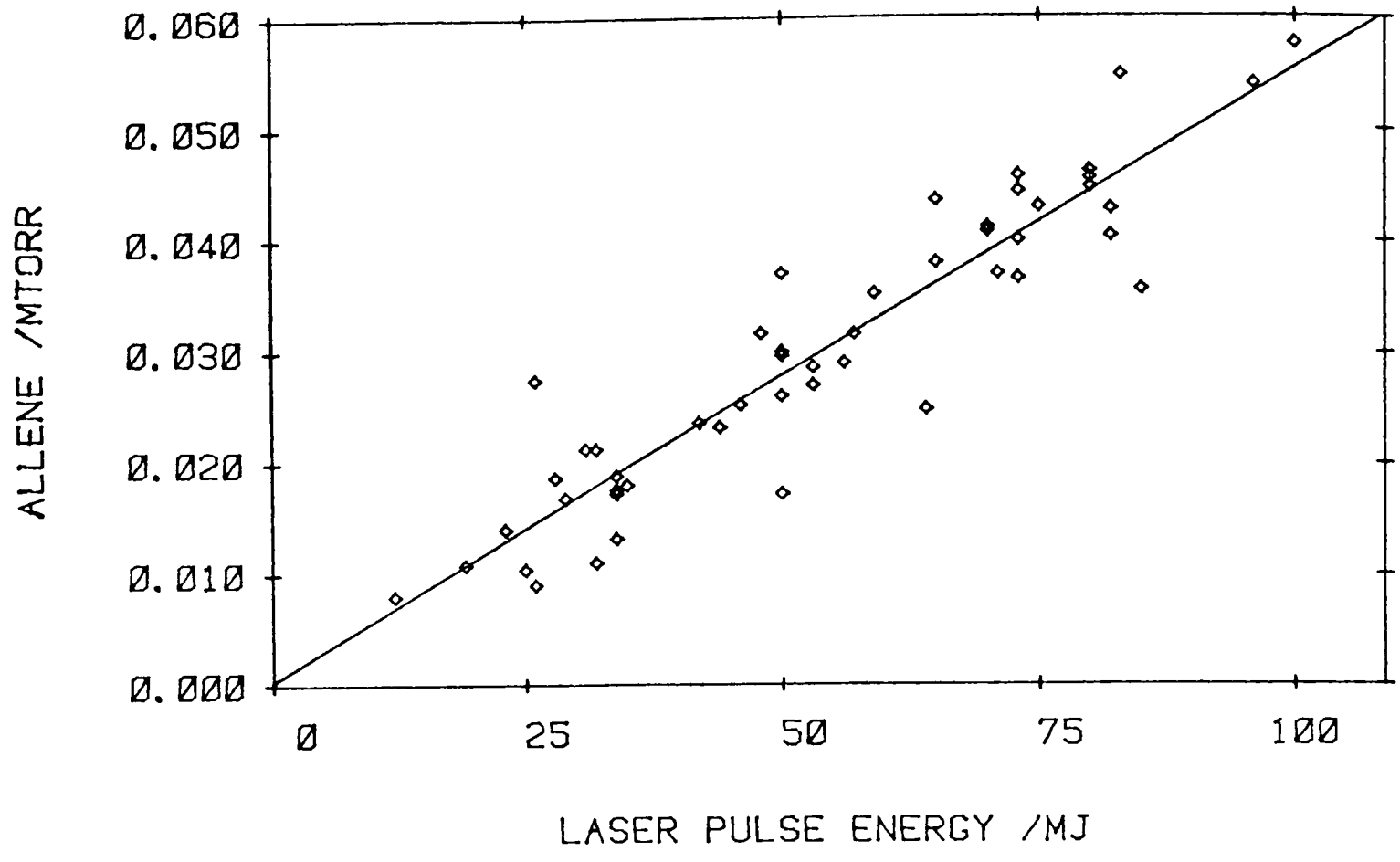

Figure 4.22. Dependence of Allene Yield on Laser Pulse Energy, 300K, all Pressures. Yields are scaled to refer to 10 laser shots and 1 Torr acetone. Multiply by 1.27 to correct for dead volume.

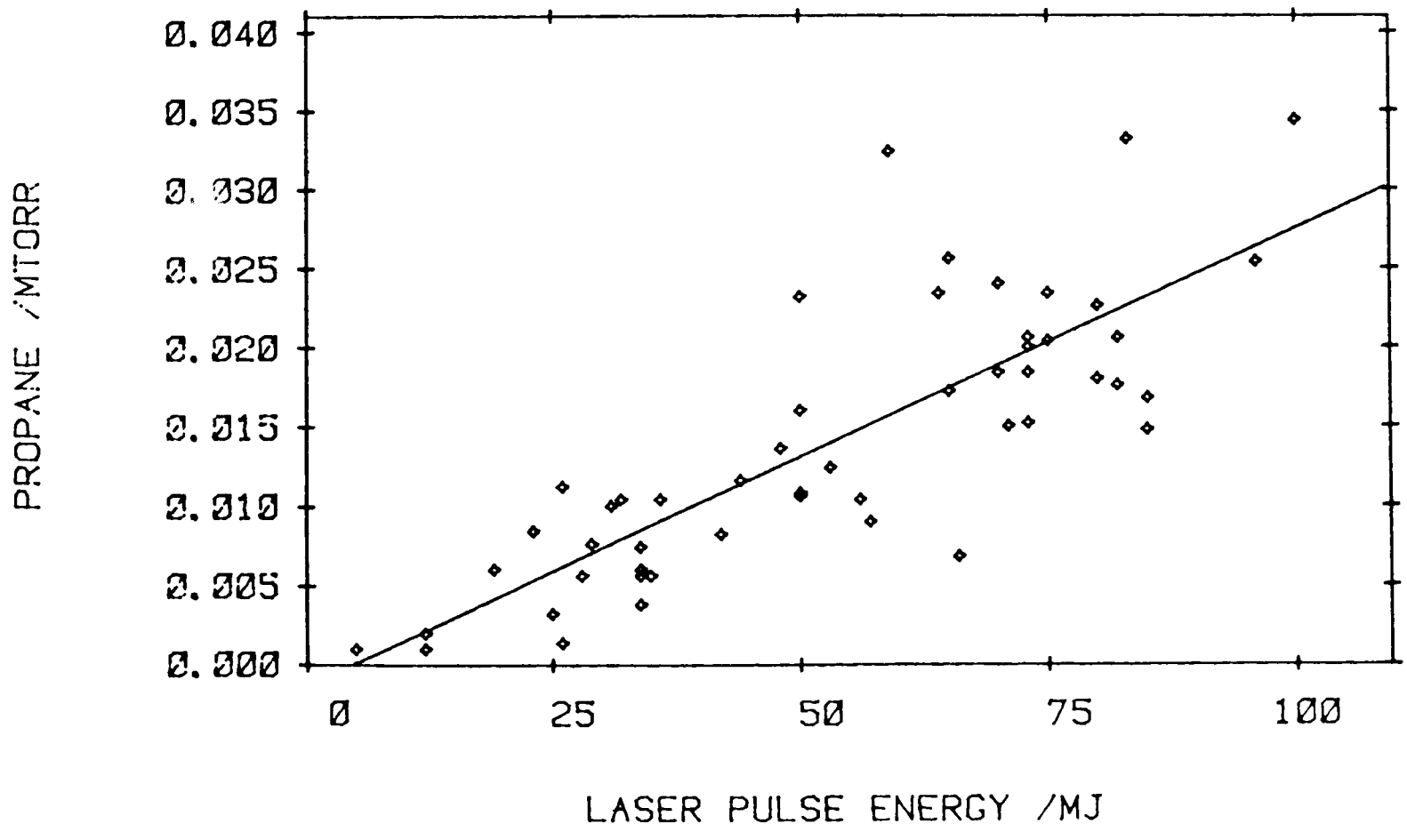

Figure 4.23. Dependence of Propane Yield on Laser Pulse Energy, 300K, all Pressures. Yields are scaled to refer to 10 laser shots and 1 Torr acetone. Multiply by 1.27 to correct for dead volume.

elution times and which was presumably caused by the elution of a very broad CH_3NO peak. The addition of ethylene had no significant effect on the allene yield. It was not possible to determine the effect of ethylene on the small yield of propane, as R_{C3H8} increased rapidly with $[C_2H_4]$ because of the formation of ethyl radicals by addition of hydrogen atoms to ethylene, as discussed in Section 4.3.1(iii)(c).

The mechanism by which allene is produced is not obvious, although the direct elimination of a water molecule would appear to be highly improbable and a stepwise fragmentation much more likely. One possible pathway could involve the cleavage of the carbon - oxygen bond, followed by elimination of molecular hydrogen from the dimethyl carbene intermediate so formed, to produce allene or methyl acetylene:

$$CH_3COCH_3 \xrightarrow[193.3\ nm]{h\nu} CH_3CCH_3^* + O \longrightarrow CH_3CCH\ ,\ CH_2CCH_2 + H_2$$

The origin of propane in the present system is even less clear. If it were indeed produced by a radical - radical process then the most likely route would be the recombination reaction between ethyl radicals and methyl radicals, which requires a mechanism for the production of ethyl radicals. Potential reactive routes to ethyl radicals such as the collisional stabilisation of the highly excited ethyl moiety formed by the reaction between triplet methylene and methyl radicals, or the unimolecular dissociation of excited MEK molecules formed by the recombination of acetonyl radicals and methyl radicals, are precluded by the insensitivity of R_{C3H8} to total pressure and laser intensity.

A further possibility is that not all excited methylene radicals produced by the photolysis of methyl radicals are stabilised to their ground state by collision with helium atoms. Assuming a rate for insertion of singlet methylene into the C-H bonds of acetone similar to the rate of reaction with ethane, then singlet methylene should react with acetone around fifty times faster than it is collisionally quenched by helium [62]. At the two lowest pressures employed in the present study, the $[He]/[CH_3COCH_3]$ ratio was 40 and some singlet methylene would thus be expected to react with the precursor to form highly vibrationally excited MEK molecules, which could dissociate to produce ethyl radicals. However, as described above, R_{C3H8} displayed no systematic dependence on laser intensity, or the $[He]/[CH_3COCH_3]$ ratio within the admittedly rather large experimental error, contrary to the predictions of such a mechanism and although some propane could result from the reaction between singlet methylene and acetone, it must be concluded that most of the observed propane must be produced via an alternative process.

Ethyl radicals could be formed by a pressure independent rearrangement and dissociation of the acetonyl radical produced in photolysis channel P2:

$$CH_3COCH_2^* \text{ =====> } C_2H_5 + CO$$

However, given the extremely low yields of allene and propane in the present experiments, the mechanisms by which they are produced are not important; of perhaps greater significance is the demonstration of the sensitivity of the sampling technique provided by the quantitative detection of such small product yields.

4.3.2 Experiments at 600K

(i) The Thermal Decomposition of Acetone

The highest temperature to which acetone can be used as a methyl radical source will be determined by its thermal stability on the timescale of the experiment concerned. At temperatures below about 600K, the thermal decomposition of acetone proceeds according to the mechanism:

$$CH_3COCH_3 \text{ =====> } CH_3 + CO + CH_3$$

$$CH_3 + CH_3COCH_3 \text{ =====> } CH_4 + CH_2COCH_3$$

$$CH_3 + CH_2COCH_3 \text{ =====> MEK}$$

$$2\ CH_2COCH_3 \text{ =====> } (CH_3COCH_2)_2$$

$$CH_3 + CH_3 \text{ =====> } C_2H_6$$

and is limited by the unimolecular initiation step, which has an experimental activation energy of 71 kcalmol^{-1} [215,216]. At higher temperatures, the thermal decomposition of the acetonyl radical becomes appreciable:

$$CH_2COCH_3 \text{ =====> } CH_2CO + CH_3$$

and at sufficiently high temperatures, the pyrolysis can be described, at low conversions, by a simple chain mechanism:

$CH_3COCH_3 \text{ =====> } CH_3 + CO + CH_3$	Initiation
$CH_3 + CH_3COCH_3 \text{ =====> } CH_4 + CH_2CO + CH_3$	Propagation
$CH_3 + CH_3 \text{ =====> } C_2H_6$	Termination

Calculation of an upper limit for the rate of acetone

decomposition, using the chain mechanism above, indicated that methane formation from the pyrolysis of acetone could become comparable to the photolytic yield of methane at around 700K, but should be negligible at temperatures below 650K. More importantly, Winkler [183] found no evidence for ketene in the near u.v. photolysis of acetone below 673K, indicating that any contribution to the photolytic methane yield from the cycle involving the thermal decomposition of acetonyl radicals should be negligible at 600K

It must be emphasised that the use of acetone as a methyl radical precursor in real time kinetic spectroscopy experiments is not subject to such severe limitations as end product analysis experiments: the much higher temperature limit ($\sim$850K) in such experiments where the precursor is flowed through the heated cell is determined by the fractional decomposition of the precursor over the experimental residence time (typically a few seconds) and the relative magnitudes of the recombination and abstraction rates for methyl radicals. Still higher temperatures could be achieved by the use of a cooled gas inlet [15] to minimise the precursor residence time.

In practice, thermal decomposition of acetone was found to be negligible under experimental conditions. Small quantities of methane were produced after leaving 1 Torr of acetone in the cell for several minutes at 600K when the cell was first used at the elevated temperature, but the cell surface was apparently conditioned over the course of a few days and subsequently, experimental mixtures could be left in the heated cell for periods much longer than the experimental residence time, without significant decomposition.

(ii) Product and Photolysis Yields

Experiments at 600K employed 10 laser shots and 0.86 Torr acetone. Two laser intensity dependences (5<I<75 mJ) were performed at total pressures of 17.2 and 345 Torr He. In addition, ethylene scavenging experiments were performed at the higher pressure with a laser pulse energy of 46±8 mJ and ethylene partial pressures of up to 2 Torr.

Ethane yields were again independent of total pressure and added ethylene, and varied linearly with I, although for a given laser energy, the fractional photolysis of the acetone precursor per shot was a factor of 1.9 greater than at 300K, with $F_{600} = (8.1\pm1.3)\times10^{-3}$ mJ^{-1}. This increase in fractional photolysis presumably arises from a temperature dependence of the acetone extinction coefficient at 193.3 nm. As discussed in the Section 4.1, the ArF wavelength falls in a region of relatively low absorption between two fairly closely spaced features of a vibrational progression belonging to a Rydberg transition.

As observed at 300K, R_{MEK} (=[MEK]x100/[C_2H_6]) decreased with total pressure, but was greater than at the lower temperature for a given pressure and depended on laser intensity, increasing with decreasing I. The dependence of R_{MEK} on pressure and I is shown in Figure 4.24. A slight increase in R_{MEK} was observed when ethylene was added to the photolysis mixtures, although there was evidence for an additional product, possibly a C_5 hydrocarbon, which eluted from the column almost simultaneously with MEK.

Like MEK, methane was also found in somewhat greater yields than observed at room temperature, for a given pressure, and similarly

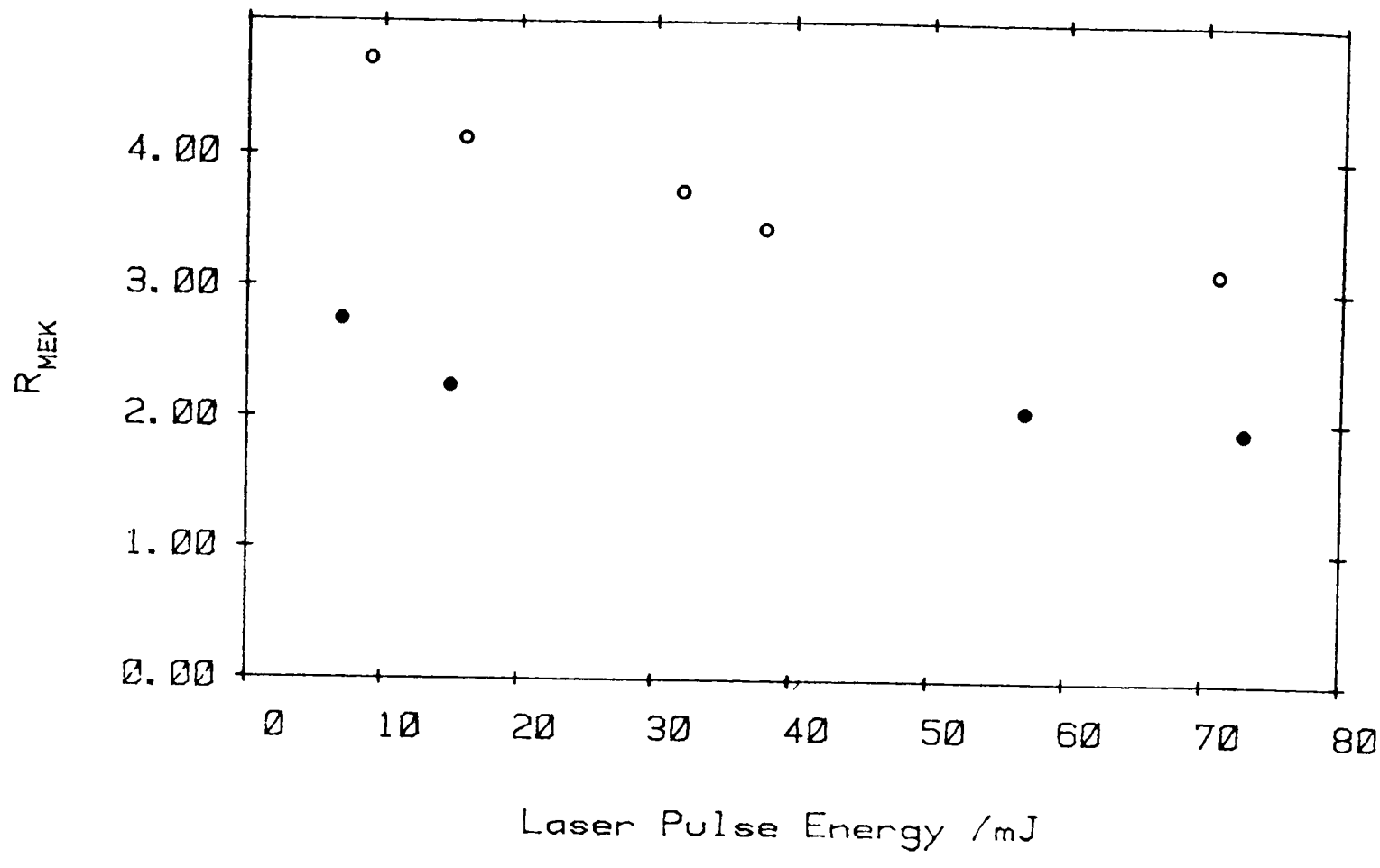

Figure 4.24. Dependence of R_{MEK} on Laser Pulse Energy, 600K.

Total pressure: ● 17.2 Torr He, o 345 Torr He.

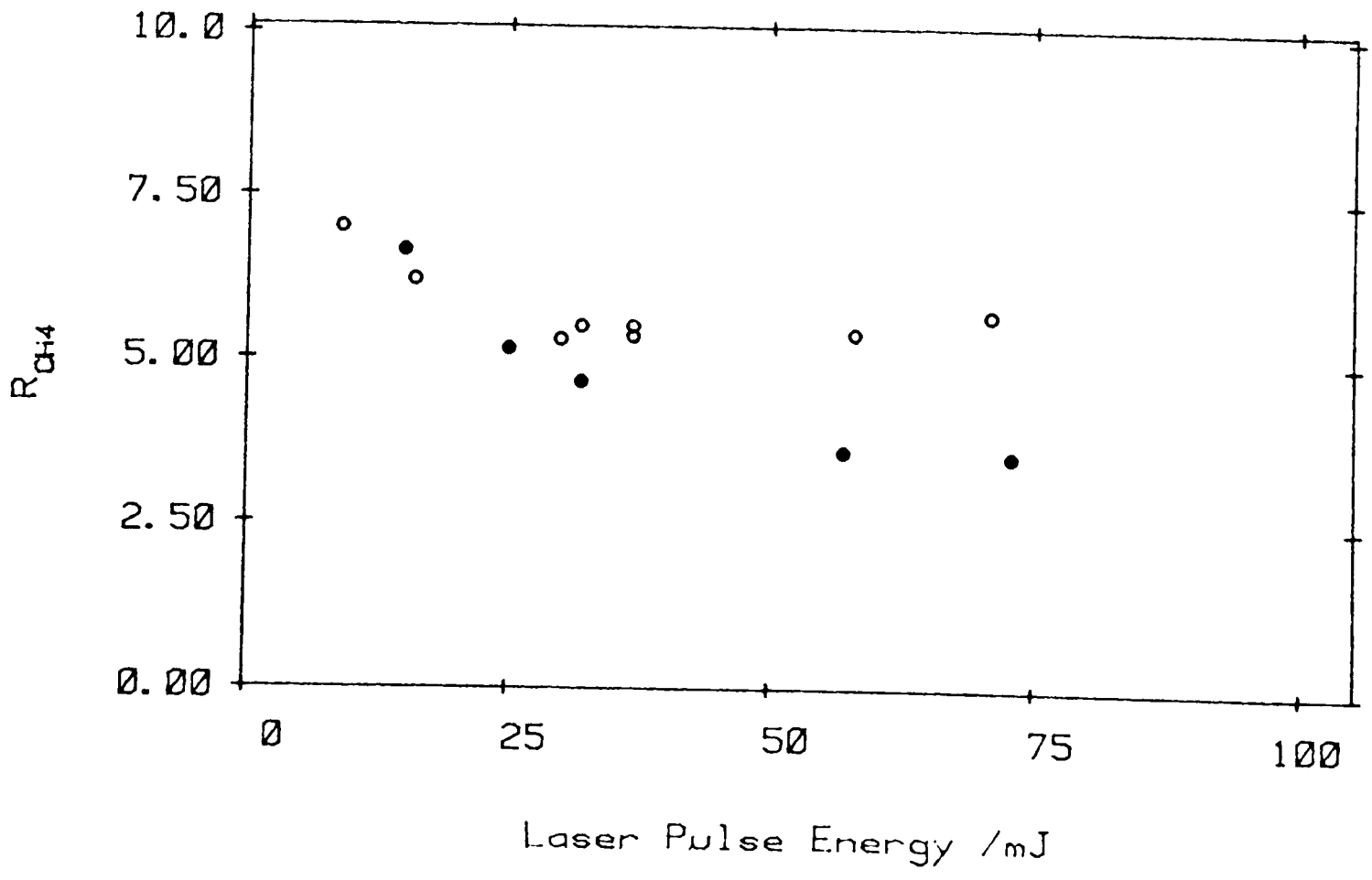

Figure 4.25. Dependence of R_{CH4} on Laser Pulse Energy, 600K.

Total pressure: ● 17.2 Torr He, o 345 Torr He.

R_{CH4} increased with pressure and decreasing laser intensity, as shown in Figure 4.25. The addition of ethylene to photolysis mixtures caused R_{CH4} to decrease rapidly up to 0.2 Torr C_2H_4 and then more slowly with increasing $[C_2H_4]$. A corresponding rapid initial rise in the yield of propane relative to ethane, R_{C3H8} was also observed, followed by an apparently linear increase in R_{C3H8} with $[C_2H_4]$. The dependences of R_{CH4}, R_{C3H8} and R_{C4H10} (see below) on $[C_2H_4]$ are shown in Figure 4.26.

Although not found in the absence of ethylene, n-butane was observed as a minor product in the scavenging experiments; R_{C4H10} increased linearly with with $[C_2H_4]$. In addition, small quantities of n-hexane ($R_{C6H14} < 0.6$), again not observed in the absence of ethylene, nor in the room temperature scavenging experiments, were found at high $[C_2H_4]$.

A non-linear intensity dependence of the yield of ethylene in the absence of scavengers experiments was again observed: R_{C2H4} increased in an approximately linear fashion from $\sim$0.2 at I = 10 mJ to $\sim$0.5 at I = 70 mJ and was independent of pressure. A linear fit to the experimental data gave $R_{C2H4} = (0.16\pm0.09) + (6.1\pm2.1)\times10^{-3}$ I, where, on the basis of the low temperature mechanism, the intercept and gradient refer respectively to the yields of molecular ethylene and ethylene produced via the photolysis of methyl radicals.

The minor products propane and allene, identified in the room temperature photolysis, were also observed at 600K, with somewhat increased yields. Both R_{C3H8} and R_{C3H4} were independent of pressure and laser intensity, with $R_{C3H8} = 0.13\pm0.08$ and $R_{C3H4} = 0.25\pm0.10$. R_{C3H4} was unaffected by the presence of ethylene.

Three additional minor products, not seen at 300K, were also

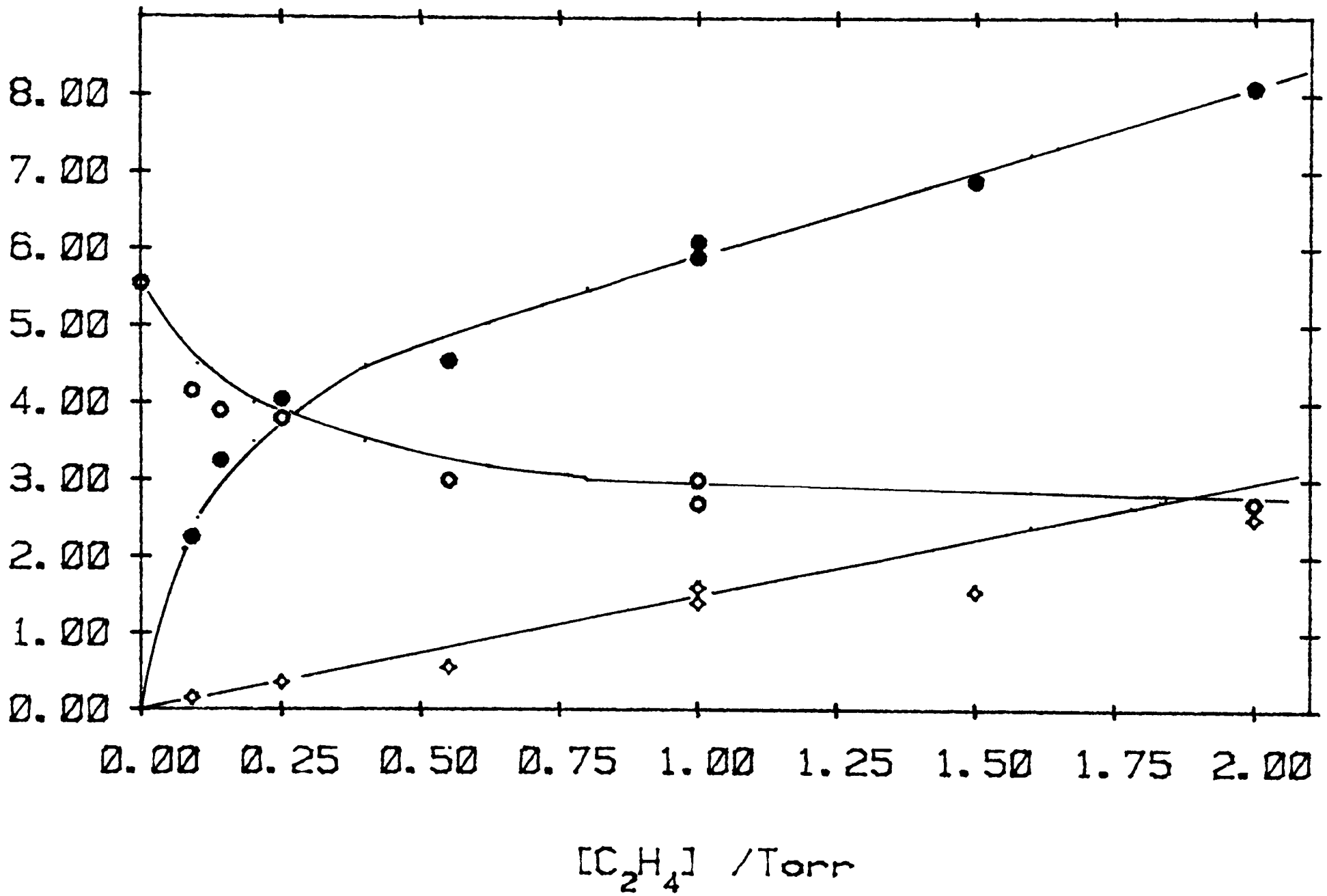

Figure 4.26. Dependence of Product Yields on $[C_2H_4]$, 600K.

Pressure 345 Torr He, I = 46±8 mJ.

o R_{CH4}, • R_{C3H8}, ◇ R_{C4H10}. Solid lines show simulated dependences, after fitting to initial hydrogen atom and methane concentrations (see text).

observed, in yields which were found to be independent of laser intensity, pressure and the presence of ethylene. The most rapidly eluting compound of the three was identified as propylene, with R_{C3H6} = 0.18±0.12. The other two minor products, which eluted at times corresponding to C_3 - C_4 hydrocarbons, were not identified, but were only present in yields similar to allene, assuming C_3 FID response factors.

Thus, with the exception of three very minor products, the end products seen in non-scavenging experiments at 600K were identical to those observed at room temperature and the photolysis scheme developed to account for the observed products at 300K should be largely applicable to experiments at the higher temperature.

The chief differences between the observed behaviour at 300K and 600K were found in the yields of methane and MEK relative to ethane. Both R_{MEK} and R_{CH4} increased with temperature and displayed a dependence on laser intensity at 600K, but not at 300K. These differences can be attributed to the radical - molecule reactions:

$$CH_3 + CH_3COCH_3 \xrightarrow{\quad} CH_4 + CH_2COCH_3 \qquad R6$$

$$H + CH_3COCH_3 \xrightarrow{\quad} H_2 + CH_2COCH_3 \qquad R7$$

which, although insignificantly slow at room temperature, have large temperature coefficients and contribute significantly to the overall kinetics at 600K. Pseudo-first-order loss rates for the removal of methyl radicals via R6 and hydrogen atoms via R7 are calculated, at 600K, to be 2.3 s^{-1} and 955 s^{-1} respectively, for an acetone partial pressure of 0.86 Torr. Although removal of methyl radicals by reaction with precursor molecules would still be very slow compared to removal by recombination at short times after the laser pulse, R6

would become more important at long reaction times and at low laser energies. Similarly, the reaction of hydrogen atoms with the precursor would be expected to be most important at low intensities. Table 4.8 lists the reactions and literature rate constants used in modelling the unscavenged experiments at 600K.

Table 4.8

Reactions and Rate Constants Used to Model the Photolysis of Acetone at 600K in the Absence of Radical Scavengers

Reaction	Rate Constant/ $molecule^{-1}cm^3s^{-1}$		Reference
	17.2 Torr	345 Torr	
R1	$2.3x10^{-11}$	$3.7x10^{-11}$	[26]
R2	$5.0x10^{-11}$	$5.0x10^{-11}$	[116]
R3	$4.0x10^{-11}$	$5.0x10^{-11}$	MVR
R4	$1.0x10^{-10}$	$1.0x10^{-10}$	Estimate
R5	$1.7x10^{-11}$	$1.7x10^{-11}$	nC_3H_7[25]
R6	$1.6x10^{-16}$	$1.6x10^{-16}$	[197]
R7	$6.9x10^{-14}$	$6.9x10^{-14}$	[196]

The presence of small quantities of n-butane and n-hexane in the scavenging experiments indicated that the addition of methyl radicals to ethylene was not negligible at 600K and that reactions involving the n-propyl radical would have to be included in the reaction scheme used to model the scavenging experiments. The reactions and rate constants added to the reaction scheme above, to allow for the presence of ethylene, are listed in Table 4.9.

Table 4.9

Additional Reactions and Rate Constants Used to Model Ethylene Scavenging Experiments at 600K

Reaction	Rate Constant/ $molecule^{-1}cm^3s^{-1}$	Reference
$H + C_2H_4 \Rightarrow C_2H_5$	3.3×10^{-12}	Chapter 2
$CH_3 + C_2H_5 \Rightarrow C_3H_8$	5.5×10^{-11}	Mean value rule
$CH_3 + C_2H_4 \Rightarrow C_3H_7$	9.0×10^{-16}	[217]
$C_3H_7 \Rightarrow CH_3 + C_2H_4$	$13.7\ s^{-1}$	[217]
$CH_3 + C_3H_7 \Rightarrow C_4H_{10}$	5.0×10^{-11}	Mean value rule
$2\ C_3H_7 \Rightarrow C_6H_{14}$	1.7×10^{-11}	[25]
$C_2H_5 + C_3H_7 \Rightarrow C_5H_{12}$	3.6×10^{-11}	Mean value rule

The limited pressure range studied at 600K, and complications caused by the abstraction reactions R6 and R7, precluded estimation of the yield of photolysis channel P2 from the observed MEK yields. The yields of hydrogen atoms and molecular methane relative to ethane could, however, be determined from the dependence of R_{CH4} and R_{C3H8} on $[C_2H_4]$. The rate constants listed above for the reactions of hydrogen atoms with methyl radicals and ethylene suggest that for an initial methyl radical concentration of 1×10^{14} cm^3 (=46mJ), hydrogen atoms should react almost exclusively with ethylene, for ethylene partial pressures above 0.4 Torr, as demonstrated by the rapid initial rise in R_{C3H8} and corresponding smaller initial fall in R_{CH4} with increasing $[C_2H_4]$ (see Figure 4.26). The discrepancy between the magnitudes of the rise in R_{C3H8} and fall in R_{CH4} is a consequence of the significant fraction of hydrogen atoms which react with the

precursor rather than by recombination with methyl radicals in the unscavenged experiments. The apparently linear increase in R_{C3H8} with $[C_2H_4]$ above 0.4 Torr C_2H_4, is presumably caused by photolysis of the scavenger. Although very little photolysis of ethylene was noticed at room temperature, the absorption coefficient of ethylene at 193.3 nm increases with temperature. As was discussed in Chapter 3, both hydrogen atoms and vinyl radicals are produced by the photolysis of C_2H_4 at 193.3 nm, with $([H]/[C_2H_3])_o \sim 5$. A small, linear increase in R_{C3H6} with $[C_2H_4]$ was observed, with a slope compatible with the above ratio, confirming that photolysis of the precursor was indeed responsible for the increased yield of hydrogen atoms with $[C_2H_4]$.

For each scavenging experiment, best fit initial concentrations of hydrogen atoms and methane were obtained from the observed yields of ethane, methane and propane by numerical integration [4] of the reaction scheme described above. As can be seen in Figure 4.27, the fitted initial hydrogen atom concentrations were reasonably linear in $[C_2H_4]$, with an intercept corresponding to the yield of hydrogen atoms in the absence of ethylene, giving $R_H = 4.18 \pm 0.24$, and the fitted yields of molecular methane showed no dependence on $[C_2H_4]$, with $R_{CH4o} = 2.01 \pm 0.46$. Correcting for the hydrogen atom yield produced via the photolysis of methyl radicals at 46 mJ gives $R_H = 3.62 \pm 0.31$.

The simulated dependences of R_{C3H8}, R_{CH4} and R_{C4H10} on $[C_2H_4]$ using the fitted values of $([H]/[CH_3])_{t=o}$ and $([CH_4]/[CH_3])_{t=o}$ and an initial methyl radical concentration of 1×10^{14} cm^3 are shown together with the experimental data in Figure 4.26. As might be expected, the observed and predicted values of R_{CH4} and R_{C3H8} are in close agreement. The simulated and observed yields of n-butane are also in

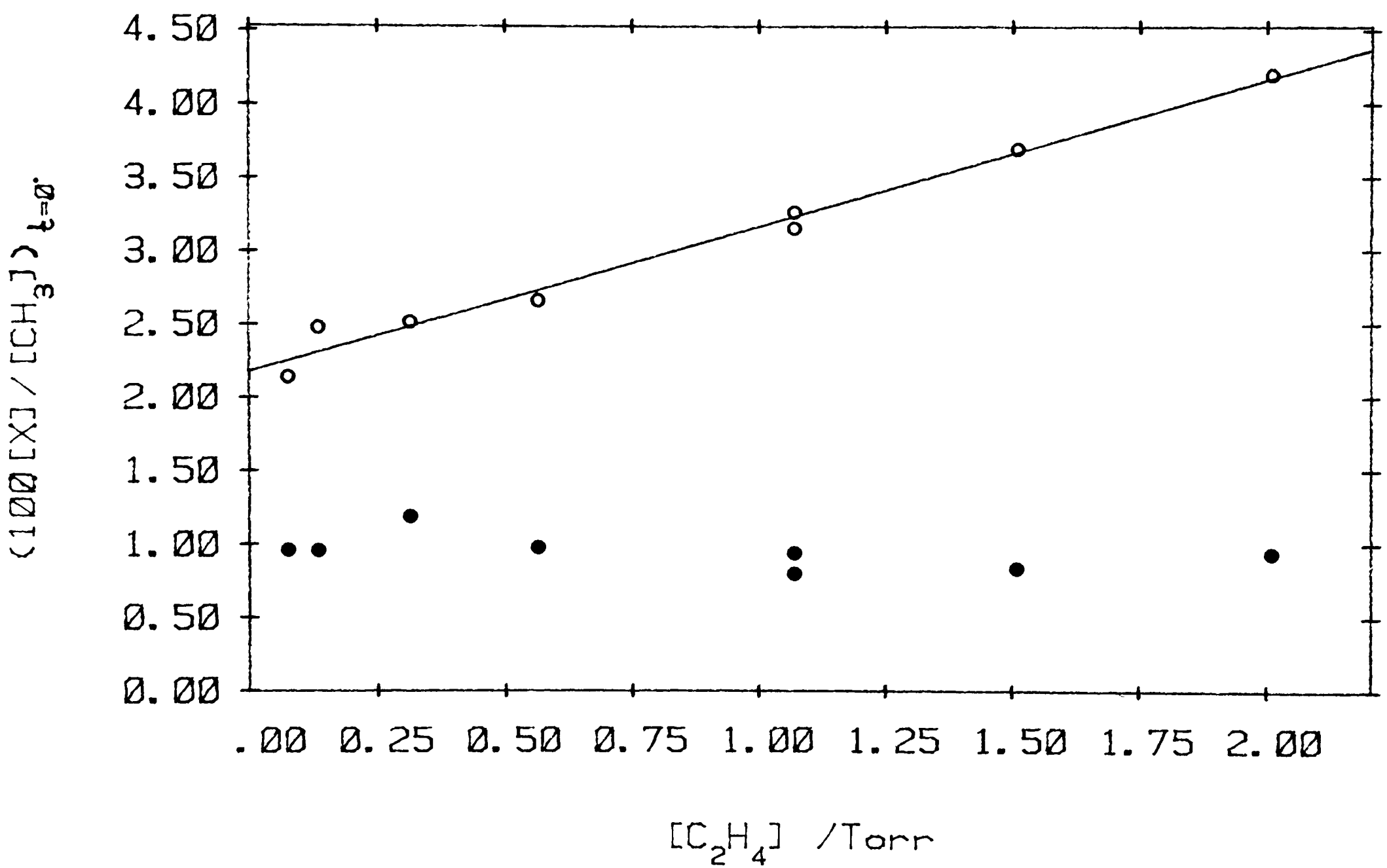

Figure 4.27. Fitted Values of $([H]/[CH_3])_o$ and $([CH_4]/[CH_3])_o$ vs. $[C_2H_4]$, 600K. o H, ● CH_4.

reasonable ageement, supporting the assumption that n-butane was formed via the addition of methyl radicals to ethylene. The slight discrepancy between the predicted and observed values of R_{C4H10} is not significant, given that the rate constant for addition of methyl radicals to ethylene is estimated to be correct only to an order of magnitude [217].

As a further check on the values of R_H and R_{CH4o} obtained from the scavenging experiments, the dependence of R_{CH4} on laser intensity and pressure was simulated using the rate constants in Table 4.8. The removal of hydrogen atoms at the cell walls was included in the simulations; its rate was calculated as described earlier in the chapter and reduced by the 50% found to bring the 300K simulated and experimental methane yields into agreement at all pressures. The results of the simulations are shown together with the experimental values of R_{CH4} in Figure 4.28. The experimental upturn in R_{CH4} at low intensities is reproduced at both pressures, although the absolute experimental values of R_{CH4} are somewhat underestimated by the simulations. Increasing the value of k_6 by a factor of two brings the predicted and experimental values of R_{CH4} into close agreement. Given the uncertainty in this indirectly measured rate constant, a change of a factor of two in its value is not significant. Alternatively, an increase in R_{CH4} would result, if the thermal decomposition of the acetonyl radical were not insignificant at 600K.

The experimental behaviour at 600K is thus consistent with the photolysis mechanism proposed to explain the results at room temperature, if the reactions of hydrogen atoms and methyl radicals with the precursor are allowed for.

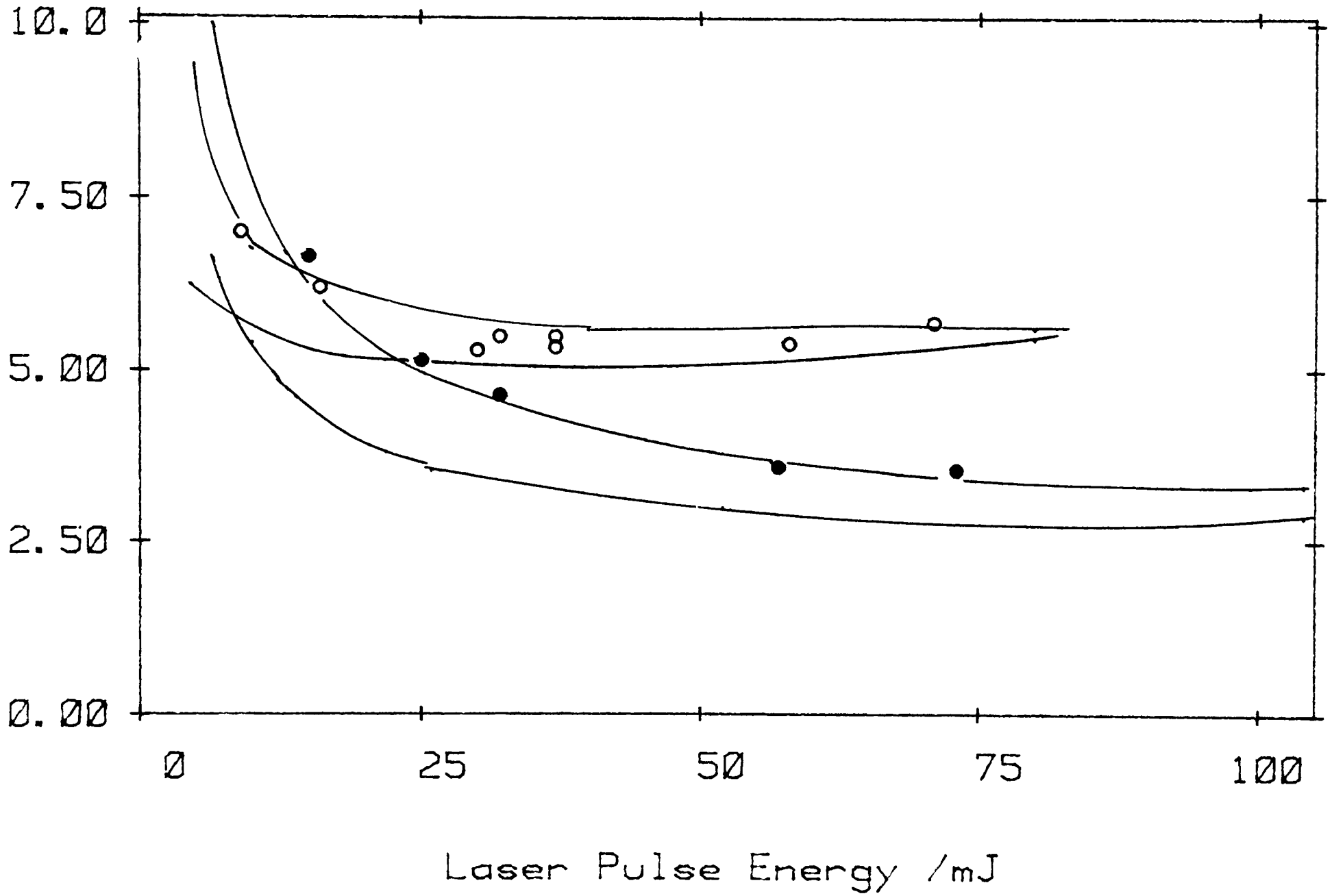

Figure 4.28. Experimental and Simulated Dependences of R_{CH4} on Laser Pulse Energy at 600K. o 17.2 Torr, o 345 Torr.

Bottom curve of each pair: Rate constants taken from Table 4.8
Top curve of each pair: Rate constants as in Table 4.8, with k_6x2.

4.4 Summary

Under all conditions employed in the present study by far the most important photolytic channel in the 193.3 nm photolysis of acetone was that producing methyl radicals and carbon monoxide:

$$CH_3COCH_3 \xrightarrow[193.3\ nm]{h\nu} CH_3 + CO + CH_3 \qquad P1$$

Methyl radicals accounted for more than 95% of the radical products of the photolysis. At least four other primary dissociative processes were identified. Of the minor photolysis proceses, the channel producing hydrogen atoms and acetonyl radicals, and that producing methane and ketene were most important.

$$CH_3COCH_3 \xrightarrow[193.3\ nm]{h\nu} H + CH_2COCH_3 \qquad P2$$

$$CH_3COCH_3 \xrightarrow[193.3\ nm]{h\nu} CH_4 + CH_2CO \qquad P3$$

Photolysis channels P1 - P3 accounted for > 99% of the observed photolysis products under all conditions. The yields Φ_i at 300 and 600K for the identified primary processes and normalised to unity, are summarised in Table 4.10.

Table 4.10

Yields for Primary Processes Occurring in the 193.3 nm Photolysis of Acetone

Photolysis Products		Φ_{300K}	Φ_{600K}
P1	$CH_3 + CO + CH_3$	0.954	0.942
P2	$H + CH_2COCH_3$	0.028	0.033
P3	$CH_4 + CH_2CO$	0.015	0.018
P4	Minor Channels	0.003	0.007

Although no significant pressure dependence of Φ_1 or Φ_4 was observed, Φ_2 and Φ_3 were obtained from data at the highest pressure employed at each temperature. As the yield of P1 is much greater than the yields of all the other channels, changes in Φ_2 and Φ_3 with pressure would not noticeably affect Φ_1; it is therefore possible that Φ_2 and particularly Φ_3, are somewhat dependent on pressure.

In addition to the primary, single - photon photolysis channels, a minor secondary photolysis process, involving the absorption of a second 193.3 nm photon by vibrationally excited methyl radicals, produced via P1, was also observed.

$$CH_3\ (V_2>4) \xrightarrow[193.3\ nm]{h\nu} CH_2 + H \qquad S1$$

The fraction of methyl radicals photolysed in this way depended linearly on laser intensity, with $([CH_2]/[CH_3])t=o$ given by $(0.31\pm0.21)F$ at 300K and $(0.48\pm0.19)F$ at 600K, where F is the fractional photolysis of the precursor per laser pulse.

In conclusion, the photolysis of acetone at 193.3 nm has been

shown to provide an extremely clean source of methyl radicals suitable for use in high temperature studies of methyl radical reaction rates. As a result of the present study, acetone has been successfully used as a methyl radical source to study the reaction between methyl radicals and oxygen at temperatures up to 825 K in this laboratory [218].

Of the minor photolysis channels, that producing hydrogen atoms, P2, is of most importance and interest. If the simple reaction scheme developed in this chapter (R1-R7) is correct, in that the only significant second-order loss process for hydrogen atoms is by reaction with methyl radicals, then the acetone system provides a means of directly measuring the rate of this very important reaction. If one assumes that the second-order methyl decay is unaffected by the presence of small quantities of other radicals, then the hydrogen atom decay can be expressed analytically, and k_2 could, in principle, be extracted from time-resolved hydrogen atom decay profiles using standard methods of data analysis, if the initial methyl radical concentration is known. An apparatus has been developed at Oxford, which enables both hydrogen atom and methyl radical concentrations to be monitored simultaneously, following excimer laser photolysis of a suitable precursor. The use of the 193.3 nm photolysis of acetone in the first direct study of the H + CH_3 reaction is described in Reference 219.

Chapter Five

The Pyrolysis of Ethane to High Conversions

5.1 Introduction

The pyrolysis - or cracking of hydrocarbons is a process of major importance to the petrochemical industry. It is the means by which the naphtha fraction of crude oil, consisting typically of C_4 - C_{12} saturated, unsaturated and aromatic hydrocarbons, is converted largely to hydrogen and small, unsaturated hydrocarbons - particularly ethylene. These small unsaturates form the chemical basis for the commercial manufacture of polymers.

Because of the large number of molecular species involved, naphtha cracking is an extremely complicated chemical process; considerations such as heat transfer and non-uniform temperature gradients serve to increase still further the difficulty of modelling hydrocarbon pyrolysis in practical situations. However, despite the large number of molecular species present, the number of important radical species is restricted at cracking temperatures by the instability of the larger radicals with respect to thermal decomposition. In practice, only saturated radicals up to C_2 and unsaturated radicals up to C_3 will be present in significant concentrations. Consequently, the study of the pyrolysis of simple hydrocarbons, such as ethane and propane should provide a good basis for the determination of those radical species and those reactions which control the overall conversion and the product distribution in the pyrolysis of heavier hydrocarbons.

Ethane cracking is used as an industrial source of ethylene and

provides a relatively simple system with which to test models of hydrocarbon pyrolysis. The pyrolysis of ethane to low conversions has frequently been studied by end product analysis methods [81,157,220-224]. Under conditions of low product concentrations where radical reactions with the products can be neglected, the pyrolysis can be adequately described by a simple chain mechanism:

C_2H_6 =====> $CH_3 + CH_3$

$CH_3 + C_2H_6$ =====> $CH_4 + C_2H_5$

C_2H_5 =====> $C_2H_4 + H$

$H + C_2H_6$ =====> $H_2 + C_2H_5$

$C_2H_5 + C_2H_5$ =====> $N\text{-}C_4H_{10}$, $C_2H_4 + C_2H_6$

Such experiments have been primarily concerned with the rate constants for the thermal decomposition of ethane and the ethyl radical, and have generally employed conversions of less than 1% and temperatures of below 1000K to minimise thermal decomposition of termination products. Lin and Back [221] did, however, perform experiments at up to 8% conversion, in order to determine some of the products of reactions between radicals and the initial pyrolysis products.

In industrial cracking furnaces, temperatures approaching 1200K are used and ethane conversions of 80 - 90% can be achieved. Under such conditions, reactions of radicals with the products of the initial pyrolysis will be of great importance in determining the final conversions and the product distributions obtained. Ethane pyrolysis at high temperatures (1200 - 4800K) has been the subject of several shock tube studies [207,225-227]. Laser schlieren and/or laser absorption were employed to follow the course of reaction, with

gas chromatographic product analysis in some cases. Again, the emphasis has largely been placed on the early stages of reaction, although Hidaka et al. [227] attempted to model the product distribution at up to 69% conversion in terms of a simple reaction scheme containing 15 reactions. Sensitivity analysis showed that the degree of conversion and product distribution was very dependent on the choice of values for a number of rate constants. The production and removal of the vinyl radical was not treated in great detail, however.

Although reactions of hydrogen atoms and the smaller (C_1 - C_2) carbon containing radicals are thought to provide the main chain propagation steps in hydrocarbon pyrolysis, allyl radicals are believed to build up to large concentrations, particularly in the pyrolysis of C_3^+ hydrocarbons, because of their low reactivity and high thermal stability [228]. Such high concentrations increase the possibility of chain termination and reduce the overall conversion at a given temperature, relative to that observed for ethane pyrolysis.

This chapter describes ethane pyrolysis experiments at conversions of up to 85%, performed under steady-state conditions using a jet-stirred reactor and at temperatures appropriate to industrial cracking furnaces. The effect of the presence of allylic radicals is investigated by co-cracking ethane with small added quantities of propylene.

A kinetic model is developed which qualitatively reproduces the experimental behaviour. It is demonstrated that the model predictions are very sensitive to a number of poorly defined rate constants.

5.2 Experimental

The experimental work presented in this chapter was performed at I.C.I. Wilton. The author gratefully acknowledges the advice, expertise and assistance provided by the Wilton staff during the course of this study.

The apparatus used in this study is shown schematically in Figure 5.1. Dilute mixtures of ethane and ethane/propylene in nitrogen were flowed through a quartz jet-stirred reactor contained in a furnace. The output from the reactor passed, in part, through a pneumatically-driven gas sample valve to atmosphere. Gas samples were injected from the valve into the microcomputer-controlled chromatograph for analysis. A more detailed description of the individual components and the operating conditions of the apparatus is given below.

5.2.1 Jet-Stirred Reactor

The jet-stirred reactor, made entirely of quartz and of a construction based on a design by Bush [229], is shown in Figure 5.2. The incoming gas was fed into the reactor through a 1/32" diameter jet orifice, set midway between the centre of the reactor and its outside wall and midway between the top and bottom of the cell, such that the gas jet from the orifice was at an angle of approximately 70° to a radius drawn through the orifice. Gas left the reactor through a 1/16" diameter exit tube set in the reactor wall at the position of the cylidrical axis of the reactor. An inset to hold a thermocouple was situated opposite the reactor exit. Both the thermocouple inset and the reactor exit were positioned so as to

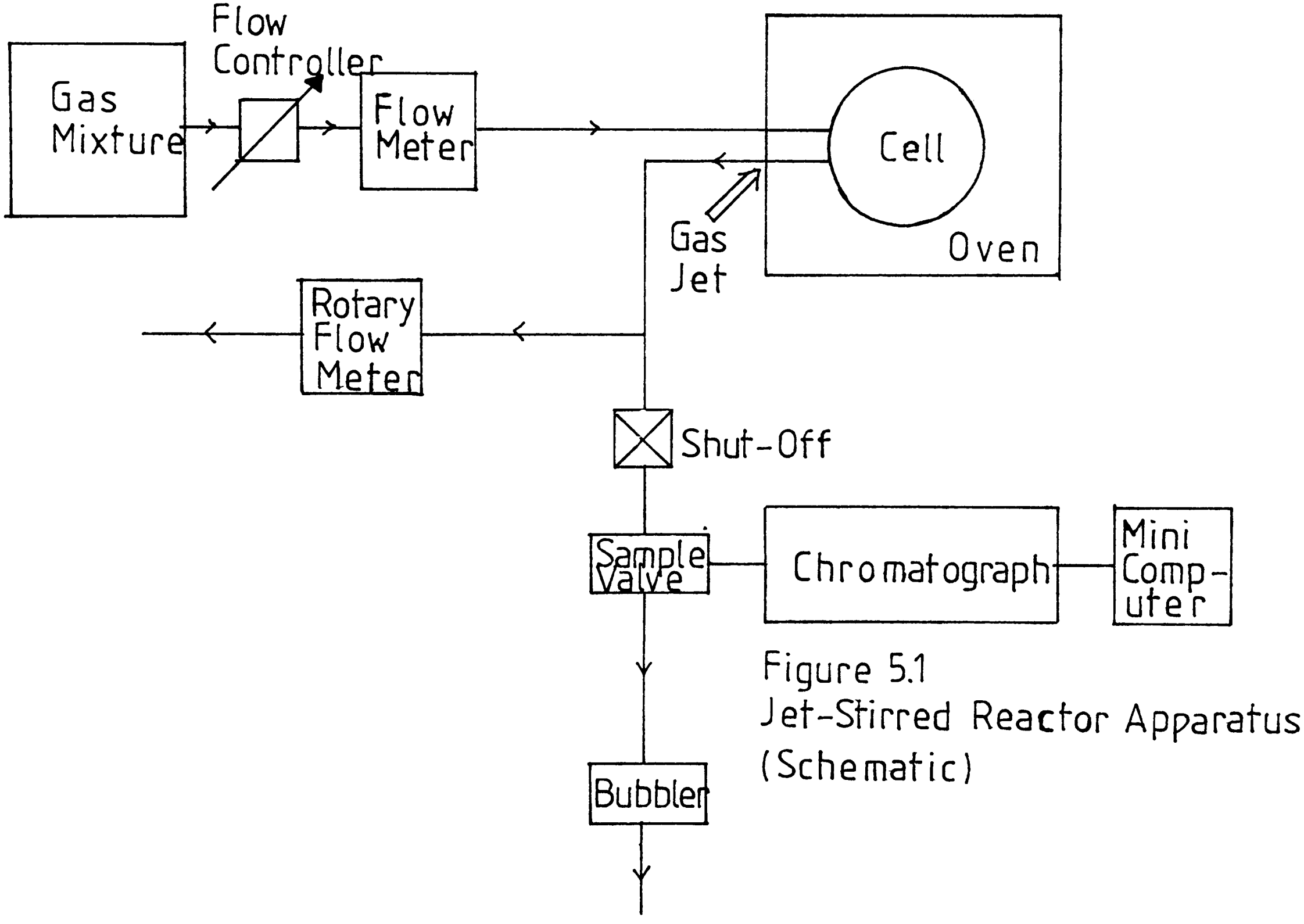

Figure 5.1
Jet-Stirred Reactor Apparatus
(Schematic)

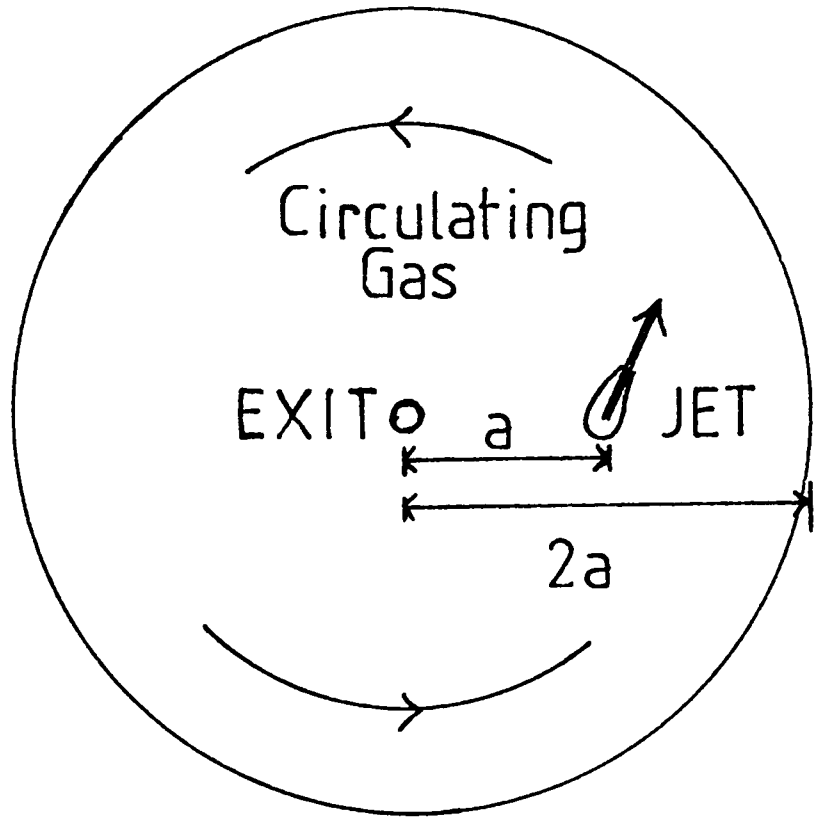

a= 1.5 cm

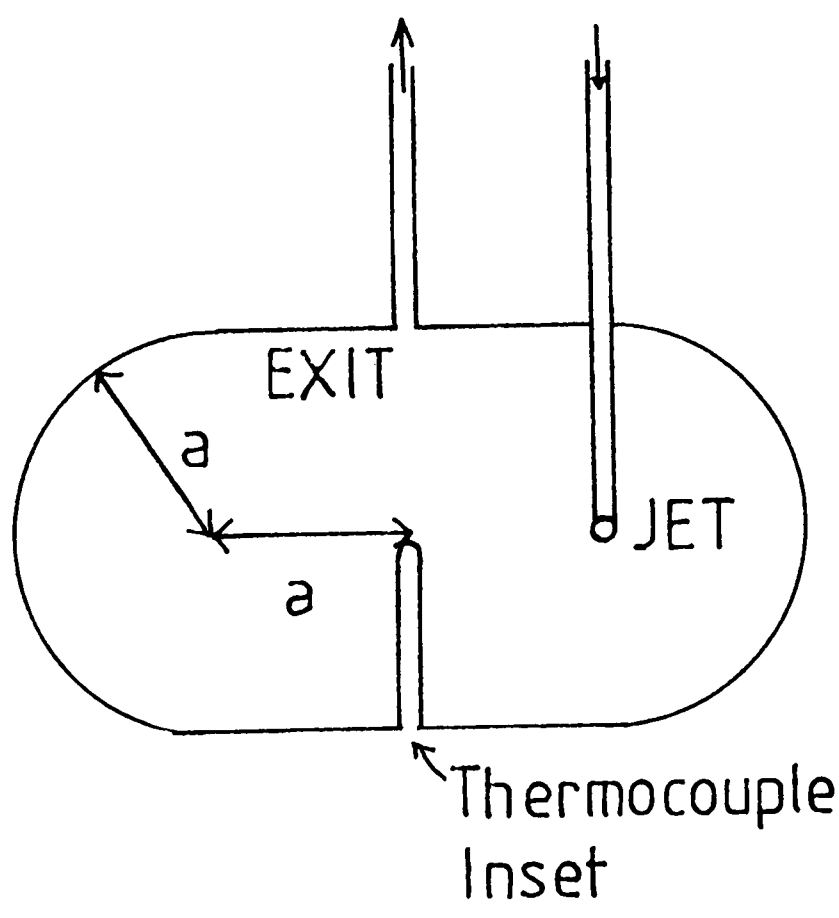

Figure 5.2
Jet-Stirred Reactor

minimise any disturbance of the flow of gas around the reactor.

The internal dimensions of the reactor were determined by the requirement that the incoming gas be thoroughly and rapidly mixed with the already circulating gas. The ratio of the circulating flow, Q, to the incoming gas flow, Q_O, is given by:

$$Q/Q_O = 0.24(L/d) \qquad \text{for } L/d > 10$$

The above expression gives a recirculation ratio of 28.6 for the present reactor. Physically, the recirculation ratio can be identified with the average number of circuits a gas molecule will make around the cell before being removed at the exit. Macroscopic mixing is controlled by bulk transport of the incoming gas around the reactor and by turbulent dispersion caused by the perpendicular velocity component of the fluid jet. Diffusive mixing on a molecular level is assumed. An individual jet is regarded as spreading out symmetrically about its centre line, until its edge hits the reactor wall, where it loses its perpendicular velocity and hence ceases to mix efficiently. The reactor design was such that the jet, spreading out at an angle of 20°, reached the reactor sides after travelling once around the reactor. Furthermore, the distance of the jet from the centre of the reactor was made equal to the radius of curvature of the outer wall, so that the spreading jet reached all surfaces simultaneously, thereby ensuring even mixing throughout the cell.

Bush analysed the gas flow and the mixing throughout a reactor of similar design, assuming that the reactor was toroidal in shape, and found good agreement between calculated and experimental dispersions. It was demonstrated that mixing was more than 95% complete at times longer than 6% of the average residence time.

5.2.2 Temperature Control and Measurement

The reactor was mounted in an electric muffle furnace, with the reactor inlet and outlet tubes inserted through holes in the furnace door. In order to minimise any reaction outside the furnace, a jet of compressed air was used to cool the outlet tube, at the point where it emerged from the furnace. The holes in the furnace door were packed with Kaowool insulation to minimise temperature gradients.

The temperature in the reactor output tube and inside the reactor was compared to that measured by the external thermocouple by inserting a second calibrated thermocouple into the output tube whilst nitrogen was flowed through the reactor at typical experimental flow rates. For an external thermocouple reading of 1120K, the temperature drop across the reactor, from the region closest to the back of the furnace to the output region, was 20K, independent of gas flow. The temperature gradient across the reactor was uniform within experimental error and the temperature at the centre of the reactor, which was 7±2K below the temperature measured by the external thermocouple, was consequently taken to be the mean gas temperature.

5.2.3 Gases, Flow Control and Calculation of Residence Times

Hydrocarbon mixtures in nitrogen ("White Spot", dry N_2, O_2<2ppm) were made up in 10l gas cylinders to a total pressure of 100 p.s.i.g. and were left overnight to ensure thorough mixing. The hydrocarbons used, i.e. ethane and propylene, were used as output from the plant cracking furnaces. Chromatographic analysis showed that the plant ethane contained 0.5% propylene by volume and trace quantities of

n-butane and 1-butene. The much smaller amounts of propylene employed contained negligible quantities of other hydrocarbons.

The flow of gas through the apparatus can be understood by reference to Figure 5.1. Pyrolysis mixtures entered the reactor from a gas cylinder via a pressure controller and a flow meter, the flow through which was controlled by a needle valve. Downstream of the reactor, the output gas vented through a rotary flow meter to atmosphere, with a bleed-off to the gas sample valve of the analysis system. The upstream flow meter was calibrated against the volume flow read on the rotary gas meter with the bleed closed. At low flow rates, where the flow meter reading was less than 10% of full scale and hence subject to considerable uncertainty, the flow through the reactor was determined, for each experiment, using the rotary gas meter. The mean residence time for a given flow rate was calculated from the equation:

$$\tau = (\text{Reactor Volume} / \text{Flow Rate}).(300 / \text{Reactor Temperature})$$

Correction for the reactor temperature was necessary, because the rotary flow meter measured volume flow under ambient conditions.

The above expression assumes that the gas in the reactor is at atmospheric pressure, although the reactor pressure would be slightly above atmospheric, if restrictions in the reactor output tube and the gas lines were important. Pressure gradients along the nylon tubes downstream of the reactor were made negligible by using 1/4" i.d. tubing; elsewhere in the apparatus 1/8" i.d. tubing was used for gas lines. The pressure drop along the 1/16" i.d. reactor output tube was calculated, using the Poiseuille formula [173] for viscous flow, to be less than 2% of the reactor pressure under all experimental

conditions. The reactor pressure was thus taken to be atmospheric.

The volume of the cell was determined to be 47.6 cm^3, from the difference in weight of the reactor when empty and when filled with water.

5.2.4 Chromatography

Chromatographic analyses were performed on a DEC LSI 11-02 - based GC / minicomputer system, developed at I.C.I. Wilton. Extensive calibrations had shown that the measured product yields should be accurate to within 2%. Analyses were performed for H_2, C_1-C_4 hydrocarbons and aromatic hydrocarbons. The chromatograph contained a number of columns, the flow of N_2 carrier gas through which was controlled by pneumatically-driven valves, actuated by the minicomputer. The columns used for the various separations are listed below.

H_2:

(i) 3m x 1/8" Porapak Q 50/80 at 80°C.

(ii) 3m x 1/8" Porapak Q 50/80 at 80°C.

C_1-C_3 Hydrocarbons:

(i) 1m x 1/8" Picric Acid on Carbopak Graphitised Carbon 80/100 at 50°C.

(ii) 5m x 1/8" Phenylisocyanate on Porasil C 80/100 at 50°C.

C_4 Hydrocarbons:

(i) 1m x 1/8" Picric Acid on Carbopak Graphitised Carbon 80/100 at 50°C.

(ii) 2m x 1/8" Picric Acid on Carbopak Graphitised Carbon 80/100 at 50°C.

(iii) 20cm x 1/8" Phenylisocyanate on Porasil C 80/100 at 50°C.

Aromatics:

(i) 20cm x 1/8" 5% OV101 80/100 at 90°C.

(ii) 2m x 1/8" 22.5% CEF on Chromosorb P 100/120 at 90°C.

(iii) 1m x 1/8" 20% Tris on Chromosorb P 60/80 at 90°C.

5.3 Results

5.3.1 Ethane Cracking Experiments

Experiments in which ethane, diluted to 5±1% by volume in nitrogen, was pyrolysed without added propylene, were performed at temperatures of between 973 and 1148K, with residence times ranging from 0.38 to 1.25 seconds. The ethane concentration was systematically varied from 2.0 to 5.2% at 1118K.

The major identified products were H_2 > C_2H_4 >> CH_4 > C_2H_2 > C_4H_6 > C_6H_6 in typical molar ratios of 50 : 45 : 7 : 3 : 0.6 : 0.1 for a 1s residence time at 1118K. In addition, small quantities (<0.1%) of N-C_4H_{10}, 1-C_4H_8, and $C_6H_5CH_3$ were observed. The hydrogen and carbon balances were checked for each experiment; they were found to be randomly scattered about zero and never exceeded ±5%, suggesting that all the major products were detected.

The conversion of ethane into products increased with temperature and residence time, as shown in Figure 5.3. The fractional molar product yields, F_X ($=100[X]/([C_2H_6]_o-[C_2H_6])$), at 1118K, are shown as a function of conversion in Figure 5.4. The

Figure 5.3. Dependence of Ethane Conversion on Temperature and Residence Time.

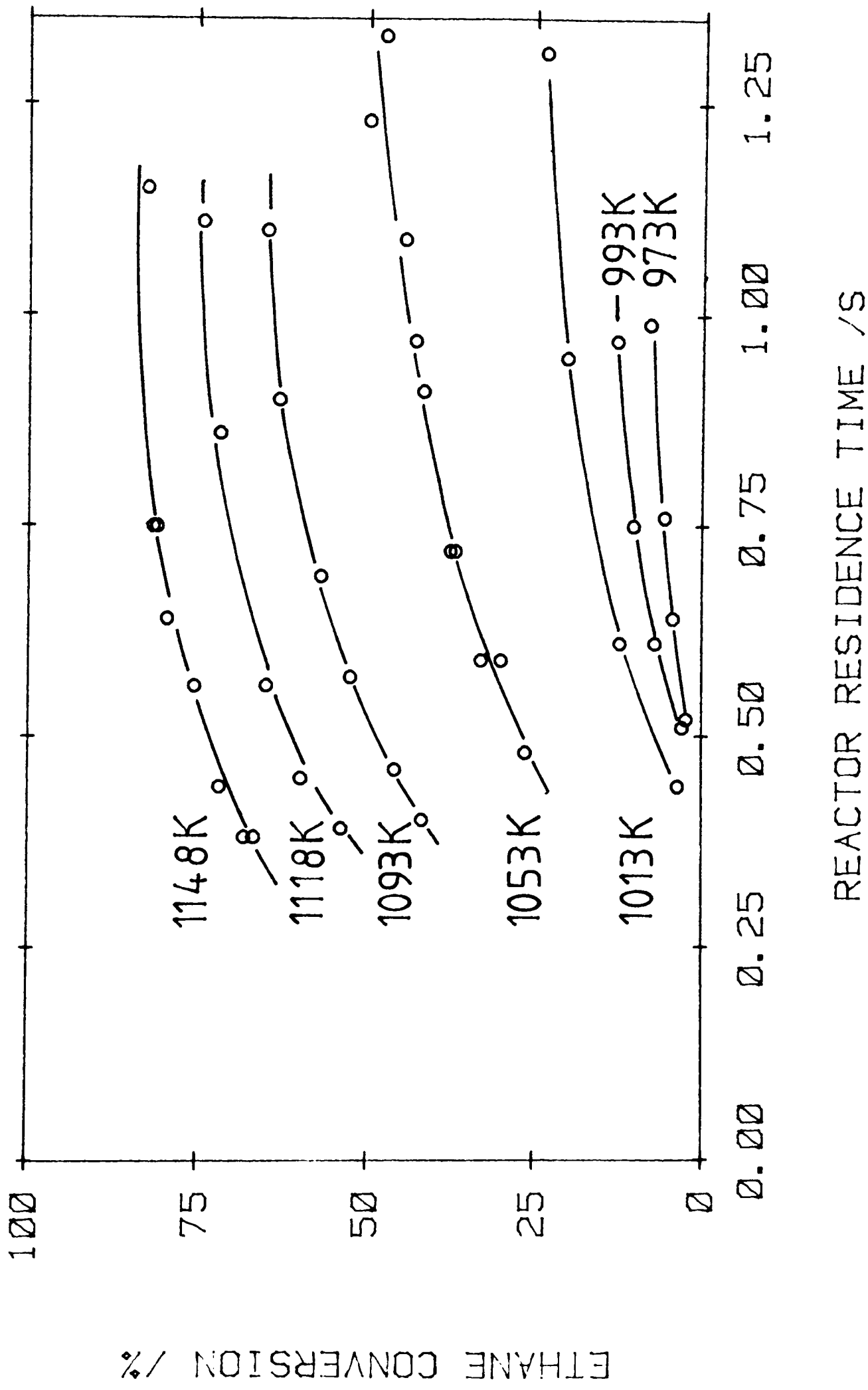

Figure 5.4. Dependence of Fractional Product Yields on the Degree of Ethane Conversion at 1118K. $F_X = 100[X]/([C_2H_6]_o - [C_2H_6])$.
o = H_2, ◇ = C_2H_4, ▷ = CH_4, ◁ = C_2H_2, ● = C_4H_6.

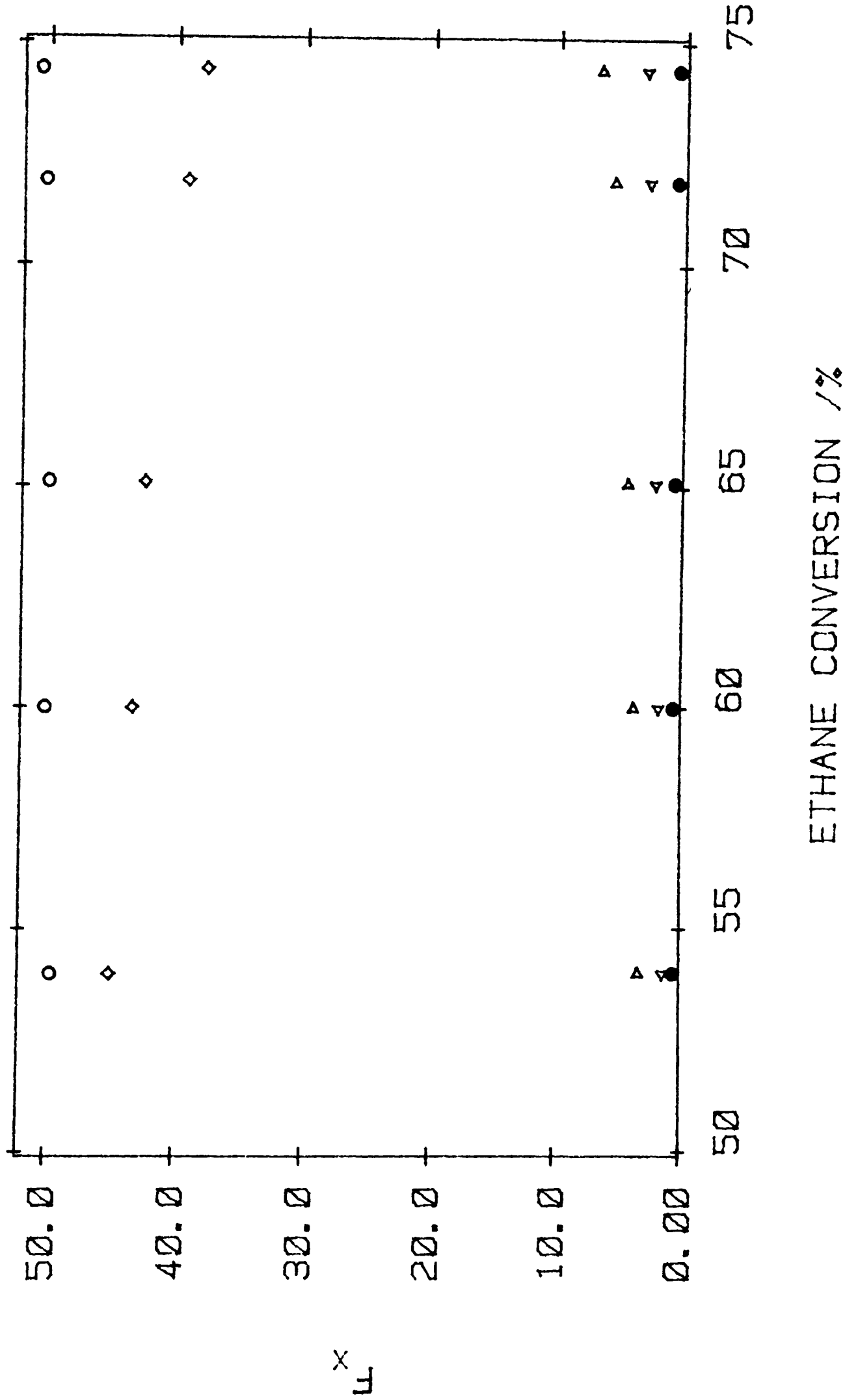

fractional hydrogen yield, F_{H2}, was virtually independent of temperature and conversion; hydrogen accounted for almost exactly half of the products by mole. A decrease in F_{C2H4} with increasing conversion and temperature, was accompanied by an increase in the minor product yields, particularly F_{C2H2} and F_{CH4}, suggesting that the minor products were formed, at least in part, via radical attack on the ethylene product.

Varying the initial ethane concetration by over a factor of two produced only minor changes in the observed behaviour. For a given residence time, the degree of conversion decreased slightly with increasing $[C_2H_6]_o$ at short residence times, but was independent of $[C_2H_6]_o$ for residence times >0.8s. Of the fractional product yields, only F_{CH4} and F_{C2H2} displayed any dependence on $[C_2H_6]_o$, respectively decreasing and increasing by 20-30%, with a reduction in $[C_2H_6]_o$ from 5% to 2% of the input gas mixture.

Over the course of a few pyrolysis runs, a grey carbonaceous deposit was observed to build up on the surfaces of the reactor. This deposit could be removed by passing air through the reactor at experimental temperatures. Immediately after decoking, ethane conversions were found to be reduced by ~10% but rapidly returned to normal. During this period of reduced conversion, F_{H2} was reduced by approximately 2%.

5.3.2 Ethane / Propylene Co-cracking Experiments

Experiments in which ethane was pyrolysed in the presence of added propylene were performed at temperatures of 1053, 1093 and 1118K. $([C_3H_6]/[C_2H_6])_o$ ratios of 0.05 and 0.1 were employed. The $([C_3H_6]/[C_2H_6])_o$ ratio in experiments where no propylene was added

was ~0.005, owing to a small propylene impurity in the ethane, as was discussed in Section 5.2.3. Figure 5.5 shows the effect of added propylene on conversion at 1093K. Ethane conversion was reduced at all temperatures by the addition of propylene to the pyrolysis mixtures, the effect becoming less pronounced with increasing temperature. The degree of conversion of the added propylene, was found to be somewhat higher than the corresponding ethane conversion, for a given set of experimental conditions, as shown in Figure 5.6. The propylene conversion in experiments with no additional propylene, beyond the small impurity contained in the ethane, was much less sensitive to temperature and residence time, as can be seen by reference to the experimental data, which is listed in Appendix 6.

Hydrogen and methane were the only products which were very sensitive to the presence of added propylene, as shown in Figure 5.7, for the data at 1118K. F_{H2} and F_{CH4} respectively increased and decreased with $[C_3H_6]_O$. No new products were observed and although analysis for C_5^+ non-aromatic hydrocarbons was not performed, the hydrogen and carbon balances were again randomly scattered about zero, suggesting that no new major products were formed.

5.4 Modelling

5.4.1 Computational Details

All simulations were performed using the FACSIMILE [4] numerical integration package. Rate constants were taken where possible from recent compilations [217,230,231]. A detailed list of the selected rate constants and notes on the choice thereof is given in Appendix

Figure 5.5. Dependence of Ethane Conversion on Initial Propylene Concentration at 1093 K.

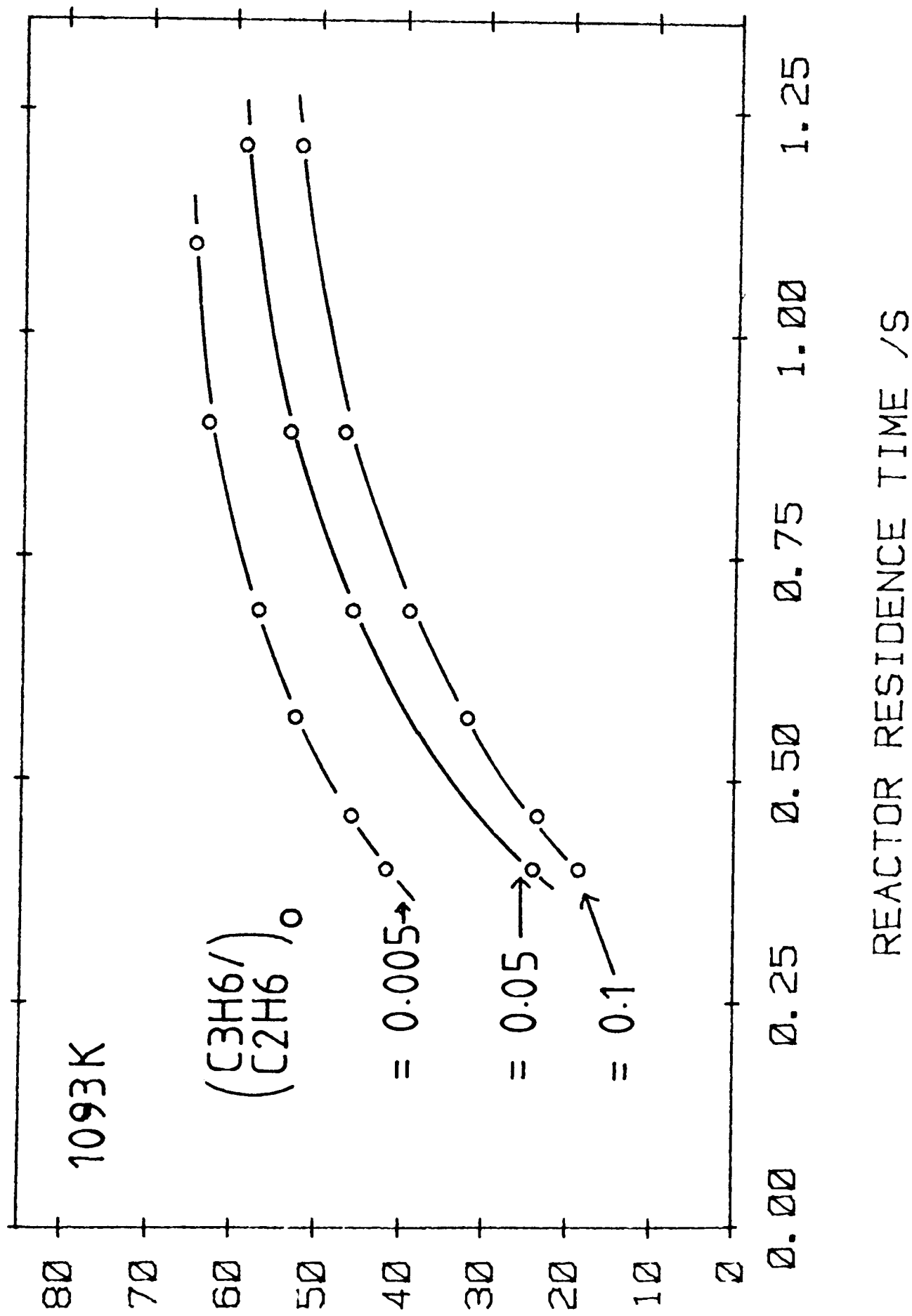

Figure 5.6. Dependence of Propylene Conversion on Temperature and Reactor Residence Time.
$([C_3H_6]/[C_2H_6])_o$: ●, 0.1; o, 0.05.

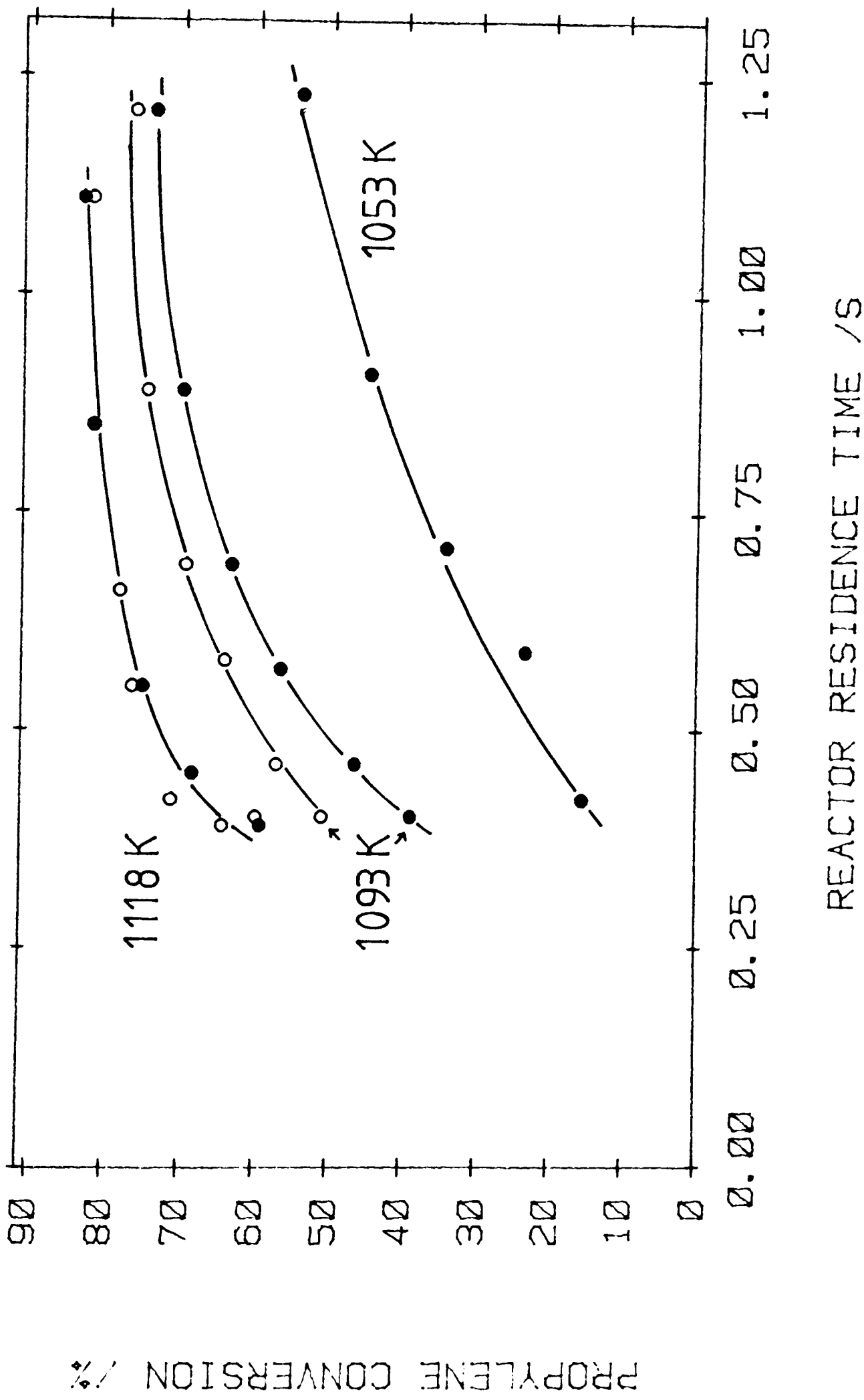

Figure 5.7. Dependence of Fractional Hydrogen and Methane Yields on Initial Propylene Concentration, 1118K. $([C_3H_6]/[C_2H_6])_o$: ●, ◆ 0.005; o, ◇ 0.05; ⊙, ◈ 0.1.

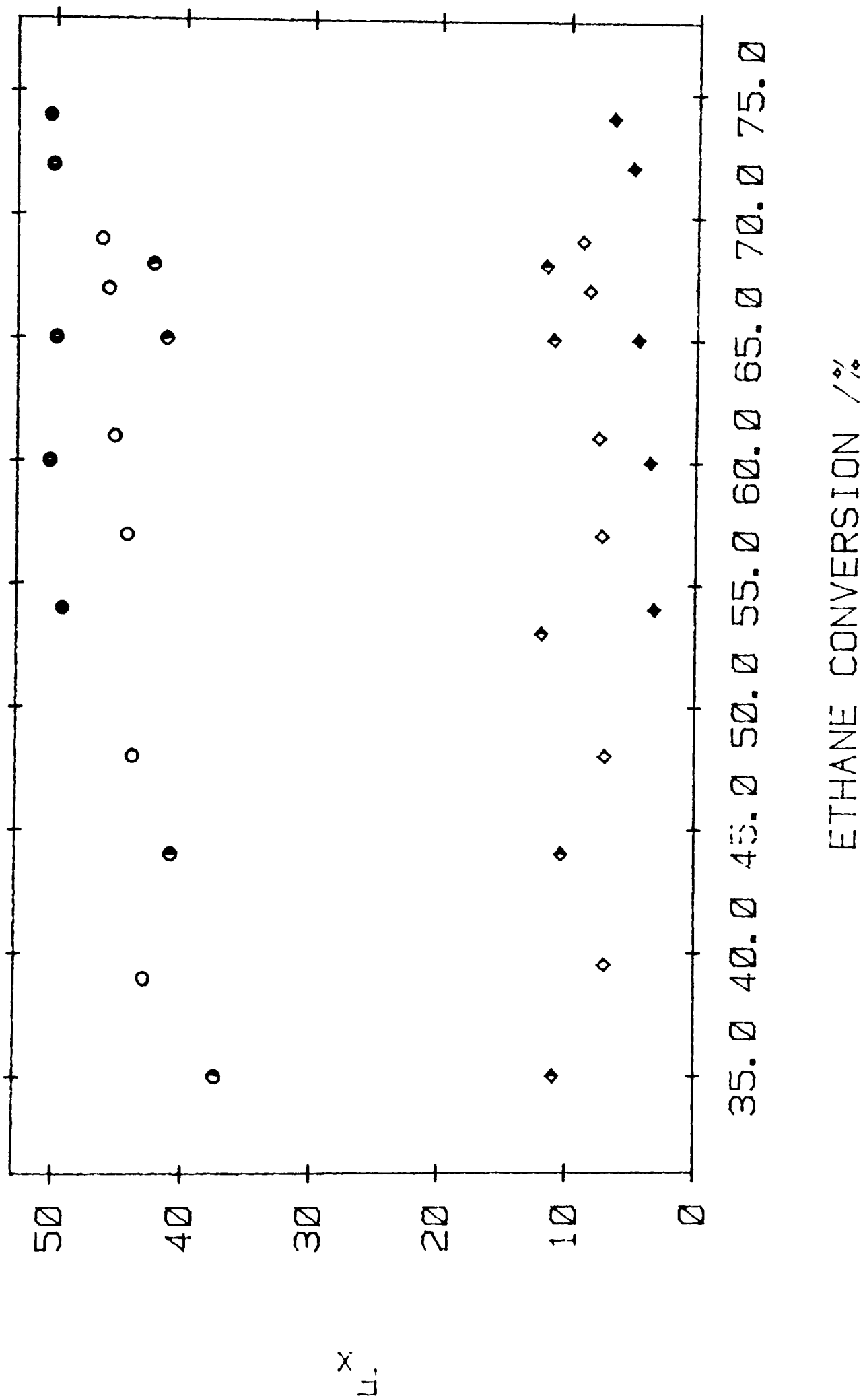

7. The estimation of important rate constants which are not available or are poorly defined in the literature, is discussed in the text.

The initial concentrations in the reactor were taken to be equal to the concentrations of the reactants in the incoming gas, adjusted to 1 Atm pressure and the experimental temperature. The steady input of reactants was simulated as a first order increase in reactant concentration from the initial concentration with a rate coefficient of $1/\tau$, where τ is the reactor residence time i.e. $d[X]/dt=[X]_o/\tau$. Similarly, the flow of gases out of the reactor was treated as a first order loss of all radicals and molecules, with a rate coefficient of $-1/\tau$.

Under all conditions, it was found that the concentrations of both the molecular and radical species reached a steady state after integrating the reaction scheme over two to three residence times. In practice, integration over 5 seconds, or four times the longest residence time was employed.

5.4.2 Thermodynamic Calculation of Rate Constants

By the principle of microscopic reversibility, the ratio of the rate constants for two reactions defining an equilibrium, is equal to the thermodynamic equilibrium constant, K_C:

$$A + B \underset{k_{-1}}{\overset{k_1}{===}} C + D \qquad k_1/k_{-1} = K_C$$

This relationship can be used to calculate one rate constant from the

other, if the equilibrium constant can be calculated, thereby reducing the number of independent parameters, and is particularly useful in cases where one rate constant is known much more accurately than the other. The equilibrium between hydrogen atoms, ethane, ethyl radicals and hydrogen provides a good example of such a situation:

$$H + C_2H_6 \equiv\equiv\equiv H_2 + C_2H_5$$

The forward reaction has been the subject of a number of studies [45,46,232]. Hydrogen atoms can be monitored directly and ethane is thermally stable at the temperatures required to produce observable rates of reaction. In contrast, the reverse reaction is extremely slow at conventional experimental temperatures and is complicated, at temperatures above 800K, by the pressure and temperature dependent thermal decomposition of the ethyl radical [233].

The approach adopted in building up the present kinetic model has been, therefore, to calculate poorly defined reverse rate constants where the forward rate constants are known. In particular, it should be possible to calculate methyl and ethyl radical rate constants accurately, as their heats of formation are well defined and their entropies can be evaluated from known moments of inertia and vibrational frequencies, using statistical mechanics, as discussed in Chapter 3 for the case of the ethyl radical. Where accurate radical parameters were not known, their entropies and enthalpies at experimental temperatures were estimated, using room temperature values and temperature dependent heat capacities taken from Benson [163]. Molecular enthalpies and entropies for molecules, other than ethylene, under the present experimental conditions, were calculated using 1000K thermodynamic parameters tabulated by Stull

[75] and the formulae:

$$\Delta H^{o}_{f,T} = \Delta H^{o}_{f,1000} + C_p^{1000}\,(T - 1000)$$

$$S^{o}_{T} = S^{o}_{1000} + C_p^{1000}\ln(T/1000)$$

The assumption of a constant C_p for each molecular species over the temperature range 1000 - 1150K does not introduce serious error into the calculated equilibrium constants.

The calculation of the forward rate constant and the equilibrium constant for the H + C_2H_4 == C_2H_5 system at cracking temperatures is discussed below. This example demonstrates the usefulness of both the thermochemical calculation of reverse rate constants and of the estimation of pressure and temperature dependent rate constants, using parametric models constructed from extensive data collected outside the required temperature and pressure range. Calculated equilibrium constants under the present experimental conditions for the H + C_2H_6 == H_2 + C_2H_5, H + CH_4 == H_2 + CH_3 and H + C_3H_6 == H_2 + C_3H_5 systems are given in Appendix 8.

Accurate estimation of the forward (k_{HAD1}) and backward (k_{D1}) rate constants in the H + C_2H_4 == C_2H_5 equilibrium is of great importance in the modelling of hydrocarbon pyrolysis since, as will be shown later, the model predictions are very sensitive to both their absolute and relative values. The calculation of the absolute values of k_{HAD1} and k_{D1} presents a particularly serious problem, as the system is well into the fall-off region at cracking temperatures.

A model describing the pressure and temperature dependence of k_{HAD1} was developed in Chapter 2, and was shown to predict the value of the rate constant at 800K and 200 Torr He pressure, as obtained in Chapter 3, to within a few percent.

Michael et al. [33] found that helium and nitrogen have equal collision efficiencies with respect to stabilisation of the excited ethyl adduct, allowing the model developed for a helium bath gas to be easily applied to the present case. For an estimated collision efficiency of 0.03 at 1100K, the reaction is predicted to be a factor of five below its high pressure limit at 1 Atm pressure. This degree of fall-off was predicted to vary only slightly with temperature over the present experimental temperature range and k_{HAD1} was taken to be given by $7.34 \times 10^{-12} \exp(-1049/T)$ molecule^{-1}cm^{3}s^{-1}.

The enthalpy and entropy changes for the reaction were calculated as a function of temperature using the formulae:

$$\Delta H^{O}_{T} = \Delta H^{O}_{298} + \int_{298}^{T} \Delta C_p \, dT$$

and

$$\Delta S^{O}_{T} = \Delta H^{O}_{298} + \int_{298}^{T} \Delta C_p d\ln T$$

The standard enthalpy and entropy changes were taken to be -36.25 kcalmol^{-1} and -20.57 calmolK^{-1}, as determined in Chapter 3. ΔC_p was expressed by the linear relationship:

$$\Delta C_p/\text{calmol}^{-1} = -3.59 + 2.01T/1000$$

which was also taken from Chapter 3. Calculated values of $\Delta H^{O}T$, $\Delta S^{O}T$ and K_1 are shown in Table 5.1.

Table 5.1

Calculated Values of ΔH^{o} , ΔS^{o} and the Equilibrium Constant for the H + C_2H_4 === C_2H_5 System at Cracking Temperatures

T/K	$\Delta H^{o}T$/kcalmol^{-1}	$\Delta S^{o}T$/calmol$^{-1}K^{-1}$	K_1/molecule$^{-1}cm^3x10^{-17}$
1053	-37.94	-23.58	7.53
1093	-38.00	-23.64	4.03
1118	-38.03	-23.68	2.77
1148	-38.07	-23.71	1.82

5.4.3 A Simple Model of Ethane Pyrolysis

Initial simulations were performed with the restricted reaction scheme below, which does not include reactions producing vinyl or allyl radicals.

Initiation Steps

C_2H_6	=====>	$CH_3 + CH_3$	RI1
C_3H_8	=====>	$CH_3 + C_2H_5$	RI2
$N\text{-}C_4H_{10}$	=====>	$C_2H_5 + C_2H_5$	RI3
$N\text{-}C_4H_{10}$	=====>	$CH_3 + H + C_3H_6$	RI4

Propagation Steps

$CH_3 + C_2H_6$	=====>	$CH_4 + C_2H_5$	RMA1
$CH_3 + H_2$	=====>	$CH_4 + H$	RMA2
$C_2H_5 + H_2$	=====>	$C_2H_6 + H$	REA1
$H + C_2H_4$	=====>	C_2H_5	RHAD1
C_2H_5	=====>	$H + C_2H_4$	RD1
$H + C_2H_6$	=====>	$H_2 + C_2H_5$	RHA1

$H + CH_4$	$\Longrightarrow H_2 + CH_3$	RHA3
$H + C_3H_8$	$\Longrightarrow H_2 + C_3H_6 + H$	RHA4
$H + C_3H_8$	$\Longrightarrow H_2 + C_2H_4 + CH_3$	RHA5
$H + N\text{-}C_4H_{10}$	$\Longrightarrow H_2 + C_3H_6 + CH_3$	RHA6
$H + N\text{-}C_4H_{10}$	$\Longrightarrow H_2 + C_2H_4 + C_2H_5$	RHAD7

Termination Steps

$CH_3 + CH_3$	$\Longrightarrow C_2H_6$	RMM1
$CH_3 + C_2H_5$	$\Longrightarrow C_3H_8$	RME1
$CH_3 + C_2H_5$	$\Longrightarrow CH_4 + C_2H_4$	RME2
$C_2H_5 + C_2H_5$	$\Longrightarrow N\text{-}C_4H_{10}$	REE1
$C_2H_5 + C_2H_5$	$\Longrightarrow C_2H_6 + C_2H_4$	REE2
$C_2H_5 + H$	$\Longrightarrow CH_3 + CH_3$	RHE1

As propane and butane did not build up to significant concentrations, if their thermal dissociations and reactions with hydrogen atoms were allowed for, their reactions with other radicals were not included.

Propyl radicals were found, by simulation, to achieve only very low concentrations, as their reactions were insignificantly slow with respect to their thermal dissociation. $N\text{-}C_3H_7$ was replaced by $CH_3 + C_2H_4$ and $I\text{-}C_3H_7$ was replaced by $H + C_3H_6$ whenever they appeared as reaction products. This procedure did not noticeably affect the results of the model.

Simulations using this simple scheme predicted conversions which were significantly higher than those seen experimentally, and although the predicted methane and hydrogen yields were in approximate agreement with experiment, the observed decrease in F_{C2H4} with increasing conversion was not reproduced by the simulations.

These discrepancies, together with the significant concentrations of acetylene and the small amounts of butadiene found in the pyrolysis products, suggest the presence of the vinyl radical, formed, presumably, from the abstraction reaction between hydrogen atoms and ethylene:

$$H + C_2H_4 \text{ =====> } H_2 + C_2H_3 \qquad \text{RHA2}$$

The addition of this extra carbon-containing radical to the system would serve to increase the number of chain termination steps and provide a route to acetylene, via the thermal decomposition:

$$C_2H_3 \text{ =====> } H + C_2H_2 \qquad \text{RD2}$$

It is instructive to look at the predicted radical concentrations and reactive fluxes through some of the more important channels, shown in Table 5.2 for a residence time of 0.6s.

Table 5.2

Radical Concentrations and Reactive Fluxes Predicted by the Simple Model. 1118K Residence Time 0.6 s

Reaction			Flux /moleculescm^{-3}s^{-1}
$H + C_2H_4$	==>	C_2H_5	1.6×10^{18}
C_2H_5	==>	$H + C_2H_4$	2.0×10^{18}
$H + C_2H_6$	==>	$H_2 + C_2H_5$	4.5×10^{17}
$C_2H_5 + H_2$	==>	$H + C_2H_6$	1.2×10^{16}
$H + CH_4$	==>	$CH_3 + H_2$	4.1×10^{16}
$CH_3 + H_2$	==>	$CH_4 + H$	6.9×10^{16}
$CH_3 + C_2H_6$	==>	$CH_4 + C_2H_5$	1.9×10^{15}
C_2H_6	==>	$CH_3 + CH_3$	9.4×10^{15}
$C_2H_5 + C_2H_5$	==>	$N\text{-}C_4H_{10}$	4.2×10^{15}
$C_2H_5 + CH_3$	==>	C_3H_8	5.5×10^{15}
$CH_3 + CH_3$	==>	C_2H_6	1.7×10^{15}
$H + C_2H_5$	==>	$CH_3 + CH_3$	7.7×10^{15}

Radical	Concentration /cm^3
C_2H_5	1.5×10^{13}
CH_3	5.9×10^{12}
H	1.9×10^{12}

Perhaps the most striking feature of the estimated fluxes is that the addition of hydrogen atoms to ethylene and the thermal decomposition of the ethyl radical are almost balanced, with fluxes approximately a factor of five greater than for any other reactions. The concentrations of hydrogen atoms and ethyl radicals are thus largely controlled, at high conversions, by the equilibrium constant for the $H + C_2H_4 == C_2H_5$ system.

The conversion of ethane into ethylene and hydrogen is mostly accomplished through the H + C_2H_6 abstraction reaction, which has a reactive flux of almost forty times that of its reverse, the reaction between ethyl radicals and hydrogen.

It appears that, at high conversion, methane is produced mostly via the reaction between methyl radicals and hydrogen, as the rate of methane production via the reaction between methyl radicals and ethane is a factor of thirty slower. The above model uses an estimate of 4.7×10^{-15} molecule^{-1}cm^{3}s^{-1} for k_{MA1} at 1118K [217], much lower than the value of 4.2×10^{-14} molecule^{-1}cm^{3}s^{-1} estimated for k_{MA2} from the rate of the H + CH_4 reaction, and the equilibrium constant for the H + CH_4 == CH_3 + H_2 system. Pacey and Purnell [71] have suggested that k_{MA1} displays strongly curved Arrhenius behaviour and calculate its value, at 1118K, to be approximately a factor of ten greater than that used above. Increasing k_{MA1} by an order of magnitude did not, however, appreciably alter the model predictions, as it was still well below k_{MA2} and the precise rate of the CH_3 + C_2H_6 reaction thus appears to be unimportant in the pyrolysis of ethane at high conversions.

Of the radical-radical reactions, the greatest flux is through the reaction between hydrogen atoms and ethyl radicals. However, as will be shown later, the hydrogen atom concentration predicted by this simple scheme is much reduced if the abstraction reaction of hydrogen atoms with ethylene is allowed for and then the flux through this reaction becomes very small in relation to that through other termination routes.

The observed reduction in experimental conversion immediately after decoking the reactor was presumably caused by heterogenous

processes. Purnell and Quinn [234] investigated the role of surfaces in the pyrolysis of n-butane at 800K and found that the rate of reaction in a carbon-coated vessel was reduced by 40 - 45%, compared to that observed in pyrex vessels of various surface-to-volume ratios, which had been cleaned by washing with nitric or hydrofluoric acid. It was concluded that heterogenous termination was taking place to a greater extent on the carbon coated walls. In the present study, a ~10% decrease in conversion was observed on removing the carbon coating by reaction with oxygen, suggesting that the removal process either increased the rate of wall termination, or reduced the rate of a heterogenous initiation. It is possible that the surface prepared by passing oxygen through the reactor at red heat was very reactive towards hydrogen atoms. Heterogenous effects are likely to be much less important in the present system than at lower temperatures as the rate of hydrogen atom removal by reaction is much faster than the rate of collision with the cell wall. Furthermore, simulations showed that the very rapid H + C_2H_4 == C_2H_5 equilibrium could only be disturbed by first-order hydrogen atom loss rates of 10^5 s^{-1} or greater. It was therefore assumed that the heterogenous removal of hydrogen atoms was negligible under normal experimental conditions. Although the possibility of a small contribution from heterogenous initiation could not be excluded, such processes do not alter the sensitivity of the model to important but poorly defined homogenous processes, as is discussed later.

The simple model presented in this section is useful in determining some of the most important reactive pathways operating in the pyrolysis of ethane. However, it is clear that we require a more detailed description, which allows for the reactions of the vinyl

radical, if the experimentally observed conversions and product distributions are to be modelled successfully.

5.4.4 Vinyl and Allyl Radical Reactions

Very little is known about the reactions of the vinyl radical. Although the radical has recently been shown to display an electronic absorption spectrum in the visible region [235], the spectrum is very weak ($\varepsilon_{max}\sim 30$) and no conventional flash photolysis/kinetic spectroscopy studies of its reaction rates have been reported. Slagle et al. [22] have, however, performed a direct study of the $C_2H_3 + O_2$ reaction using photoionisation mass spectrometric detection of the radical. Callear [236] has investigated the effect of temperature (300 - 500K) and hydrogen concentration on the product yields arising from the mercury photosensitised decomposition of hydrogen in the presence of acetylene. An estimate of the rate constant for the reaction of vinyl radicals with hydrogen was made, giving $k_{VA2} = 9.4 \times 10^{-14} \exp(-5.5 kcal/RT)$.

$$C_2H_3 + H_2 \quad =====> \quad C_2H_4 + H \qquad \text{RVA2}$$

However, the approximations made in evaluating k_{VA2} led to a factor of three estimate of the uncertainty in the rate constant. Furthermore, the quoted A-factor is more than an order of magnitude below evaluations of the A-factors for other alkyl radical + H_2 reactions and the activation energy is at least a factor of two smaller than the activation energy for the $CH_3 + H_2$ reaction, suggesting that the above Arrhenius expression could be seriously in error at cracking temperatures. No data is available on the rates

of vinyl reactions with hydrocarbon molecules. Some estimates of the rates of vinyl reactions with hydrogen atoms are available [230], although the information was obtained indirectly in each case. This reaction will also not be of great importance in pyrolysis systems, because of the rapid reactions of hydrogen atoms with molecular species.

The most important reaction producing vinyl radicals in ethane pyrolysis will be the abstraction reaction:

$$H + C_2H_4 \text{ ====> } H_2 + C_2H_3 \qquad \text{RHA2}$$

Although Arrhenius parameters have been reported for this reaction on several occasions [167-172], they have invariably been arrived at indirectly and show a great deal of scatter; estimates of k_{HA2} at 1118K vary from 2.8×10^{-13} to 3.4×10^{-11} molecule^{-1}cm^{3}s^{-1}.

An estimate of the reactivity of vinyl radicals relative to other hydrocarbon radicals and of the rate of production of vinyl radicals via RHA2 could be derived from the thermodynamic parameters of the radical, if they were known to any reasonable accuracy. Unfortunately, however, the heat of formation of the vinyl radical is the subject of considerable debate at the present time, with recently published estimates varying from 63.4 [164,237] to 72 [238] kcalmol^{-1}. Therefore, any estimate of the rates of reactions with activation barriers, involving the production or removal of vinyl radicals, must be subject to large uncertainty: a change of 8.6 kcalmol^{-1} in the activation energy for a reation at 1118K, leads to a corresponding change in the rate of reaction of almost a factor of fifty.

In an attempt to evaluate the effect of variation in the chosen

value of $\Delta H_f^o(C_2H_3)$ on the model predictions, a self consistent set of rate constants for the reactions

$H + C_2H_4$	=====> $C_2H_3 + H_2$	RHA2
$C_2H_3 + H_2$	=====> $H + C_2H_4$	RVA2
$H + C_2H_2$	=====> C_2H_3	RHAD2
C_2H_3	=====> $H + C_2H_2$	RD2
$C_2H_3 + C_2H_6$	=====> $C_2H_4 + C_2H_5$	RVA1

was developed. Of the above reactions, only the limiting high pressure rate constant for the addition of hydrogen atoms to acetylene is well defined [162]. By analogy with the results for the addition of hydrogen atoms to ethylene, this reaction will be at least a factor of five below its high pressure limit at 1118K and 1 Atm pressure. Initially, an upper limit of $1.84x10^{-12}exp(-2410calmol^{-1}/RT)$ $molecule^{-1}cm^3s^{-1}$ was assumed and the rate of vinyl radical decomposition was calculated from an estimate of the equilibrium constant for the $H + C_2H_2 == C_2H_3$ system.

Two of the recent kinetic determinations of the heat of formation of the vinyl radical agree on a value of 63.4±2 $kcalmol^{-1}$ [164,236], which gives an estimate of the bond dissociation energy for the C_2H_3-H bond of 103±2 $kcalmol^{-1}$, similar to the 104.3 $kcalmol^{-1}$ CH_3-H bond energy in methane. Thus, as a first approximation, vinyl radical rate constants were set equal to the rate constants for the appropriate methyl radical reactions when a value of 63.4 $kcalmol^{-1}$ was chosen for the vinyl heat of formation. For higher values of $\Delta H^o f,298(C_2H_3)$, the vinyl radical reaction rates were scaled by a factor of $exp((\Delta H-63.4)/2RT)$, to allow for an increased reactivity with increasing C_2H_3-H bond strength. This

approach is justified in part by the observation that the activation energies for radical abstraction of hydrogen atoms from hydrocarbons vary linearly with the strength of the bond being broken, as was first noted by Evans and Polanyi [1]. For methyl radicals, the activation energy increases by approximately 1 $kcalmol^{-1}$ for every 2 $kcalmol^{-1}$ increase in bond energy, as assumed for vinyl radicals above.

Having estimated the vinyl radical rate constants k_{VA1} and k_{VA2}, k_{HA2} was calculated from K_6, equilibrium constant for the H + C_2H_4 == H_2 + C_2H_3 system. The estimated rate constants which are dependent on the vinyl heat of formation, are shown, in molecular units, together with K_6 and K_2 ($=k_{HAD2}/k_{D2}$), as a function of $\Delta H^{O}f,298(C_2H_3)$ and for a temperature of 1118K, in Table 5.3.

Table 5.3

Calculated Rate Constants and K_6 as a Function of $\Delta H^{O}_{f,298}(C_2H_3)$ at 1118K

$\Delta H^{O}_{f,298}(C_2H_3)$ /$kcalmol^{-1}$	63.4	64.0	65.0	67.0	70.5
$k_{VA1}/10^{-15}$	4.7	5.5	6.8	10.6	23.8
$k_{VA2}/10^{-14}$	4.2	4.8	6.0	9.3	21.0
$k_{HA2}/10^{-12}$	3.0	2.6	2.1	1.3	0.61
K_6	70.6	54.0	34.5	14.1	2.90
$K_2/10^{-16}$	4.2	3.2	2.1	0.88	0.17

The following reactions were added to the reaction scheme to allow for the presence of vinyl radicals:

$H + C_2H_4 \quad =====> H_2 + C_2H_3$ RHA2

$C_2H_3 + C_2H_6 \Longrightarrow C_2H_4 + C_2H_5$		RVA1
$C_2H_3 + H_2 \Longrightarrow C_2H_4 + H$		RVA2
$C_2H_3 + C_2H_4 \Longrightarrow C_4H_6 + H$		RVAD1
$H + C_2H_2 \Longrightarrow C_2H_3$		RHAD2
$C_2H_3 \Longrightarrow C_2H_2 + H$		RD2
$H + C_2H_3 \Longrightarrow C_2H_4$		RAV1
$CH_3 + C_2H_3 \Longrightarrow C_3H_6$		RMV1
$C_2H_5 + C_2H_3 \Longrightarrow 1\text{-}C_4H_8$		REV1
$C_2H_3 + C_2H_3 \Longrightarrow 1,3\text{-}C_4H_6$		RVV1
$1\text{-}C_4H_8 \Longrightarrow CH_3 + C_3H_5$		RI6
$H + 1\text{-}C_4H_8 \Longrightarrow CH_3 + C_3H_6$		RHAD3
$H + C_4H_6 \Longrightarrow C_2H_4 + C_2H_3$		RHAD4

With the above kinetic scheme, however, the concentration of propylene was observed to build up to several times the amount present as an impurity in the reactant mixtures. In order to prevent this build up of propylene, the reactions between hydrogen atoms and propylene, and its thermal decomposition, were added to the scheme.

$H + C_3H_6 \Longrightarrow CH_3 + C_2H_4$		RHAD 6
$H + C_3H_6 \Longrightarrow H_2 + C_3H_5$		RHA8
$C_3H_6 \Longrightarrow CH_3 + C_2H_3$		RI7

The rate constant for the abstraction reaction RHA8 is poorly defined, as is discussed in more detail in Section 5.4.6 and an initial estimate of $k_{HA8} = 5.3 \times 10^{-11} \exp(-3500/RT)$ [217] was used for the simulations at low $[C_3H_6]$. Although the lowest energy pathway for the thermal decomposition of propylene will be that producing H + C_3H_5, the Arrhenius A factor will be up to two orders of magnitude

higher for the pathway producing CH_3 + C_2H_3, and a number of studies have shown that the latter is the dominant decomposition route at cracking temperatures [239-242].

The reactions RHA8 and RI6 introduce allyl radicals into the system. Little is known of its reactions with hydrocarbons, although its reactions by self-recombination and recombination with NO and O_2 have been directly studied [23,28]. It is believed that the allyl radical is thermally stable at cracking temperatures and reacts only very slowly by addition and abstraction, because of the weakness of the C_3H_5-H bond (87.8 $kcalmol^{-1}$). The major removal pathways for allyl radicals will therefore involve recombination with other radicals. Tulloch et al. [23] have shown that there is no barrier to allyl radical self-recombination and therefore the rates of allyl radical recombinations should be similar to those of other carbon - containing radicals.

$C_3H_5 + C_3H_5 \Longrightarrow C_6H_{10}$	RAA1
$C_3H_5 + C_2H_5 \Longrightarrow 1\text{-}C_5H_{10}$	RAE1
$C_3H_5 + C_2H_3 \Longrightarrow 1,4\text{-}C_5H_8$	RAV1
$C_3H_5 + CH_3 \Longrightarrow 1\text{-}C_4H_8$	RAE1
$C_3H_5 + H \Longrightarrow C_3H_6$	RAH1

By analogy with methyl, the major allyl abstraction pathways will involve reaction with hydrogen and ethane:

$C_3H_5 + C_2H_6 \Longrightarrow C_3H_6 + C_2H_5$	RAA3
$C_3H_5 + H_2 \Longrightarrow C_3H_6 + H$	RAA2

k_{AA2} was calculated from the equilibrium constant for the C_3H_5 + H_2 == C_3H_6 + H system and k_{HA8}. Again by analogy with methyl, the allyl

abstraction reaction with ethane will be unimportant compared to its reaction with hydrogen. An approximate value for k_{AA3} was taken from the review of Allara and Shaw [217]. The new allyl recombination products were assumed to be removed by thermal decomposition or by reaction with hydrogen atoms:

$1\text{-}C_5H_{10}$	=====> $C_3H_5 + C_2H_5$	RI7
$1,4\text{-}C_5H_8$	=====> $C_3H_5 + C_2H_3$	RI8
$1,5\text{-}C_6H_{10}$	=====> $C_3H_5 + C_3H_5$	RI9
$H + 1\text{-}C_5H_{10}$	=====> $C_2H_5 + C_3H_6$	RHAD7
$H + 1,4\text{-}C_5H_8$	=====> $C_3H_5 + C_2H_4$	RHAD9
$H + 1,5\text{-}C_6H_{10}$	=====> $C_3H_5 + C_3H_6$	RHAD9

5.4.5 Effect of $\Delta H^{O}_{f,298}(C_2H_3)$ on Model

The effect of varying the vinyl radical heat of formation between 63.4 and 70.5 $kcalmol^{-1}$ on the degree of conversion and on the yield of methane, predicted using the scheme described above, for a temperature of 1118K, is shown in Figures 5.8 and 5.9. It is clear that the model is extremely dependent on the choice of vinyl radical rate constants. Sensitivity coefficients referring to ethane conversion and fractional product yields, for the more important rate constants, are given in Table 5.4. The sensitivity coefficients were calculated for a 10% increase in the parameter referred to, i.e. $S_X = \log(X/X_O)/\log(1.1)$. Any rate constants defined relative to each other, as was described earlier, were decoupled for the purposes of the sensitivity analysis.

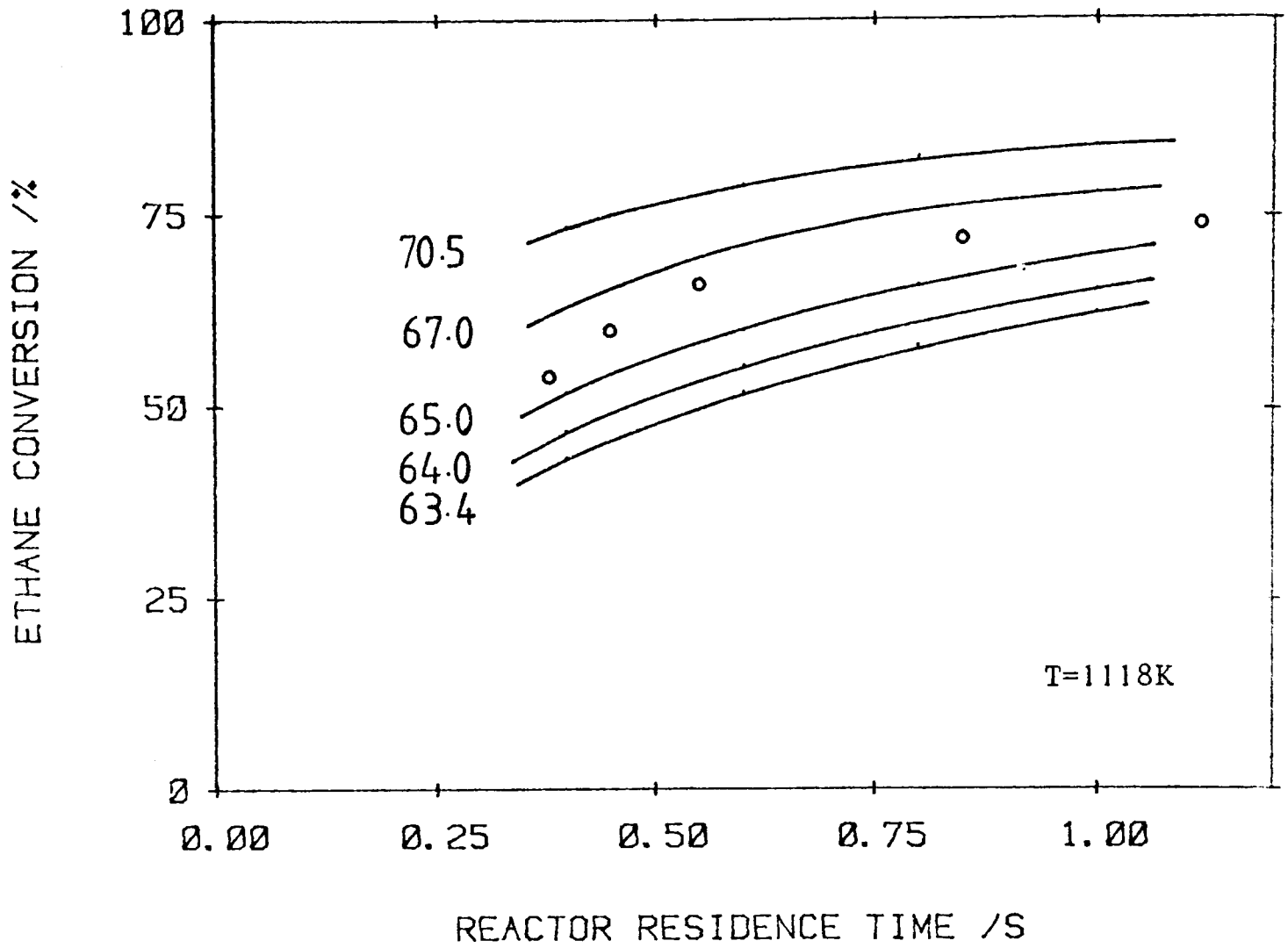

Figure 5.8. Dependence of Predicted Ethane Conversion on the Vinyl Radical Heat of Formation. Circles: Experiment Data. Curves: Model Predictions. Each curve is labelled with the appropriate vinyl heat of formation in kcalmol^{-1}.

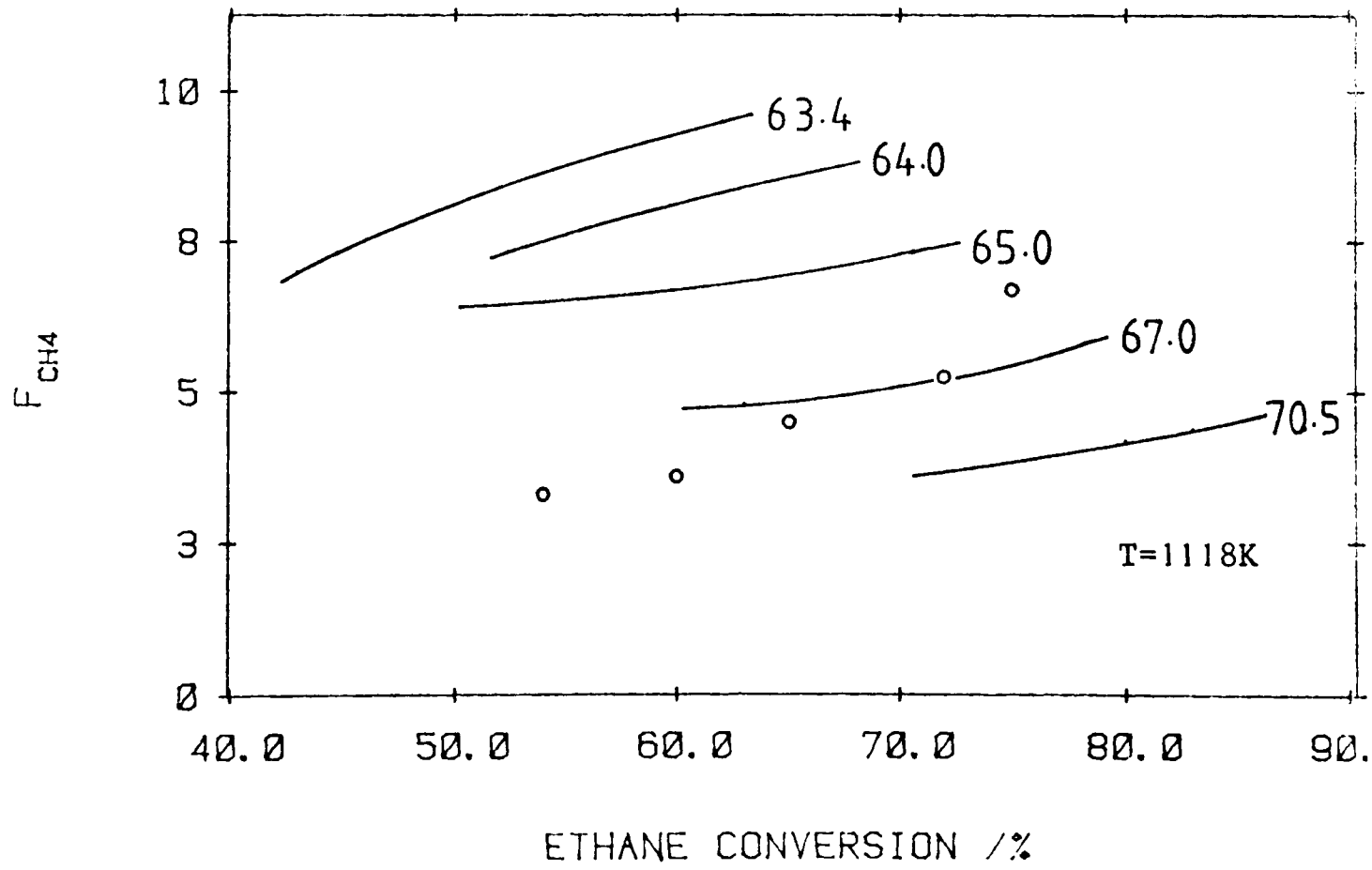

Figure 5.9. Dependence of the Predicted Fractional Methane Yield, on the Chosen Vinyl Radical Heat of Formation. Circles: Experimental Data. Curves: Model Predictions Each Curve is marked with the appropriate vinyl heat of formation in kcalmol^{-1}.

Table 5.4.

Sensitivity Coefficients for Ethane Pyrolysis, Calculated at 1118K with $\Delta H^{o}_{f,298}(C_2H_3)$= 65.0 and a Residence Time of 0.5 s

Parameter	$S_{CONVERSION}$	S_{H2}	S_{CH4}	S_{C2H2}	S_{C2H4}
k_{HAD1}	-0.02	0.01	0.19	-0.07	0.00
k_{D1}	0.04	0.02	-0.33	0.06	-0.01
$k_{HAD1}+k_{D1}$	0.02	0.01	-0.14	0.06	-0.01
k_{HAD2}	-0.01	0.01	0.03	-0.18	0.02
k_{D2}	0.03	0.03	-0.12	0.76	-0.10
$k_{HAD2}+k_{D2}$	0.03	0.03	-0.09	0.58	-0.07
k_{VA2}	0.06	-0.02	-0.10	-0.38	0.07
k_{HA2}	-0.09	0.03	0.16	0.58	-0.12
$k_{VA2}+k_{HA2}$	-0.03	0.01	0.06	0.21	-0.04
k_{I1}	0.10	-0.03	0.53	0.15	-0.04
k_{HA1}	0.15	0.02	-0.50	-0.28	0.05

The overall conversion is most sensitive to the rates of the abstraction reaction of hydrogen atoms with ethane and the thermal decomposition of ethane, as might be expected, but is also strongly dependent on the rate constants for the production and removal of vinyl radicals, k_{HA2} and k_{VA2}.

It is important to note that the yields of acetylene and, in particular, methane, are both very sensitive to a number of model parameters, in addition to the estimated vinyl radical rate constants. Any attempt to fit the vinyl radical rates to the present data would have to allow for uncertainty in the other model

parameters. Even the best determined rate constants in the present scheme are probably only reliable to within a factor of two. The effect of such a variation in k_{HAl} on the predicted conversion and on the methane yield, is shown in Figures 5.10 and 5.11. The model predictions are clearly extremely sensitive to variations in k_{HAl} in particular and many other "known" parameters in general. Any estimate of the vinyl heat of formation or of the magnitudes of its rate constants, from fitting to the present data, would thus be at best highly qualitative and potentially misleading.

The complicating effect of introducing the reactions of vinyl and allyl reactions into the pyrolysis scheme can be seen by reference to the calculated reactive fluxes and radical concentrations in Table 5.5.

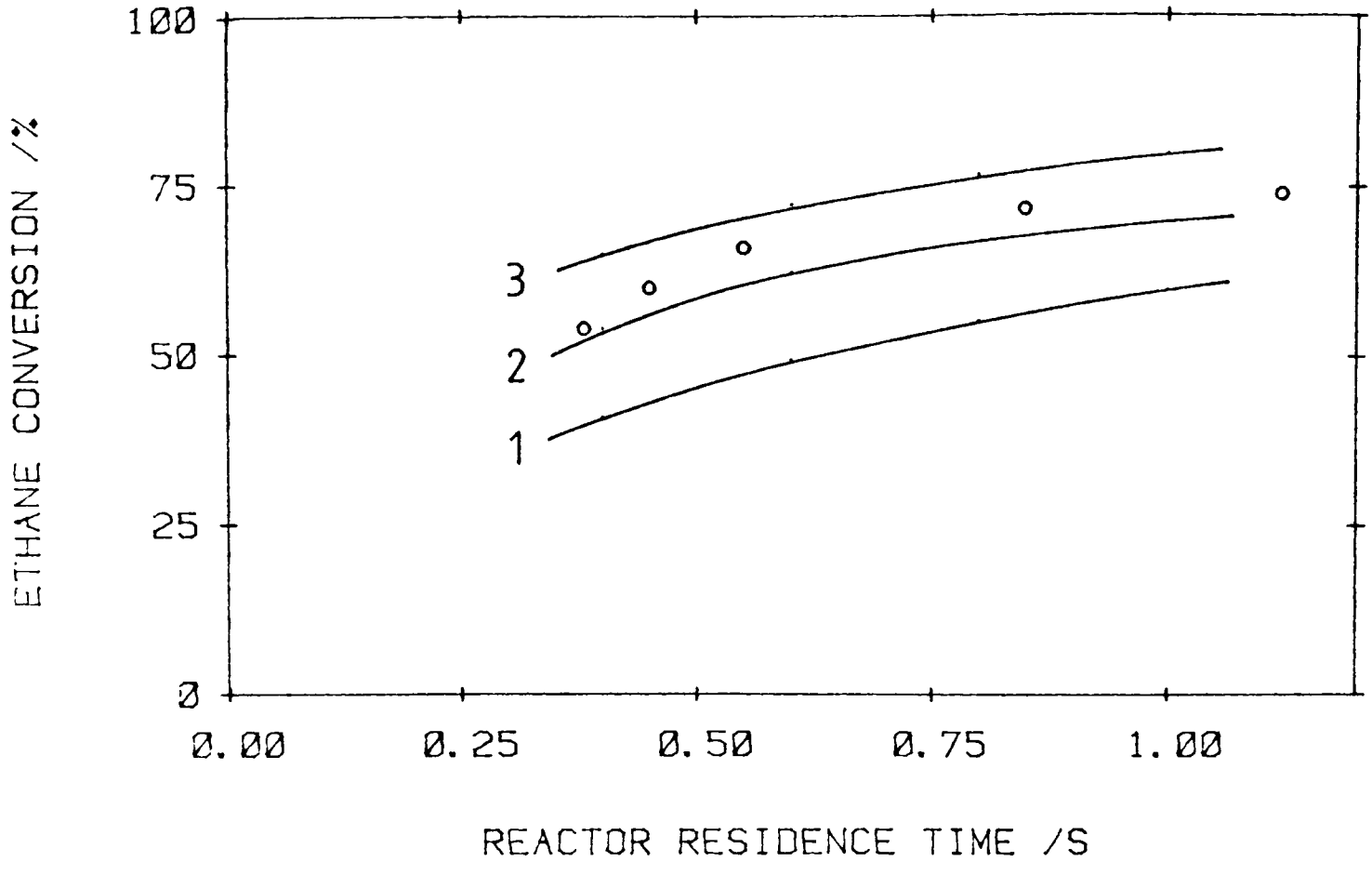

Figure 5.10. Dependence of the Predicted Ethane Conversion at 1118K on the $H+C_2H_6$ Rate Constant. Circles: Experimental Data. Curves: Model Predictions.

1 : $k_{HA1} = 4.5 \times 10^{-22} T^{3.5} \exp(-2662/T)$ molecule^{-1}cm^{3}s^{-1}.

2 : $k_{HA1} = 9.0 \times 10^{-22} T^{3.5} \exp(-2662/T)$ molecule^{-1}cm^{3}s^{-1}.

3 : $k_{HA1} = 1.8 \times 10^{-21} T^{3.5} \exp(-2662/T)$ molecule^{-1}cm^{3}s^{-1}.

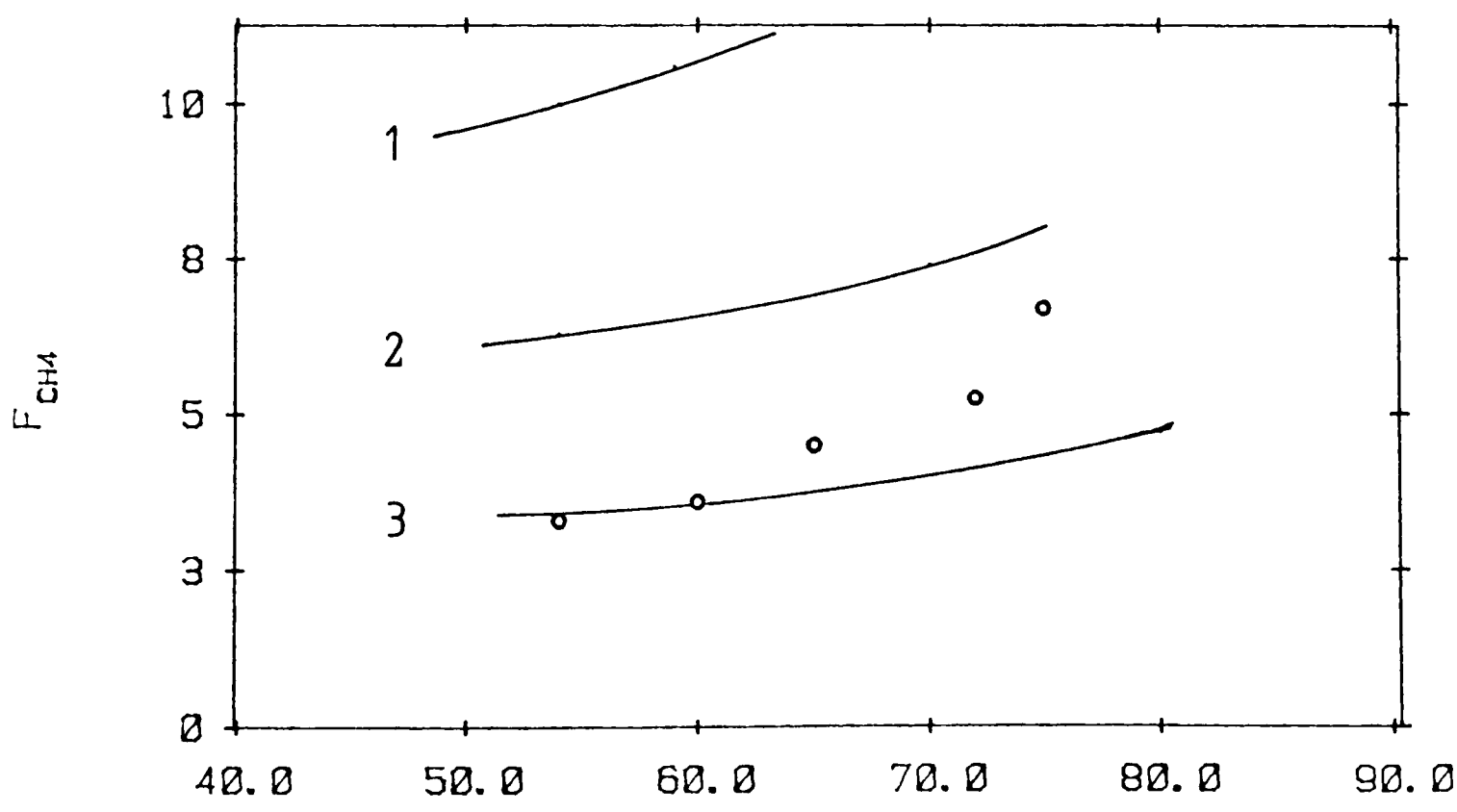

Figure 5.11. Dependence of the Predicted Fractional Methane Yield at 1118K on the $H+C_2H_6$ Rate Constant. Circles: Experimental Data. Curves: Model Predictions.

1 : $k_{HA1} = 4.5 \times 10^{-22} T^{3.5} \exp(-2662/T)$ molecule^{-1}cm^{3}s^{-1}.

2 : $k_{HA1} = 9.0 \times 10^{-22} T^{3.5} \exp(-2662/T)$ molecule^{-1}cm^{3}s^{-1}.

3 : $k_{HA1} = 1.8 \times 10^{-21} T^{3.5} \exp(-2662/T)$ molecule^{-1}cm^{3}s^{-1}.

Table 5.5

Radical Concentrations and Reactive Fluxes In the Pyrolysis of Ethane. Vinyl and Allyl Reactions Included.

$\Delta H^{o}_{f,298}(C_2H_3)$ = 65.0 kcalmol^{-1}, 1118K, 1.0 s Residence Time

Reaction	Flux / moleculecm^{3}s^{-1}	Reaction	Flux / moleculecm^{3}s^{-1}
RHAD1	3.0×10^{17}	RHAD2	7.9×10^{15}
RD1	6.1×10^{17}	RD2	4.0×10^{16}
RHA1	3.0×10^{17}	RAA1	1.7×10^{16}
REA1	2.8×10^{15}	RAM1	1.1×10^{16}
RHA2	3.0×10^{17}	RAV1	2.2×10^{16}
RVA2	1.5×10^{17}	RAE1	8.5×10^{15}
RVA1	1.1×10^{16}	RVM1	4.9×10^{15}
RHA3	5.6×10^{16}	RVV1	2.9×10^{15}
RMA2	1.7×10^{16}	RVE1	3.7×10^{15}
RMA1	4.2×10^{15}		

Radical Concentrations /cm^3

C_3H_5	2.5×10^{13}
C_2H_3	1.2×10^{13}
C_2H_5	5.0×10^{12}
CH_3	4.0×10^{12}
H	5.5×10^{11}

The equilibrium between hydrogen atoms, ethylene and ethyl radicals is now not established, as a substantial fraction of the hydrogen atom flux is diverted through the H + C_2H_4 ==> H_2 + C_2H_3 reaction. Although the methyl radical concentration is similar to that predicted by the simple model described earlier and the ethyl

radical concentration is reduced by a factor of three, the overall radical concentration is doubled and the hydrogen atom concentration is much reduced, resulting in a lower ethane conversion.

Perhaps the most surprising result,is the prediction that the allyl radical is the most abundant radical species even when propylene is present in only very low concentrations. Indeed, removing the input of propylene only reduced the allyl radical concentration by 16%, as significant quantities of propylene were produced by the recombination reaction between vinyl and methyl radicals. Furthermore, reducing the rate of the abstraction reaction between hydrogen atoms and propylene by an order of magnitude also only reduced the allyl concentration by 16%: it appears that the equilibria between allyl recombinations and the thermal dissociation of the recombination products largely determine the predicted allyl concentrations. Only small concentrations (<0.025% of total) of allyl recombination products were predicted to build up, with the result that the removal of more reactive radicals by recombination with allyl radicals is rapidly reversible and allyl concentrations as high as $2.5x10^{13}$ cm^3 do not have a marked effect on the predicted system behaviour. The removal of all allyl producing reactions did not significantly alter the concentrations of the other radicals or the end product distribution and resulted in an increase in the overall ethane conversion of less than 2%. However, the importance of the thermal dissociations of the allyl recombination products could be demonstrated by reducing their rates to zero, so that all radicals which reacted by recombination with allyl radicals were effectively removed from the system. The model conversions were then reduced by up to 5% by the presence of allyl radicals.

All variations in the model parameters described thus far failed to reduce the predicted acetylene yield sufficiently to bring it into agreement with the experimental yields. It can be seen from Table 5.5 that the rate of production of vinyl radicals by the addition of hydrogen atoms to acetylene is much less than the rate of vinyl decomposition; the acetylene yield would consequently be expected to be less dependent on k_{HAD2} than k_{D2}, as is indeed confirmed by the sensitivity analysis. Although the ratio k_{HAD2}/k_{D2} is fixed by the chosen vinyl radical thermochemistry, an upper estimate of k_{HAD2} was taken and it is probable that the reaction is significantly further into the fall off region than the $H + C_2H_4$ reaction. Reducing k_{HAD2} and hence k_{D2} by a factor of two was found to bring the predicted and observed acetylene yields into broad agreement.

For the purposes of modelling the effects of added propylene, a vinyl heat of formation of 65.0 $kcalmol^{-1}$ was adopted. The rate expressions for the hydrogen atom abstraction reaction with ethane and its addition to acetylene were taken to be $1.47x10^{-21}T^{3.5}exp(-2662/T)$ and $9.2x10^{-13}exp(-2410calmol^{-1}/RT)$ $molecule^{-1}cm^3s^{-1}$ respectively. With these assumptions the model reproduces the observed conversions and major product yields reasonably well as shown in Figures 5.12 and 5.13. The experimental results could almost certainly be better reproduced by careful adjustment of the model parameters within their often very large uncertainties but, given the interdependence of the model parameters, such an approach could not be used to unambiguously determine any of the rate constants involved.

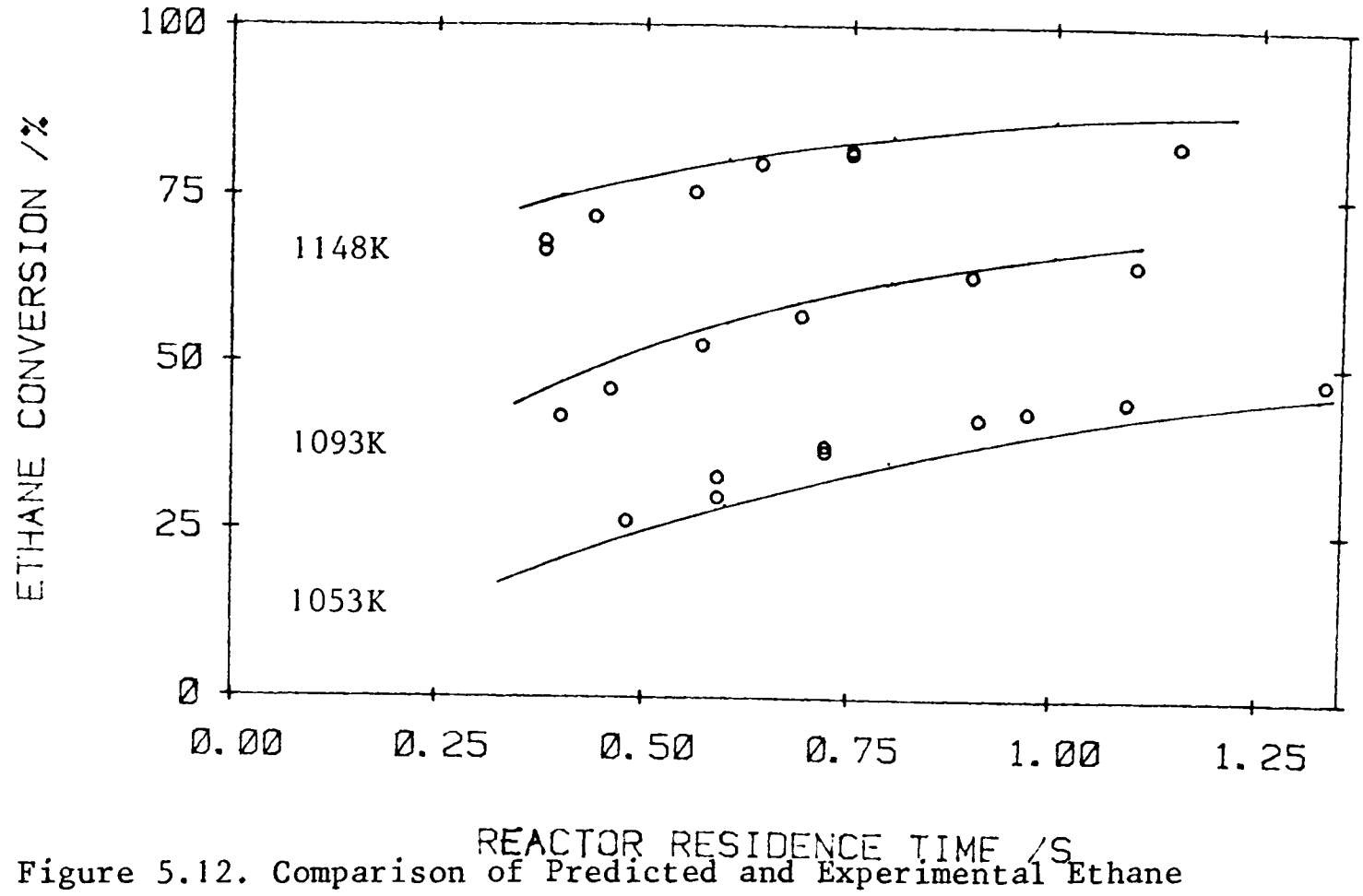

Figure 5.12. Comparison of Predicted and Experimental Ethane Conversion, for Temperatures of 1148, 1093 and 1053K. Circles: Experimental Data. Curves: Model Predictions Using $k_{HA1} = 1.47 \times 10^{-21} T^{3.5} \exp(-2662/T)$ and $k_{HAD2} = 9.2 \times 10^{-13} \exp(-2410 cal/RT)$ molecule^{-1}cm^{3}s^{-1}.

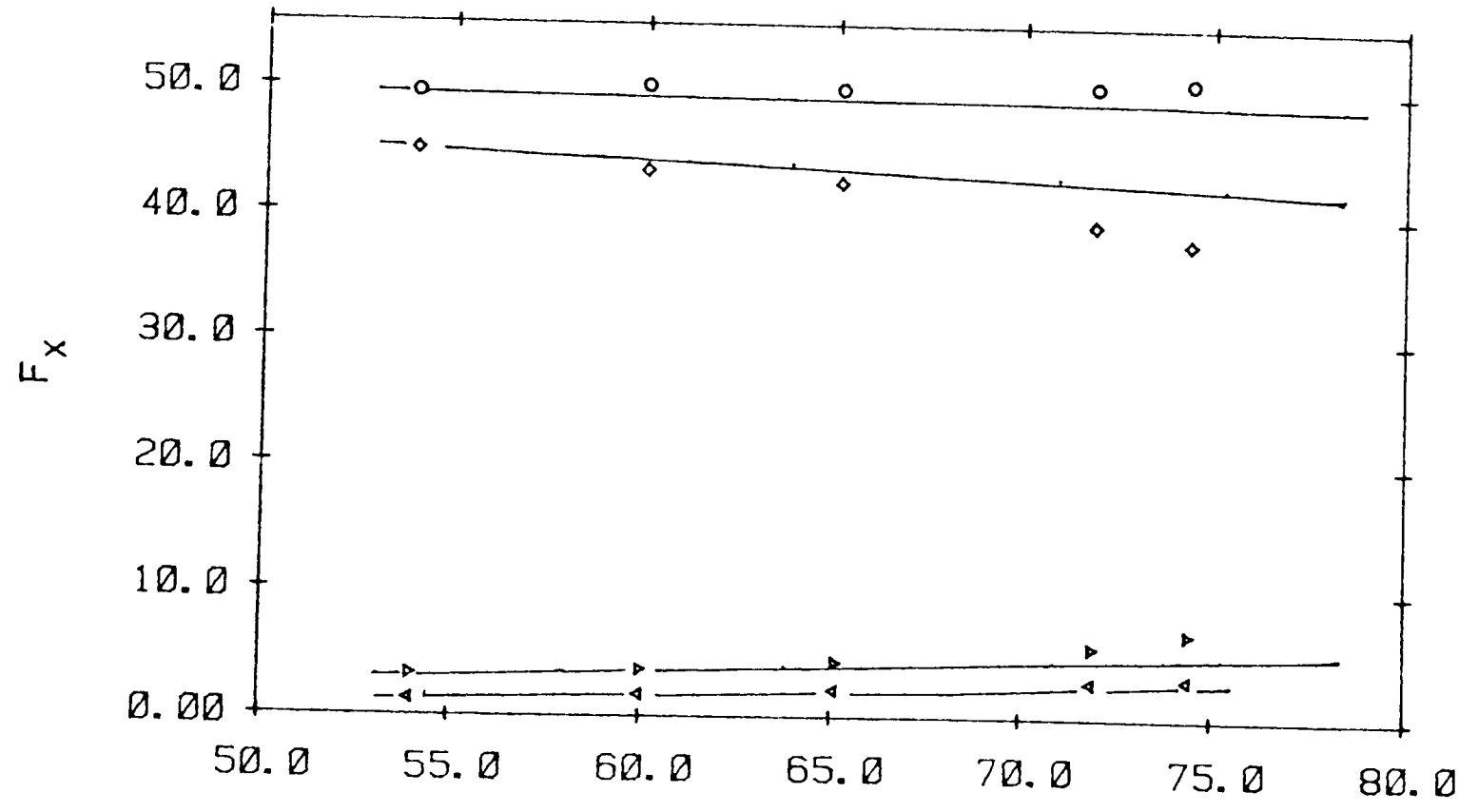

Figure 5.13. Comparison of Predicted and Experimental Fractional Product Yields at 1118K. Solid Lines: Model Predictions Using $k_{HA1} = 1.47 \times 10^{-21} T^{3.5} \exp(-2662/T)$ and $k_{HAD2} = 9.2 \times 10^{-13} \exp(-2410 cal/RT)$ molecule^{-1}cm^{3}s^{-1}. H_2 o, C_2H_4 ◇, CH_4 ▷, C_2H_2 ◁.

5.4.6 Modelling the Propylene Inhibition of Ethane Pyrolysis

The major routes leading to the removal of propylene in pyrolysis systems will involve its addition and abstraction reactions with hydrogen atoms:

$H + C_3H_6 \text{ ======> } I\text{-}C_3H_7$ RHAD5

$H + C_3H_6 \text{ ======> } N\text{-}C_3H_7$ RHAD6

$H + C_3H_6 \text{ ======> } H_2 + C_3H_5$ RHA8

The n-propyl and i-propyl radicals formed in the addition reactions will be short lived at cracking temperatures and will rapidly decompose to $CH_3 + C_2H_4$ and $H + C_3H_6$ respectively. Thus, only the non-terminal addition to produce n-propyl radicals will be of importance.

$H + C_3H_6 \text{ ======> } CH_3 + C_2H_4$ RHAD6

Although the rate constant for terminal addition has been directly measured [52,243], estimates of the activation energy for non-terminal addition are based on the the relative yields of end products arising from n-propyl and i-propyl radicals at room temperature [244], with the assumption that the Arrhenius A factors for the two additions are identical. Reviews by Allara and Shaw [217] and Kerr and Parsonage [231] recommend $k_{HAD6} = 1.3x10^{-11}exp(-2,900calmol^{-1}/RT)$ $molecule^{-1}cm^3s^{-1}$ and although this expression should be adequate around 300K, the assumptions involved in estimating the activation energy could lead to serious errors at pyrolysis temperatures.

The generally recommended expression for k_{HA8} is subject to even

greater uncertainty. Allara and Shaw use the average of two very different room temperature values of k_{add}/k_{abs} (0.082 [97] and 0.42 [245]) and the assumption that $A_{abs}= 1.7x10^{-10}$ $molecule^{-1}cm^3s^{-1}$ to estimate an activation energy of 3.5 $kcalmol^{-1}$. By analogy with the H + C_2H_6 reaction, which has an A factor of $2x10^{-10}$ $molcule^{-1}cm^3$, one might expect the A factor for RHA8 to be around $1x10^{-10}$ $molecule^{-1}cm^3$ on the basis of the lower number of abstractable hydrogen atoms. Walker [247] has recently found $k_{HA8}= (3.5\pm1.3)x10^{-13}$ $molecule^{-1}cm^3s^{-1}$ at 753K and estimates $k_{HA8}= 2.1x10^{-11}exp(-6000calmol^{-1}/RT)$, leading to a value of k_{HA8} which is a factor of 25 lower than that recommended by Allara and Shaw at 1118K.

Much work clearly needs to be done on both the abstraction and non-terminal addition reactions of hydrogen atoms with propylene. For the purposes of simulating the experimental data, the Arrhenius expressions $k_{HAD6}= 1.3x10^{-11}exp(-2900calmol^{-1}/RT)$ and $k_{HA8}= 5.3x10^{-11}exp(-3500calmol^{-1}/RT)$ were initiallly chosen for the two reactions.

The addition of carbon-containing radicals to propylene is known to be much slower than hydrogen atom addition. Furthermore, the additions of methyl and ethyl radicals produce C_4 and C_5, radicals which decompose very rapidly at cracking temperatures, generally regenerating the reactants:

$CH_3 + C_3H_6$ =====

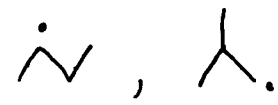

$C_2H_5 + C_3H_6$ =====



In the case of the non-terminal addition of ethyl radicals, two decomposition pathways are possible:

$C_2H_5 + C_3H_6$ =====  ===== $CH_3 + C_4H_8$

However such a mechanism for the interconversion of alkyl radicals will be extremely slow compared to other routes such as the reaction of methyl radicals with ethane, RMA1, and will not significantly affect the overall kinetics. The addition reactions of methyl and ethyl radicals with propylene and other unsaturated products were thus assumed to be unimportant.

The addition of vinyl radicals to propylene was considered explicitly and the reactions

$C_2H_3 + C_3H_6$ =====> $C_4H_6 + CH_3$ RVAD2

and $C_2H_3 + C_3H_6$ =====> $C_5H_8 + H$ RVAD3

were included in the scheme with rate constants assumed to be equal to that for the addition of vinyl radicals to ethylene, but were found to affect the model predictions only slightly. The abstraction reactions

$CH_3 + C_3H_6$ =====> $CH_4 + C_3H_5$ RMA4

$C_2H_3 + C_3H_6$ =====> $C_2H_4 + C_3H_5$ RVA3

were similarly found to be unimportant.

Simulations using the rate constants for the reactions of hydrogen atoms with propylene discussed above, qualitatively reproduced the experimental dependence of conversion and hydrogen yield on $[C_3H_6]_o$, but the experimental propylene conversions and increase in methane yield with $[C_3H_6]_o$ were significantly underestimated.

Varying the abstraction rate constant at 1118K between the value

recommended by Allara and Shaw ($3.5x10^{-11}$ molecule^{-1}cm^{3}s^{-1}) and that suggested by Walker ($1.4x10^{-12}$ molecule^{-1}cm^{3}s^{-1}) did not markedly alter the propylene conversion. This is because the rate of the C_3H_5 + H_2 reaction was fixed in direct proportion to the abstraction rate by the calculated equilibrium constant, resulting in near equilibrium between the two reactions when the highest value of k_{HA8} was used. Under all conditions, the flux through the back reaction was a significant fraction of the flux through the hydrogen atom abstraction and even at the highest $([C_3H_6]/[C_2H_6])_O$ ratios, the allyl radical concentration was never more than five times that predicted in the absence of added propylene, despite a 20 fold increase in $[C_3H_6]_O$. Increasing k_{HA8} did increase the methane yield somewhat, but the model still significantly underestimated F_{CH4}.

Both the propylene conversion and the fractional methane yield could be increased if the addition rate constant k_{HAD6} were made larger. Increasing k_{HAD6} by a factor of four to $5.2x10^{-11}exp(-2900calmol^{-1}/RT)$ was found to give reasonable agreement with experiment, as shown in Figures 5.14 and 5.15, although such a large increase in k_{HAD6} could only be accommodated if the A factor were substantially greater than that estimated at room temperature.

The predicted reduction in ethane conversion with increasing $[C_3H_6]_O$ showed a complex dependence on both k_{HA8} and k_{HAD6}. For a residence time of 1s at 1118K and a $([C_3H_6]/[C_2H_6])_O$ ratio of 0.1, the experimental reduction in conversion, compared to experiments with no added propylene was around 7%. Varying k_{HA8} between $1.4x10^{-12}$ and $3.5x10^{-11}$ molecule^{-1}cm^{3}s^{-1} increased the predicted reduction in conversion from 5.5 to 10.0%, if the lower value for k_{HAD6} of $3.6x10^{-12}$ molecule^{-1}cm^{3}s^{-1} was used. Setting k_{HAD6} to the value of

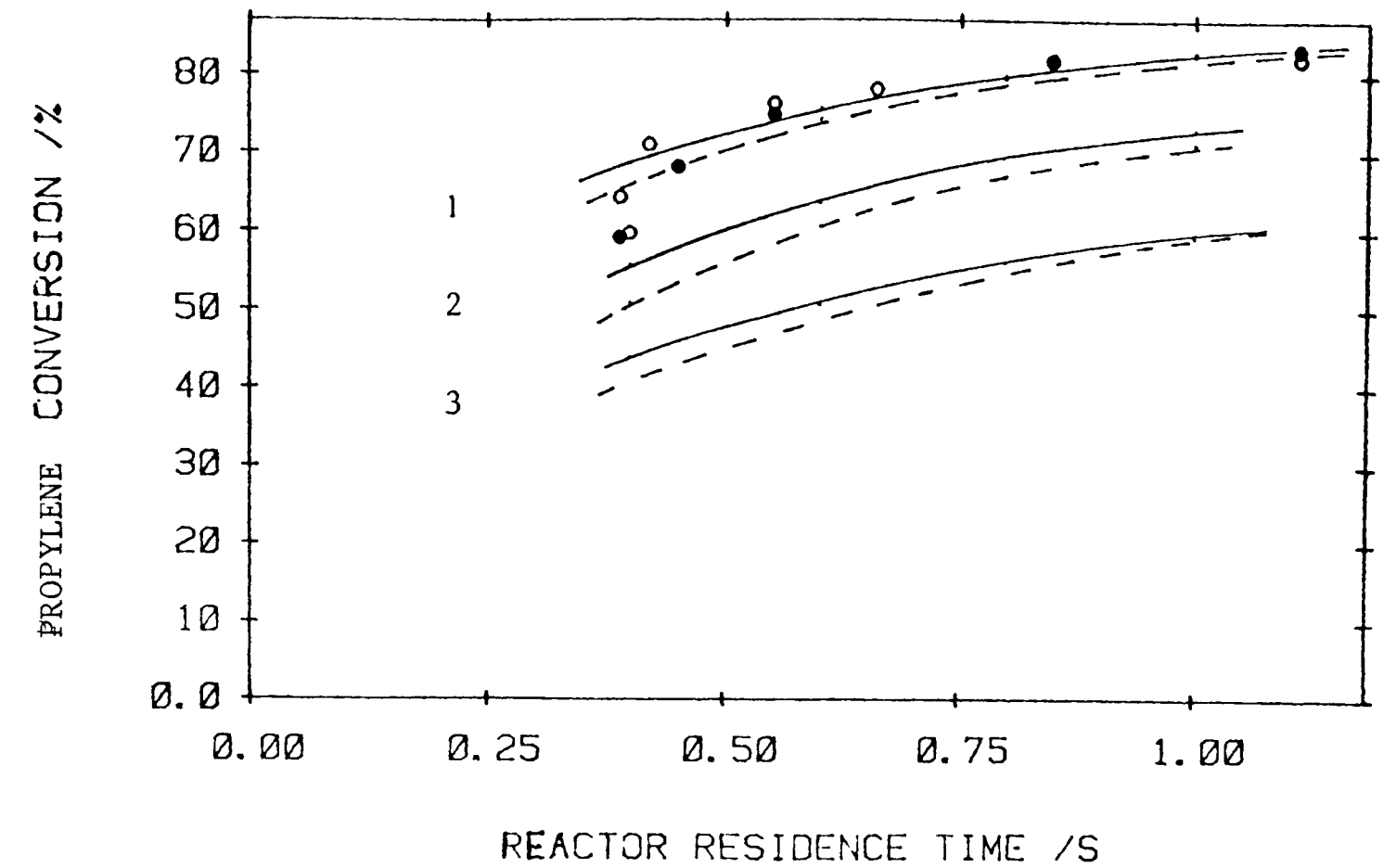

Figure 5.14. Dependence of Predicted Propylene Conversion on k_{HAD6} at 1118K. Circles: Experimental Data. $([C_3H_6]/[C_2H_6])_o$ = 0.05, o; 0.1, ●.
Dashed Lines: Model Predictions, $([C_3H_6]/[C_2H_6])_o$=0.1.

Solid Lines: Model Predictions, $([C_3H_6]/[C_2H_6])_o$ = 0.05.

1: k_{HAD6} = 5.2×10^{-11} exp(-2.9kcal/RT) $molecule^{-1} cm^3 s^{-1}$.
2: " = 2.6 " " "
3: " = 1.3 " " "

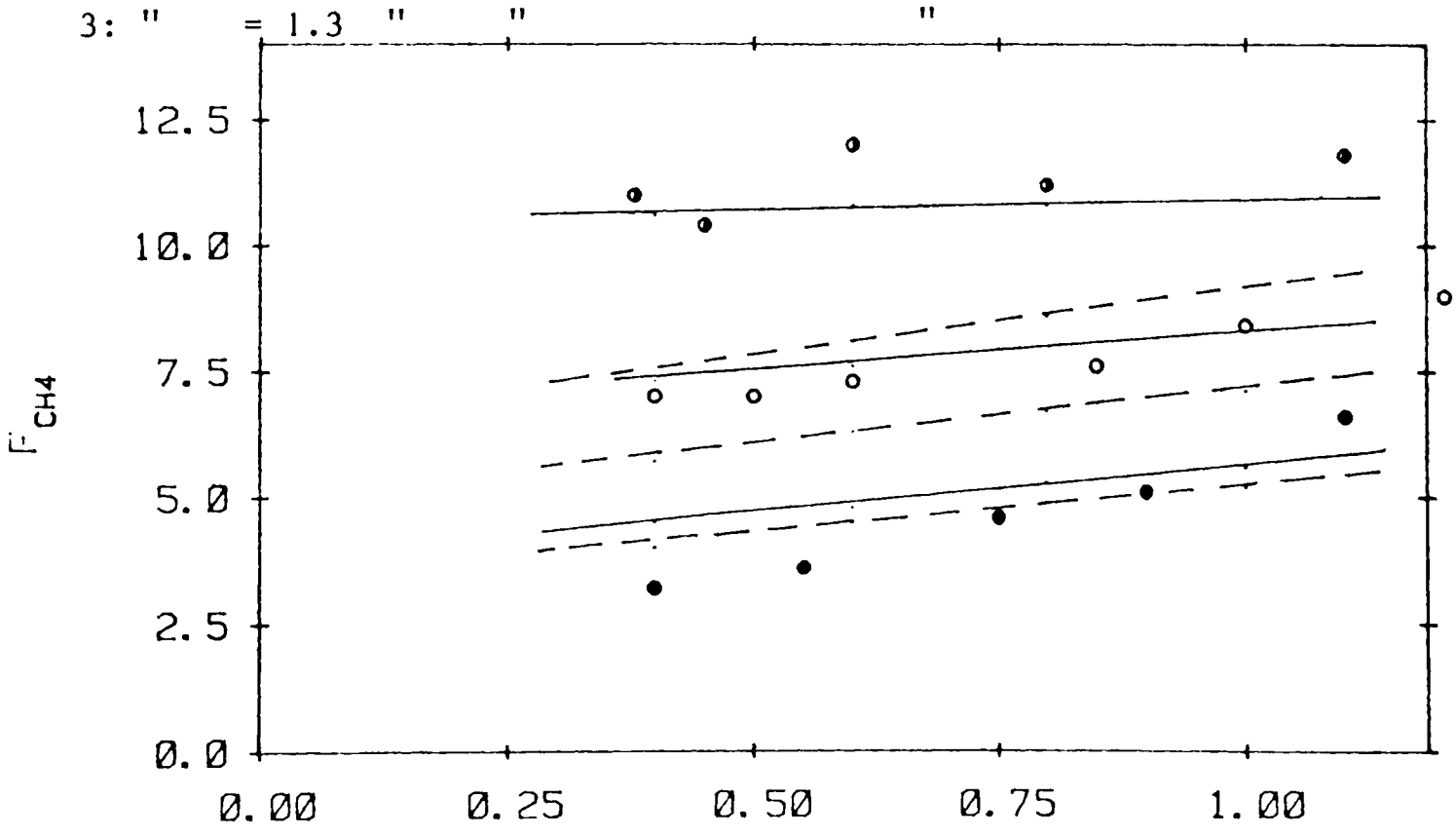

Figure 5.15. Dependence of Predicted Fractional Methane Yield on k_{HAD6} at 1118K. Circles: Experimental Data. $([C_3H_6]/[C_2H_6])_o$= ●, 0.005; o, 0.05; ●, 0.1. Dashed lines: Model Predictions, with k_{HAD6}= 1.3×10^{-11} exp(-2.9kcal/RT) $molecule^{-1} cm^3 s^{-1}$. Solid Lines: Model Predictions, with k_{HAD6}= 5.2×10^{-11} exp(-2.9kcal/RT) $molecule^{-1}$ c s^{-1}

$1.4x10^{-11}$ $molecule^{-1}cm^3s^{-1}$ required in order to reproduce the experimental propylene conversions, increased the reduction by 0.7% for the lowest value of k_{HA8}, but reduced it by 1.6% for the highest value of k_{HA8}. With the highest value of k_{HA8}, the flux through the abstraction was always greater than that through the addition, whereas the opposite held for the lowest value of k_{HA8}. This suggested that although the abstraction has the greater effect on conversion, both reactions lead to a net reduction in conversion as they both convert hydrogen atoms into less reactive radicals. Assuming that the addition rate constant is given by $k_{HAD6} = 5.2x10^{-11}exp(-2900cal/RT)$ $molecule^{-1}cm^3s^{-1}$ in order to fit the experimental methane yields and propylene conversions, then the overall reduction in ethane conversion was best reproduced by values of k_{HA8} in the middle of the range studied i.e. corresponding to the expression $k_{HA8} = 5.3x10^{-11}exp(-3500cal/RT)$ $molecule^{-1}cm^3s^{-1}$.

5.5 Conclusions

A model of ethane pyrolysis has been developed which qualitatively reproduces the observed dependence of ethane conversion and product distribution on temperature, reactor residence time and the concentration of added propylene inhibitor. However, the model predictions were shown to be very sensitive to the often poorly defined rates of a large number of reactions.

In particular, the absence of accurate data on the abstraction reaction of hydrogen atoms with ethylene:

$$H + C_2H_4 \text{ =====> } H_2 + C_2H_3$$

and the subsequent reactions of the vinyl radical, has been shown to place severe limitations on the detailed modelling of hydrocarbon pyrolysis using currently available kinetic information. The present substantial uncertainty surrounding the heat of formation and the reactions of the vinyl radical could be removed if studies similar to those presented in Chapters 2 and 3 were performed for the H + C_2H_2 reaction. A full pressure and temperature dependence of the addition rate constant would enable a model to be developed to accurately predict its absolute rate constant under the conditions found in industrial pyrolysis and the vinyl heat of formation could be unequivocally determined by direct observation of the H + C_2H_2 == C_2H_3 equlibrium. Furthermore, if the heat of formation of the vinyl radical were known, then reasonable estimates of its presently almost completely unknown reaction rates could be made, using thermochemical methods.

In general, the model was found to be extremely sensitive to the rates of hydrogen atom addition and abstraction reactions. Even the relatively small experimental uncertainty in what might be thought to be a very well studied reaction, the abstraction reaction with ethane

$$H + C_2H_6 \text{ =====> } H_2 + C_2H_5$$

was shown to introduce large uncertainties in the model predictions.

The inhibition of ethane pyrolysis by propylene was shown to be largely controlled by the addition and abstraction reactions of hydrogen atoms with the olefin.

$$H + C_3H_6 \text{ =====> } CH_3 + C_2H_4$$

$$H + C_3H_6 \text{ =====> } H_2 + C_3H_5$$

In conclusion, it is clear that very precise, direct information on a number of reactions is required if further progress is to be made towards a full understanding of hydrocarbon pyrolysis systems under conditions leading to high conversions.

1. M.G.Evans & M.Polanyi, Trans. Farad. Soc., 34, 11 (1938).

2. C.W.Gear, Commun. ACM, 14, 176 (1971).

3. C.W.Gear, Commun. ACM, 14, 185 (1971).

4. E.M.Chance, A.R.Curtis, I.P.Jones & C.R.Kirby, "FACSIMILE: A Computer Program For Flow and Chemistry Simulation, and General Initial Value Problems", AERE-R 8775, Harwell (1977).

5. D.Edelson, Comput. Chem. 1, 29 (1976).

6. R.N.Stabler & J.P.Cheside, Int.J.Chem.Kin., 10, 461 (1978).

7. M.B.Carver & A.W.Boyd, Int.J.Chem.Kin., 11, 1097 (1979).

8. R.K.Kee, J.A.Miller & T.H.Jefferson, "Chemkin: A General-Purpose, Problem-Independent, Transportable, Fortran Chemical Kinetics Code Package" SAN80-8003, Sandia (1980).

9. R.I.Cukier, H.B.Levine & K.E.Schuler, J.Comput.Phys., 26, 1 (1978).

10. J.T.Hwang, E.P.Dougherty, S.Rabitz & H.Rabitz, J.Chem.Phys., 69, 5180 (1978).

11. M.A.Kramer, R.J.Kee & H.Rabitz, "Chemsen: A Computer Code For Sensitivity Analysis of Elementary Chemical Reaction Models", Princeton University.

12. E.P.Dougherty & H.Rabitz, J.Chem.Phys., 72, 6571 (1980).

13. A.R.Ravishankara & R.L.Thompson, Chem.Phys.Lett., 99, 377 (1983).

14. A.R.Ravishankara, J.M.Nicovich, R.L.Thompson & F.P. Tully, J.Phys.Chem., 85, 2498 (1981).

15. W.Felder, A.Fontijn, H.N.Voltrauer & D.R.Voorhees, Rev. Sci. Instrum. 51, 195 (1980).

16. P.W.Fairchild, G.P.Smith & D.R.Crosley, 19 t h Int. Symp. Comb.,

107 (1982).

17. D.A.Parkes, D.M. Paul & C.P.Quinn, J.Chem.Soc.Farad.Trans.I, 72, 1935 (1978).

18. H.Adachi, N.Basco & D.G.L.James, Int.J.Chem.Kin., 11, 995 (1979).

19. D.M.Golden, K.Y.Choo, M.J.Perona & L.W.Piskiewic, Int.J.Chem.Kin., 8, 381 (1976).

20. T.Koike & K.Moringa, Bull.Chem.Soc.Jpn., 54, 2439 (1981).

21. J.E.Baggott & M.J.Pilling, Royal Society of Chemistry Ann. Reports C (1982).

22. I.R.Slagle, J.-Y.Park, M.C.Heaven & D.Gutman, J.Am.Chem.Soc. 106, 4356 (1984).

23. J.M.Tulloch, M.T.Macpherson, C.A.Morgan & M.J.Pilling, J.Phys.Chem., 86, 3812 (1982).

24. D.A.Parkes & C.P.Quinn, J.Chem.Soc.Farad.Trans.I, 72, 1952 (1976).

25. H.Adachi & N.Basco, Int.J.Chem.Kin., 13, 367 (1981).

26. M.T.Macpherson, M.J.Pilling & M.J.C.Smith, J.Phys.Chem., 89, 2268 (1985).

27. E.A.Selzer & K.D.Bayes, J.Phys.Chem., 87, 392 (1983).

28. C.A.Morgan, M.J.Pilling & J.M.Tulloch, J.Chem.Soc. Farad.Trans.II, 78, 1323 (1982).

29. M.J.Pilling & M.J.C.Smith, J.Phys.Chem., 89, 4713 (1985).

30. P.H.Wine & A.R.Ravishankara, Chem.Phys., 69, 365 (1982).

31. J.A.Davidson, C.M.Sadowski, H.I.Schiff, G.E.Streit, C.J.Howard, D.A.Jennings & A.L.Schmeltekopf, J.Chem.Phys. , 64, 57 (1976).

32. J.W.Cox, H.H.Nelson & J.R.McDonald, Chem.Phys., 96, 175 (1985).

33. J.V.Michael, D.T.Osbourne & G.N.Suess, J.Chem.Phys., 58, 2800

(1973).

34. M.N.R.Ashfold, M.A.Fullstone, G.Hancock & G.W.Ketley, Chem.Phys., 55, 245 (1981).

35. I.R.Slagle & D.Gutman, J.Am.Chem.Soc., 104, 4741 (1982).

36. H.Reisler, M.S.Mangir & C.Wittig, J.Chem.Phys., 73, 2280 (1980).

37. L.Pasternak & J.R.McDonald, Chem.Phys., 43, 173 (1979).

38. V.Subba Rao & G.B.Skinner, J.Phys.Chem., 88, 4362 (1984).

39. C.C.Chang & G.B.Skinner, 18th Int. Symp. Comb. 915 (1981).

40. D.Benfield & G.B.Skinner, J.Phys.Chem., 87, 3732 (1983).

41. P.Frank & Th.Just, Ber.Bunsen.Phys.Chem. 89, 181 (1985).

42. G.P.Smith, P.W.Fairchild & D.R.Crosley, J.Chem.Phys., 81, 2667 (1984).

43. U.C.Sridharan & F.Kaufman, Chem.Phys.Lett., 102, 45 (1983).

44. H.Hoffmeyer, O.Horie, P.Potzinger & B.Reimann, J.Phys.Chem., 89, 2901 (1985).

45. P.Camilleri, R.M.Marshall & J.H.Purnell, J.Chem.Soc. Farad.Trans.I, 70, 1434 (1974).

46. J.Lede & J.Villermaux, Can.J.Chem., 56, 392 (1978).

47. J.-Y.Park & D.Gutman, J.Phys.Chem., 87, 1844 (1983).

48. T.Hikada, J.A.Eyre & L.M.Dorfman, J.Chem.Phys., 54, 3422 (1971).

49. K.Yang, J.Am.Chem.Soc., 84, 719 (1962).

50. D.Mihelcic, V.Schubert, F.Hofler & P.Potzinger, Ber. Bunsen.Phys.Chem. 79, 1230 (1975).

51. K.Sugawara, K.Okazaki & S.Sato, Bull.Chem.Soc.Jpn., 54, 2872 (1981).

52. G.W.Harris & J.N.Pitts Jr., J.Chem.Phys., 77, 3994 (1982).

53. K.Sugawara, K.Okazaki & S.Sato, Chem.Phys.Lett., 78, 259 (1981).

54. O.Klais, P.C.Anderson & M.J.Kurylo, Int.J.Chem.Kin., 12, 469

(1980).

55. U.C.Sridharan, B.Reimann & F.Kaufman, J.Chem.Phys., 73, 1286 (1980).

56. G.Inoue, M.Okuda & W.Akimoto, J.Chem.Phys., 75, 2060 (1981).

57. B.D.Cannon, J.S.Robertshaw, I.W.M.Smith & M.D.Williams , Chem.Phys.Lett., 105, 380 (1984).

58. J.E.Spencer, H.Endo & G.P.Glass, 16 t h Int.Symp.Comb. , 829 (1976).

59. T.-X.Xiang, L.M.Torres & W.A.Guillory, J.Chem.Phys., 83, 1623 (1985).

60. C.J.Hochanadel, J.A.Ghormley, J.W.Boyle & P.J.Ogren, J.Phys.Chem., 81, 3 (1977).

61. C.Anastasi & P.Maw, J.Chem.Soc.Farad.Trans.I, 78, 2423 (1982).

62. A.O.Longford, H. Petek & C.B.Moore, J.Chem.Phys., 78, 6650 (1983).

63. R.Lesclaux, J.C.Soulignac & P.V.Khe, Chem.Phys.Lett., 43, 520 (1976).

64. R.Lesclaux, B.Veyret & P.Roussel, Ber.Bunsen.Phys.Chem., 89, 330 (1985).

65. J.P.Reilly, J.H.Clark, C.B.Moore & G.C.Pimentel, J.Chem.Phys., 69, 4381 (1978).

66. G.A.Laguna & S.L.Baughcum, Chem.Phys.Lett., 88, 568 (1982).

67. R.P.Ruiz & K.D.Bayes, J.Phys.Chem., 88, 2592 (1984).

68. I.R.Slagle & D.Gutman, J.Am.Chem.Soc., 107, 5342 (1985).

69. Y.-P.Lee & C.J.Howard, J.Chem.Phys., 77, 756 (1982).

70. M.J.Kurylo & R.B.Timmons, J.Chem.Phys., 50, 5076 (1969).

71. P.D.Pacey & J.H.Purnell, J.Chem.Soc.Farad.Trans.I, 68, 1462 (1972).

72. R.Zellner, J.Phys.Chem., 83, 18 (1979).

73. J.Troe, Ber.Bunsen.Phys.Chem., 87, 161 (1983).

74. R.Gilbert, K.Luther & J.Troe, Ber.Bunsen.Phys.Chem., 87, 169 (1983).

75. D.R.Stull, E.F.Westrum Jr. & G.C.Sinke, "The Chemical Thermodynamics of Organic Compounds", John Wiley & Sons (1969).

76. D.M.Golden & S.W.Benson, Chem.Rev., 69, 125 (1969).

77. D.F.McMillan & D.M.Golden, Ann.Rev.Phys.Chem., 493 (1982).

78. W.Tsang, Int.J.Chem.Kin., 10, 821 (1978).

79. W.Tsang, J.Am.Chem.Soc., 107, 2872 (1985).

80. A.L.Castelhano, P.R.Marriot & D.Griller, J.Am.Chem.Soc., 103, 4262 (1981).

81. P.D.Pacey & J.H.Wilamasena, J.Phys.Chem., 84, 2221 (1980).

82. J.R.Cao & M.H.Back, Int.J.Chem.Kin., 16, 961 (1984).

83. J.H.Purnell & C.P.Quinn, J.Chem.Soc., 4049 (1964).

84. J.Pacansky, D.E.Horne, G.P.Gardini & J.Bargon, J.Phys.Chem., 81, 2149 (1977).

85. J.Pacansky & M.Dupius, J.Chem.Phys., 71, 2095 (1979).

86. J.Pacansky & H.Coufal, J.Chem.Phys., 72, 5285 (1980).

87. J.Pacansky & H.Coufal, J.Chem.Phys., 72, 3298 (1980).

88. J.Pacansky, D.W.Brown & J.S.Chang, J.Phys.Chem., 85, 2562 (1981).

89. J.Pacansky & M.Dupius, J.Am.Chem.Soc., 104, 415 (1982).

90. J.Pacansky & B.Schraeder, J.Chem.Phys., 78, 1033 (1983).

91. J.Pacansky & A.Gutierrez, J.Phys.Chem., 87, 3074 (1983).

92. V.P.Strunin, A.F.Dodonov, G.K.Lavrovskaya & V.T. Talrose, Kinetics and Catalysis, 7, 610 (1966).

93. J.V.Michael & R.E.Weston Jr., J.Chem.Phys., 45, 3632 (1966).

94. W.Braun & M.Lenzi, Disc.Farad.Soc., 44, 252 (1967).

95. J.M.Brown & B.A.Thrush, Trans.Farad.Soc., 63, 630 (1967).

96. J.V.Michael & D.T.Osbourne, Chem.Phys.Lett., 3, 402 (1969).

97. G.R.Wooley & R.J.Cvetanovic, J.Chem.Phys., 50, 4697 (1969).

98. R.J.Cvetanovic & L.C.Doyle, J.Chem.Phys., 50, 4705 (1969).

99. J.H.Knox & D.G.Dalgleish, Int.J.Chem.Kin., 1, 69 (1969).

100. A.A.Westenberg & N.de Haas, J.Chem.Phys., 50, 707 (1969).

101. J.A.Eyre, T.Hikada & L.M.Dorfman, J.Chem.Phys., 53, 1281 (1970).

102. M.J.Kurylo, N.C.Peterson & W.Braun, J.Chem.Phys., 53, 2776 (1970).

103. M.P.Halstead, D.A.Leathard, R.M.Marshall & J.H. Purnell, Proc.Roy.Soc.A, 316, 575 (1970).

104. J.R.Barker, D.G.Keil, J.V.Michael & D.T.Osbourne, J.Chem.Phys., 52, 2079 (1970).

105. T.Hikada, J.A.Eyre & L.M.Dorfman, J.Chem.Phys., 54, 3422 (1971).

106. R.D.Penzhorn & B.de B.Darwent, J.Chem.Phys., 55, 1508 (1971).

107. L.Teng & W.E.Jones, J.Chem.Soc.Farad.Trans.I, 68, 1267 (1972).

108. J.A.Cowfer & J.V.Michael, J.Chem.Phys., 62, 3504 (1975).

109. G.Pratt & I.Veltman, J.Chem.Soc.Farad.Trans.I, 72, 1733 (1976).

110. E.B.Gordon, B.I.Ivanov, A.P.Perminov & Balalaev, Chem. Phys. 35, 79 (1978).

111. J.H.Lee, J.V.Michael, W.A.Payne & L.J.Stief, J.Chem.Phys., 68, 1817 (1978).

112. Y.Ishikawa, M.Yamabe, A.Noda & S.Sato, Bull.Chem.Soc. Jpn., 51, 2488 (1978).

113. K.Oka & R.J.Cvetanovic, Can.J.Chem., 57, 777 (1979).

114. R.Ellul, P.Potzinger, B.Reimann & P.Camilleri, Ber. Bunsen.Phys.Chem., 85, 407 (1981).

115. K.Sugawara, K.Okazaki & S.Sato, Bull.Chem.Soc.Jpn., 54, 358 (1981).

116. M.Brouard, D.Phil. Thesis, University of Oxford (1986).

117. S.P.McOwan, Part II Thesis, University of Oxford (1985).

118. W.Braun & T.Carrington, J.Quant.Spectrosc.Radiat. Trans., 9, 1133 (1969).

119. P.R.Bevington, "Data Reduction and Error Analysis for the Physical Sciences", McGraw-Hill (1969).

120. R.A.Back & D.W.L.Griffiths, J.Chem.Phys., 46, 4839 (1967).

121. J.M.Nicovitch & A.R.Ravishankara, J.Phys.Chem., 88, 2534 (1984).

122. S.Madronich & W.Felder, J.Phys.Chem., 88, 1857 (1984).

123. H.Okabe, "Photochemistry of Small Molecules", J.Wiley & Sons (1978).

124. K.F.Preston and R.F.Barr, J.Chem.Phys., 54, 3347 (1971).

125. H.Yamazaki & R.J.Cvetanovic, J.Chem.Phys., 41, 3703 (1964).

126. K.F.Preston & R.J.Cvetanovic, J.Chem.Phys., 45, 2888 (1966).

127. G.Paraskevopoulos & R.J.Cvetanovic, J.Am.Chem.Soc., 91, 7572 (1969).

128. R.Browarzik & F.Stull, J.Phys.Chem., 88, 6004 (1984).

129. H.E.Hunziker, H.Kneppe & H.R.Wendt, J.Photochem., 17, 377 (1981).

130. K.Schofield, J.Photochem., 9, 55 (1978).

131. P.H.Wine & A.R.Ravishankara, Chem.Phys.Lett., 77, 103 (1981).

132. D.L.Baulch, R.A.Cox, P.J.Crutzen, R.F.Hampson Jr., J.A.Kerr, J.Troe & R.T.Watson, J.Phys.Chem.Ref.Dat., 11, 327 (1982).

133. W.B.De More, J.Phys.Chem., 73, 391 (1969).

134. R.F.Heidner III & D.Husain, Int.J.Chem.Kin., 6, 77 (1974).

135. R.Zellner & K.Lorentz, J.Phys.Chem., 88, 984 (1984).

136. W.Braun, C.Carlone,T.Carrington,G. Van Volkenburgh & R.A.Young J.Chem.Phys., 53, 4244 (1970).

137. M.Bartels, K.Hoyermann & R.Sievert, 19 t'h Int.Symp.Comb., 61 (1982).

138. V.N.Kondratiev, NSRDS COM-72-100 14 (1972).

139. R.Atkinson, R.A.Perry & J.N.Pitts Jnr., Chem.Phys.Lett., 44, 204 (1976).

140. R.McDiarmid, J.Phys.Chem., 84, 64 (1980).

141. P.J.Robinson & K.A.Holbrook, "Unimolecular Reactions", Wiley (1972).

142. I.Oref & B.S.Rabinovitch, J.Phys.Chem., 72, 4488 (1968).

143. D.G.Truhlar, W.L.Hase & J.T.Hynes, J.Phys.Chem., 87, 2664 (1983).

144. D.C.Tardy & B.S.Rabinovitch, J.Chem.Phys., 45, 3720 (1966).

145. J.Troe, J.Phys.Chem., 83, 114 (1979).

146. A.E.C. de Cobos, H.Hippler & J.Troe, J.Phys.Chem., 88, 5083 (1984).

147. C.J.Cobos, H.Hippler, K.Luther, A.R.Ravishankara & J.Troe, J.Phys.Chem., 89, 4332 (1985).

148. J.Pacansky & M.Dupuis, J.Chem.Phys., 68, 4276 (1978).

149. J.L.Duncan, Mol.Phys., 28, 1177 (1974).

150. J.L.Duncan, D.C.McKean & P.D.Mallinson, J.Mol.Spectrosc., 45, 221 (1973).

151. W.L.Hase & H.B.Schlegel, J.Phys.Chem., 86, 3901 (1982).

152. W.L.Hase, Acc.Chem.Res., 16, 258 (1983).

153. W.L.Hase, R.J.Wolf & C.S.Sloane, J.Chem.Phys., 76, 2771 (1982).

154. M.Quack & J.Troe, in "Gas Kinetics & Energy Tranfer", eds. P.G.Ashmore & R.J.Donovan, Chemical Society Specialist Periodical Reports, 2, 175 (1977).

155. E.E.Nikitin, "Theory of Elementary Atomic and Molecular Processes in Gases", Oxford University Press (1974).

156. L.F.Loucks & K.J.Laidler, Can.J.Chem., 45, 2795 (1967).

157. M.C.Lin & M.H.Back, Can.J.Chem., 44, 2357 (1966).

158. R.McDiarmid & E.Charney, J.Chem.Phys., 47, 1517 (1967).

159. A.J.Merer & R.S.Mulliken, J.Chem.Phys., 50, 1026 (1969).

160. M.C.Sauer Jr. & L.M.Dorfman, J.Chem.Phys., 35, 497 (1961).

161. P.Borrell, A.Cervenka & J.W.Turner, J.Chem.Soc.B 2293 (1971).

162. W.A.Payne & L.J.Stief, J.Chem.Phys., 64, 1150 (1976).

163. S.W.Benson, "Thermochemical Kinetics" 2nd Ed., Wiley (1976).

164. G.Ayranchi & M.H.Back, Int.J.Chem.Kin., 13, 897 (1981).

165. M.Brouard, personal communication.

166. M.Abramowitz & I.A.Stegun, Eds., "Handbook of Mathematical Functions", Dover (1970).

167. R.R.Baldwin, R.F.Simmons & R.W.Walker, Trans.Farad.Soc., 62, 2486 (1966).

168. Th.Just, P.Roth & R.Damm, 16th Int.Symp.Comb., 961 (1976).

169. G.B.Skinner, R.G.Sweet & S.K.Davis, J.Phys.Chem., 75, 1 (1971).

170. S.W.Benson & G.R.Haugen, J.Phys.Chem., 71, 1735 (1967).

171. J.Peeters & G.Mahren, Comb.Inst.European Symp., 53 (1973).

172. Yu.P.Lampolskii, Kinetics and Catalysis, 15, 938 (1973).

173. P.W.Atkins, "Physical Chemistry", Oxford University Press (1978).

174. L.Wolniewicz, J.Chem.Phys., 78, 6173 (1983).

175. JANAF Thermochemical Tables, 2nd Ed., D.R.Stull, H.Prophet, NSRDS-NBS37, Catalog No. C48:37, U.S. Government Printing Office, Washington D.C. (1971).

176. C.F.Melius, personal communication.

177. M.T.Macpherson, M.J.Pilling & M.J.C.Smith, Chem.Phys.Lett., 94, 430 (1983).

178. J.E.Baggott, M.A.Coles, A.Davis, P.D.Lightfoot, M.T.Macpherson & M.J.Pilling, to be published.

179. R.B.Cundall & A.S.Davies, Prog.React.Kinet., 4, 149 (1967) and references therein.

180. A.Gandini & P.A.Hackett, J.Am.Chem.Soc., 99, 6195 (1977).

181. G.D.Greenblatt, S.Ruhman & Y.Haas, Chem.Phys.Lett., 112, 200 (1984).

182. H.Adachi, N.Basco & D.G.L.James, Chem.Phys.Lett., 59, 502 (1978).

183. C.A.Winkler, Trans.Farad.Soc., 31, 761 (1935).

184. D.S.Herr & W.A.Noyes Jr., J.Am.Chem.Soc., 62, 2052 (1940).

185. W.M.Manning, J.Am.Chem.Soc., 56, 2589 (1934),

186. J.P.Howe & W.A.Noyes Jr., J.Am.Chem.Soc., 58, 1404 (1936).

187. P.Potzinger & G. Von Bunau, Ber.Bunsen.Phys.Chem., 72, 195 (1968).

188. J.S.Lake & A.J.Harrison, J.Chem.Phys., 30, 361 (1959).

189. M.B.Robin, "Higher Excited States of Polyatomic Molecules" Wiley (1974).

190. M.B.Robin & N.A.Keubler, J.Mol.Spectrosc., 33, 274 (1970).

191. B.Thompson, "Fundamentals of Gas Analysis by Gas Chromatography", Varian Associates Inc. (1977).

192. A.E.Ledford & W.Braun, Rev.Sci.Instrum., 48, 537 (1977).

193. M.J.C.Smith, D.Phil. Thesis, University of Oxford (1985).

194. G.Perkins, in "Gas Chromatography", Eds. Brenner, Callen & Weiss, Academic Press (1982).

195. E.Hecht & A.Zajac, "Optics", Addison-Westley (1974).

196. J.A.Kerr, in "Comprehensive Chemical Kinetics", Eds. G.H.Bamford & C.F. H.Tipper, Elsevier Scientific (1976).

197. K.C.Ferguson & J.T.Pearson, Trans.Farad.Soc., 66, 910 (1970).

198. L.Batt & S.I.Mowat, Int.J.Chem.Kin., 16, 603 (1984).

199. D.A.Parkes, Chem.Phys.Lett., 77, 527 (1981).

200. J.W.Davies, personal communication.

201. F.O.Rice & K.F.Herzfeld, J.Am.Chem.Soc., 56, 284 (1934).

202. R.K.Brinton, J.Am.Chem.Soc., 83, 1541 (1961).

203. J.Troe, J.Phys.Chem., 87, 1800 (1983).

204. L.J.-T.Lin & P.Ausloos, J.Photochem., 1, 453 (1972).

205. A.B.Callear & H.E.Van Den Bergh, Chem.Phys.Lett., 5, 23 (1970).

206. J.J.Ahumada, J.V.Michael & D.T.Osbourne, J.Chem.Phys., 57, 3736 (1972).

207. J.H.Keiffer & K.A.Budach, Int.J.Chem.Kin., 16, 679 (1984).

208. A.B.Callear & P.M.Wood, Chem.Phys.Lett., 5, 128 (1970).

209. M.J.Pilling, J.A.Robertson & G.J.Rogers, Int.J.Chem.Kin., 8, 883 (1976).

210. W.Braun, A.M.Bass & M.J.Pilling, J.Chem.Phys., 52, 5131 (1970).

211. G.Herzberg "Electronic Spectra of Polyatomic Molecules", Van Nostrand (1966).

212. C.Yamada, E.Hirota & K.Kawaguchi, J.Chem.Phys., 75, 5256 (1981).

213. R.K.Sparks, K.Shobotake, L.R.Carlson & Y.T.Lee, J.Chem.Phys.,75, 3838 (1981).

214. T.Nagata, M.Suzuki, K.Suzuki,T.Kankaru & T.Kondow, Chem.Phys. 88, 163 (1984).

215. M.Swarc & J.Watson Taylor, J.Chem.Phys., 23, 2310 (1955).

216. D.Clark & H.O.Pritchard, J.Chem.Soc., 2136 (1956).

217. D.L.Allara & R.Shaw, J.Phys.Chem.Ref.Data, 9, 523 (1980).

218. M.Kieffer, personal communication.

219. M.Brouard, M.T.Macpherson, M.J.Pilling, J.M.Tulloch & A.P. Williamson, Chem.Phys.Lett., 113, 413 (1985).

220. M.C.Lin & M.H.Back, Can.J.Chem., 44, 505 (1966).

221. M.C.Lin & M.H.Back, Can.J.Chem., 44, 2369 (1966).

222. A.B.Trenwith, J.Chem.Soc.Farad.Trans.I, 75, 614 (1979).

223. S.Corbel, P.M.Marquaire & G.M.Come, Chem.Phys.Lett., 80, 34 (1981).

224. K.Kanan, H.Purnell & A.Sepherad, Int.J.Chem.Kin., 15, 845 (1983).

225. A.Burcat, G.B.Skinner, R.W.Crosley & K.Scheller, Int.J.Chem.Kin., 5, 345 (1973).

226. D.B.Olsen, T.Tanzawara & W.C.Gardiner, Int.J.Chem.Kin., 11, 23 (1979).

227. Y.Hikada, S.Shiba, H.Takuma & M.Suga, Int.J.Chem.Kin., 17, 441 (1985).

228. D.Edelson & D.L.Allara, Int.J.Chem.Kin., 12, 605 (1980).

229. S.F.Bush, Trans.Instn.Chem.Engrs., 47, T59 (1969).

230. J.Warnatz, in "Combustion Chemistry" ed. W.C.Gardiner, Springer-Verlag (1984).

231. J.A.Kerr & M.J.Parsonage, "Evaluated Kinetic Data for Gas Phase Addition Reactions", CRC Press, Butterworths (1972).

232. J.R.Cao & M.H.Back, Can.J.Chem., 62, 86 (1984).

233. J.R.Cao & M.H.Back, Can.J.Chem., 60, 3039 (1982).

234. J.H.Purnell & C.P.Quinn, J.Chem.Soc., 4128 (1961).

235. H.E.Hunziker, H.Kneppe, A.D.McLean, P.Siegbahn & H.R.Wendt, Can.J.Chem., 61, 993 (1983).

236. A.B.Callear & G.B.Smith, Chem.Phys.Lett., 105, 119 (1984).

237. J.H.Kieffer, H.C.Wei, R.D.Kern & C.H.Wu, Int.J.Chem.Kin., 17, 225 (1985).

238. R.B.Sharma, N.M.Semo & W.S.Koski, Int.J.Chem.Kin., 17, 831 (1985).

239. R.M.Marshall, J.H.Purnell & B.C.Shurlock, Can.J.Chem., 44, 2778 (1966).

240. G.A.Chappell & H.Shaw, J.Phys.Chem., 72, 4672 (1968).

241. A.Burcat, Fuel, 54, 87 (1975).

242. J.H.Kieffer, M.Z.Al-Alami & K.A.Budach, J.Phys.Chem., 86, 808 (1982).

243. M.J.Kurylo, N.C.Peterson & W.Braun, J.Chem.Phys., 54, 4662 (1971).

244. W.E.Falconer & W.A.Sunder, Int.J.Chem.Kin., 3, 395 (1971).

245. B.de B.Darwent & R.Roberts, Disc.Farad.Soc., 14, 55 (1953).

246. R.W.Walker, personal communication.

247. D.L.Baulch & J.Duxbury, Combustion and Flame, 37, 313 (1980).

Appendix 1

Calculation of Initial Atom Concentrations in H + C_2H_4 Experiments

60 mJ pulse, dimensions 0.8x2.4 cm ==> 31.6 $mJcm^{-2}$.

Defocusing lens expands beam to ↶ 1.9x5.5 cm at monitoring zone: 31.6 $mJcm^{-2}$ ==> 5.8 $mJcm^{-2}$.

Four surfaces, 2 at window, 2 at lens, ↶4% normal incidence reflection loss at each: 5.8 $mJcm^{-2}$ ==> 5 $mJcm^{-2}$.

Each 193.3 nm photon carries $1x10^{-18}$ J: flux incident upon monitoring zone = $5x10^{15}$ $photoncm^{-2}$.

For $[N_2O]$ = $1x10^{15}$ $moleculecm^{-3}$, σ = $1.1x10^{-19}$ $molecule^{-1}cm^2$, σc = $1.1x10^{-4}$ cm^{-1}. ==> $5.5x10^{11}$ photons absorbed per cm.

Quantum Yield for $O(^1D)$ production > 0.97.

==> $[O(^1D)]_o$ = $5.5x10^{11}$ cm^{-3} for a 60 mJ laser pulse.

This estimate represents an upper limit, as absorption losses in the cell window and defocusing lens have been ignored.

Appendix 2. First-Order Rate Constants
From Chapter 2

Appendix 3. First-Order Rate Constants
From Chapter 3

Appendix 4. Listing of the Chromatographic Method Used in Acetone Photolysis Studies

```
DUAL CHANNEL METHOD: ACETDUAL                0:46    0 JAN 79

SECTION 1: BASIC
PAGE 1
  CONTROL
  PRIMARY METHOD: CONTROLS INSTRUMENT/AUTOSAMPLER AS REQUIRED
    METHOD: ACETFID
  SECONDARY: NO CONTROL UNLESS SEPARATE INSTRUMENT OR AUTOSAMPLER
    METHOD: ACETTCD
    INJECT OR RECALC: I
  <RECALC ONLY>
    DATA FILE:
    LOCATION: U
  SYNCHRONOUS START: Y

PAGE 2
  REPORT INSTRUCTIONS
  WHERE TO REPORT: L
  COPIES: 0
  TITLE:
  RATIO RESULTS: N

PAGE 3
  PLOT INSTRUCTIONS
  DUAL PLOT: Y
  PRIMARY PLOT: L

PAGE 4
  CHART SPEED
    PAGES OR CM/MIN: C
    INIT VALUE:  0.0
   LINE# TIME  CHART SPEED
   1       8.00      0.5
```

SINGLE CHANNEL METHOD: ACETFID 0:47 0 JAN 79

SECTION 1: BASIC
PAGE 1
ANALYSIS PARAMETERS
CHANNEL: 1
CALCULATION: ES
AREA/HT: A
STOP TIME: 91.00
NUMB EXPECTED PKS: 200
EQUILIBRATION TIME: 0
UNRETAINED PK TIME: 0.00
UNIDENT PK FACTOR: 0.000000
SLICE WIDTH: 10

PAGE 2
SAMPLE PARAMETERS
RUN TYPE: A
SAMPLE ID:
DIVISOR: 1.000000
AMT STD: 1.000000
MLTPLR: 1.000000

PAGE 3
REPORT INSTRUCTIONS
WHERE TO REPORT: L
COPIES: 2
TITLE: JUCOL RESULTS
FORMAT: E
DECIMAL PLACE: 4
RESULT UNITS: MTORR
REPORT UNIDENT PKS: Y
REPORT INSTRUMENT CONDITIONS: N

PAGE 4
PLOT INSTRUCTIONS
PLOT: Y
ZERO OFFSET: 10
ANNOTATION
RETENTION TIME: Y
PLOT CONTROL: Y
TIME TICKS: Y
TIME EVENTS: N
PK START/END: Y

PAGE 5
CHART SPEED
PAGES OR CM/MIN: C
INIT VALUE: 0.0

LINE#	TIME	CHART SPEED
1	8.00	0.5

PAGE 6
PLOT ATTEN
INIT PLOT ATTEN: 8

SECTION 2: TIME EVENTS
PAGE 1

LINE#	TIME	EVENT	VALUE
1	0.00	PR	100
2	0.00	SN	5
3	0.00	T%	5.0
4	0.00	WI	10
5	9.00	SB	5
6	10.50	II	10.50
7	18.00	WI	20
8	25.00	SB	4
9	37.00	WI	35
10	40.00	SB	1
11	40.50	II	40.50

SECTION 3: PEAK TABLE
PAGE 1
STD PK#: 0
RELATIVE RETEN PK#: 0

RESOLUTION PK#: 0
RESOLUTION MINIMUM: 0.0
FACT%: 5.0
IDENTIFICATION TIME WINDOWS +/-
REF
%: 10
MIN: 0.00
NON REF
%: 5
MIN: 0.00

PAGE 2

PK#	TIME	NAME	FACTOR	AMOUNT	REF GR#	MUST LO	MUST HI
1	12.60	*METHANE	0.065600	1.000000		0.000000	0.000000
2	18.60	*ETHYLENE	0.032000	1.000000		0.000000	0.000000
3	20.40	*ETHANE	0.031500	1.000000		0.000000	0.000000
4	28.50	*PROPYLENE	0.020800	1.000000		0.000000	0.000000
5	29.20	*PROPANE	0.020500	1.000000		0.000000	0.000000
6	30.50	*ALLENE	0.020800	1.000000		0.000000	0.000000
7	41.10	*ACETONE	0.034500	1.000000		0.000000	0.000000
8	51.80	*MEK	0.020700	1.000000		0.000000	0.000000

SECTION 4: GC INSTRUMENT CONTROL
PAGE 1
COL TEMP
ISO/INIT COL TEMP: 30
INIT HOLD TIME: 15.00

STEP#	FINAL TEMP	RATE	HOLD TIME
1	50	2.0	0.00
2	180	5.0	40.00

PAGE 2
DETECTORS
DET A TYPE: FID
DET B TYPE: TCD

LN#	TIME	SIDE	ATTN	RANGE	ZERO
1	0.00	A	1	12	Y
2	0.00	B	1	.5	Y
3	40.00	A	1	10	N
4	48.00	A	1	12	N

PAGE 3
TEMP/FLOW
INJ A TEMP: 250
INJ B TEMP: 250
ION TEMP: 250
TCD TEMP: 250
TCD FIL TEMP: 0
AUX TEMP:
COL A FLOW:
COL B FLOW:

PAGE 4

LN#	TIME	RELAY ON	RELAY OFF
1	0.00	23	
2	0.01	3	2
3	0.02		23
4	8.00	23	

SINGLE CHANNEL METHOD: ACETTCD 1:05 0 JAN 79

SECTION 1: BASIC
PAGE 1
ANALYSIS PARAMETERS
CHANNEL: 2
CALCULATION: A%
AREA/HT: A
STOP TIME: 28.00
NUMB EXPECTED PKS: 50
EQUILIBRATION TIME: 0
UNRETAINED PK TIME: 0.00
UNIDENT PK FACTOR: 0.000000
SLICE WIDTH: 10

PAGE 2
SAMPLE PARAMETERS
RUN TYPE: A
SAMPLE ID:
DIVISOR: 1.000000
AMT STD: 1.000000
MLTPLR: 1.000000

PAGE 3
REPORT INSTRUCTIONS
WHERE TO REPORT: L
COPIES: 1
TITLE:
FORMAT: N
DECIMAL PLACE: 4
RESULT UNITS: MTORR
REPORT UNIDENT PKS: Y
REPORT INSTRUMENT CONDITIONS: N

PAGE 4
PLOT INSTRUCTIONS
PLOT: Y
ZERO OFFSET: 10
ANNOTATION
RETENTION TIME: Y
PLOT CONTROL: Y
TIME TICKS: Y
TIME EVENTS: N
PK START/END: Y

PAGE 5
CHART SPEED
PAGES OR CM/MIN: C
INIT VALUE: 0.0

LINE#	TIME	CHART SPEED
1	8.00	0.5

PAGE 6
PLOT ATTEN
INIT PLOT ATTEN: 8

SECTION 2: TIME EVENTS
PAGE 1

LINE#	TIME	EVENT	VALUE
1	0.00	PR	200
2	0.00	SN	5
3	0.00	T%	5.0
4	0.00	WI	8
5	0.00	II	4.90
6	5.00	SB	8
7	10.50	II	10.50

SECTION 3: PEAK TABLE
PAGE 1
STD PK#: 0
RELATIVE RETEN PK#: 0
RESOLUTION PK#: 0
RESOLUTION MINIMUM: 0.0
FACT%: 5.0
IDENTIFICATION TIME WINDOWS +/-

```
  REF
    %: 20
    MIN:    0.00
  NON REF
    %: 10
    MIN:    0.00

PAGE 2
   PK# TIME  NAME          FACTOR    AMOUNT REF GR# MUST LO    MUST HI
   1    11.20 *CO         1.000000 1.000000        0.000000 0.000000


SECTION 4: GC INSTRUMENT CONTROL
PAGE 1
  COL TEMP
    ISO/INIT COL TEMP:  30
    INIT HOLD TIME:  20.00

PAGE 2
  DETECTORS
  DET A TYPE: FID
  DET B TYPE: TCD
   LN#  TIME SIDE ATTN RANGE ZERO
   1     0.00  A                Y
   2     0.00  B                Y

PAGE 3
  TEMP/FLOW
  INJ A TEMP:
  INJ B TEMP:
  ION TEMP:
  TCD TEMP:
  TCD FIL TEMP:
  AUX TEMP:
  COL A FLOW:
  COL B FLOW:

PAGE 4
```

Appendix 5. Product Yields From
Acetone Photolysis Experiments

Accompanying material
stored separately.
Search OLIS for shelfmark.

Appendix 6. Product Yields From
Ethane Pyrolysis Experiments.

Appendix 7

Reactions and Rate Constants Used to Model Ethane Pyrolysis Experiments

Rate constants are in molecular units, activation energies in $kcalmol^{-1}$. Several rate constants were calculated from the rates of the reverse reactions, using thermochemical methods, or were evaluated by Dr. M.J.Pilling. Such rate constants are labelled [MJP].

Initiation Reactions

R_{I1} C_2H_6 =====> $CH_3 + CH_3$

$k_{I1} = 2.0x10^{16}exp(-87.4/RT)$

Taken from the review by Baulch and Duxbury [247], k_{1I} reduced by 20% to allow for fall-off.

R_{I2} $N\text{-}C_4H_{10}$ =====> $2\ C_2H_5$

$k_{I2} = 2.0x10^{17}exp(-82.9/RT)$ [MJP].

R_{I3} $N\text{-}C_4H_{10}$ =====> $CH_3 + N\text{-}C_3H_7$

$k_{I3} = 1.0x10^{17}exp(-83.4/RT)$ [MJP].

R_{I4} C_3H_8 =====> $CH_3 + C_2H_5$

$k_{I5} = 1.0x10^{17}exp(-85.1/RT)$ [MJP].

R_{I5} C_3H_6 =====> $CH_3 + C_2H_3$

$k_{I6} = 1.3x10^{16}exp(-85.8/RT)$ [240].

R_{I6} $1\text{-}C_4H8$ =====> $C_3H_5 + CH_3$

$k_{I6} = 1.3x10^{16}exp(-73.4/RT)$ [217].

R_{I7} $1\text{-}C_5H_{10}$ =====> $C_3H_5 + C_2H_5$

k_{I7} = $1.0x10^{16}exp(-71.4/RT)$ [217].

R_{I8} C_5H_8 =====> C_2H_3 + C_3H_5

k_{I8} = $1.0x10^{16}exp(-77.2/RT)$. Estimate, using the same A factor as k_{I7}, but with an increased activation energy to allow for the greater bond dissociation energy, assuming $\Delta H_f(C_2H_3)$=63.4 $kcalmol^{-1}$.

R_{I9} C_6H_{10} =====> 2 C_3H_5

k_{I9} = $2.5x10^{14}exp(-59.4/RT)$ [217].

Radical Decomposition Reactions

R_{D1} C_2H_5 =====> C_2H_4 + H

Rate constant calculated from the reverse reaction and equilibrium constant for the system. See Chapter 5 for details.

R_{D2} C_2H_3 =====> C_2H_2 + H

Rate constant calculated from the rate of the reverse reaction and the equilibrium constant for the system. See Chapter 5 for details.

Addition Reactions

R_{HAD1} H + C_2H_4 =====> C_2H_5

k_{HAD1} = $7.34x10^{-12}exp(-2.084/RT)$

k_{HAD1} was calculated at cracking temperatures using the model developed in Chapter 2, and found to be approximately a factor of five below its high pressure limit. See Chapter 5 for details.

R_{HAD2} H + C_2H_2 =====> C_2H_3

k_{HAD2} = $9.2x10^{-13}exp(-2.410/RT)$

k_{HAD2} was initially taken , by analogy with k_{HAD1}, to be a factor of five below its high pressure limit, but was reduced by

a further factor of two, to bring the predicted and observed acetylene into reasonable agreement. See Chapter 5 for details.

R_{HAD3} $H + 1\text{-}C_4H_8 \Longrightarrow CH_3 + C_2H_4$

$k_{HAD3} = 1.7 \times 10^{-11} \exp(-2.00/RT)$ Estimate.

R_{HAD4} $H + C_4H_6 \Longrightarrow C_2H_3 + C_2H_4$

$k_{HAD4} = k_{HAD3}$

R_{HAD6} $H + C_3H_6 \Longrightarrow CH_3 + C_2H_4$

$k_{HAD6} = 5.2 \times 10^{-11} \exp(-2.9/RT)$

The effect of variations in k_{HAD6} on the model predictions is discussed in the text.

R_{HAD7} $H + 1\text{-}C_5H_{10} \Longrightarrow C_2H_5 + C_3H_6$

$k_{HAD7} = k_{HAD3}$

R_{HAD8} $H + C_6H_{10} \Longrightarrow C_3H_5 + C_3H_6$

$k_{HAD8} = k_{HAD3}$

Abstraction Reactions

R_{HA1} $H + C_2H_6 \Longrightarrow H_2 + C_2H_5$

$k_{HA1} = 1.47 \times 10^{-21} T^{3.5} \exp(-2622/T)$ [230]. The effect of variations in this rate constant on the model predictions is discussed in Chapter 5.

R_{HA2} $H + C_2H_4 \Longrightarrow H_2 + C_2H_3$

k_{HA2} was linked to k_{HA3} by the thermochemistry chosen for the vinyl radical. See Chapter 5 for details.

R_{HA3} $H + CH_4 \Longrightarrow H_2 + CH_3$

$k_{HA3} = 3.6x10^{-20}T^{3}exp(-4402/T)$ [230].

R_{HA4} $H + N\text{-}C_4H_{10} =====> H_2 + C_2H_4 + C_2H_5$

k_{HA4} assumed to be equal to k_{HA5}.

R_{HA5} $H + N\text{-}C_4H_{10} =====> H_2 + C_3H_6 + CH_3$

$k_{HA5} = 1.2x10^{-10}exp(-7.15/RT)$ [MJP].

R_{HA6} $H + C_3H_8 =====> H_2 + C_3H_6 + H$

$k_{HA6} = 2.5x10^{-11}exp(-5.86/RT)$ [MJP].

R_{HA7} $H + C_3H_8 =====> H_2 + C_2H_4 + CH_3$

$k_{HA\&} = 3.2x10^{-11}exp(-7.84/RT)$ [MJP].

R_{HA8} $H + C_3H_6 =====> H_2 + C_3H_5$

$k_{HA8} = 5.3x10^{-11}exp(-3.5/RT)$

The effect of variation of this very uncertain rate constant is discussed in the text of Chapter 5.

R_{MA1} $CH_3 + C_2H_6 =====> CH_4 + C_2H_5$

$k_{MA1} = 7.9x10^{-13}exp(-11.5/RT)$ Estimate, using an average A factor for methyl radical abstraction reactions and an Evans-Polyani plot to calculate the activation energy. The effect of increasing the value of k_{MA1} to that recommended by Pacey and Purnell, is discussed in Chapter 5.

R_{MA2} $CH_3 + C_2H_4 =====> CH_4 + C_2H_3$

$k_{MA2} = 7.9x10^{-13}exp(-11.5/RT)$. Estimate, using an average A factor for methyl abstraction reactions and an Evans-Polyani plot to calculate the activation energy. Eact is increased by 1 $kcalmol^{-1}$ for every 2 $kcalmol^{-1}$ increase in $\Delta H_f(C_2H_3)$ above 63.4 $kcalmol^{-1}$.

R_{MA3} $CH_3 + H_2 \Longrightarrow CH_4 + H$

k_{MA3} was calculated from k_{HA3} and the equilibrium constant for the system. See Chapter 5 for details.

R_{MA4} $CH_3 + C_3H_6 \Longrightarrow CH_4 + C_3H_5$

$k_{MA4} = 2.6 \times 10^{-13} \exp(-8.8/RT)$ [217].

R_{EA1} $C_2H_5 + H_2 \Longrightarrow C_2H_6 + H$

k_{EA1} was calculated from k_{HA1} and the equilibrium constant for the reaction. See Chapter 5 for details.

R_{VA1} $C_2H_3 + C_2H_6 \Longrightarrow C_2H_4 + C_2H_5$

k_{VA1} was linked to k_{MA1} by the thermochemistry chosen for the vinyl radical. See Chapter 5 for details.

R_{VA2} $C_2H_3 + H_2 \Longrightarrow C_2H_4 + H$

k_{VA2} was linked to k_{MA3} by the thermochemistry chosen for the vinyl radical. See Chapter 5 for details.

R_{VA3} $C_2H_3 + CH_4 \Longrightarrow C_2H_4 + CH_3$

k_{VA3} was linked to k_{MA2} by the thermochemistry chosen for the vinyl radical. See Chapter 5 for details.

R_{VA4} $C_2H_3 + C_3H_6 \Longrightarrow C_2H_4 + C_3H_5$

k_{VA4} was linked to k_{MA4} by the thermochemistry chosen for the vinyl radical. See Chapter 5 for details.

R_{AA2} $C_3H_5 + C_2H_6 \Longrightarrow C_3H_6 + C_2H_5$

$k_{MA5} = 1.3 \times 10^{-12} \exp(-20.5/RT)$ [217].

R_{AA3} $C_3H_5 + H_2 \Longrightarrow C_3H_6 + H$

k_{AA3} was calculated from k_{HA8} and the equilibrium constant for the system. See Chapter 5 for details.

Recombination Reactions

R_{MM1} $CH_3 + CH_3 \Longrightarrow C_2H_6$

$k_{MM1} = 4.0 \times 10^{-11}$ Estimate from direct study at lower temperatures [26].

R_{EE1} $C_2H_5 + C_2H_5 \Longrightarrow N\text{-}C_4H_{10}$

$k_{EE1} = 2.1 \times 10^{-11}$ [18].

R_{EE2} $C_2H_5 + C_2H_5 \Longrightarrow C_2H_4 + C_2H_6$

$k_{EE2} = 0.15 k_{EE1}$ [18].

R_{EM1} $C_2H_5 + CH_3 \Longrightarrow C_3H_8$

$k_{EM1} = 5.8 \times 10^{-11}$ Mean Value Rule.

R_{EM2} $C_2H_5 + CH_3 \Longrightarrow C_2H_4 + CH_4$

$k_{EM2} = 0.04 k_{EM1}$ [217].

R_{HE1} $H + C_2H_5 \Longrightarrow CH_3 + CH_3$

$k_{HE1} = 2.0 \times 10^{-10}$ Upper Estimate.

R_{HV1} $H + C_2H_3 \Longrightarrow C_2H_4$

$k_{HV1} = 1.0 \times 10^{-10}$ Estimate.

R_{AH1} $H + C_3H_5 \Longrightarrow C_2H_3 + CH_3$

$k_{AH1} = 1.0 \times 10^{-10}$ Estimate.

R_{VV1} $C_2H_3 + C_2H_3 \Longrightarrow C_4H_6$

$k_{VV1} = 2.1 \times 10^{-11}$ Assumed same as k_{EE1} [18].

R_{VE1} $C_2H_3 + C_2H_5 \Longrightarrow 1\text{-}C_4H_8$

$k_{VE1} = 5.5x10^{-11}$ Estimate.

R_{VM1} $C_2H_3 + CH_3 \Longrightarrow C_3H_6$

$k_{VM1} = 5.5x10^{-11}$ Estimate.

R_{AA1} $C_3H_5 + C_3H_5 \Longrightarrow C_6H_{10}$

$k_{AA1} = 1.7x10^{-11}\exp(0.25/RT)$ [23].

R_{AM1} $C_3H_5 + CH_3 \Longrightarrow 1\text{-}C_4H_8$

$k_{AM1} = 5.5x10^{-11}$ Estimate.

R_{AV1} $C_3H_5 + C_2H_3 \Longrightarrow C_5H_{10}$

$k_{AV1} = 5.5x10^{-11}$ Estimate.

R_{AE1} $C_3H_5 + C_2H_5 \Longrightarrow C_5H_{12}$

$k_{AE1} = 5.5x10^{-11}$ Estimate.

Appendix 8

Calculated Equilibrium Constants

K_3: $H + C_2H_6 \equiv\equiv\equiv H_2 + C_2H_5$

K_4: $H + CH_4 \equiv\equiv\equiv H_2 + CH_3$

K_5: $H + C_3H_6 \equiv\equiv\equiv H_2 + C_3H_5$

K_6: $H + C_2H_4 \equiv\equiv\equiv H_2 + C_2H_3$

K_2 and K_6 are calculated assuming $\Delta H^{o}_{f,298}(C_2H_3) = 65$ kcalmol^{-1}.

Equilibrium constants in molecular units, temperatures in K.

Temperature	1053	1093	1118	1148
Equilibrium Constant				
$K_2/10^{-16}$	2.0	2.0	2.1	2.1
K_3	1249	1222	1210	1196
K_4	23.4	23.6	23.7	23.8
K_5	12600	9476	8020	6630
K_6	35.5	34.9	34.5	34.1